

UNIVERSITY OF THE BASQUE COUNTRY / EUSKAL
HERRIKO UNIBERTSITATEA

DOCTORAL THESIS

**Anharmonic effects in thermoelectric and
2D materials**

Author:

Unai ASEGUNOLAZA
AGUIRRECHE

Supervisors:

Dr. Ion ERREA and Dr. Aitor
BERGARA

*A thesis submitted in fulfillment of the requirements
for the degree of physics*

May 30, 2020

Declaration of authorship

I, Unai ASEGUINOLAZA AGUIRRECHE, declare that this thesis titled, "Anharmonic effects in thermoelectric and 2D materials" and the work presented in it are my own. I confirm that:

- This work was done wholly or mainly while in candidature for a research degree at this University.
- Where any part of this thesis has previously been submitted for a degree or any other qualification at this University or any other institution, this has been clearly stated.
- Where I have consulted the published work of others, this is always clearly attributed.
- Where I have quoted from the work of others, the source is always given. With the exception of such quotations, this thesis is entirely my own work.
- I have acknowledged all main sources of help.
- Where the thesis is based on work done by myself jointly with others, I have made clear exactly what was done by others and what I have contributed myself.

Signed:

Date:

Contents

Declaration of authorship	iii
Introduction	1
I Theoretical background	5
1 The adiabatic Born-Oppenheimer approximation	7
2 The electronic problem	11
2.1 Independent electron approximation	11
2.2 Density functional theory	12
2.3 Crystal periodicity and plane wave basis	15
2.4 Computational method	16
2.5 Pseudopotentials	17
3 The ionic problem	19
3.1 The harmonic approximation	19
3.2 Phonons from density functional perturbation theory	22
3.3 Phonons from the finite displacements method	23
3.4 Long-wavelength vibrations in polar materials	25
3.5 Anharmonic effects in solids	27
3.6 Perturbation theory of the phonon-phonon interaction	28
3.7 The stochastic self-consistent harmonic approximation	33
3.7.1 The stress tensor in the self-consistent harmonic approximation	36
3.7.2 The free energy Hessian and second-order phase transitions within the SSCHA	37
3.7.3 Perturbative limit of the SSCHA	38
3.7.4 Dynamical properties of solids and phonon frequencies within the SSCHA	39
4 Lattice thermal conductivity	45
4.1 Single mode relaxation time approximation (SMA)	49
4.2 Exact solution of the linearized BTE	50
II Thermoelectric monochalcogenides	51
5 Bulk SnSe	53
5.1 Introduction	53
5.2 Structure and high symmetry points	54
5.3 Calculation details	55
5.4 Phase transition	56

5.5 Phonons in <i>Cmcm</i> SnSe	60
5.6 Lattice thermal conductivity of <i>Cmcm</i> SnSe	62
5.7 Conclusions	64
6 Bulk SnS	69
6.1 Introduction	69
6.2 Calculation details	69
6.3 Electronic transport	70
6.4 Phase transition	72
6.5 Phonons in <i>Cmcm</i> SnS	73
6.6 Lattice thermal conductivity of <i>Cmcm</i> SnS	74
6.7 Conclusions	74
7 Monolayer SnSe	79
7.1 Introduction	79
7.2 Crystal structure and high symmetry points	80
7.3 Calculation details	80
7.4 Ferroelectric phase transition	81
7.5 Problem for calculating lattice thermal conductivity	83
7.6 Conclusions	84
III Phonons in 2D materials	85
8 2D materials: Graphene	87
8.1 Introduction	87
8.2 Crystal structure	89
8.3 Empirical potential benchmark and calculation parameters	91
8.4 Graphene without stress	92
8.5 Graphene phonons	95
8.6 Root mean square displacements and linewidths	97
8.7 SCHA applied to a continuum membrane Hamiltonian	98
8.8 Conclusions	104
Conclusions	107
IV Appendices	111
A Mathematical formulas and derivations for the membrane model	113
B Interpolation of SSCHA dynamical matrices	119
C Mathematical proof of quadratic harmonic ZA dispersion	121
V Bibliography	123
Bibliography	125

List of Figures

1	Record ZT materials	2
2	Thermoelectric physical magnitudes	3
2.1	DFT self-consistent cycle	17
3.1	SnS phonon spectrum	27
3.2	Diagrammatic representation of Dyson equation	29
3.3	Diagrammatic representation of the self-energy	30
3.4	Lorentzian and harmonic spectral functions	32
3.5	Flowchart of the SSCHA minimization process.	41
3.6	One dimensional example of the SSCHA	42
3.7	Free energy as a function of temperature in a second-order phase transition	42
3.8	Diagrammatic representation of SSCHA Dyson equation	43
3.9	SSCHA and harmonic spectral functions	43
4.1	Heat flow from the hot to the cold side	45
4.2	Thermal conductivity of CoSb_3	47
4.3	Feynman diagrams for three phonon scattering events	48
5.1	SnSe crystal structure	54
5.2	1BZ of $Cmcm$ SnSe	55
5.3	Phonon eigenvector patterns in $Cmcm$ SnSe	57
5.4	Phonon collapse in SnSe	58
5.5	Wyckoff z parameter of the 4c Wyckoff position in $Pnma$ SnSe	59
5.6	Harmonic phonons of $Cmcm$ SnSe exchanging the b and c lattice parameters.	60
5.7	Harmonic phonons of $Cmcm$ SnSe with different volumes.	61
5.8	Phonons in the Lorentzian approximation in SnSe	62
5.9	Comparison of phonons in the Lorentzian approximation and INS experiments.	63
5.10	Nonperturbative spectral function in SnSe	65
5.11	Perturbative and nonperturbative spectral functions in SnSe	66
5.12	Lattice thermal conductivity of SnSe	67
5.13	Thermal properties of $Cmcm$ SnSe	68
6.1	Band structure and P_F of SnS and SnSe	71
6.2	Phonon collapse in SnS	73
6.3	Phonons within the Lorentzian approximation in SnS	76
6.4	Lattice thermal conductivity of SnS and SnSe	77
7.1	Monolayer SnSe crystal structure	80
7.2	Distortion pattern associated to the Γ_1 mode.	81
7.3	Harmonic phonons of monolayer SnSe	82
7.4	Phonon collapse in monolayer SnSe	83

7.5	Anharmonic phonons in monolayer SnSe.	84
8.1	Root mean square atomic displacements of carbon atoms in graphene calculated using the harmonic dispersion	88
8.2	Graphene harmonic phonons	89
8.3	Graphene linewidths calculated within perturbation theory	90
8.4	Harmonic phonon spectrum of graphene calculated with the empirical potential and <i>ab initio</i> .	91
8.5	Harmonic, SSCHA and physical static frequencies using the DFT and machine learning (ML) forces.	92
8.6	Pressure as a function of the lattice parameter in graphene	92
8.7	Lattice parameter of graphene as a function of temperature	93
8.8	Graphene total energy U	94
8.9	Molecular dynamics run.	95
8.10	Molecular dynamics results.	96
8.11	Quasiharmonic free energy of graphene.	97
8.12	Graphene harmonic and anharmonic ZA phonons	98
8.13	Graphene static and dynamic phonons	98
8.14	E2g mode temperature dependent frequency shift	99
8.15	SSCHA root mean square atomic displacements and linewidths	100
8.16	ZA harmonic and anharmonic phonons in the membrane model.	102
8.17	δa as a function of temperature in the membrane model.	103
8.18	Atomistic and membrane linewidths calculated within the SSCHA and within perturbation theory in graphene	104
8.19	Fourth-order term contribution to the linewidth in graphene. Spectral function within the Lorentzian and non-Lorentzian approximations	105

List of Tables

5.1	Reduced \mathbf{q} vectors of the high symmetry points in the Brillouin zone of the $Cmcm$ phase.	55
5.2	Experimental and theoretical lattice parameters of $Cmcm$ SnSe	57
7.1	Reduced \mathbf{q} vectors of the high symmetry points in the Brillouin zone of the $Pnmm$ and $Pnm2_1$ phases.	81

Introduction

Thermoelectricity is a material property with an endless applications list. It allows to transform a temperature gradient into a voltage via the Seebeck effect[1, 2]. In the reverse way, it allows to transform a voltage into a temperature gradient via the Peltier effect[3, 4]. State of the art materials have very low thermoelectric efficiencies, which make them only useful in very specific applications. For example, one of the main historical applications of thermoelectric materials has been the radioisotope thermoelectric generator for NASA's space crafts[2]. Recent materials advances and an increasing awareness of energy and environmental conservation issues have rekindled prospects for automotive applications. Regarding the cooling applications, thermoelectric devices are interesting in electronic cooling, due to their high reliability and compact packaging[4]. For these reasons, the two fundamental research lines in the thermoelectric community are the following:

1. Find and synthesize materials with a higher thermoelectric efficiency.
2. Find and understand physical and chemical mechanisms that increase the thermoelectric efficiency.

The efficiency of a thermoelectric material is measured by the figure of merit

$$ZT = S^2\sigma T / \kappa. \quad (1)$$

ZT is a dimensionless number. S is the Seebeck coefficient, σ the electrical conductivity, T the temperature, and κ the thermal conductivity. With $ZT \simeq 3$ in a broad temperature range, the thermoelectric materials would be competitive against combustion engines in terms of efficiency in transforming heat into electricity[5]. In Fig. 1 we show the maximum figure of merit ZT_{max} of record thermoelectric materials as a function of the year when they were discovered or synthesized. As we can see, there is no material with ZT_{max} as high as 3. Even though there are some materials with a ZT_{max} of 2, this only happens for very narrow temperature ranges[6]. This limits the applications of these materials.

The power factor PF is the product of the squared Seebeck coefficient and the electrical conductivity. The idea behind a good thermoelectric material is very simple. We need materials with a high power factor and low thermal conductivity, the so called electron crystals and phonon glasses. The main problem behind the increase of ZT is the fact that the physical magnitudes that are involved are correlated among themselves. This correlation limits the ZT . In Fig. 2 we show a cartoon of the physical magnitudes that appear in the numerator of ZT as a function of the doping for a given temperature. We choose to plot the physical magnitudes as a function of the doping because it is one of the simplest manipulations to be applied. If we have a look to Fig. 2 we can see what is the fundamental limitation of the power factor. The electrical conductivity increases as a function of the carrier concentration, the Seebeck coefficient has the opposite trend, which makes the PF to have a peak

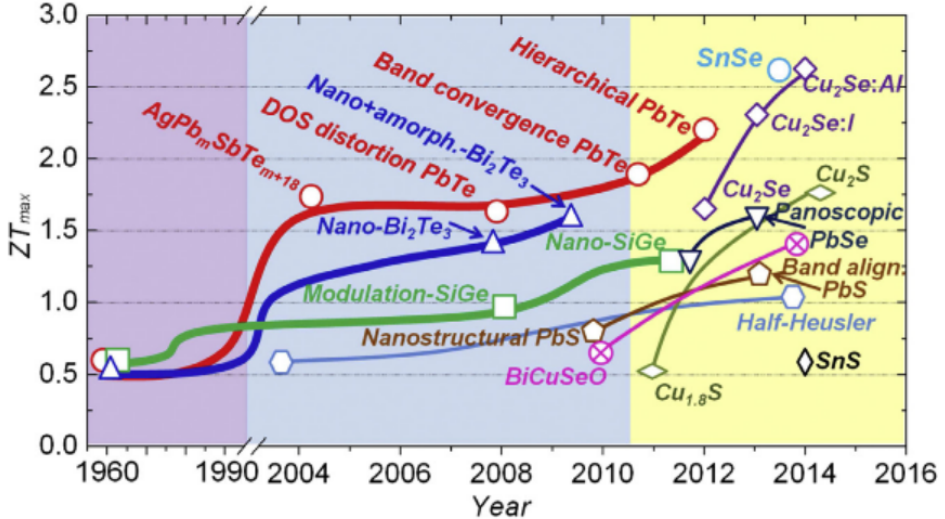


FIGURE 1: Record ZT materials as a function of the year. The figure is taken from reference[5].

that cannot be increased without further different manipulations. On top of this, the thermal conductivity of typical semiconductors increases as a function of the carrier concentration. This further decreases the carrier concentration at which the maximum ZT is obtained, but does not open any possibility to increase ZT . Obviously, apart from the fundamental limitations given by correlation, there are practical and technical limitations.

There are different ways to increase the thermoelectric efficiency of a material by physical and chemical manipulation. Materials have been doped[7, 8, 9] or nanosstructured[10, 11] in order to get a high power factor combined with a low thermal conductivity, yielding, i.e., $ZT \simeq 2.2$ in PbTe[12]. It has been shown that, in the proximity to a phase transition ZT may also soar, as in the case of Cu_2Se [13]. In these cases the thermal conductivity abruptly decreases close to the transition, reaching ZT values as high as 2.5.

In the last years, it has been shown that intrinsic semiconductors with an intrinsically low thermal conductivity may be materials with a very high ZT [6, 14]. The total thermal conductivity is the sum of electronic and lattice thermal conductivities. In intrinsic semiconductors, the main contribution to the thermal conductivity comes from the lattice as there are not many available charge carriers at normal temperatures. Therefore, the challenge is to find intrinsic semiconductors with an intrinsically low lattice thermal conductivity. The best thermoelectric material in this family is SnSe[6] with a ZT_{max} of 2.6. This material is not only the best thermoelectric in this family, but the best thermoelectric material overall.

At this point, theoretical material science plays a crucial role. Theory could reduce the experimental effort by searching for materials with an intrinsically low lattice thermal conductivity. The first-principles calculation of the lattice thermal conductivity is a complicated task and it is computationally demanding[15]. Anyways, nowadays it is included in the toolkit[16] of any theoretical material scientist. However, it has been found that, the intrinsically low lattice thermal conductivity

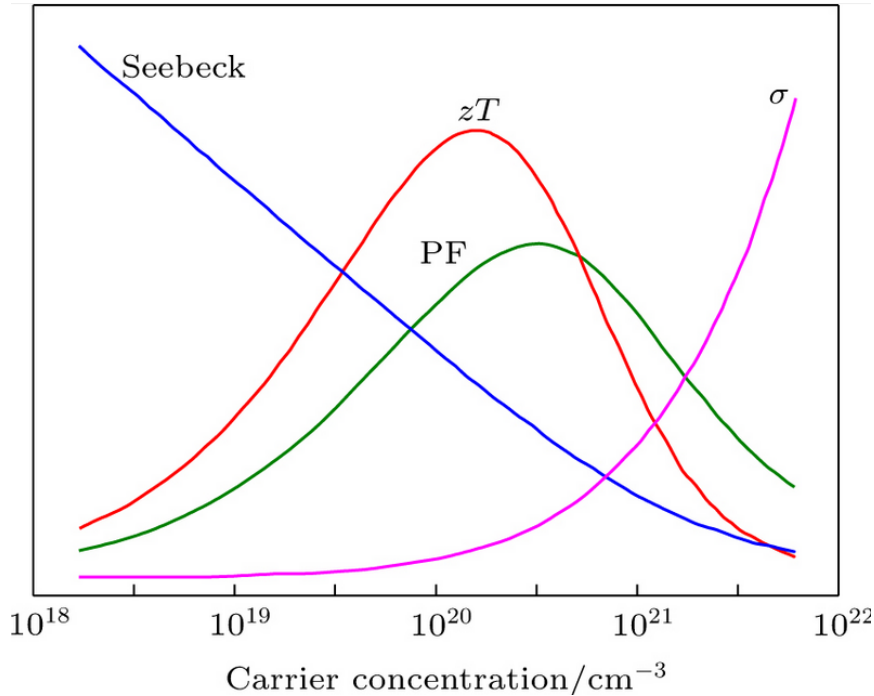


FIGURE 2: Electrical conductivity and Seebeck coefficient as a function of the carrier concentration in a typical semiconductor.

is frequently associated to a strongly anharmonic lattice[6, 17]. This is the case, for instance, in SnSe. The strong anharmonicity not only causes low thermal conductivity, it also creates interesting properties, such as, structural phase transitions. These structural phase transitions, in many cases, make thermoelectric materials more efficient[13]. However, materials that suffer continuous structural phase transitions are, usually, unstable within the harmonic approximation. The theory for calculating the lattice thermal conductivity is built on top of the harmonic approximation by using perturbation theory[18]. This is not possible when the system is unstable within the harmonic approximation. Furthermore, the perturbative approach is questionable in strongly anharmonic materials, even if they are stable within the harmonic approximation. The calculation of the transition temperature is, for the same reason, a complicated task. In the last years there have been several methods and implementations[19, 20, 21] that try to overcome these problems.

One of the main purposes of this thesis is to understand and predict this structural phase transformations that occur in thermoelectric materials and study what is the role they play in the thermoelectric efficiency. Once the structural and vibrational properties of these materials are studied, another purpose is to calculate the lattice thermal conductivity and understand what makes it so low in these materials with high ZT . For this purpose, we have chosen the most efficient thermoelectric material SnSe and its isoelectronic counterpart SnS. In order to account for the anharmonic effects at a nonperturbative level we have applied the so called stochastic self-consistent harmonic approximation[22, 23, 24, 25] (SSCHA).

In many cases, these structural phase transitions break the inversion symmetry of the material[17, 26]. This opens the door to interesting physical properties, such

as ferroelectricity. It has been shown that both properties, high thermoelectric efficiency and ferroelectricity, can coexist in the same material, as it happens in SnTe[17, 27]. There is an experimental work[26] showing that the dimensionality could dramatically change the transition temperature to the ferroelectric state. In the same work[26] they show that monolayer SnTe has a robust ferroelectric state that can be switched with an electric field. Thin film ferroelectrics are key for modern device applications[28]. However, it is known that there is a critical thickness for thin ferroelectrics, below which the depolarization field destroys the ferroelectric state[29, 30, 31]. This effect decreases the transition temperature to the ferroelectric state as a function of the sample thickness[32, 33] and sets a fundamental limit for technological applications. Monolayer SnSe could suffer a similar phase transition, which makes it a very promising candidate for technological applications. In this thesis we have studied the ferroelectric phase transition in monolayer SnSe[34]. We have also tried to study the thermal properties of monolayer SnSe.

As shown in the previous paragraph, there could be two dimensional (2D) multifunctional materials, which are interesting in thin film technologies. The acoustic out-of-plane vibrational modes play a crucial role[35] in the heat transfer in two dimensional materials. The understanding of the mechanical and thermal properties of these phonon modes is far from trivial. Even the possibility of having crystalline order in 2D has been long questioned[36, 37] due to the existence of these modes. It has been theoretically shown that the harmonic approximation fails[38] in the understanding of the acoustic out-of-plane mode, leading to unphysical consequences. Motivated by this we have studied the anharmonic effects in the out-of-plane acoustic phonon modes of graphene.

Long made short, the purpose of this thesis is to study the anharmonic effects in materials where the harmonic approximation and perturbation theory break down. For that purpose we have chosen technologically relevant candidates, such as, very efficient thermoelectric materials, 2D ferroelectrics, and graphene. In chapters 1, 2, 3, and 4 we show the theoretical background needed to study the electronic, vibrational, and thermal properties of the materials. In chapters 5 and 6 we show the results corresponding to bulk SnSe and SnS thermoelectrics. In chapter 7 we study the vibrational properties of monolayer SnSe. Finally, in chapter 8 we study the anharmonic effects in the atomic vibrations of graphene.

Part I

Theoretical background

Chapter 1

The adiabatic Born-Oppenheimer approximation

In the atomic scale, matter can be described as a set of electrons and ions interacting via the Coulomb interaction. These particles are arranged in a different way depending on the state of the system: gas, liquid, amorphous solid, crystalline solid, plasma... The correct formalism to study any of these systems is quantum mechanics, which reduces to solving the time-independent Schrödinger equation

$$H|\Psi_A\rangle = E_A|\Psi_A\rangle, \quad (1.1)$$

where H is the Hamiltonian of the system, E_A the eigenvalue with quantum number A and, $|\Psi_A\rangle$ its eigenvector. The corresponding eigenfunction is given by

$$\langle \mathbf{r}, \mathbf{R} | \Psi_A \rangle = \Psi_A(\mathbf{r}_1, \dots, \mathbf{r}_N, \mathbf{R}_1, \dots, \mathbf{R}_M) = \Psi_A(\mathbf{r}, \mathbf{R}), \quad (1.2)$$

with N electrons at positions $\mathbf{r} \equiv \{\mathbf{r}_1, \dots, \mathbf{r}_N\}$ and M ions at positions $\mathbf{R} \equiv \{\mathbf{R}_1, \dots, \mathbf{R}_M\}$. In the non-relativistic case and in the absence of external forces, the Hamiltonian in atomic units can be written as follows[39]

$$\begin{aligned} H = & \frac{1}{2} \sum_i^N \mathbf{p}_i^2 + \frac{1}{2} \sum_j^M \frac{\mathbf{P}_j^2}{m_j} - \sum_i^N \sum_j^M \frac{Z_j}{|\mathbf{r}_i - \mathbf{R}_j|} + \frac{1}{2} \sum_{i \neq j}^N \frac{1}{|\mathbf{r}_i - \mathbf{r}_j|} \\ & + \frac{1}{2} \sum_{i \neq j}^M \frac{Z_i Z_j}{|\mathbf{R}_i - \mathbf{R}_j|} = T_e + T_I + V_{e,I} + V_{e,e} + V_{I,I}, \end{aligned} \quad (1.3)$$

where \mathbf{p}_i and \mathbf{P}_j are electronic and ionic momentum operators, Z_j is the ionic charge, and m_j the ionic mass. T_e and T_I are the electronic and ionic kinetic energy operators, respectively, and $V_{e,I}$, $V_{e,e}$, and $V_{I,I}$ are the electron-ion, electron-electron and ion-ion Coulomb interaction terms. Unless otherwise stated, we will use atomic units in the whole manuscript.

The solution of this eigenvalue problem would provide us with the exact non-relativistic structure of matter given by $\Psi_A(\mathbf{r}, \mathbf{R})$. However, the problem has $3(N + M)$ degrees of freedom ($N, M \sim 10^{23}$ for macroscopic samples of matter) and the Coulomb interaction makes impossible to separate the many-body Hamiltonian into single-particle ones. This makes the problem unsolvable. Nevertheless, from these equations we can already state that all the properties of a material are a consequence of the Coulomb interaction and the many-body character of the Hamiltonian.

If we want to calculate the properties of matter, we need to use approximations right from the beginning. The first approximation we will apply is the Born-Oppenheimer approximation (BOA), which, as we will see in the following paragraphs, will allow us to separate the total Hamiltonian into electronic and ionic parts. The BOA is based on the huge difference of masses between electrons and ions ($m_j \sim 10^3$), which makes the electrons move much faster[40] and, therefore, adapt instantaneously to the slower motion of the ions.

We will start by separating the total Hamiltonian H into electronic H^e and ionic H^I parts. As we have assumed that ions do not move from the electronic point of view, the electronic Hamiltonian can be built with the terms of the total Hamiltonian that depend only on electronic degrees of freedom and take the ionic configuration \mathbf{R} as a parameter

$$H^e(\mathbf{R}) = T_e + V_{e,I}(\mathbf{R}) + V_{e,e} + V_{I,I}(\mathbf{R}). \quad (1.4)$$

We have included the ion-ion term because from the electronic point of view it is a constant as \mathbf{R} is a parameter. We define the electronic eigenvalue problem

$$H^e(\mathbf{R})|\psi_\alpha^e(\mathbf{R})\rangle = E_\alpha^e(\mathbf{R})|\psi_\alpha^e(\mathbf{R})\rangle, \quad (1.5)$$

where α is the quantum number of the electronic system. As the Hamiltonian only depends on \mathbf{R} parametrically, the same stays for the eigenvalues $E_\alpha^e(\mathbf{R})$ and eigenfunctions

$$\langle \mathbf{r} | \psi_\alpha^e(\mathbf{R}) \rangle = \psi_\alpha^e(\mathbf{r}; \mathbf{R}). \quad (1.6)$$

Since the electronic eigenfunctions form a complete set in \mathbf{r} space, it is possible to write any state of the total system as a linear combination of vectorial products expanded only on the electronic degrees of freedom

$$|\Psi_{\alpha\beta}\rangle = \sum_{\alpha'} C_{\alpha'\alpha\beta} |\psi_{\alpha'\beta}^I\rangle \otimes |\psi_{\alpha'}^e(\mathbf{R})\rangle, \quad (1.7)$$

where $C_{\alpha'\alpha\beta}$ is a complex tensor containing the expansion coefficients, $|\psi_{\alpha'\beta}^I\rangle$ is the eigenvector of the still to be determined H^I , and $\alpha\beta$ define the total quantum number A in Eq. 1.1. If we project Eq. 1.7 with $\langle \mathbf{r}, \mathbf{R} |$ we can see that the total wave function is an expansion of products of ionic and electronic wave functions

$$\Psi_{\alpha\beta}(\mathbf{r}, \mathbf{R}) = \sum_{\alpha'} C_{\alpha'\alpha\beta} \psi_{\alpha'\beta}^I(\mathbf{R}) \psi_{\alpha'}^e(\mathbf{r}; \mathbf{R}). \quad (1.8)$$

The α' index in $\psi_{\alpha'\beta}^I(\mathbf{R})$ points out that the ionic states depend on the electronic quantum number. However, we have not determined H^I yet. For that purpose, we plug $|\Psi_{\alpha\beta}\rangle$ in Eq. 1.1 and project it onto $\langle \psi_{\alpha'}^e(\mathbf{R}) |$

$$\langle \psi_{\alpha'}^e(\mathbf{R}) | H | \Psi_{\alpha\beta} \rangle = E_{\alpha\beta} \langle \psi_{\alpha'}^e(\mathbf{R}) | \Psi_{\alpha\beta} \rangle. \quad (1.9)$$

Plugging Eq. 1.7 in Eq. 1.9 and using $H = H^e + T_I$ we obtain

$$C_{\alpha'\alpha\beta} E_{\alpha'}^e(\mathbf{R}) |\psi_{\alpha'\beta}^I\rangle + \sum_{\alpha''} C_{\alpha''\alpha\beta} \langle \psi_{\alpha'}^e(\mathbf{R}) | T_I [|\psi_{\alpha''}^e(\mathbf{R})\rangle \otimes |\psi_{\alpha''\beta}^I\rangle] = C_{\alpha'\alpha\beta} E_{\alpha\beta} |\psi_{\alpha'\beta}^I\rangle, \quad (1.10)$$

where

$$T_I = \sum_j \frac{\mathbf{P}_j^2}{2m_j} = \sum_j \frac{[\mathbf{P}_j^2]_I}{2m_j} + \sum_j \frac{1}{2m_j} (2[\mathbf{P}_j]_I [\mathbf{P}_j]_e + [\mathbf{P}_j^2]_e) = [T_I]_I + \Delta H. \quad (1.11)$$

In the previous equation we have defined new operators $[O]_I$ and $[O]_e$ as an operator O acting only on $|\psi^e\rangle$ and $|\psi^I\rangle$ states, respectively. Eq. 1.10 is exact but we still have coupled electronic and ionic equations.

The last step for getting H^I is the so called adiabatic approximation. This approximation assumes that the electronic states cannot be excited by the ionic kinetic energy, so we only consider $\alpha' = \alpha$ in Eq. 1.10 and neglect ΔH . In this way Eq. 1.10 is simplified into a Schrödinger equation for the ions

$$H^I |\psi_{\alpha\beta}^I\rangle = E_{\alpha\beta} |\psi_{\alpha\beta}^I\rangle, \quad (1.12)$$

where

$$H^I \equiv H_\alpha^I = [T_I]_I + E_\alpha^e(\mathbf{R}). \quad (1.13)$$

The right hand side of Eq. 1.13 shows that the ions move in an effective potential energy surface $U_\alpha(\mathbf{R}) = E_\alpha^e(\mathbf{R})$ and this surface is different for different electronic eigenstates α . It has been shown that for the great majority of the crystals at normal conditions the quantum number α can be dropped from the ionic problem and only consider the electronic ground state. This happens because the electrons adapt instantaneously to the ground state and the ionic Hamiltonian can be rewritten

$$H^I = T_I + U(\mathbf{R}), \quad (1.14)$$

where $U(\mathbf{R}) \equiv E_0^e(\mathbf{R})$ is the ground state energy of the electronic Hamiltonian. In this way the electronic and ionic problems are decoupled and ionic eigenstates do not depend on electronic quantum numbers anymore. Now, we can write any eigenstate of the Born-Oppenheimer Hamiltonian ($H_{BO} = H^e + H^I$) as a tensor product of individual electronic and ionic eigenstates

$$|\Psi_{\alpha\beta}\rangle = |\psi_\alpha^e(\mathbf{R})\rangle \otimes |\psi_\beta^I\rangle \equiv |\alpha, \beta\rangle. \quad (1.15)$$

In this basis H_{BO} is diagonal

$$\langle \alpha' \beta' | H_{BO} | \alpha \beta \rangle = E_{\alpha\beta} \delta_{\alpha\alpha'} \delta_{\beta\beta'}. \quad (1.16)$$

The BOA has proven to be an excellent approximation for calculating and understanding electronic and vibrational properties of different materials. In this thesis we will not go beyond this approximation, however, it is important to note that there are physical properties that arise due to the electronic excitations by the ionic motions, such as, electrical resistivity, superconductivity... Even if these properties point out that the BOA is not enough for describing many material's properties, the picture of the separate electronic and ionic systems can be kept and treat their coupling as a perturbation.

Chapter 2

The electronic problem

In this section we will see how to solve the electronic part given by the BOA. We will drop the \mathbf{R} parametric dependence introduced in chapter 1 for simplifying the notation in this chapter. If we have a look at the electronic Hamiltonian in Eq. 1.4, we realize that the electron-electron interaction $V_{e,e}$ potential couples the equations via the two-body operator $|\mathbf{r}_i - \mathbf{r}_j|^{-1}$ and makes impossible to separate the many-body Hamiltonian into single-particle ones. In this thesis we will apply a mean-field theory named density functional theory (DFT) for transforming the many-body problem into a single-particle one and solve it. First of all, we will see what is the advantage of transforming the many-body system into a single-particle one by analyzing the independent electron approximation.

2.1 Independent electron approximation

The simplest mean-field approximation for the electron-electron interaction is setting it to 0, the so called independent electron approximation. By neglecting this term, the electrons do not see each other and we are left with a system of N non-interacting particles under an external potential

$$V_{ext}(\mathbf{x}) = \sum_j^M \frac{Z_j}{|\mathbf{x} - \mathbf{R}_j|}, \quad (2.1)$$

where \mathbf{x} denotes any electronic position. Now it is possible to separate the Hamiltonian into single-particle Hamiltonians $H^e = \sum_i^N H_i^e = \sum_i^N [T_e(\mathbf{r}_i) + V_{ext}(\mathbf{r}_i)]$ and get the single electron states $|\phi_{\alpha_i}\rangle$ from

$$\left(-\frac{\nabla^2}{2} + V_{ext} \right) |\phi_{\alpha_i}\rangle = \epsilon_{\alpha_i} |\phi_{\alpha_i}\rangle, \quad (2.2)$$

where ϵ_{α_i} are the eigenvalues and $\langle \mathbf{x} | \phi_{\alpha_i} \rangle = \phi_{\alpha_i}(\mathbf{x})$ the eigenfunctions. Within the independent electron approximation, any total wave function of the electronic system could be given by a Slater determinant[41]

$$\psi_{\alpha}^e(\mathbf{r}) = \frac{1}{\sqrt{N!}} \begin{vmatrix} \phi_{\alpha_1}(\mathbf{r}_1) & \phi_{\alpha_1}(\mathbf{r}_2) & \dots & \phi_{\alpha_1}(\mathbf{r}_N) \\ \phi_{\alpha_2}(\mathbf{r}_1) & \phi_{\alpha_2}(\mathbf{r}_2) & \dots & \phi_{\alpha_2}(\mathbf{r}_N) \\ \vdots & \vdots & \ddots & \vdots \\ \phi_{\alpha_N}(\mathbf{r}_1) & \phi_{\alpha_N}(\mathbf{r}_2) & \dots & \phi_{\alpha_N}(\mathbf{r}_N) \end{vmatrix}, \quad (2.3)$$

with $\alpha \equiv \alpha_1, \alpha_2 \dots \alpha_N$ and $\langle \mathbf{r}_j | \phi_{\alpha_i} \rangle = \phi_{\alpha_i}(\mathbf{r}_j)$ being the single-electron wave function of the j^{th} electron at the α_i^{th} state.

This derivation shows that transforming the many-body system into a single-particle one is very convenient and makes the solution for many-electron systems possible. However, neglecting the electron-electron interaction is a very bad approximation[40] because it is responsible for many physical properties. In this work we will apply DFT to get a more accurate mean-field theory for the electronic system.

2.2 Density functional theory

The formalism of DFT[42, 43] was mainly developed in the 60's by Kohn, Hohenberg, and Sham and it became very popular in the 90's when the computational power got strong enough for its implementation. Since two decades it is one of the state of the art methods for studying solid state and molecular systems. Kohn and Sham were awarded with the Nobel Prize in 1998 for their contributions to DFT.

The main ingredient of DFT is the ground state electronic density

$$n_0(\mathbf{x}) = \langle \psi_0^e | n(\mathbf{x}) | \psi_0^e \rangle = \langle \psi_0^e | \sum_i^N \delta(\mathbf{x} - \mathbf{r}_i) | \psi_0^e \rangle = \\ N \int (\dots) \int d\mathbf{r}_2 \dots d\mathbf{r}_N \psi_0^{e*}(\mathbf{x}, \mathbf{r}_2, \dots, \mathbf{r}_N) \psi_0^e(\mathbf{x}, \mathbf{r}_2, \dots, \mathbf{r}_N), \quad (2.4)$$

together with two theorems. The first theorem states that for any system of interacting particles in an external potential $V_{ext}(\mathbf{x})$, $V_{ext}(\mathbf{x})$ is uniquely determined, except for a constant, by the ground state density $n_0(\mathbf{x})$. Since the Hamiltonian is fully determined, it follows that all the properties of the system are completely determined given only $n_0(\mathbf{x})$. The second theorem states that a universal functional of the total energy $E^e[n_0(\mathbf{x})]$ can be defined for any $V_{ext}(\mathbf{x})$. The minimum of this functional is the ground state energy of the system and the density that minimizes the functional is the exact ground state density. Therefore, the functional $E^e[n_0(\mathbf{x})]$ alone is sufficient to determine the exact ground state energy and density.

In our case the external potential is the electron-ion interaction

$$V_{ext}(\mathbf{x}) = \sum_j^M \frac{Z_j}{|\mathbf{x} - \mathbf{R}_j|} = \sum_j^M v_{ext}(\mathbf{x} - \mathbf{R}_j). \quad (2.5)$$

In order to apply these two theorems to the many-body electronic problem, Kohn and Sham proposed a new way of interpreting the electronic system. Their goal was to find a single-particle problem that would minimize the $E^e[n_0]$ functional. For that purpose, they replaced the interacting electronic system with a non-interacting one that would have exactly the same ground state density. The Hamiltonian of the non-interacting system or the Kohn-Sham Hamiltonian is separable

$$H^e(\mathbf{r}) = \sum_i^N \left[-\frac{1}{2} \nabla_{\mathbf{r}_i}^2 + V^{KS}(\mathbf{r}_i) \right] = \sum_i^N H^{KS}(\mathbf{r}_i), \quad (2.6)$$

where the Kohn-Sham one-electron ground state vectors $|\phi_{0i}\rangle$ fulfill

$$H^{KS} |\phi_{0i}\rangle = \epsilon_{0i} |\phi_{0i}\rangle. \quad (2.7)$$

The total Kohn-Sham state of this non-interacting system $|\psi_0^{KS}\rangle$ is built with a Slater determinant as in Eq. 2.3. Now, the main ingredient of DFT can be written as the sum of densities of single-particle densities

$$n_0(\mathbf{x}) = \sum_i^N |\phi_{0i}|^2. \quad (2.8)$$

Eq. 2.7 is equivalent to Eq. 2.2 in the independent electron approximation, the difference is that $V^{KS}(\mathbf{r}_i)$ includes the electron-electron interaction in a mean-field form. However, even if we know that it exists, we do not know the functional form of V^{KS} yet.

We will see now how to get the V^{KS} functional. The electronic energy functional can be written as

$$E^e[n_0] = T_e[n_0] + E_{e,e}[n_0] + E_{ext}[n_0], \quad (2.9)$$

where the functional form of the electron-ion energy is

$$E_{ext}[n_0] = \int d\mathbf{x} n_0(\mathbf{x}) V_{ext}(\mathbf{x}). \quad (2.10)$$

The energy functionals of $T_e[n_0]$ and $E_{e,e}[n_0]$ are not so straightforward to obtain. It is convenient to split the electronic kinetic energy functional in two parts $T_e[n_0] = T_e^{KS}[n_0] + T_C[n_0]$. The first term is the Kohn-Sham or the independent electron kinetic energy. As the total Kohn-Sham wave function $|\psi_0^{KS}\rangle$ can be written as an expansion of Kohn-Sham state $|\phi_{0i}\rangle$ products, $T_e^{KS}[n_0]$ accounts for the single-particle kinetic energy via \mathbf{p}_i . $T_C[n_0]$ provides the correlation kinetic energy, which arises due to the fact that the motion of one electron affects the motion of another. It is important to note that $T_e^{KS}[n_0]$ accounts for most of the total electronic kinetic energy. The functional form of $T_e^{KS}[n_0]$ is

$$\begin{aligned} T_e^{KS}[n_0] &= \langle \psi_0^{KS} | T_e^{KS} | \psi_0^{KS} \rangle = \\ &= -\frac{1}{2} \sum_i^N \langle \phi_{0i} | \nabla^2 | \phi_{0i} \rangle = -\frac{1}{2} \sum_i^N \int d\mathbf{x} \phi_{0i}^*(\mathbf{x}) \nabla^2 \phi_{0i}(\mathbf{x}), \end{aligned} \quad (2.11)$$

where the density dependence of $T_e^{KS}[n_0]$ is implicit as it comes from the density dependence of $\phi_{0i}(\mathbf{x})$. Something similar can be done with the electron-electron energy functional, we separate the total functional into the single-electron and correlation parts

$$E_{e,e}[n_0] = E_{e,e}^{KS}[n_0] + E_{e,e,C}[n_0], \quad (2.12)$$

where the Kohn-Sham electron-electron energy functional contains the Hartree $E_H[n_0]$ and exchange $E_X[n_0]$ terms

$$E_{e,e}^{KS} = E_H[n_0] + E_X[n_0], \quad (2.13)$$

which can be written as

$$E_H[n_0] = \frac{1}{2} \int \int d\mathbf{x} d\mathbf{x}' \frac{n_0(\mathbf{x}) n_0(\mathbf{x}')}{|\mathbf{x} - \mathbf{x}'|}, \quad (2.14)$$

$$E_X[n_0] = -\frac{1}{2} \sum_{i,j} \int \int d\mathbf{x} d\mathbf{x}' \frac{\phi_{0i}^*(\mathbf{x}) \phi_{0i}(\mathbf{x}') \phi_{0j}^*(\mathbf{x}') \phi_{0j}(\mathbf{x})}{|\mathbf{x} - \mathbf{x}'|}. \quad (2.15)$$

The Hartree energy accounts for the interaction that an electronic density has with itself. The exchange term accounts for the antisymmetric nature of the wave function with respect to the exchange of any two particle coordinates and the quantized nature of electrons, meaning it corrects the self-interaction of each electron wrongly included in $E_H[n_0]$. Again, the $E_{e,e,C}[n_0]$ energy is the potential correlation energy that $E_{e,e}^{KS}[n_0]$ lacks.

Now we can rewrite the total energy functional as

$$E^e[n_0] = T_e^{KS}[n_0] + E_{ext}[n_0] + E_H[n_0] + E_X[n_0] + T_C[n_0] + E_{e,e,C}[n_0]. \quad (2.16)$$

Correlation energies arise due to the many-body character of the system and can only be calculated exactly by solving the many-body Schrödinger equation[44]. The only terms that need an approximation are the correlation energies $T_C[n_0]$ and $E_{e,e,C}[n_0]$, however, the calculation of $E_X[n_0]$ is more expensive than the calculations of $T_e^{KS}[n_0]$, $E_{ext}[n_0]$ and $E_H[n_0]$. Thus, it is very common in DFT to give an approximate functional for the exchange energy as well. In the end the total energy functional can be written as

$$E^e[n_0] = T_e^{KS}[n_0] + E_{ext}[n_0] + E_H[n_0] + E_{xc}[n_0], \quad (2.17)$$

where $E_{xc}[n_0]$ contains the exchange and correlation functionals and it is named exchange-correlation energy.

Now we minimize the total electronic energy functional with respect to $\phi_{0_i}^*(\mathbf{x})$

$$\frac{\delta}{\delta \phi_{0_i}^*(\mathbf{x})} \left(E^e[n_0] - \sum_j \epsilon_j \left(\int d\mathbf{x} \phi_{0_j}^*(\mathbf{x}) \phi_{0_j}(\mathbf{x}) - 1 \right) \right) = 0, \quad (2.18)$$

where ϵ_j are Lagrange multipliers related to the normalization condition of the single-particle wave functions. Using Eq. 2.8 we can get

$$-\frac{1}{2} \nabla^2 \phi_{0_i}(\mathbf{x}) + \left(\frac{\delta E_{ext}[n_0]}{\delta n_0(\mathbf{x})} + \frac{\delta E_H[n_0]}{\delta n_0(\mathbf{x})} + \frac{\delta E_{xc}[n_0]}{\delta n_0(\mathbf{x})} \right) \phi_{0_i}(\mathbf{x}) = \epsilon_i \phi_{0_i}(\mathbf{x}). \quad (2.19)$$

We know from the second Hohenberg and Kohn theorem that the density that minimizes the total electronic energy functional is the exact ground state energy. Since electrons are fermions, the ground-state density is

$$n_0(\mathbf{x}) = \sum_i f_{0_i} |\phi_{0_i}(\mathbf{x})|^2, \quad (2.20)$$

where f_{0_i} is the Fermi-Dirac distribution function given by

$$f_{\alpha_i} = \frac{2}{e^{\beta(\epsilon_{\alpha_i} - \epsilon_F)} + 1}, \quad (2.21)$$

with $\beta = 1/(k_B T)$ k_B being the Boltzmann's constant, T the temperature, and ϵ_F the Fermi energy or the highest occupied energy. The 2 factor in Eq. 2.21 accounts for the spin degeneracy because in this work we have not included spin dependent terms in the electronic Hamiltonian. Now for obtaining $V^{KS}(\mathbf{x})$ we compare Eq. 2.7 with

Eq. 2.19 and we get

$$V^{KS}(\mathbf{x}) = V_{ext}(\mathbf{x}) + \int d\mathbf{x}' \frac{n_0(\mathbf{x}')}{|\mathbf{x} - \mathbf{x}'|} + \frac{\delta E_{xc}[n_0]}{\delta n_0(\mathbf{x})} = V_{ext}(\mathbf{x}) + V_H(\mathbf{x}) + V_{xc}(\mathbf{x}). \quad (2.22)$$

With the knowledge of the functional form of the exchange-correlation energy we would get the ground state density and energy exactly. However, the functional is not known and approximations are necessary. Since the first DFT implementations many functionals [45, 46] for E_{xc} have been proposed with their benefits and pathologies. The analysis and development of exchange-correlation functionals is a science on itself and it is out of the scope of this thesis. For this reason we will not go further in this topic. In this work we have made use of the most simple and common functionals, the LDA[45] (local density approximation) and GGA[46] (generalized gradient approximation). The LDA takes the functional of the homogeneous electron gas[47] by assuming that the electronic density of the system is homogeneous. Thus, the E_{xc} at each point depends only on the density at that point. The GGA not only considers the density of the system at each point but includes a gradient correction. In this work we have used the PBE[46] parametrization of the GGA. These approximations seem too simple but provide surprisingly good results as the density of the valence electrons in normal solids is not so far from the homogeneous electron gas[39].

2.3 Crystal periodicity and plane wave basis

In this section we will see how the Kohn-Sham wave functions of a crystalline material can be expanded on plane waves and how this is applied to the DFT formalism. A crystalline solid is formed by the periodic repetition of its unit cell. Since the system is periodic, the Hamiltonian must be periodic and the following symmetry holds for the Kohn-Sham potential V^{KS}

$$V^{KS}(\mathbf{x} + \mathbf{T}) = V^{KS}(\mathbf{x}), \quad (2.23)$$

where \mathbf{T} is a general lattice vector. Bloch's theorem[40] states that the eigenstates of a single electron Hamiltonian with a periodic potential can be chosen to have the form of a plane wave times a function with the periodicity of the lattice

$$\phi_{n\mathbf{k}}(\mathbf{x}) = u_{n\mathbf{k}}(\mathbf{x})e^{i\mathbf{k}\cdot\mathbf{x}}, \quad (2.24)$$

where $u_{n\mathbf{k}}(\mathbf{x} + \mathbf{T}) = u_{n\mathbf{k}}(\mathbf{x})$ is the periodic part of the Kohn-Sham state $\phi_{n\mathbf{k}}(\mathbf{x})$. Note that the quantum number i is now splitted in a band index n and a \mathbf{k} point, where \mathbf{k} is a vector inside the first Brillouin zone (1BZ). One can apply Born-von Karman periodic boundary conditions[40] on $\phi_{n\mathbf{k}}(\mathbf{x})$, in that case the number of allowed wave vectors \mathbf{k} in the 1BZ is finite and equals the number of unit cells in the crystal.

In the calculations performed in this work we have used a plane wave basis with

$$\langle \mathbf{x} | \mathbf{k} \rangle = \frac{1}{\sqrt{\Omega}} e^{i\mathbf{k}\cdot\mathbf{x}}, \quad (2.25)$$

where Ω is the total volume of the crystal. Taking into account that $u_{n\mathbf{k}}(\mathbf{x})$ is periodic, only reciprocal lattice vectors \mathbf{G} , for which

$$e^{i\mathbf{G}\cdot\mathbf{T}} = 1, \quad (2.26)$$

contribute to the plane wave expansion and the Kohn-Sham state can be written as

$$|\phi_{n\mathbf{k}}\rangle = \sum_{\mathbf{G}} c_{n\mathbf{k}+\mathbf{G}} |\mathbf{k} + \mathbf{G}\rangle, \quad (2.27)$$

where $\langle \mathbf{x} | \phi_{n\mathbf{k}} \rangle = \phi_{n\mathbf{k}}(\mathbf{x})$. Therefore, for a given \mathbf{k} point within the 1BZ, the single-particle wave functions can be expanded as in Eq. 2.27.

Once we have decided to expand the electronic wave functions in a plane wave basis, H^{KS} has to be diagonalized at every \mathbf{k} point allowed by the Born-von Karman boundary conditions within the 1BZ. The eigenvalues obtained at each \mathbf{k} point yield the single-particle energies, or band energies, $\epsilon_{n\mathbf{k}}$. In order to get the band energies for a given \mathbf{k} point, the matrix that needs to be diagonalized looks like

$$\langle \mathbf{k} + \mathbf{G} | H^{KS} | \mathbf{k} + \mathbf{G}' \rangle = \frac{1}{2} |\mathbf{k} + \mathbf{G}|^2 \delta_{\mathbf{G}\mathbf{G}'} + V^{KS}(\mathbf{G} - \mathbf{G}'). \quad (2.28)$$

The equality in Eq. 2.28 is easy to get taking into account that the kinetic energy is diagonal in the plane wave basis and $V^{KS}(\mathbf{k})$ is the Fourier transform of $V^{KS}(\mathbf{x})$. The eigenvalues of the matrix will be the energies $\epsilon_{n\mathbf{k}}$ and, for a given quantum number $n\mathbf{k}$, the eigenvector will be formed by the $c_{n\mathbf{k}+\mathbf{G}}$ coefficients. So far we have all the elements of Eq. 2.27 and finally, the electron density can be calculated from the Kohn-Sham states as

$$n_0(\mathbf{x}) = \sum_n \sum_{\mathbf{k}}^{1BZ} f_{n\mathbf{k}} |\phi_{n\mathbf{k}}(\mathbf{x})|^2, \quad (2.29)$$

where the sum extends to the 1BZ.

2.4 Computational method

In section 2.2 we have described the basics of DFT. We have seen that instead of solving a many-body problem, we can solve a single-particle system that has the same ground state density and energy. However, in the formalism the electronic density is the input and output at the same time, because we need it for constructing the Kohn-Sham potential V^{KS} . Therefore, the problem must be solved in a self-consistent way as explained in Fig. 2.1

First of all we need a guess for the electronic density, which, for instance, can be the sum of the atomic electronic densities. With this density we can build the Kohn-Sham potential and solve the Kohn-Sham equations. With the eigenfunctions of the solution we can build a new density and repeat the process. We will consider that the total energy of the system is converged when the difference in energy between two steps, ΔE , is smaller than the threshold energy ϵ .

In this thesis we have used the *Quantum Espresso*[16] software package which implements the self-consistent procedure and uses a plane wave basis to expand the

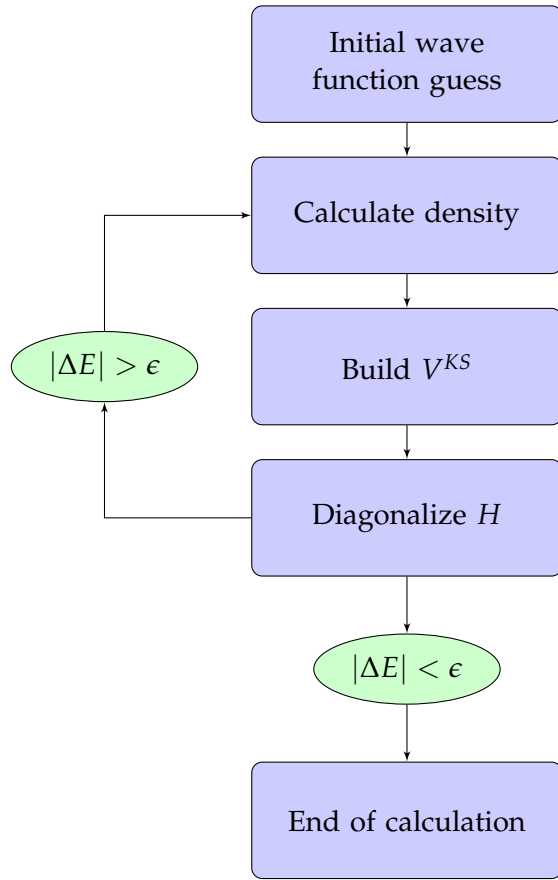


FIGURE 2.1: Flowchart of the self-consistent cycle for solving the Kohn-Sham equation. ΔE and ϵ are the energy difference between current cycle and the previous and the chosen threshold, respectively.

Kohn-Sham wave functions as described in section 2.3. As we have seen in the plane wave expansion in Eq. 2.27, in principle, the sum contains an infinite number of \mathbf{G} reciprocal vectors. In practice, a cutoff energy E_{cutoff} is taken so that the \mathbf{G} vectors satisfy

$$\frac{1}{2}|\mathbf{k} + \mathbf{G}|^2 \leq E_{cutoff}. \quad (2.30)$$

The proper value of E_{cutoff} is system dependent because highly localized states require the inclusion of a large amount of \mathbf{G} vectors in the expansion.

We have seen as well that H^{KS} need to be diagonalized in every \mathbf{k} allowed by the Born-Von Karman boundary conditions within the 1BZ. If the crystal is infinite, we have infinite matrices to diagonalize and, therefore, we divide the 1BZ in a Monkhorst-Pack[48] grid. This grid must be optimised to provide the convergence in energy that we want to achieve.

2.5 Pseudopotentials

Finally, we will introduce the concept of the pseudopotentials[39], which is used in the *Quantum Espresso* framework for speeding up the calculations.

Atoms in a solid are composed by a nucleus and core and valence electrons. Valence electrons are responsible for the interaction among different atoms in a solid, thus, one could think about not including the core electrons in the electronic problem. However, this is a very bad approximation because all the electronic eigenfunction of the system must be orthogonal, which means that core and valence electronic wave functions have to be orthogonal among themselves. On top of that, the core electrons have a non-negligible contribution to the external potential v_{ext} .

In order to account for the core electrons in the external potential and make the valence electronic wave functions smoother close to the nuclei, pseudopotentials are used. First of all the electronic wave functions of the atoms are calculated within DFT. Once we have all the wave functions, we have to decide which ones are core and which ones valence electrons. We take the valence electronic wave functions $\phi_i(\mathbf{x})$ and we create new wave functions $\phi_i^{ps}(\mathbf{x})$ which are smoother than the original ones below a given radius R_c . With this pseudo wave function of the valence electrons we will solve the Schrödinger equation in Eq. 2.7 and we will get the potential $v_i^{ps}(\mathbf{x})$ for each orbital channel. That pseudopotential is the one we will use to build v_{ext} , which takes into account the inner electrons of the ion.

The smooth part of the pseudo wave function is non-unique and it is different for different pseudopotentials. In this work we have applied norm-conserving[49, 50] (NC), ultrasoft[51] (US), and projector augmented[52] (PAW) pseudopotentials. In NC pseudopotentials the charge enclosed by the core radius in the all-electron wave function is preserved in the pseudo wave function. US pseudopotentials relax the norm-conserving constraint allowing for a smoother core part of the wave function and, thus, requiring less plane waves, yet compromising transferability from one system to another and making more testing necessary to avoid spurious results. PAW pseudopotentials have smaller radial cutoffs and reconstruct the exact valence wave function with all nodes in the core region.

Chapter 3

The ionic problem

The adiabatic BOA allowed us to separate the electronic and ionic problems. So far, we have shown how to solve the electronic part. Electronic degrees of freedom are responsible for many properties of solids, nevertheless, many other, such as, thermal and electrical resistivity arise due to ionic degrees of freedom.

In order to study the dynamics of ions we have to solve the nuclear Schrödinger equation in Eq. 1.12. As we saw in Eq. 1.14, the ions move in a potential given by the previously calculated electronic total ground state energy which is usually named Born-Oppenheimer Energy Surface (BOES).

The BOES has around 10^{23} degrees of freedom and it is an extremely complex energy landscape. The nuclear Hamiltonian is unsolvable unless the problem is simplified by applying approximations. The first non-trivial approximation we can adopt to solve this problem is the harmonic approximation, which is a low-order expansion of the BOES in the atomic displacements and is justified by the fact that in many solids the atomic displacements are much smaller than the interatomic distances[40].

3.1 The harmonic approximation

From now on the ions are not frozen and are allowed to move. The harmonic approximation departs from the classical picture where the atoms oscillate around their equilibrium positions. These equilibrium positions are defined as the minimum of the BOES. In this framework the position of the s^{th} atom in the m^{th} unit cell can be described as

$$\mathbf{R}_s(\mathbf{T}_m) = \mathbf{T}_m + \boldsymbol{\tau}_s + \mathbf{u}_s(\mathbf{T}_m) = \mathbf{R}_s^0(\mathbf{T}_m) + \mathbf{u}_s(\mathbf{T}_m), \quad (3.1)$$

where $\mathbf{u}_s(\mathbf{T}_m)$ is the displacement of the atom from its equilibrium position $\mathbf{R}_s^0(\mathbf{T}_m)$, \mathbf{T}_m is the lattice vector from the origin to the origin of the m^{th} cell, and $\boldsymbol{\tau}_s$ is the basis vector that denotes the equilibrium position of the atom inside the unit cell. Once we have set the equilibrium atomic positions we can Taylor expand the BOES in the atomic displacements

$$U(\mathbf{R}) = U(\mathbf{R}^0) + \sum_{n=2}^{\infty} U_n, \\ U_n = \frac{1}{n!} \sum_{\substack{s_1 \dots s_n \\ \alpha_1 \dots \alpha_n \\ \mathbf{T}_1, \dots, \mathbf{T}_n}} {}^{(n)}\phi_{s_1 \dots s_n}^{\alpha_1 \dots \alpha_n}(\mathbf{T}_1, \dots, \mathbf{T}_n) u_{s_1}^{\alpha_1}(\mathbf{T}_1) \dots u_{s_n}^{\alpha_n}(\mathbf{T}_n), \quad (3.2)$$

with

$$\phi_{s_1 \dots s_n}^{(n)}(\mathbf{T}_1, \dots, \mathbf{T}_n) = \frac{\partial^n U}{\partial u_{s_1}^{\alpha_1}(\mathbf{T}_1) \dots \partial u_{s_n}^{\alpha_n}(\mathbf{T}_n)} \Big|_{\mathbf{R}^0}. \quad (3.3)$$

The number of possible \mathbf{T} lattice vectors is equal to the number of unit cells. The atom index s goes from 1 to N_s , the number of atoms per unit cell, and α runs on the Cartesian coordinates x, y , and z . $\phi_{s_1 \dots s_n}^{(n)}(\mathbf{T}_1, \dots, \mathbf{T}_n)$ are the n body force-constants (n BFC). For the 2BFC we omit the index (2). As a rigid shift of the crystal cannot change the energy of the system, 2BFC fulfill the following equality

$$\sum_{\mathbf{T}_1, \alpha_1, s_1} \phi_{s_1 s_2}^{\alpha_1 \alpha_2}(\mathbf{T}_1, \mathbf{T}_2) = 0, \quad (3.4)$$

which is named acoustic sum rule (ASR). The ASR can be generalized to any nBFC.

In principle, the ionic configuration \mathbf{R} depends on the three lattice vectors of the system $\mathbf{R} \equiv \mathbf{R}(\{\mathbf{a}_i\}) i = 1, 2, 3$ and, therefore, the BOES also depends on them. The Born-Oppenheimer stress tensor can be defined as

$$P_{\alpha\beta}^{BO}(\mathbf{R}) = -\frac{1}{\Omega} \frac{\partial U(\mathbf{R})}{\partial \epsilon_{\alpha\beta}} \Big|_{\epsilon=0}, \quad (3.5)$$

where $\epsilon_{\alpha\beta}$ is the strain tensor. From now on we will suppose that the BOES is defined for any stress tensor and \mathbf{R}^0 is the atomic configuration that minimizes that BOES. It is important to note that the stress tensor in Eq. 3.5 does not include any effect from the thermal or quantum fluctuations of the ions, it is just the derivative of the total electronic energy with respect to the strain tensor.

Since we are at a local minimum of the BOES, the first-order term U_1 is zero by definition, thus, the lowest-order approximation we can do for the nuclear motion is to keep the terms up to second-order in the atomic displacements. The lowest-order approximation is named harmonic approximation. The harmonic Hamiltonian reads

$$H^I(\mathbf{R}) \simeq \sum_{\mathbf{T}s\alpha} \frac{(P_s^\alpha(\mathbf{T}))^2}{2m_s} + U(\mathbf{R}^0) + U_2(\mathbf{R}). \quad (3.6)$$

We will name higher-order terms ($n > 2$) anharmonic terms. It is convenient to Fourier transform the 2BFC with the following general Fourier transform for any nBFC

$$\phi_{s_1 \dots s_n}^{(n)}(\mathbf{T}_1, \dots, \mathbf{T}_n) = \frac{1}{N_{\mathbf{q}}^{n-1}} \sum_{\mathbf{q}_1 \dots \mathbf{q}_n} e^{i(\mathbf{q}_1 \cdot \mathbf{T}_1 + \dots + \mathbf{q}_n \cdot \mathbf{T}_n)} \phi_{s_1 \dots s_n}^{(n)}(\mathbf{q}_1, \dots, \mathbf{q}_n), \quad (3.7)$$

where $N_{\mathbf{q}}$ is the number of \mathbf{q} points in the 1BZ, or equivalently, the number of allowed \mathbf{T} lattice vectors. Due to the translational symmetry of the crystal, 2BFC have translational invariance and only depend on $\mathbf{T} = \mathbf{T}_1 - \mathbf{T}_2$. Therefore, only the terms with $\mathbf{q}_1 = -\mathbf{q}_2$ are non-zero in Eq. 3.7 and the equation can be rewritten

$$\phi_{s_1 s_2}^{\alpha_1 \alpha_2}(\mathbf{q}) = \phi_{s_1 s_2}^{\alpha_1 \alpha_2}(\mathbf{q}, -\mathbf{q}) = \sum_{\mathbf{T}} \phi_{s_1 s_2}^{\alpha_1 \alpha_2}(\mathbf{T}, 0) e^{-i\mathbf{q} \cdot \mathbf{T}}, \quad (3.8)$$

where $\mathbf{q} = \mathbf{q}_1 = -\mathbf{q}_2$. In the same way we can define the Fourier transforms of the displacement and momentum operators

$$u_s^\alpha(\mathbf{q}) = \frac{1}{\sqrt{N_q}} \sum_{\mathbf{T}} e^{i\mathbf{q}\cdot\mathbf{T}} u_s^\alpha(\mathbf{T}), \quad (3.9)$$

$$P_s^\alpha(\mathbf{q}) = \frac{1}{\sqrt{N_q}} \sum_{\mathbf{T}} e^{-i\mathbf{q}\cdot\mathbf{T}} P_s^\alpha(\mathbf{T}). \quad (3.10)$$

We will see that these definitions will allow us to diagonalize the ionic Hamiltonian. First of all we assume the following transformations with the bosonic ladder operators

$$u_s^\alpha(\mathbf{q}) = \sum_\mu \frac{1}{\sqrt{2m_s\omega_\mu(\mathbf{q})}} \epsilon_{s\mu}^\alpha(\mathbf{q}) (b_{\mu\mathbf{q}} + b_{\mu-\mathbf{q}}^\dagger), \quad (3.11)$$

$$P_s^\alpha(\mathbf{q}) = -i \sum_\mu \sqrt{\frac{m_s\omega_\mu(\mathbf{q})}{2}} \epsilon_{s\mu}^\alpha(\mathbf{q}) (b_{\mu\mathbf{q}} - b_{\mu-\mathbf{q}}^\dagger), \quad (3.12)$$

that satisfy the following commutation algebra

$$[b_{\mu\mathbf{q}}, b_{\mu'\mathbf{q}'}^\dagger] = \delta_{\mu\mu'} \delta_{\mathbf{q}\mathbf{q}'}, \quad [b_{\mu\mathbf{q}}, b_{\mu'\mathbf{q}'}] = 0, \quad [b_{\mu\mathbf{q}}^\dagger, b_{\mu'\mathbf{q}'}^\dagger] = 0. \quad (3.13)$$

The polarization vectors and phonon frequencies are calculated solving the eigenvalue problem of the dynamical matrix $D_{s_1 s_2}^{\alpha_1 \alpha_2}(\mathbf{q}) = \phi_{s_1 s_2}^{\alpha_1 \alpha_2}(\mathbf{q}) / \sqrt{m_{s_1} m_{s_2}}$

$$\omega_\mu^2(\mathbf{q}) \epsilon_{s_1 \mu}^{\alpha_1}(\mathbf{q}) = \sum_{s_2} \sum_{\alpha_2} D_{s_1 s_2}^{\alpha_1 \alpha_2}(\mathbf{q}) \epsilon_{s_2 \mu}^{\alpha_2}(\mathbf{q}). \quad (3.14)$$

By using these definitions, the ionic Hamiltonian in the harmonic approximation can be written as a sum of independent harmonic oscillators[40, 53, 54]

$$H^I = U(\mathbf{R}^0) + \sum_\mu \sum_{\mathbf{q}}^{1BZ} \omega_\mu(\mathbf{q}) \left(b_{\mu\mathbf{q}}^\dagger b_{\mu\mathbf{q}} + \frac{1}{2} \right), \quad (3.15)$$

with the following eigenenergies

$$E_\mu^{mode}(\mathbf{q}) = U(\mathbf{R}^0) + \omega_\mu(\mathbf{q}) \left(n_{\mu\mathbf{q}} + \frac{1}{2} \right). \quad (3.16)$$

$\epsilon_{s\mu}(\mathbf{q})$ and $\omega_\mu(\mathbf{q})$ are the polarization vector (of atom s in the unit cell) and the frequency of mode μ with momentum \mathbf{q} , respectively. $n_{\mu\mathbf{q}}$ denotes the occupation level of a mode, when a given mode is excited to the $n_{\mu\mathbf{q}}^{th}$ level, we would say that we have $n_{\mu\mathbf{q}}$ phonons of that mode. We will name $\omega_\mu(\mathbf{q})$ *phonon frequencies* and their dispersion with respect to momentum *phonon spectrum*. The ASR makes $D_{s_1 s_2}^{\alpha_1 \alpha_2}(\mathbf{q} = 0)$ to have three null eigenvalues, which correspond to the three acoustic branches at the Γ point.

Finally, the energy of a total ionic state $|\beta\rangle = |n_{1\mathbf{q}_1} \dots n_{3N_s\mathbf{q}_1} \dots n_{3N_s\mathbf{q}_{N_q}}\rangle$, is given by

$$E_\beta = U(\mathbf{R}^0) + \sum_\mu \sum_{\mathbf{q}}^{1BZ} \omega_\mu(\mathbf{q}) \left(n_{\mu\mathbf{q}} + \frac{1}{2} \right). \quad (3.17)$$

As phonons are bosons, they follow Bose-Einstein statistics and the total energy at a given temperature can be calculated as

$$E(T) = U(\mathbf{R}^0) + \sum_{\mu} \sum_{\mathbf{q}}^{1BZ} \omega_{\mu}(\mathbf{q}) \left(n_B(\omega_{\mu}(\mathbf{q})) + \frac{1}{2} \right), \quad (3.18)$$

where

$$n_B(\omega_{\mu}(\mathbf{q})) = (e^{\beta\omega_{\mu}(\mathbf{q})} - 1)^{-1} \quad (3.19)$$

is the Bose-Einstein distribution function. The zero point energy (ZPE) is defined as

$$E_{ZPE} = E(T=0) = U(\mathbf{R}^0) + \frac{1}{2} \sum_{\mu} \sum_{\mathbf{q}}^{1BZ} \omega_{\mu}(\mathbf{q}) \quad (3.20)$$

and arises from the quantum fluctuations of the atoms at $T = 0$ K.

3.2 Phonons from density functional perturbation theory

We have seen that within the simplest approximation to study the motion of nuclei we need to calculate second derivatives of $U(\mathbf{R})$ at the minimum of the BOES or the 2BFC. We can start by calculating the first-order derivatives of $U(\mathbf{R})$. By using the Hellmann-Feynman theorem [55, 56] we get

$$\frac{\partial U}{\partial u_{s_1}^{\alpha_1}(\mathbf{T}_1)} = \langle \psi_0^e | \frac{\partial H^e}{\partial u_{s_1}^{\alpha_1}(\mathbf{T}_1)} | \psi_0^e \rangle = \frac{\partial V_{I,I}}{\partial u_{s_1}^{\alpha_1}(\mathbf{T}_1)} + \int d\mathbf{x} n(\mathbf{x}) \frac{\partial V_{ext}(\mathbf{x})}{\partial u_{s_1}^{\alpha_1}(\mathbf{T}_1)}, \quad (3.21)$$

since the only explicit dependence on the nuclear coordinates of H^e comes from the external potential V_{ext} and the nuclei-nuclei Coulomb interaction $V_{I,I}$. Now if we compute the second derivative with respect to the atomic displacements we get

$$\begin{aligned} \phi_{s_1 s_2}^{\alpha_1 \alpha_2}(\mathbf{T}_1, \mathbf{T}_2) &= \frac{\partial^2 U}{\partial u_{s_1}^{\alpha_1}(\mathbf{T}_1) \partial u_{s_2}^{\alpha_2}(\mathbf{T}_2)} \Big|_{\mathbf{R}^0} = \int d\mathbf{x} \frac{\partial n(\mathbf{x})}{\partial u_{s_1}^{\alpha_1}(\mathbf{T}_1)} \Big|_{\mathbf{R}^0} \frac{\partial V_{ext}(\mathbf{x})}{\partial u_{s_2}^{\alpha_2}(\mathbf{T}_2)} \Big|_{\mathbf{R}^0} + \\ &+ \int d\mathbf{x} n(\mathbf{x}) \frac{\partial^2 V_{ext}(\mathbf{x})}{\partial u_{s_1}^{\alpha_1}(\mathbf{T}_1) \partial u_{s_2}^{\alpha_2}(\mathbf{T}_2)} \Big|_{\mathbf{R}^0} + \frac{\partial^2 V_{I,I}}{\partial u_{s_1}^{\alpha_1}(\mathbf{T}_1) \partial u_{s_2}^{\alpha_2}(\mathbf{T}_2)} \Big|_{\mathbf{R}^0}. \end{aligned} \quad (3.22)$$

The last equation shows that the second derivatives of the BOES not only require the knowledge of the density $n(\mathbf{x})$ but also of its derivatives with respect to nuclear displacements $\frac{\partial n(\mathbf{x})}{\partial u_s^{\alpha}(\mathbf{T})}$. We already know how to calculate the electronic density by solving the electronic problem using DFT, now we will see how to calculate $\frac{\partial n(\mathbf{x})}{\partial u_s^{\alpha}(\mathbf{T})}$ using Density Functional Perturbation Theory (DFPT)[57, 58, 59].

The main idea behind DFPT is to apply first-order perturbation theory to calculate the change on the Kohn-Sham orbitals when the ions displace from their equilibrium positions. With the change on these orbitals one is able to calculate the variation of the electronic density and, consequently, the 2BFC. The first step is to make a first-order expansion of the electronic Hamiltonian, the eigenvalues, the eigenfunctions and, the density (see Eqs. 2.7 and 2.8 for the Kohn-Sham problem and the density)

- $H^{KS} \rightarrow H^{KS} + \Delta H^{KS}$

- $\epsilon_{n\mathbf{k}} \rightarrow \epsilon_{n\mathbf{k}} + \Delta\epsilon_{n\mathbf{k}}$
- $|\phi_{n\mathbf{k}}\rangle \rightarrow |\phi_{n\mathbf{k}}\rangle + |\Delta\phi_{n\mathbf{k}}\rangle$
- $n(\mathbf{x}) \rightarrow n(\mathbf{x}) + \Delta n(\mathbf{X}),$

where $\langle \mathbf{x} | \Delta\phi_{n\mathbf{k}} \rangle = \Delta\phi_{n\mathbf{k}}(\mathbf{x})$. With these ingredients we obtain another eigenvalue problem at linear order

$$(H^{KS} - \epsilon_{n\mathbf{k}}) |\Delta\phi_{n\mathbf{k}}\rangle = -(\Delta H^{KS} - \Delta\epsilon_{n\mathbf{k}}) |\phi_{n\mathbf{k}}\rangle, \quad (3.23)$$

and by deriving Eq. 2.20 we get

$$\Delta n(\mathbf{x}) = 2Re \sum_n \sum_{\mathbf{k}}^{1BZ} 2[\theta(\epsilon_F - \epsilon_{n\mathbf{k}})] \phi_{n\mathbf{k}}^*(\mathbf{x}) \Delta\phi_{n\mathbf{k}}(\mathbf{x}), \quad (3.24)$$

where $\theta(\epsilon)$ is the zero temperature Fermi-Dirac distribution function. Eq. 3.23 is known as the Sternheimer equation[60]. Finally, the linear change of the Hamiltonian can be derived using functional derivatives

$$\Delta H^{KS}(\mathbf{x}) = \Delta V_{ext}(\mathbf{x}) + \int d\mathbf{x}' K(\mathbf{x}, \mathbf{x}') \Delta n(\mathbf{x}'), \quad (3.25)$$

where $K(\mathbf{x}, \mathbf{x}')$ is the functional derivative of the electron-electron interaction potential with respect to the density

$$K(\mathbf{x}, \mathbf{x}') = \frac{\delta V_H(\mathbf{x})}{\delta n(\mathbf{x}')} + \frac{\delta V_{xc}(\mathbf{x})}{\delta n(\mathbf{x}')}. \quad (3.26)$$

Equivalently, as the kinetic energy has no first-order contribution,

$$\Delta H^{KS}(\mathbf{x}) = \Delta V^{KS}(\mathbf{x}) = \Delta V_{ext}(\mathbf{x}) + \Delta V_H(\mathbf{x}) + \Delta V_{xc}(\mathbf{x}). \quad (3.27)$$

The combination of Eqs. 3.23, 3.24, and 3.25 forms a set of equations for the perturbed system that can be solved in a self-consistent way. The formalism we have described can give the derivatives of the density that we need to calculate the dynamical matrices and it is implemented in the *Quantum Espresso* software package[16].

3.3 Phonons from the finite displacements method

In this section we will see how we can calculate the 2BFC just by calculating the forces given by the Hellman-Feynman theorem in different supercells. In the harmonic approximation the α_1 Cartesian component of the force exerted on the atom at position $\mathbf{R}_{s_1}(\mathbf{T}_1)$ is

$$f_{s_1}^{\alpha_1}(\mathbf{T}_1) = - \sum_{\mathbf{T}_2 s_2 \alpha_2} \phi_{s_1 s_2}^{\alpha_1 \alpha_2}(\mathbf{T}_1, \mathbf{T}_2) u_{s_2}^{\alpha_2}(\mathbf{T}_2), \quad (3.28)$$

We can arrive to that expression just by taking the derivative of Eq. 3.6. The 2BFC can be calculated as

$$\phi_{s_1 s_2}^{\alpha_1 \alpha_2}(\mathbf{T}_1, \mathbf{T}_2) = - \frac{\partial f_{s_1}^{\alpha_1}(\mathbf{T}_1)}{\partial u_{s_2}^{\alpha_2}(\mathbf{T}_2)} \simeq - \frac{f_{s_1}^{\alpha_1}[u_{s_2}^{\alpha_2}](\mathbf{T}_1)}{u_{s_2}^{\alpha_2}}, \quad (3.29)$$

by displacing once at a time all the atoms of the lattice along the three Cartesian components by $u_{s_2}^{\alpha_2}(\mathbf{T}_2)$, and calculating the forces $f_{s_1}^{\alpha_1}[u_{s_2}^{\alpha_2}](\mathbf{T}_1)$ induced on the atom at $\mathbf{R}_{s_1}(\mathbf{T}_1)$. Eq. 3.29 computes the 2BFC using forward differences. For numerical reasons it can be advantageous in some cases to use central differences.

Since the crystal is invariant under translations of any lattice vector, it is only necessary to displace atoms in one primitive cell and calculate the forces induced on all the other atoms of the crystal. From now on we will assume that this is understood and put simply $\mathbf{T}_2 = 0$.

It is important to point that the 2BFC $\phi_{s_1 s_2}^{\alpha_1 \alpha_2}(\mathbf{T}_1, \mathbf{T}_2)$ in Eq. 3.3 are the 2BFC in the infinite lattice. Therefore, there is no restriction on the lattice vectors \mathbf{T} . However, the calculation of the 2BFC expressed in Eqs. 3.28 and 3.29 can only be done in supercell geometry. Using the supercell geometry we can only calculate the dynamical matrices at wavevectors that are reciprocal lattice vectors of the superlattice, so, without further approximations the calculation of the infinite lattice 2BFC is impossible.

Our assumption will be the following: the infinite lattice 2BFC $\phi_{s_1 s_2}^{\alpha_1 \alpha_2}(\mathbf{T}_1, \mathbf{T}_2)$ vanishes when the separation $|\mathbf{R}_{s_1}(\mathbf{T}_1) - \mathbf{R}_{s_2}(\mathbf{T}_2)|$ is such that the positions $\mathbf{R}_{s_1}(\mathbf{T}_1)$ and $\mathbf{R}_{s_2}(\mathbf{T}_2)$ lie in different Wigner-Seitz (WS) cells[40] of the chosen superlattice. Mathematically speaking, we are assuming that if we take the WS cell centered on $\mathbf{R}_{s_2}(\mathbf{T}_2)$, then the infinite lattice value of the 2BFC $\phi_{s_1 s_2}^{\alpha_1 \alpha_2}(\mathbf{T}_1, \mathbf{T}_2)$ is equally zero if $\mathbf{R}_{s_1}(\mathbf{T}_1)$ is in a different WS cell; it is equal to the supercell value if $\mathbf{R}_{s_1}(\mathbf{T}_1)$ is within the same WS cell; and it is equal to the supercell value divided by an integer P if $\mathbf{R}_{s_1}(\mathbf{T}_1)$ lies on the boundary of the same WS cell, where P is the number of WS cells having $\mathbf{R}_{s_1}(\mathbf{T}_1)$ on their boundary. With this assumption, the 2BFC will converge to the correct infinite lattice values as the size of the supercell systematically increases. The procedure explained in this paragraph is important for a proper Fourier interpolation (see Eq. 3.7) of 2BFC.

So far we have described a method to properly converge the 2BFC to the infinite lattice 2BFC by calculating the forces in different supercell sizes. For that purpose, we need to move all the atoms one by one in the three Cartesian directions and calculate the resulting forces in all the other atoms. This procedure gives a number of displacements for which, the forces must be computed. The number of displacements can be reduced by using the symmetries of the system. The symmetries include: translations, permutations, and space group symmetry operations. By using these symmetries many elements of the 2BFC matrix can be related, therefore, it is not necessary to calculate all of them explicitly.

For example, let's take the case of space group S and imagine we calculate the 2BFC $\phi_{s_1}(\mathbf{T}, 0)$. Then, if the atom 1 and 2 are related by the symmetry operation S , we can write

$$\boldsymbol{\phi}_{s_2}(\mathbf{T}, 0) = \mathbf{B}(S) \boldsymbol{\phi}_{\lambda_{s_1}(S)1}(\mathbf{T}, 0) \mathbf{B}(S^{-1}), \quad (3.30)$$

where $\mathbf{B}(S)$ is the 3×3 matrix representing the point group part of S in Cartesian coordinates and $\lambda_s(S)$ indicates the atom of the crystal where the atom $\mathbf{R}_s(\mathbf{T})$ is brought because of the action of the symmetry operation S . In Eq. 3.30 we have made use of the matrix notation by using bold symbols. This procedure is repeated then for all the atoms of the primitive cell. A similar procedure can be applied for

the translational symmetry and the permutation symmetry of the 2BFC.

It must be pointed, that the harmonic approximation becomes better and better as the displacement are made smaller and smaller. However, this can not be taken to the limit because the smaller are the displacements the smaller are the induced forces and the level of accuracy is always finite. So, one can not make too small displacements but, usually, a fraction of a percentage of the nearest neighbour distance is a good compromise.

3.4 Long-wavelength vibrations in polar materials

The formalisms we have described so far are general for metals and insulators and allow the calculation of phonon frequencies and polarization vectors at any \mathbf{q} point of the 1BZ. However, in polar semiconductors and insulators, the long-range character of the Coulomb forces gives rise to macroscopic electric fields for longitudinal optic (LO) phonons in the long-wavelength limit. In this limit, phonons are coupled to these macroscopic electric fields and their energy is shifted.

The physics of the system can be understood within the Huang's phenomenological model[54] for a cubic lattice with two atoms per unit cell and easily generalized for any kind of lattice. This is just a simple model to understand the physics behind this effect. The most general quadratic expression of the energy as a function of the phonon optic coordinates \mathbf{u} and the electric field \mathbf{E} is

$$E(\mathbf{u}, \mathbf{E}) = \frac{1}{2}m\omega_0^2 u^2 - \frac{\Omega_{cell}}{8\pi}\epsilon_\infty - Z^*\mathbf{u} \cdot \mathbf{E}, \quad (3.31)$$

where m is the nuclear reduced mass (defined as $m = m_1 m_2 / (m_1 + m_2)$ for two masses m_1 and m_2), ϵ_∞ the electronic dielectric constant of the crystal (the static dielectric constant with $\mathbf{u} = 0$), ω_0 the frequency of the mode without taking into account the coupling to the electric field, Ω_{cell} is the volume of the unit cell, and the coupling Z^* , between the atomic displacements and the electric field, is known as the Born effective charge of the ions. The conjugate variables to \mathbf{u} and \mathbf{E} are the force \mathbf{f} acting on the ions and the electrical induction \mathbf{D}

$$\mathbf{f} \equiv -\frac{\partial E}{\partial \mathbf{u}} = -m\omega_0^2 \mathbf{u} + Z^* \mathbf{E}, \quad (3.32)$$

$$\mathbf{D} \equiv -\frac{4\pi}{\Omega_{cell}} \frac{\partial E}{\partial \mathbf{E}} = \frac{4\pi}{\Omega_{cell}} Z^* \mathbf{u} + \epsilon_\infty \mathbf{E}. \quad (3.33)$$

In the absence of free external charges, Maxwell's equations give

$$\nabla \times \mathbf{E} \sim i\mathbf{q} \times \mathbf{E} = 0, \quad (3.34)$$

$$\nabla \cdot \mathbf{D} \sim i\mathbf{q} \cdot \mathbf{D} = 0. \quad (3.35)$$

For transverse modes, where the electric field is perpendicular to the phonon momentum, Eq. 3.34 gives $\mathbf{E}_T = 0$ (\mathbf{E}_T is the transversal component of the electric field), and Eq. 3.32 $\mathbf{f}_T = -m\omega_0^2 \mathbf{u}$. Therefore the transverse frequency is $\omega_T = \omega_0$. For longitudinal modes, where the electric field is parallel to the phonon momentum, Eq. 3.35 gives $\mathbf{D}_L = 0$ and Eq. 3.33 gives $\mathbf{E}_L = -4\pi Z^* / (\Omega_{cell} \epsilon_\infty) \mathbf{u}$ (\mathbf{E}_L is the longitudinal

component of the electric field). Eq. 3.32 gives $\mathbf{f}_L = -(m\omega_0^2 + 4\pi Z^{*2}/(\Omega_{cell}\epsilon_\infty))\mathbf{u}$. Therefore, the longitudinal frequency is $\omega_L = \sqrt{\omega_0^2 + 4\pi Z^{*2}/(\Omega_{cell}\epsilon_\infty m)}$. These results clearly show that the frequency of longitudinal modes in the long-wavelength limit have an extra term that arises due to the coupling with the electric field. The formalism can be generalized for crystals with any symmetry and in these cases the Born effective charges and the electronic dielectric constant will be tensors.

If we want to define the 2BFC in the long-wavelength limit, they can be split into the sum of an analytic and a nonanalytic contributions

$$\phi_{s_1 s_2}^{\alpha_1 \alpha_2} = \phi_{s_1 s_2}^{an} + \phi_{s_1 s_2}^{na}, \quad (3.36)$$

where the analytic part is the matrix obtained from DFPT, for instance, the perturbation being a zone-center phonon displacement at zero macroscopic electric field. The nonanalytic part has the general form

$$\phi_{s_1 s_2}^{na} = \frac{4\pi}{\Omega_{cell}} \frac{(\mathbf{q} \cdot \mathbf{Z}_{s_1}^*)_{\alpha_1} (\mathbf{q} \cdot \mathbf{Z}_{s_2}^*)_{\alpha_2}}{\mathbf{q} \cdot \epsilon_\infty \cdot \mathbf{q}}. \quad (3.37)$$

From Eq. 3.37 we can see that for the nonanalytic part of the 2BFC at $\mathbf{q} = 0$ we need the macroscopic dielectric constant of the system and the Born effective charges, which can be calculated within the DFPT formalism explained in section 3.2[61].

In order to have a little bit of intuition on how to calculate these quantities, the first-principles calculation of $\epsilon_\infty^{\alpha\beta}$ and $Z_s^{*\alpha\beta}$ can be started from the definition of the macroscopic electric polarization of the medium,

$$P_\alpha = \frac{1}{\Omega_{cell}} \sum_{s\beta} \left[Z_s^{*\alpha\beta} u_s^\beta + \frac{\epsilon_\infty^{\alpha\beta} - \delta_{\alpha\beta}}{4\pi} E_\beta \right], \quad (3.38)$$

$\delta_{\alpha\beta}$ being the Kronecker delta. The macroscopic polarization definition must be read as a tensor equation stating that the Born effective charge tensor of the s th ion with respect to a periodic displacement of all the ions of the s species at zero macroscopic electric field

$$Z_s^{*\alpha\beta} = \Omega_{cell} \frac{\partial P_\alpha}{\partial u_s^\beta (\mathbf{q} = 0)} \Big|_{\mathbf{E}=0}, \quad (3.39)$$

while the electronic dielectric constant tensor is the derivative of the polarization with respect to the macroscopic electric field at clamped ions

$$\epsilon_\infty^{\alpha\beta} = \delta_{\alpha\beta} + 4\pi \frac{\partial P_\alpha}{\partial E_\beta} \Big|_{\mathbf{u}_s(\mathbf{q}=0)=0}. \quad (3.40)$$

For a better understanding, in Fig. 3.1 we show the ab initio phonon spectrum of SnS . As we can see, in practice, the correction for the longitudinal optic modes in the long-wavelength limit translates into a different gap between the longitudinal and transverse modes for different directions in the 1BZ. The reason is that for different directions in the 1BZ the frequency of the longitudinal modes is different.

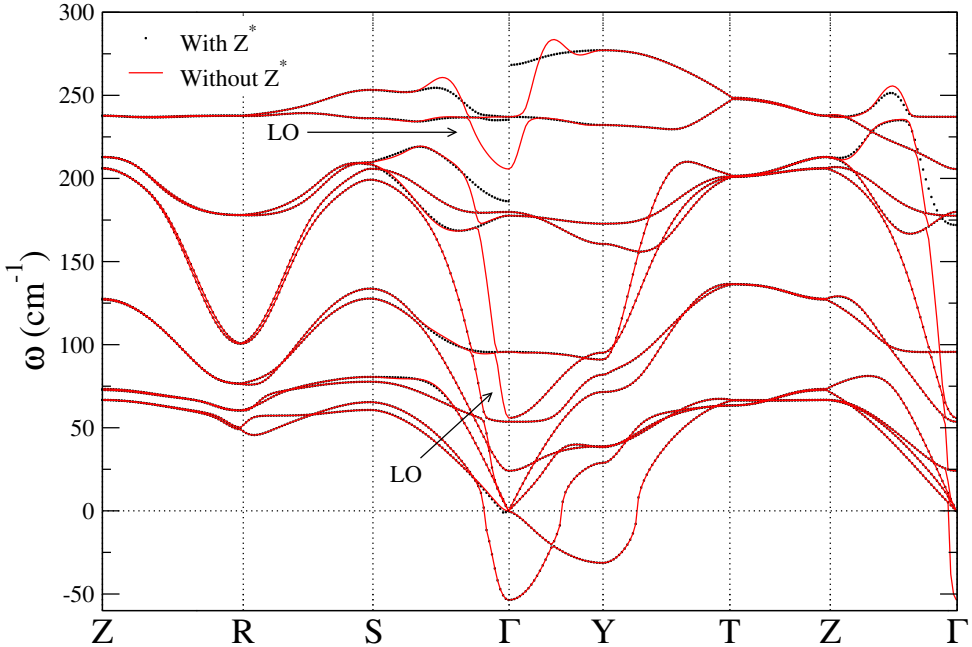


FIGURE 3.1: Ab initio phonon dispersion of SnS including the coupling of the longitudinal optic modes with the macroscopic electric field (black circles) and without including it (red lines). The LO modes are denoted with arrows.

3.5 Anharmonic effects in solids

The harmonic approximation allows to diagonalize the ionic Hamiltonian and, therefore, provides well defined quasiparticles named phonons which do not interact among themselves. For that purpose we have seen that we need to truncate the Taylor expansion of the external potential at the second-order within the small atomic displacements assumption. This assumption seems to be valid in most solids for temperatures below the melting point, specially for obtaining phonon frequencies and its associated physical properties[54]. However, the non-interacting picture has limitations and it is not able to explain many physical phenomena that arise due to the anharmonic terms in Eq. 3.2. Probably, one of the most representative examples of anharmonicity is the non-zero thermal resistivity of materials which is translated into a finite thermal conductivity. Within the harmonic approximation the phonon basis diagonalizes the Hamiltonian and, therefore, if the system is in an eigenstate it will stay there forever. This means that the lifetime of these states is infinite and they can carry thermal energy without any resistance. In reality, obviously, solids have a finite thermal conductivity. It is also well known that the peaks observed in neutron scattering experiments have a measurable width, which is inversely proportional to the lifetime of a phonon. The harmonic approximation is also unable to describe more basic properties such as the temperature dependence of phonon frequencies and the thermal expansion of solids.

Anharmonicity can be treated within perturbation theory by calculating higher-order terms of the Taylor expansion of the BOES. This approximation holds when the anharmonic coefficients of the Taylor expansion are much smaller than the harmonic ones. This means that the potential can be described with the second-order

term of the Taylor expansion of the BOES in the range defined by the ionic fluctuations and anharmonic terms are just a small correction. It can be the case that ionic displacements cannot be considered small anymore and higher-order terms become as important as, or even more, than the second-order ones. The origin of such big displacements can be temperature when a solid is close to melting. It can also happen that at low temperatures or even at 0 K the harmonic and perturbative regimes break down in the presence of very light atoms[62] or when the crystal is close to dynamical instabilities, as it happens in ferroelectrics[17, 63] or in materials that show charge density wave transitions[64, 65].

When perturbation theory breaks down one needs to apply nonperturbative methods. One way of including anharmonic effects at a nonperturbative level is to use molecular dynamics simulations[19, 66, 67, 20, 21, 68, 69, 70]. This method usually requires long simulation times and, as it follows Newtonian dynamics, its applications are limited to temperatures above the Debye temperature. The Newtonian limitation can be overcome by applying path integral molecular dynamics[71] which are even more computationally expensive as they require to simulate the quantum fluctuations. There is another family of methods[23, 22, 72, 73, 74, 75, 76, 77] that have been developed mainly inspired by the self-consistent harmonic approximation (SCHA) formulated by Hooton[78]. The SCHA uses the variational Gibbs-Bogoliubov (GB) principle to approximate the free energy of the ionic Hamiltonian with the free energy calculated with a trial harmonic density matrix for the same system, which does not coincide with the harmonic density matrix obtained from the harmonic approximation.

In this thesis we have applied the perturbative method[18] and a stochastic implementation of the SCHA, the so called stochastic self-consistent harmonic approximation (SSCHA)[22, 23, 24, 25]. In the following sections we will discuss both of them.

3.6 Perturbation theory of the phonon-phonon interaction

In this section we will see what is the correction that the lowest-order perturbation theory makes to the harmonic result. We will see that this approximation not only gives an anharmonic lineshift to the harmonic frequencies, but also an anharmonic linewidth, which makes clear that the phonons do not diagonalize the anharmonic Hamiltonian and they will no longer have an infinite lifetime. Therefore, this theory will allow us to calculate properties, such as, the lattice thermal conductivity and the phonon spectral function measured in inelastic scattering experiments.

We will name the harmonic Hamiltonian $H^{(0)}$ and we will treat the anharmonic part as a small perturbation of $H^{(0)}$. With $G_{s_1 s_2}^{\alpha_1 \alpha_2}(T_1, T_2; z)$ and $G_{s_1 s_2}^{\alpha_1 \alpha_2(0)}(T_1, T_2; z)$ we indicate the Green's functions of the total ionic Hamiltonian H^I and $H^{(0)}$ for the variable $\sqrt{m_s} u_s^\alpha(T)$, respectively. We define the Green's function in time space as $\bar{G}_{s_1 s_2}^{-1}(\mathbf{T}_1, \mathbf{T}_2; t) = \langle \sqrt{m_{s_1}} u_{s_1}^{\alpha_1}(\mathbf{T}_1, 0) \sqrt{m_{s_2}} u_{s_2}^{\alpha_2}(\mathbf{T}_2, t) \rangle$. The Green's function of the Harmonic Hamiltonian is given by

$$\bar{G}_{s_1 s_2}^{-1}(\mathbf{T}_1, \mathbf{T}_2; z) = z^2 \delta_{s_1 s_2} \delta_{\alpha_1 \alpha_2} \delta_{\mathbf{T}_1 \mathbf{T}_2} - D_{s_1 s_2}^{\alpha_1 \alpha_2}(\mathbf{T}_1, \mathbf{T}_2). \quad (3.41)$$

The relation between the full and harmonic Green's functions is given by the Dyson equation

$$\overset{-1}{\mathbf{G}}(z) = \overset{-1}{\mathbf{G}}^{(0)}(z) - \mathbf{\Pi}^{(0)}(z), \quad (3.42)$$

which is equivalent to

$$\mathbf{G}(z) = \mathbf{G}^{(0)}(z) + \mathbf{G}^{(0)}(z)\mathbf{\Pi}^{(0)}(z)\mathbf{G}(z). \quad (3.43)$$

In the previous equations we have used the matrix notation and we use bold symbols to emphasize it. In Fig. 3.2 we show the diagrammatic representation of Eq. 3.43. With $\mathbf{\Pi}^{(0)}(z)$ we denote the harmonic self-energy, the self-energy obtained by

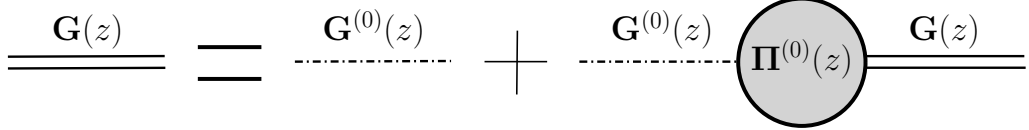


FIGURE 3.2: Diagrammatic representation of the Dyson equation in Eq. 3.43. The dashed line corresponds to the harmonic propagator. The double solid line corresponds to the full propagator.

taking $H^{(0)}$ as noninteracting unperturbed Hamiltonian. At the lowest perturbative order, the harmonic self-energy can be written as

$$\mathbf{\Pi}^{(0)}(z) \simeq \overset{(T)}{\mathbf{\Pi}}^{(0)} + \overset{(L)}{\mathbf{\Pi}}^{(0)} + \overset{(B)}{\mathbf{\Pi}}^{(0)}(z), \quad (3.44)$$

where $\overset{(T)}{\mathbf{\Pi}}^{(0)}$, $\overset{(L)}{\mathbf{\Pi}}^{(0)}$, and $\overset{(B)}{\mathbf{\Pi}}^{(0)}(z)$ are the loop, tadpole and bubble harmonic self-energies, respectively, which have the following expressions

$$\overset{(L)}{\Pi}_{s_1 s_2}^{\alpha_1 \alpha_2(0)}(\mathbf{T}_1, \mathbf{T}_2) = -\frac{1}{2} \sum_{\substack{s_3 s_4 \\ \alpha_3 \alpha_4 \\ \mathbf{T}_3, \mathbf{T}_4}}^{(4)} D_{s_1 s_2 s_3 s_4}^{\alpha_1 \alpha_2 \alpha_3 \alpha_4}(\mathbf{T}_1, \mathbf{T}_2, \mathbf{T}_3, \mathbf{T}_4) \left[\frac{1}{\beta} \sum_l G_{s_3 s_4}^{\alpha_3 \alpha_4(0)}(\mathbf{T}_3, \mathbf{T}_4; i\eta_l) \right], \quad (3.45)$$

$$\begin{aligned} \overset{(T)}{\Pi}_{s_1 s_2}^{\alpha_1 \alpha_2(0)}(\mathbf{T}_1, \mathbf{T}_2) &= -\frac{1}{2} \sum_{\substack{s_3 s_4 s_5 s_6 \\ \alpha_3 \alpha_4 \alpha_5 \alpha_6 \\ \mathbf{T}_3, \mathbf{T}_4, \mathbf{T}_5, \mathbf{T}_6}}^{(3)} D_{s_1 s_3 s_4}^{\alpha_1 \alpha_3 \alpha_4}(\mathbf{T}_1, \mathbf{T}_3, \mathbf{T}_4) G_{s_3 s_4}^{\alpha_3 \alpha_4(0)}(\mathbf{T}_3, \mathbf{T}_4; 0) \\ &\quad \times D_{s_2 s_5 s_6}^{\alpha_2 \alpha_5 \alpha_6}(\mathbf{T}_2, \mathbf{T}_5, \mathbf{T}_6) \left[\frac{1}{\beta} \sum_l G_{s_5 s_6}^{\alpha_5 \alpha_6(0)}(\mathbf{T}_5, \mathbf{T}_6; i\eta_l) \right], \end{aligned} \quad (3.46)$$

$$\begin{aligned} \overset{(B)}{\Pi}_{s_1 s_2}^{\alpha_1 \alpha_2(0)}(\mathbf{T}_1, \mathbf{T}_2; z) &= -\frac{1}{2} \sum_{\substack{s_3 s_4 s_5 s_6 \\ \alpha_3 \alpha_4 \alpha_5 \alpha_6 \\ \mathbf{T}_3, \mathbf{T}_4, \mathbf{T}_5, \mathbf{T}_6}}^{(3)} D_{s_1 s_3 s_4}^{\alpha_1 \alpha_3 \alpha_4}(\mathbf{T}_1, \mathbf{T}_3, \mathbf{T}_4) D_{s_2 s_5 s_6}^{\alpha_2 \alpha_5 \alpha_6}(\mathbf{T}_2, \mathbf{T}_5, \mathbf{T}_6) \\ &\quad \times \left[\frac{1}{\beta} \sum_l G_{s_3 s_4}^{\alpha_3 \alpha_4(0)}(\mathbf{T}_3, \mathbf{T}_4; i\eta_l) G_{s_5 s_6}^{\alpha_5 \alpha_6(0)}(\mathbf{T}_5, \mathbf{T}_6; z - i\eta_l) \right]. \end{aligned} \quad (3.47)$$

In these expressions we have generalized the definition of the harmonic dynamical matrix to the n th order (for the second-order we omit the index (2))

$$D_{s_1 \dots s_n}^{(n)}(\alpha_1, \dots, \alpha_n)(\mathbf{T}_1, \dots, \mathbf{T}_n) = \frac{\phi_{s_1 \dots s_n}^{(n)}(\alpha_1, \dots, \alpha_n)(\mathbf{T}_1, \dots, \mathbf{T}_n)}{\sqrt{m_{s_1} \dots m_{s_n}}}, \quad (3.48)$$

and $\eta_l = 2\pi l/\beta$ is the l th Matsubara frequency[79]. In Fig. 3.3 we include the diagrammatic representations of the self-energy and Feynman diagrams of the tadpole, loop, and bubble self-energies.



FIGURE 3.3: Diagrammatic representation of the self-energy and Feynman diagrams for the tadpole, loop, and bubble self-energies. The dashed line corresponds to the harmonic phonons and dots represent the interaction vertices. Within perturbation theory at the lowest-order there are third and fourth-order vertices, which means that there are three and four phonon interactions.

Note that the loop and tadpole self-energy terms do not depend on the frequency z and they are real. The tadpole self-energy can be divided into optical and acoustic contributions. The tadpole optical T_O diagram includes the effect of an optical phonon at the Γ point and it accounts for the relaxation of internal coordinates due to anharmonic effects. If internal atomic coordinates are fixed by symmetry, the T_O diagram vanishes and does not contribute[80]. On the contrary, if Wyckoff positions have free parameters[81], the T_O diagram accounts for the effect of quantum and thermal fluctuations in the internal coordinates. An alternative way of accounting for the T_O diagram is to minimize the free energy within the quasiharmonic approximation (QHA)[82]. For the internal coordinates that minimize the free energy within the QHA the T_O diagram vanishes. These equilibrium atomic positions might be different from \mathbf{R}^0 obtained from the minimum of the BOES. The T_A diagram includes the effect of an acoustic phonon in the limit of $\mathbf{q} \rightarrow \Gamma$ and accounts for the cell parameters relaxation. It can also be calculated within the QHA.

From $G(z)$ we can calculate the one-phonon spectral function as $\tilde{\sigma} = -2ImTr[G(\omega + i0^+)]$. Note that in the previous expression we have applied the change $z \rightarrow \omega + i0^+$. Peaks in the spectral function as a function of ω signal the presence of collective vibrational excitations, phonon quasiparticles, having certain energies. The sharper are the peaks the more lasting are these quasiparticles, their lifetime being inversely proportional to the width. A broad spectral function means that anharmonicity has removed the existence of quasiparticles with definite identity. This kind of information can be probed with inelastic scattering experiments,

for example.

We take advantage of the lattice periodicity also in this case and, Fourier transforming with respect to lattice indices, we consider separated spectral functions $-2\text{ImTr}[G(\mathbf{q}, \omega + i0^+)]$ for each \mathbf{q} point in the 1BZ. We find convenient to multiply the spectral function by $\omega/2\pi$

$$\tilde{\sigma}(\mathbf{q}, \omega) = -\frac{\omega}{\pi} \text{ImTr}[\omega^2 \mathbf{1} - \mathbf{D}(\mathbf{q}) - \Pi(\mathbf{q}, \omega + i0^+)]^{-1}, \quad (3.49)$$

because its ω integral over the real axis gives the total number of modes and, in the zero self-energy case, it gives equal Dirac's delta peaks at the non-interacting harmonic phonon frequencies. Evaluating the phonon spectral function through Eq. 3.49 requires the inversion of a matrix. If the mode mixing can be neglected, we can get a diagonal self-energy by applying the following transformation

$$\Pi_\mu(\mathbf{q}, \omega) = \sum_{\substack{s_1 s_2 \\ \alpha_1 \alpha_2}} \epsilon_{\mu s_1}^{\alpha_1}(\mathbf{q}) \Pi_{s_1 s_2}^{\alpha_1 \alpha_2}(\mathbf{q}, \omega + i0^+) \epsilon_{\mu s_2}^{\alpha_2}(\mathbf{q}). \quad (3.50)$$

The spectral function is then given by

$$\begin{aligned} \tilde{\sigma}(\mathbf{q}, \omega) = \sum_\mu \frac{1}{2} & \left[\frac{1}{\pi} \frac{-\text{Im}\mathcal{Z}_\mu(\mathbf{q}, \omega)}{[\omega - \text{Re}\mathcal{Z}_\mu(\mathbf{q}, \omega)]^2 + [\text{Im}\mathcal{Z}_\mu(\mathbf{q}, \omega)]^2} \right] + \\ & \sum_\mu \frac{1}{2} \left[\frac{1}{\pi} \frac{\text{Im}\mathcal{Z}_\mu(\mathbf{q}, \omega)}{[\omega + \text{Re}\mathcal{Z}_\mu(\mathbf{q}, \omega)]^2 + [\text{Im}\mathcal{Z}_\mu(\mathbf{q}, \omega)]^2} \right] \end{aligned} \quad (3.51)$$

with $\mathcal{Z}_\mu(\mathbf{q}, \omega) = \sqrt{\omega_\mu^2(\mathbf{q}) + \Pi_\mu(\mathbf{q}, \omega + i0^+)}$, where we consider the positive value of the square root. The spectral function calculated in Eq. 3.51 does not have any given line shape.

The equations given by perturbation theory only hold when the corrections to the harmonic frequencies are much smaller than the harmonic value. In this case $\Pi_\mu(\mathbf{q}, \omega)$ is small compared to $\omega_\mu^2(\mathbf{q})$ and it is justified to approximate $\Pi_\mu(\mathbf{q}, \omega) \sim \Pi_\mu(\mathbf{q}, \omega_\mu(\mathbf{q}))$, which turns $\tilde{\sigma}(\mathbf{q}, \omega)$ into a sum of Lorentzian functions.

$$\begin{aligned} \tilde{\sigma}(\mathbf{q}, \omega) = \sum_\mu \frac{1}{2} & \left[\frac{1}{\pi} \frac{\Gamma_\mu(\mathbf{q})}{[\omega - \omega_\mu(\mathbf{q}) - \Delta_\mu(\mathbf{q})]^2 + [\Gamma_\mu(\mathbf{q})]^2} \right] \\ & + \sum_\mu \frac{1}{2} \left[\frac{1}{\pi} \frac{\Gamma_\mu(\mathbf{q})}{[\omega + \omega_\mu(\mathbf{q}) + \Delta_\mu(\mathbf{q})]^2 + [\Gamma_\mu(\mathbf{q})]^2} \right], \end{aligned} \quad (3.52)$$

where

$$\Omega_\mu(\mathbf{q}) = \text{Re}\mathcal{Z}_\mu(\mathbf{q}, \omega_\mu(\mathbf{q})), \quad (3.53)$$

$$\Gamma_\mu(\mathbf{q}) = -\text{Im}\mathcal{Z}_\mu(\mathbf{q}, \omega_\mu(\mathbf{q})) \quad (3.54)$$

are the shifted frequency (with respect to the harmonic frequency) and half-width at half-maximum (HWHM) of mode μ , respectively. In this limit, the lifetime of a phonon $\mu\mathbf{q}$ is defined as the inverse linewidth (full width at half maximum, FWHM)

$$\tau_\mu(\mathbf{q}) = \frac{1}{2\Gamma_\mu(\mathbf{q})}. \quad (3.55)$$

These are well defined phonons with their frequencies and linewidths. In Fig. 3.4 we qualitatively describe the Lorentzian cross section. We can see that anharmonicity

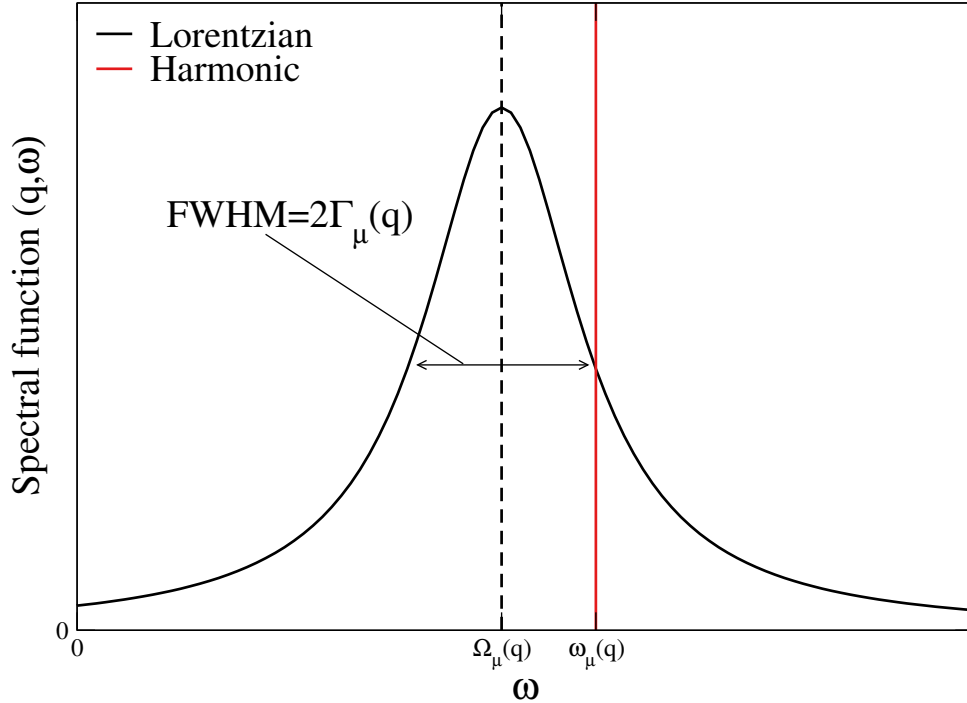


FIGURE 3.4: Lorentzian and harmonic spectral functions. The harmonic spectral function is a Dirac's delta. The Lorentzian has a well defined full width at half maximum (FWHM) and a well defined energy $\Omega_\mu(\mathbf{q})$.

within perturbation theory provides two anharmonic properties. A lineshift with respect to the harmonic value $\Omega_\mu(\mathbf{q}) - \omega_\mu(\mathbf{q})$ and a linewidth $2\Gamma_\mu(\mathbf{q})$ (FWHM), which does not exist within the harmonic theory.

As we can see from Eqs. 3.45, 3.47, and 3.46 in order to account for the phonon-phonon interactions at the lowest-order in perturbation theory we need to calculate the $D_{s_1,s_2,s_3}^{(3)\alpha_1\alpha_2\alpha_3}(\mathbf{T}_1, \mathbf{T}_2, \mathbf{T}_3)$ and $D_{s_1s_1,s_3s_4}^{(4)\alpha_1\alpha_2\alpha_3\alpha_4}(\mathbf{T}_1, \mathbf{T}_2, \mathbf{T}_3, \mathbf{T}_4)$ anharmonic dynamical matrices. The straightforward way of calculating these coefficients is to apply finite differences in the BOES[83] as explained in section 3.3 for the second-order. However, this method requires calculation in supercells that are commensurate with the phonons that interact, therefore, they require calculations in big supercells in order to achieve convergence. Furthermore, the number of elements to be determined is huge, complicating the finite difference approach. An alternative, and more elegant, procedure for the third-order anharmonic coefficients is to apply the $2n + 1$ theorem[84], which allows to get the $(2n + 1)^{th}$ derivatives of the BOES with the knowledge of the n^{th} derivatives of the electronic density. The latter method is more complicated to implement[18], but allows to make the calculations in the unit cell independently of the modes that are considered.

3.7 The stochastic self-consistent harmonic approximation

The perturbative formalism we have described in section 3.6 assumes that phonons can be described as distinct particles. This assumption is only valid when the anharmonic self-energy is small compared to the separation between harmonic frequencies. There is one extreme case in which perturbation theory cannot be even applied, it is when there are imaginary frequencies within the harmonic approximation, which means that the system is unstable within this approximation.

A formalism that can be applied in the cases where perturbation theory fails, even in the cases where there are harmonic instabilities, is the variational approach defined by the self-consistent harmonic approximation (SCHA)[78], which has been implemented in a stochastic framework in the so called stochastic self-consistent harmonic approximation (SSCHA)[22, 23, 24, 25].

The exact vibrational free energy of a solid is given by the sum of the total energy and entropic contributions

$$F_H = \text{tr}(\rho_{H^I} H^I) + \frac{1}{\beta} \text{tr}(\rho_{H^I} \ln \rho_{H^I}), \quad (3.56)$$

where $\rho_{H^I} = e^{-\beta H^I} / \text{tr}(e^{-\beta H^I})$ is the density matrix defined by the Hamiltonian H^I of the system. In the SSCHA ρ_{H^I} is substituted by a trial density matrix $\rho_{\mathcal{H}}$ defined by a trial Hamiltonian $\mathcal{H} = T_I + \mathcal{U}$ where T_I is the true kinetic energy of the ions and \mathcal{U} a trial potential. Then, we can define

$$\mathcal{F}_{H^I}[\mathcal{H}] = \text{tr}(\rho_{\mathcal{H}} H^I) + \frac{1}{\beta} \text{tr}(\rho_{\mathcal{H}} \ln \rho_{\mathcal{H}}), \quad (3.57)$$

and by the GB principle we know that

$$F_{H^I} \leq \mathcal{F}_{H^I}[\mathcal{H}]. \quad (3.58)$$

By adding and subtracting $\text{tr}(\rho_{\mathcal{H}} \mathcal{H})$ we can rewrite $\mathcal{F}_{H^I}[\mathcal{H}]$ as

$$\mathcal{F}_{H^I}[\mathcal{H}] = F_{\mathcal{H}} + \text{tr}[\rho_{\mathcal{H}}(U - \mathcal{U})], \quad (3.59)$$

where $\mathcal{F}_{H^I}[\mathcal{H}]$ is the function we need to minimize with respect to \mathcal{H} in order to get a good approximation for the free energy of the system. The equations we have written so far are valid for any trial potential \mathcal{U} . The main idea behind the SSCHA is that \mathcal{U} is taken to be a harmonic potential and can be parametrized as

$$\mathcal{U} = \frac{1}{2} \sum_{\substack{s_1 s_2 \\ \alpha_1 \alpha_2 \\ \mathbf{T}_1 \mathbf{T}_2}} \Phi_{s_1 s_2}^{\alpha_1 \alpha_2}(\mathbf{T}_1, \mathbf{T}_2) u_{s_1}^{\alpha_1}(\mathbf{T}_1) u_{s_2}^{\alpha_2}(\mathbf{T}_2). \quad (3.60)$$

The $u_s^\alpha(\mathbf{T})$ atomic displacements are different from the $u_s^\alpha(\mathbf{T})$. $u_s^\alpha(\mathbf{T})$ measure the displacements from the minimum of the BOES $R_s^{0\alpha}(\mathbf{T})$ while $u_s^\alpha(\mathbf{T})$ measure the displacements from trial equilibrium positions $\mathcal{R}_s^\alpha(\mathbf{T})$. We will name these trial equilibrium positions centroids. The same applies to $\Phi_{s_1 s_2}^{\alpha_1 \alpha_2}(\mathbf{T}_1, \mathbf{T}_2)$, which are trial 2BFC and not the harmonic ones $\phi_{s_1 s_2}^{\alpha_1 \alpha_2}(\mathbf{T}_1, \mathbf{T}_2)$. The advantage of choosing a trial potential

which is harmonic is that $\rho_{\mathcal{H}}$ and $F_{\mathcal{H}}$ have closed analytical forms.

$$\begin{aligned}\rho_{\mathcal{H}}(\mathbf{R}) &= \langle \mathbf{R} | \rho_{\mathcal{H}} | \mathbf{R} \rangle = \\ &= A_{\mathcal{H}} \exp \left(- \sum_{\substack{s_1 s_2 \\ \alpha_1 \alpha_2 \\ \mathbf{T}_1 \mathbf{T}_2 \\ \mu}} \frac{\sqrt{m_{s_1} m_{s_2}}}{2 a_{\mu \mathcal{H}}^2} \epsilon_{\mu \mathcal{H}}^{s_1 \alpha_1}(\mathbf{T}_1) \epsilon_{\mu \mathcal{H}}^{s_2 \alpha_2}(\mathbf{T}_2) u_{s_1}^{\alpha_1}[\mathbf{T}_1](\mathbf{R}) u_{s_2}^{\alpha_2}[\mathbf{T}_2](\mathbf{R}) \right), \quad (3.61)\end{aligned}$$

$$F_{\mathcal{H}} = \sum_{\mu} \left[\frac{\Omega_{\mu}^{(S)}}{2} + T \ln \left(1 - e^{-\beta \Omega_{\mu}^{(S)}} \right) \right], \quad (3.62)$$

where $A_{\mathcal{H}}$ is a normalization constant and $a_{\mu \mathcal{H}} = \sqrt{\coth(\beta \Omega_{\mu}^{(S)} / 2) / (2 \Omega_{\mu}^{(S)})}$ is called the normal length. $\rho_{\mathcal{H}}(\mathbf{R})$ is the probability to find the system described by \mathcal{H} in the general ionic configuration \mathbf{R} . In normal coordinates space, $\rho_{\mathcal{H}}(\mathbf{R})$, is a product of Gaussians and the normal length is their standard deviation, which is given by the $\Omega_{\mu}^{(S)}$ frequencies. These Gaussians are centered in the centroid positions. $\Omega_{\mu}^{(S)}$ and $\epsilon_{s \mu \mathcal{H}}^{\alpha}$ are the frequencies and polarization vectors that diagonalize the SSCHA dynamical matrix $D_{s_1 s_2}^{\alpha_1 \alpha_2(S)}(\mathbf{T}_1, \mathbf{T}_2) = \Phi_{s_1 s_2}^{\alpha_1 \alpha_2}(\mathbf{T}_1, \mathbf{T}_2) / (\sqrt{m_{s_1} m_{s_2}})$.

The only parameters that contains the trial harmonic potential are $\mathcal{R}_s^{\alpha}(\mathbf{T})$ and $\Phi_{s_1 s_2}^{\alpha_1 \alpha_2}(\mathbf{T}_1, \mathbf{T}_2)$ with respect to which $\mathcal{F}_H[\mathcal{H}]$ needs to be minimized. For the minimization we can apply a conjugate gradient (CG) algorithm and at the end of the minimization, which is done in a subspace that preserves the crystal symmetries, we will get the \mathbf{R} positions or centroids and $\Phi_{s_1 s_2}^{\alpha_1 \alpha_2}(\mathbf{T}_1, \mathbf{T}_2)$ 2BFC that minimize the free energy including anharmonic effects.

For the CG minimization we need the expressions of the function and its derivatives with respect to \mathbf{R} and $\Phi_{s_1 s_2}^{\alpha_1 \alpha_2}(\mathbf{T}_1, \mathbf{T}_2)$

$$\mathcal{F}_H[\mathcal{H}] = F_{\mathcal{H}} + \int d\mathbf{R} [U(\mathbf{R}) - \mathcal{U}(\mathbf{R})] \rho_{\mathcal{H}}(\mathbf{R}), \quad (3.63)$$

$$\nabla_{\mathbf{R}} \mathcal{F}_H[\mathcal{H}] = - \int d\mathbf{R} [\mathbf{f}(\mathbf{R}) - \mathbf{f}_{\mathcal{H}}(\mathbf{R})] \rho_{\mathcal{H}}(\mathbf{R}), \quad (3.64)$$

$$\begin{aligned}\nabla_{\Phi} \mathcal{F}_H[\mathcal{H}] &= - \sum_{\substack{s_1 s_2 \\ \alpha_1 \alpha_2 \\ \mathbf{T}_1 \mathbf{T}_2 \\ \mu}} \sqrt{\frac{m_{s_1}}{m_{s_2}}} (\epsilon_{s_1 \mu \mathcal{H}}^{\alpha_1}(\mathbf{T}_1) \nabla_{\Phi} \ln a_{\mu \mathcal{H}} + \nabla_{\Phi} \epsilon_{s_1 \mu \mathcal{H}}^{\alpha_1}(\mathbf{T}_1)) \epsilon_{s_2 \mu \mathcal{H}}^{\alpha_2}(\mathbf{T}_2) \\ &\times \int d\mathbf{R} [f_{s_1}^{\alpha_1}[\mathbf{T}_1](\mathbf{R}) - f_{s_1 \mathcal{H}}^{\alpha_1}[\mathbf{T}_1](\mathbf{R})] (R_{s_2}^{\alpha_2}(\mathbf{T}_2) - \mathcal{R}_{s_2}^{\alpha_2}(\mathbf{T}_2)) \rho_{\mathcal{H}}(\mathbf{R}). \quad (3.65)\end{aligned}$$

$\mathbf{f}(\mathbf{R})$ is the vector formed by all the atomic forces for the ionic configuration \mathbf{R} and $\mathbf{f}_{\mathcal{H}}(\mathbf{R})$ are the forces defined by \mathcal{H}

$$f_{s_1 \mathcal{H}}^{\alpha_1}[\mathbf{T}_1](\mathbf{R}) = - \sum_{s_2 \alpha_2 \mathbf{T}_2} \Phi_{s_1 s_2}^{\alpha_1 \alpha_2}(\mathbf{T}_1, \mathbf{T}_2) u_{s_2}^{\alpha_2}[\mathbf{T}_2](\mathbf{R}). \quad (3.66)$$

The only non-analytic terms in these equations are the integrals and the actual forces $\mathbf{f}(\mathbf{R})$.

A possible procedure for evaluating the integrals is to get higher order coefficients in the Taylor expansion, which is a difficult and time-consuming task. Within the SSCHA framework, these integrals are evaluated stochastically by using the relationship

$$\int \mathbf{O}(\mathbf{R})\rho_{\mathcal{H}}(\mathbf{R})d\mathbf{R} \simeq \frac{1}{N_c} \sum_{I=1}^{N_c} \mathbf{O}(\mathbf{R}_I) \equiv \langle \mathbf{O} \rangle_{\rho_{\mathcal{H}}}. \quad (3.67)$$

The set of \mathbf{R}_I ionic configurations is created according to the distribution $\rho_{\mathcal{H}}(\mathbf{R})$. \mathbf{O} is any operator that only depends on the ionic configuration and N_c is the number of configurations we have created. The equality in Eq. 3.67 holds when $N_c \rightarrow \infty$. As we are dealing with a stochastic framework, the statistical error scales as $1/\sqrt{N_c}$. The advantage of using Eq. 3.67 is that the gradients in Eqs. 3.64 and 3.65 can be calculated by getting the forces acting on atoms in supercells in the configurations given by $\rho_{\mathcal{H}}$, which are easily extracted from electronic ground state calculations thanks to the Hellmann-Feynman theorem[56].

Once we calculate the gradient of the free energy, we can apply the CG method to minimize the free energy. The flowchart of the SSCHA method is the following. An initial guess \mathcal{H}_0 (in the first step $j = 0$) is made for the trial Hamiltonian. This guess can be the harmonic Hamiltonian. However, it needs to be stable so we need to find another guess for materials with imaginary frequencies in the harmonic approximation. This trial Hamiltonian \mathcal{H}_0 is used to create N_c ionic configurations according to $\rho_{\mathcal{H}_0}(\mathbf{R})$. We calculate the energies and atomic forces in each configuration and, finally, we are able to evaluate the integrals in Eq. 3.63, 3.64, and 3.65. This way we are able to perform a CG step and a new \mathcal{H}_j is obtained.

At this point we would need to create new configurations by using the new $\rho_{\mathcal{H}_j}(\mathbf{R})$. However, this would be very inefficient as we would need to calculate energies and forces again. Instead, one can use a reweighting importance sampling technique by changing Eq. 3.67 by

$$\int \mathbf{O}(\mathbf{R})\rho_{\mathcal{H}_j}(\mathbf{R})d\mathbf{R} \simeq \frac{1}{N_c} \sum_{I=1}^{N_c} \mathbf{O}(\mathbf{R}_I) \frac{\rho_{\mathcal{H}_j}}{\rho_{\mathcal{H}_{j_0}}}, \quad (3.68)$$

where j_0 is the latest iteration at which configurations were created. As long as

$\left\langle \frac{\rho_{\mathcal{H}_j}}{\rho_{\mathcal{H}_{j_0}}} \right\rangle_{\rho_{\mathcal{H}_{j_0}}}$ is not far from unity the configurations created with \mathcal{H}_{j_0} can be reused.

We can control this deviation from unity to get the statistical convergence or precision that we want. However, $\left\langle \frac{\rho_{\mathcal{H}_j}}{\rho_{\mathcal{H}_{j_0}}} \right\rangle_{\rho_{\mathcal{H}_{j_0}}}$ can get far from unity if all the weight

constantly drifts from the uniform value, or it can remain close to unity if the configurations spread a lot. Thus, a more reliable statistical parameter to check is the Kong-Liu effective sample size[25]

$$N_{eff} = \frac{\left(\sum_I \rho_{\mathcal{H}_j}(\mathbf{R}_I) \right)^2}{\sum_I \rho_{\mathcal{H}_j}^2} < N_c. \quad (3.69)$$

A critical threshold can be defined as $\eta = \frac{N_{eff}}{N_c}$. The effective sample size counts how

many configurations are actually contributing to the Monte Carlo average, even if the $\rho_{\mathcal{H}_j}(\mathbf{R}_I)$ are properly normalized. Finally, we will consider that the SSCHA minimization is converged when the gradient gets so small that the free energy change is less than a given threshold and the statistical criteria are fulfilled. In Fig. 3.5 we can see a scheme of the SSCHA minimization.

In Fig. 3.6 we show the application of the SSCHA in a one dimensional BOES at zero temperature. The potential we have chosen is $U(x) = -0.5x^2 + 0.5x^4$ and it is represented with a solid black line. The second derivative of this potential at the equilibrium position is negative, therefore, the harmonic approximation completely breaks down and perturbation theory cannot be applied in this case. We show the harmonic part of the potential with a solid red line. We have solved the problem exactly by solving the Schrödinger equation for a particle with unitary mass. We show the ground state wave function with a dashed black line and the ground state energy with a pointed black line. The SSCHA results at zero temperature are shown in blue. As we can see, the SSCHA is able to find a very good approximation for the ground state energy and wave functions even if perturbation theory cannot be applied in this case.

3.7.1 The stress tensor in the self-consistent harmonic approximation

In Eq. 3.5 we saw how to calculate the Born-Oppenheimer stress tensor which does not include any effect from the thermal and quantum fluctuations of the ions. In this section we will see how to calculate the SSCHA stress tensor $P_{\alpha\beta}^{SSCHA}$ which will include these effects at an anharmonic level.

In this section, the parameters of the trial Hamiltonian are \mathcal{R} , $\Phi_{s_1 s_2}^{\alpha_1 \alpha_2}(\mathbf{T}_2, \mathbf{T}_2)$ and $\{\mathbf{a}_i\}$. We will assume that \mathcal{R} are the internal coordinates and $\{\mathbf{a}_i\}$ are the lattice vectors that define the unit cell. Within the SSCHA, the stress tensor is defined as the derivative of the free energy with respect to the strain tensor

$$P_{\alpha\beta}^{SSCHA}(\mathcal{R}, \{\mathbf{a}_i\}) = -\frac{1}{\Omega} \left. \frac{\partial \mathcal{F}_H[\mathcal{R}, \{\mathbf{a}_i\}]}{\partial \epsilon_{\alpha\beta}} \right|_{\epsilon=0}, \quad (3.70)$$

where we assume that the trial 2BFC are the ones that minimize the trial free energy for the given centroids and lattice vectors. Strain affects lattice vectors and average central positions

$$\mathbf{a}'_i = \mathbf{a}_i^\alpha + \sum_{\beta=1}^3 \epsilon_{\alpha\beta} \mathbf{a}_i^\beta, \quad (3.71)$$

$$\mathcal{R}'_n^\alpha = \mathcal{R}_n^\alpha + \sum_{\beta=1}^3 \epsilon_{\alpha\beta} \mathcal{R}_n^\beta. \quad (3.72)$$

This is equivalent to performing a strain keeping fixed the internal crystal coordinates of the system. In order to compare the SSCHA stress tensor with the BO one, the SSCHA tensor can be divided into three parts[25]:

$$P_{\alpha\beta}^{SSCHA}(\mathcal{R}, \{\mathbf{a}_i\}) = P_{\alpha\beta}^{BO}(\mathcal{R}, \{\mathbf{a}_i\}) + P_{\alpha\beta}^{FLC}(\mathcal{R}, \{\mathbf{a}_i\}) + P_{\alpha\beta}^{FRC}(\mathcal{R}, \{\mathbf{a}_i\}), \quad (3.73)$$

where $P_{\alpha\beta}^{BO}$ is the static contribution from the BO stress in Eq. 3.5, $P_{\alpha\beta}^{FLC}$ is the contribution of the fluctuations to the stress, and $P_{\alpha\beta}^{FRC}$ is an extra term that takes into

account the work necessary to move the centroids according to the applied strain. The expressions for these stress tensors are

$$\begin{aligned} P_{\alpha\beta}^{FLC}(\mathcal{R}, \{\mathbf{a}_i\}) &= \langle P_{\alpha\beta}^{BO}(\mathcal{R}, \{\mathbf{a}_i\}) \rangle_{\rho_H} - P_{\alpha\beta}^{BO}(\mathcal{R}, \{\mathbf{a}_i\}) - \\ &\quad - \frac{1}{2\Omega} \sum_{s\mathbf{T}} \langle (f_s^\alpha(\mathbf{T})\mathbf{u}_s^\beta(\mathbf{T}) + f_s^\beta(\mathbf{T})\mathbf{u}_s^\alpha(\mathbf{T})) \rangle_{\rho_H}, \end{aligned} \quad (3.74)$$

$$P_{\alpha\beta}^{FRC}(\mathcal{R}, \{\mathbf{a}_i\}) = \frac{1}{2\Omega} \sum_{s\mathbf{T}} (\mathcal{R}_s^\beta(\mathbf{T}) \langle f_s^\alpha(\mathbf{T}) - f_{s\mathcal{H}}^\alpha(\mathbf{T}) \rangle_{\rho_H} + \mathcal{R}_s^\alpha(\mathbf{T}) \langle f_s^\beta(\mathbf{T}) - f_{s\mathcal{H}}^\beta(\mathbf{T}) \rangle_{\rho_H}). \quad (3.75)$$

The last term in Eq. 3.74 makes fluctuations on pressure disappear in pure harmonic crystals[25], that is why we say that $P_{\alpha\beta}^{BO}$ does not include the effect of fluctuations.

The SSCHA stress tensor can be calculated with the knowledge of the BOES, the atomic forces and the BO stress tensor. The stochastic framework in Eq. 3.67 is also valid for the stress calculation.

3.7.2 The free energy Hessian and second-order phase transitions within the SSCHA

In section 3.7 we have seen how to get an approximation for the vibrational free energy. For that purpose, the SSCHA uses trial centroids and 2BFC and will provide us with the \mathcal{R} and Φ that minimize the free energy of the system. In this section we will see how to calculate the free energy Hessian within the SSCHA and use it to predict second-order phase transitions where the order parameters are the centroids \mathcal{R} .

Displacive transitions occur, for instance, in materials with ferroelectric or charge density wave transitions. In this kind of phase transitions, according to Landau's theory of second-order phase transitions[85], at high temperature the free energy has a minimum in a high symmetry configuration \mathcal{R}_{hs} , but, on lowering the temperature, \mathcal{R}_{hs} becomes a saddle point at the transition temperature T_c . Therefore, the free energy Hessian evaluated at \mathcal{R}_{hs} , $\partial^2 F / \partial \mathcal{R} \partial \mathcal{R}|_{\mathcal{R}_{hs}}$, at high temperature is positive definite but it develops one or multiple negative eigendirections at T_c .

In Fig. 3.7 we can see a schematic representation of the free energy \mathcal{F} with respect to the order parameter Q (a particular position of the centroids in this case) for different temperatures for a system with a second-order phase transition. As we can see, at $T > T_c$, the second derivative of the free energy with respect to Q is positive, and the system stays in the high symmetry phase. As temperature decreases, at $T = T_c$, $\partial^2 F / \partial Q^2$ equals 0, and once the temperature gets below the transition temperature the free energy develops some minima and the system goes to the low symmetry phase. In second-order phase transitions the process is reversible and the critical temperature does not change by approaching T_c from below or above.

The SSCHA free energy Hessian can be computed by using the analytic formula[24]

$$\frac{\partial^2 \mathcal{F}}{\partial \mathcal{R} \partial \mathcal{R}} = \Phi + \overset{(3)}{\Phi} \Lambda(0) [\mathbf{1} - \overset{(4)}{\Phi} \Lambda(0)]^{-1} \overset{(3)}{\Phi}, \quad (3.76)$$

where

$$\overset{(n)}{\Phi} = \left\langle \frac{\partial^n U}{\partial \mathbf{R}^n} \right\rangle_{\rho_H}, \quad n > 2, \quad (3.77)$$

are the non-perturbative nBFC which should not be confused with the perturbative nBFC in Eq. 3.3 that are calculated as n^{th} derivatives of the BOES at the atomic positions defined as the minimum of the BOES. In Eq. 3.76 the value $z = 0$ of the fourth-order tensor $\Lambda(z)$ is used. For a generic complex number $z \Lambda(z)$ is defined as

$$\begin{aligned} \Lambda_{s_1 s_2 s_3 s_4}^{\alpha_1 \alpha_2 \alpha_3 \alpha_4}(\mathbf{T}_1, \mathbf{T}_2, \mathbf{T}_3, \mathbf{T}_4; z) = & -\frac{1}{2} \sum_{\mu\nu} \tilde{F}(z, \Omega_\mu^{(S)}, \Omega_\nu^{(S)}) \sqrt{\frac{1}{2m_{s_1}\Omega_\mu^{(S)}}} \epsilon_{s_1\mu\mathcal{H}}^{\alpha_1}(\mathbf{T}_1) \times \\ & \times \sqrt{\frac{1}{2m_{s_2}\Omega_\nu^{(S)}}} \epsilon_{s_2\nu\mathcal{H}}^{\alpha_2}(\mathbf{T}_2) \sqrt{\frac{1}{2m_{s_3}\Omega_\mu^{(S)}}} \epsilon_{s_3\mu\mathcal{H}}^{\alpha_3}(\mathbf{T}_3) \sqrt{\frac{1}{2m_{s_4}\Omega_\nu^{(S)}}} \epsilon_{s_4\nu\mathcal{H}}^{\alpha_4}(\mathbf{T}_4), \end{aligned} \quad (3.78)$$

where \tilde{F} is defined as

$$\begin{aligned} \tilde{F}(\omega, \omega_1, \omega_2) = & \left[\frac{2(\omega_1 + \omega_2)[1 + n_B(\omega_1) + n_B(\omega_2)]}{(\omega_1 + \omega_2)^2 - (\omega + i\delta)^2} \right] + \\ & + \left[\frac{2(\omega_1 - \omega_2)[n_B(\omega_2) - n_B(\omega_1)]}{(\omega_2 - \omega_1)^2 - (\omega + i\delta)^2} \right]. \end{aligned} \quad (3.79)$$

In all the systems considered in this thesis, $\overset{(4)}{\Phi}\Lambda(0)$ is negligible compared to the unity, therefore, we can rewrite Eq. 3.76 as

$$\frac{\partial^2 \mathcal{F}}{\partial \mathcal{R} \partial \mathcal{R}} = \overset{(3)}{\Phi} + \overset{(3)}{\Phi}\Lambda(0)\overset{(3)}{\Phi}. \quad (3.80)$$

We will define the phonons defined from the free energy as the eigenvalues ($\Omega_\mu^{(F)}(\mathbf{q})$) of the Fourier transform of

$$D_{s_1 s_2}^{\alpha_1 \alpha_2 (F)}(\mathbf{T}_1, \mathbf{T}_2) = \frac{1}{\sqrt{m_{s_1} m_{s_2}}} \frac{\partial^2 \mathcal{F}}{\partial \mathcal{R}_{s_1}^{\alpha_1}(\mathbf{T}_1) \partial \mathcal{R}_{s_2}^{\alpha_2}(\mathbf{T}_2)}. \quad (3.81)$$

Evaluating through Eq. 3.76 the free energy Hessian at \mathcal{R}_{hs} and studying its spectrum as a function of temperature, we can predict the occurrence of a displacive phase transition and estimate T_c .

3.7.3 Perturbative limit of the SSCHA

In this part we will analyze the perturbative limit of the SSCHA in order to make an analogy with perturbation theory and understand better the anharmonic phonons within the SSCHA.

From the SSCHA equations, retaining only the lowest-order correction to the harmonic values $\mathcal{R}_{s(0)}^\alpha(\mathbf{T})$ (with the subindex (0) we mark that these centroid positions are the minimum of the BOES) and ϕ , the following can be obtained[24]

$$\mathbf{D}^{(S)} \simeq \mathbf{D} + \overset{(T)}{\Pi}^{(0)} + \overset{(L)}{\Pi}^{(0)}, \quad (3.82)$$

where $\Pi^{(0)}$ and $\Pi^{(0)}$ are the tadpole and loop contributions to the harmonic self-energy and \mathbf{D} is the harmonic dynamical matrix. From this equation it is clear that, in the perturbative limit, the anharmonic lineshift of the auxiliary $\mathbf{D}^{(S)}$ dynamical matrix with respect to the harmonic one is given by the tadpole and loop contributions to the self-energy. It is extremely interesting to note that the SSCHA could be used to include the loop and tadpole diagrams to the self-energy in materials where the perturbation theory works but the calculation of the 4BFC is too cumbersome. Then, the remaining bubble self-energy could be added on top of the SSCHA by using perturbation theory[86].

In order to obtain the dynamical matrix that comes from the free energy defined in Eq. 3.81 and be able to predict second-order phase transitions, we need also the harmonic static bubble

$$\mathbf{D}^{(F)} \simeq \mathbf{D} + \Pi^{(0)} + \Pi^{(0)} + \Pi^{(0)}(0) \simeq \mathbf{D}^{(S)} + \Pi^{(0)}(0). \quad (3.83)$$

It is interesting to observe that, at the lowest perturbative order, the free energy curvature takes into account only the static harmonic bubble, whereas within perturbation theory (see Eq. 3.44 in section 3.6) the self-energy depends on the frequency. This is consistent with the fact that the SSCHA is a static theory. It is also interesting to note that Eq. 3.83 shows that $\Phi\Lambda(0)$ is neglected in the curvature formula, which means that it is discarded at lowest perturbative order. In the next section we describe a possible dynamic extension for the SSCHA studied in Ref. [24] that can potentially calculate the lifetime of phonons in the nonperturbative regime.

3.7.4 Dynamical properties of solids and phonon frequencies within the SSCHA

So far we have seen that the SSCHA is a static theory, which means that we cannot access dynamical properties, such as, the linewidth of a phonon which makes impossible the calculation of spectral functions or the thermal conductivity of a solid.

Within the SSCHA it is possible to formulate a valid ansatz in order to calculate dynamical properties of crystals. The main idea behind this ansatz is to take the nonperturbative version of Eq. 3.83 and assume the frequency dependence of the bubble self-energy. We show the diagrammatic representation of this ansatz in Fig. 3.8. In Fig. 3.8 the SSCHA Green's function is defined as

$$G_{s_1 s_2}^{-1}(\mathbf{T}_1, \mathbf{T}_2; z) = z^2 \delta_{s_1 s_2} \delta_{\alpha_1 \alpha_2} \delta_{\mathbf{T}_1 \mathbf{T}_2} - D_{s_1 s_2}^{\alpha_1 \alpha_2(S)}(\mathbf{T}_1, \mathbf{T}_2). \quad (3.84)$$

The diagrammatic representation in Fig. 3.8 is translated into the following Dyson equation

$$\mathbf{G}(z) = \mathbf{G}^{(S)}(z) + \mathbf{G}^{(S)}(z) \Pi^{(S)}(z) \mathbf{G}(z). \quad (3.85)$$

This ansatz is justified by the fact that in the lowest-order perturbative limit it

gives the same result as the perturbation theory in section 3.6. Within this assumptions, the SSCHA self-energy can be written as[24]

$$\Pi^{(S)}(z) = M^{-\frac{1}{2}} \overset{(3)}{\Phi} \Lambda(z) [1 - \overset{(4)}{\Phi} \Lambda(z)]^{-1} \overset{(3)}{\Phi} M^{-\frac{1}{2}}, \quad (3.86)$$

where $M_{ab} = \delta_{ab}m_a$ is the mass matrix. As in the static case, we can neglect the fourth-order term and rewrite the remaining self-energy, which is the bubble self-energy

$$\Pi^{(S)}(z) \simeq \overset{(B)}{\Pi}^{(S)}(z) = M^{-\frac{1}{2}} \overset{(3)}{\Phi} \Lambda(z) \overset{(3)}{\Phi} M^{-\frac{1}{2}}, \quad (3.87)$$

With this self-energy, basically, we get an analogous theory of the perturbation theory, but instead of having harmonic frequencies $\omega_\mu(\mathbf{q})$ we have the auxiliary phonon frequencies $\Omega_\mu^{(S)}(\mathbf{q})$ and instead of having the perturbative 3BFC $\overset{(3)}{\phi}_{s_1 s_2 s_3}^{\alpha_1 \alpha_2 \alpha_3}(\mathbf{T}_1, \mathbf{T}_2, \mathbf{T}_3)$ we have the nonperturbative ones $\overset{(3)}{\Phi}_{s_1 s_2 s_3}^{\alpha_1 \alpha_2 \alpha_3}(\mathbf{T}_1, \mathbf{T}_2, \mathbf{T}_3)$. By setting $z = 0$ we recover the static limit and these phonons are equivalent to the ones defined from the free energy Hessian ($D^{(F)}$) in section 3.7.2.

At this points we can recalculate the spectral function by using the 3BFC given by the SSCHA. In this case, as we are working with a non-perturbative theory, the Lorentzian approximation is not justified, and its validity must be checked in each system. In Fig. 3.9 we show a cartoon situation where the Lorentzian approximation does not hold. In this case the spectral functions are not Lorentzians and they can show strongly anharmonic features such as: shoulders, satellite peaks... As the Lorentzian picture is lost, $\Gamma_\mu(\mathbf{q})$ and $\Omega_\mu(\mathbf{q})$ are not good representatives of that phonon. The spectral function of these kind of materials can be very difficult to study from an experimental point of view, since more peaks than modes can appear or two modes can appear as only one. It is important to remark that even in non-perturbative anharmonicity is important in a system the Lorentzian approximation may hold.

The SSCHA has proven to be an extremely powerful method for including anharmonic effects at a nonperturbative level. It has been successfully applied in bulk and monolayer materials including superconductors[22, 87], materials undergoing charge density wave transitions[65, 88] and ferroelectric transitions[17], thermoelectric materials[89]...



FIGURE 3.5: Flowchart of the SSCHA minimization process.

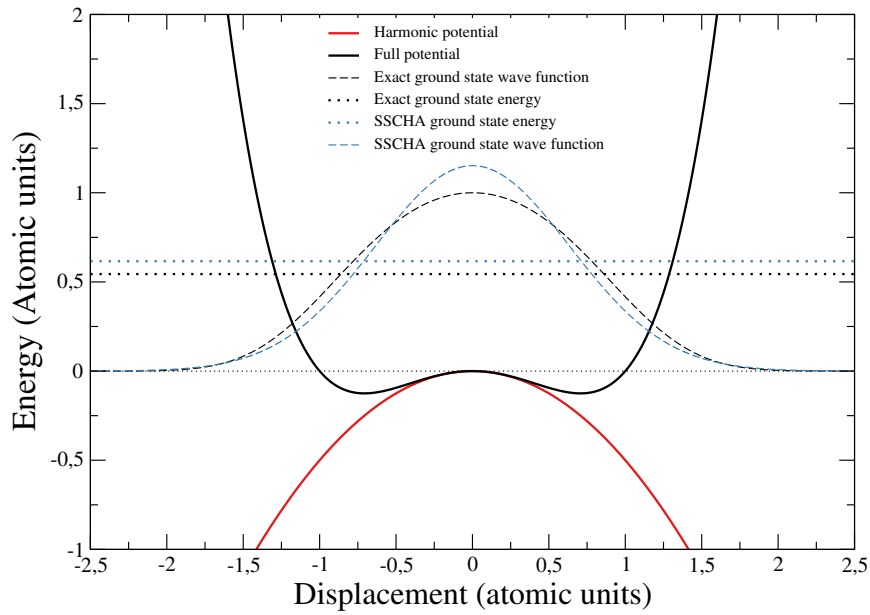


FIGURE 3.6: One dimensional example of the SSCHA with atomic units for energy and displacement. The actual potential and the harmonic one are the black and red solid curves, respectively. The ground state SSCHA at zero temperature and exact wave functions are shown with dashed curves. Dotted lines show the energy of each ground state wave function.

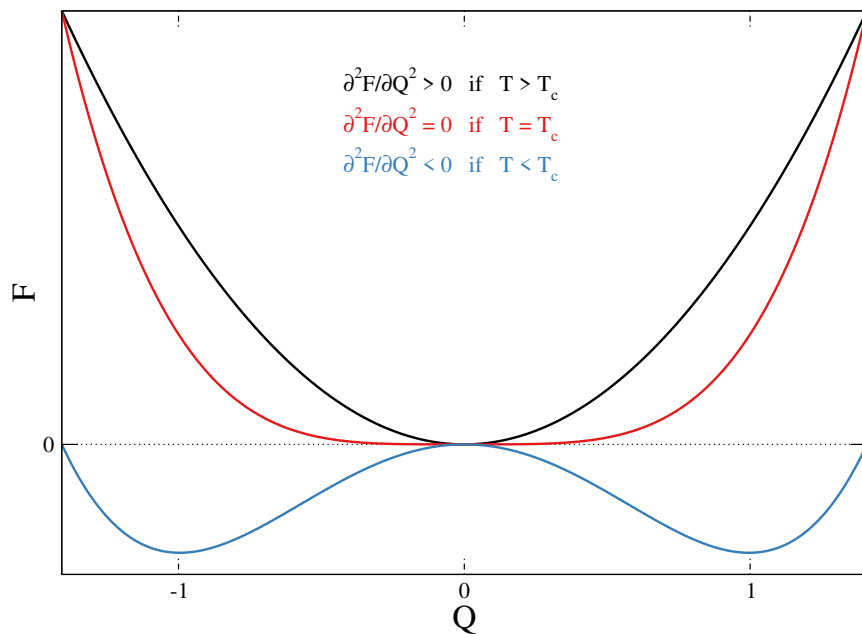


FIGURE 3.7: Free energy as a function of the order parameter for three different temperatures in a system with a second-order phase transition. The blue line corresponds to a temperature below the critical temperature, the red line to the critical temperature and the black line to a temperature above the critical temperature.

$$\overline{\overline{G(z)}} = \overline{\overline{G^{(S)}(z)}} + \overline{\overline{G^{(S)}(z) \Pi^{(S)}(z) G(z)}}$$

FIGURE 3.8: Diagrammatic representation of the Dyson equation got with a dynamical ansatz within the SSCHA. The dashed line corresponds to the SSCHA propagator. The double solid line corresponds to the full propagator.

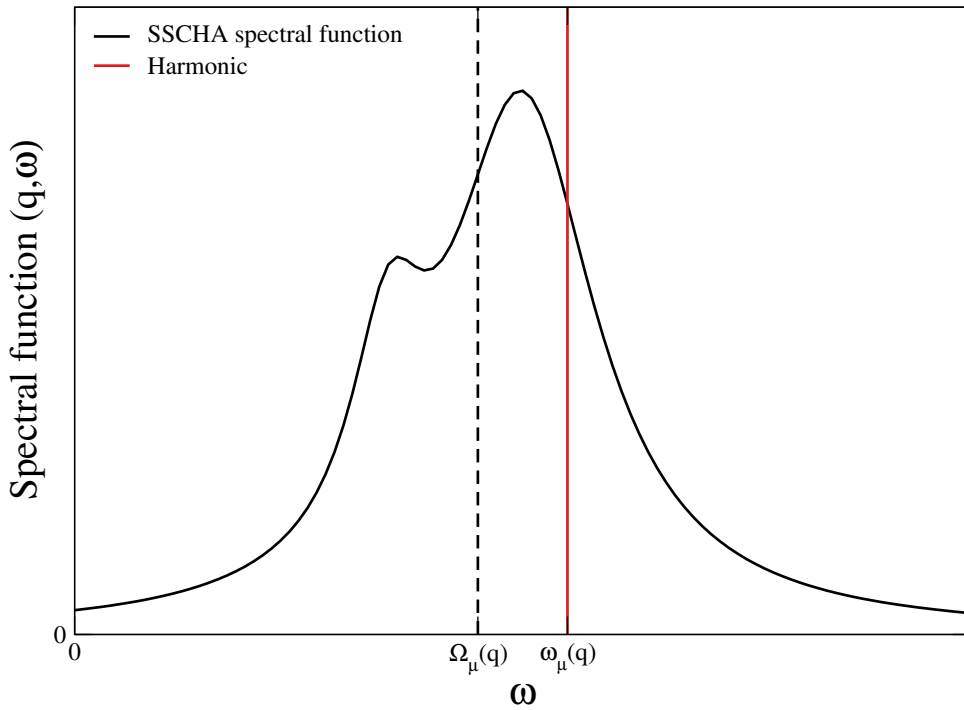


FIGURE 3.9: SSCHA and harmonic spectral functions where the Lorentzian approximation does not hold.

Chapter 4

Lattice thermal conductivity

The thermal conductivity of solids is mainly given by the electronic and lattice contributions[90]. The electronic thermal conductivity accounts for the heat conducted by the free electrons and the lattice thermal conductivity accounts for the phonon heat conduction. In metallic materials with free electrons, the thermal conductivity to electrical conductivity ratio at low temperatures is given by the Wiedemann-Franz law and it states that it is proportional to the Lorenz number multiplied by the temperature[40]. In these kind of materials the two contributions, electronic and lattice thermal conductivities, are of the same order of magnitude and both need to be calculated in order to get a good approximation of the total thermal conductivity. Instead, in insulators and intrinsic semiconductors there are no free electrons and the heat is mainly transported by phonons. As in this thesis we have studied semiconductor materials, we will only describe how to calculate the lattice thermal conductivity.

When a gradient of temperature ∇T is applied to a crystal, there will be a heat flux propagating in the material from the hot to the cold side (see Fig. 4.1). We



FIGURE 4.1: Setup where the heat (Q) is flowing from the hot (T_2) to the cold side (T_1). The figure is taken from khanacademy.org.

will assume for simplicity, without loss of generality, that the gradient is along the x Cartesian direction. The phonon heat flux density parallel to the temperature gradient can be written[91]

$$\frac{1}{N_{\mathbf{q}} \Omega_{cell}} \sum_{\mathbf{q}\mu} \omega_{\mu}(\mathbf{q}) v_{\mu}(\mathbf{q}) n_{\mathbf{q}\mu} = -\kappa_l^{xx} \frac{\partial T}{\partial x}, \quad (4.1)$$

where $\omega_\mu(\mathbf{q})$ is the frequency of phonon $\mu\mathbf{q}$, $v_\mu^\alpha(\mathbf{q}) = \frac{\partial\omega_\mu(\mathbf{q})}{\partial q_\alpha}$ is the phonon group velocity of phonon $\mu\mathbf{q}$, $n_{\mathbf{q}\mu}$ is the perturbed phonon population by the temperature gradient, κ_l^{xx} is the diagonal component of the lattice thermal conductivity in the temperature gradient direction, and $N_{\mathbf{q}}$ is the number of \mathbf{q} points taken in the 1BZ. Eq. 4.1 is known as the Fourier law of the phonon heat conduction and we can see that the knowledge of the perturbed phonon population $n_{\mathbf{q}\mu}$ allows the calculation of the lattice thermal conductivity. The equation that provides the perturbed phonon population was formulated by Peierls[92]

$$-v_\mu(\mathbf{q}) \frac{\partial T}{\partial x} \left(\frac{\partial n_{\mathbf{q}\mu}}{\partial T} \right) + \frac{\partial n_{\mathbf{q}\mu}}{\partial t} \Big|_{\text{scatt}} = 0, \quad (4.2)$$

and it is named, Boltzmann transport equation (BTE). In Eq. 4.2 the group velocity is supposed to be in the x Cartesian direction, that is why we omit the Cartesian index. The first term indicates the phonon diffusion due to the temperature gradient and the second term the scattering rate due to all the scattering processes, which can be intrinsic or extrinsic. The intrinsic scattering arises in perfect and infinite crystalline materials and is created by the anharmonic phonon-phonon scattering. The main contribution of the intrinsic scattering arises from the three-phonon scattering processes shown in Fig. 4.3. There are two: the first is the normal scattering where the momenta of the three phonons that interact are in the 1BZ

$$\mathbf{q}_1 + \mathbf{q}_2 + \mathbf{q}_3 = 0 \quad (4.3)$$

and, therefore, the crystal and total momentum are conserved. The second is the umklapp scattering, where the crystal momentum is conserved but not the total momentum, and one of the three phonon momenta is out of the 1BZ

$$\mathbf{q}_1 + \mathbf{q}_2 + \mathbf{q}_3 = \mathbf{G}, \quad (4.4)$$

\mathbf{G} being a reciprocal lattice vector. The normal scattering processes do not create thermal resistivity but can change the phonon population[93, 90], the umklapp scattering processes do create thermal resistivity. The contribution of these three phonon scattering processes to the phonon self-energy was studied in sections 3.6 and 3.7.4 and it is included in the bubble self-energy diagram in Fig. 3.3. We will see below how to calculate the thermal conductivity associated to them using the line width extracted from the bubble self-energy. Regarding the extrinsic scattering processes, there are different types and all of them create thermal resistivity: defects, impurities, boundaries... In high quality samples, at room temperature, the intrinsic scattering is usually the one playing the dominant role in balancing the perturbation due to the temperature gradient.

In order to clarify the effect of the different scattering mechanisms on the thermal conductivity, in Fig. 4.2 we show the experimental thermal conductivity of CoSb_3 [94] as a function of temperature. By looking at this figure we will describe the different regimes of the thermal conductivity as a function of temperature. At low temperatures (temperatures are always compared to the Debye temperature of the solid) the thermal conductivity increases and at a point starts to saturate, finally, it reaches a maximum and at high temperatures it constantly decreases. At low temperatures the extrinsic scattering is the dominant one because there is not enough energy for populating phonons and creating three phonon scattering events. The boundary scattering makes the thermal conductivity vanish at 0 K. Since the mobility of phonons



FIGURE 4.2: Experimental thermal conductivity of $CoSb_3$ [94] as a function of temperature and theoretical fitting with different power laws corresponding to different scattering mechanisms.

increases with temperature but they do not see the defects due to their low values of mobility, the thermal conductivity increases with temperature. At some point, the temperature starts to be high enough for the phonons to see defects and, therefore, the thermal conductivity of the solid starts to saturate. At high temperature, umklapp scattering processes start to dominate the total scattering and the thermal conductivity starts to decrease.

As we will deal with highly pure solids at temperatures that are higher than the Debye temperature, we will only include the intrinsic scattering in the scattering term in the BTE. If extrinsic scattering processes are neglected, the thermal conductivity approaches infinity as temperature decreases and decreases monotonically as temperature increases. Therefore, the thermal conductivities calculated in this thesis are only valid in the high temperature region where umklapp processes dominate.

Eq. 4.2 must be solved self-consistently. In the most general approach[95], which assumes that the perturbation from the phonon equilibrium distribution is small, the temperature gradient of the perturbed phonon population is replaced with the temperature gradient of the equilibrium phonon population. Thus, we replace $\frac{\partial n_{\mathbf{q}\mu}}{\partial T}$ by $\frac{\partial n_B(\omega_\mu(\mathbf{q}))}{\partial T}$. In the case of the scattering term in Eq. 4.2 we can expand it about its equilibrium value in terms of a first-order perturbation $f_{\mathbf{q}\mu}^{EX}$ (which is the quantity that we want to get)

$$n_{\mathbf{q}\mu} \simeq n_B(\omega_\mu(\mathbf{q})) + n_B(\omega_\mu(\mathbf{q}))(n_B(\omega_\mu(\mathbf{q})) + 1) \frac{\partial T}{\partial x} f_{\mathbf{q}\mu}^{EX}. \quad (4.5)$$



FIGURE 4.3: Feynman diagrams for three phonon scattering events. The one in the left corresponds to $P_{\mathbf{q}_1\mu_1, \mathbf{q}_2\mu_2}^{\mathbf{q}_3\mu_3}$, where two phonons collide ($\mathbf{q}_1\mu_1, \mathbf{q}_2\mu_2$) to create a new one ($\mathbf{q}_3\mu_3$), and the one in the right corresponds to $P_{\mathbf{q}_1\mu_1}^{\mathbf{q}_2\mu_2, \mathbf{q}_3\mu_3}$, where one phonon ($\mathbf{q}_1\mu_1$) is splitted in two phonon modes ($\mathbf{q}_2\mu_2, \mathbf{q}_3\mu_3$).

By using this equation, the linearized BTE can be written as[96]

$$\begin{aligned} v_\mu(\mathbf{q}) \left(\frac{\partial n_B(\omega_\mu(\mathbf{q}))}{\partial T} \right) = & \sum_{\substack{\mu_1\mu_2 \\ \mathbf{q}_1\mathbf{q}_2}} [P_{\mathbf{q}_\mu, \mathbf{q}_1\mu_1}^{\mathbf{q}_2\mu_2}(f_{\mathbf{q}\mu}^{EX} + f_{\mathbf{q}_1\mu_1}^{EX} - f_{\mathbf{q}_2\mu_2}^{EX}) \\ & + \frac{1}{2} P_{\mathbf{q}_\mu}^{\mathbf{q}_1\mu_1, \mathbf{q}_2\mu_2}(f_{\mathbf{q}\mu}^{EX} - f_{\mathbf{q}_1\mu_1}^{EX} - f_{\mathbf{q}_2\mu_2}^{EX})]. \quad (4.6) \end{aligned}$$

The EX superscript of the first-order perturbation f^{EX} denotes the exact solution of the linearized BTE. In Eq. 4.6 $P_{\mathbf{q}_\mu, \mathbf{q}_1\mu_1}^{\mathbf{q}_2\mu_2}$ is the scattering rate at the equilibrium of a process where a phonon mode \mathbf{q}_μ scatters by absorbing another mode $\mathbf{q}_1\mu_1$ to generate a third phonon $\mathbf{q}_2\mu_2$. $P_{\mathbf{q}_\mu}^{\mathbf{q}_1\mu_1, \mathbf{q}_2\mu_2}$ is the scattering rate at the equilibrium of a process where a phonon mode \mathbf{q}_μ decays in two phonons $\mathbf{q}_1\mu_1$ and $\mathbf{q}_2\mu_2$. We can see the diagrams of these scattering processes in Fig. 4.3. The two scattering rates have the forms

$$\begin{aligned} P_{\mathbf{q}_\mu, \mathbf{q}_1\mu_1}^{\mathbf{q}_2\mu_2} = & \frac{2\pi}{N_{\mathbf{q}}} \sum_{\mathbf{G}} |{}^{(3)}\phi_{\mu\mu_1\mu_2}(\mathbf{q}, \mathbf{q}_1, \mathbf{q}_2)|^2 \\ & \times n_B(\omega_\mu(\mathbf{q})) n_B(\omega_{\mu_1}(\mathbf{q}_1)) [n_B(\omega_{\mu_2}(\mathbf{q}_2)) + 1] \delta_{\mathbf{q} + \mathbf{q}_1 - \mathbf{q}_2, \mathbf{G}} \\ & \times \delta(\omega_\mu(\mathbf{q}) + \omega_{\mu_1}(\mathbf{q}_1) - \omega_{\mu_2}(\mathbf{q}_2)), \quad (4.7) \end{aligned}$$

$$\begin{aligned} P_{\mathbf{q}_\mu}^{\mathbf{q}_1\mu_1, \mathbf{q}_2\mu_2} = & \frac{2\pi}{N_{\mathbf{q}}} \sum_{\mathbf{G}} |{}^{(3)}\phi_{\mu\mu_1\mu_2}(\mathbf{q}, -\mathbf{q}_1, -\mathbf{q}_2)|^2 \\ & \times n_B(\omega_\mu(\mathbf{q})) [n_B(\omega_{\mu_1}(\mathbf{q}_1)) + 1] [n_B(\omega_{\mu_2}(\mathbf{q}_2)) + 1] \delta_{\mathbf{q} - \mathbf{q}_1 - \mathbf{q}_2, \mathbf{G}} \\ & \times \delta(\omega_\mu(\mathbf{q}) - \omega_{\mu_1}(\mathbf{q}_1) - \omega_{\mu_2}(\mathbf{q}_2)). \quad (4.8) \end{aligned}$$

In the previous equations we have written the anharmonic 3BFC in normal coordinates space. For that purpose we need to apply the following transformation to the atomic displacements in the nBFC in Eq. 3.3

$$X_{\mathbf{q}\mu} = \frac{1}{N_{\mathbf{q}}} \sum_{\mathbf{T}s\alpha} \sqrt{2m_s\omega_\mu(\mathbf{q})} \epsilon_{s\mu}^{\alpha*}(\mathbf{q}) u_s^\alpha(\mathbf{T}) e^{-i\mathbf{q}\cdot\mathbf{T}}. \quad (4.9)$$

For simplifying the equations above, we can rewrite Eq. 4.6 in matrix form

$$\mathbf{A}\mathbf{f}^{EX} = \mathbf{b}, \quad (4.10)$$

where $b_{\mathbf{q}\mu} = -v_\mu(\mathbf{q})\omega_\mu(\mathbf{q})n_B(\omega_\mu(\mathbf{q}))[n_B(\omega_\mu(\mathbf{q})) + 1]$ and

$$\begin{aligned} A_{\mathbf{q}\mu, \mathbf{q}_1\mu_1} &= \sum_{\substack{\mu_2\mu_3 \\ \mathbf{q}_2\mathbf{q}_3}} \left(P_{\mathbf{q}\mu, \mathbf{q}_3\mu_3}^{\mathbf{q}_2\mu_2} + \frac{P_{\mathbf{q}\mu, \mathbf{q}_2\mu_2}^{\mathbf{q}_3\mu_3}}{2} \right) \delta_{\mathbf{q}\mathbf{q}_1, \mu\mu_1} \\ &\quad - \sum_{\mathbf{q}_2\mu_2} (P_{\mathbf{q}\mu, \mathbf{q}_2\mu_2}^{\mathbf{q}_1\mu_1} - P_{\mathbf{q}\mu, \mathbf{q}_1\mu_1}^{\mathbf{q}_2\mu_2} + P_{\mathbf{q}_1\mu_1, \mathbf{q}_2\mu_2}^{\mathbf{q}\mu}). \end{aligned} \quad (4.11)$$

For getting the two equations above we have used $P_{\mathbf{q}\mu}^{\mathbf{q}_1\mu_1, \mathbf{q}_2\mu_2} = P_{\mathbf{q}_1\mu_1, \mathbf{q}_2\mu_2}^{\mathbf{q}\mu}$ from the balance condition $n_B(\omega_\mu(\mathbf{q}))[n_B(\omega_{\mu_1}(\mathbf{q}_1)) + 1][n_B(\omega_{\mu_2}(\mathbf{q}_2)) + 1] = [n_B(\omega_\mu(\mathbf{q})) + 1]n_B(\omega_{\mu_1}(\mathbf{q}_1))n_B(\omega_{\mu_2}(\mathbf{q}_2))$ valid under the assumption $\omega_\mu(\mathbf{q}) = \omega_{\mu_1}(\mathbf{q}_1) + \omega_{\mu_2}(\mathbf{q}_2)$. In this form the matrix \mathbf{A} is symmetric and positive semidefinite[91] and it can be splitted as $\mathbf{A} = \mathbf{A}^{in} + \mathbf{A}^{out}$ where

$$A_{\mathbf{q}\mu, \mathbf{q}_1\mu_q}^{out} = \frac{n_B(\omega_\mu(\mathbf{q}))[n_B(\omega_\mu(\mathbf{q})) + 1]}{\tau_\mu(\mathbf{q})} \delta_{\mu\mu_1} \delta_{\mathbf{q}\mathbf{q}_1}, \quad (4.12)$$

$$A_{\mathbf{q}\mu, \mathbf{q}_1\mu_1}^{in} = - \sum_{\mathbf{q}_2\mu_2} P_{\mathbf{q}\mu, \mathbf{q}_2\mu_2}^{\mathbf{q}_1\mu_1} - P_{\mathbf{q}\mu, \mathbf{q}_1\mu_1}^{\mathbf{q}_2\mu_2} + P_{\mathbf{q}_1\mu_1, \mathbf{q}_2\mu_2}^{\mathbf{q}\mu}, \quad (4.13)$$

where $\tau_\mu(\mathbf{q})$ is the phonon relaxation time or lifetime defined in Eq. 3.55. The \mathbf{A}^{out} diagonal matrix accounts for the depopulation of phonon states due to the anharmonic scattering while the \mathbf{A}^{in} matrix describes their repopulation due the incoming scattered phonons.

Eq. 4.10 can be solved by inverting the \mathbf{A} matrix

$$\mathbf{f}^{EX} = \mathbf{A}^{-1} \mathbf{b}. \quad (4.14)$$

Finally, with knowledge of \mathbf{f}^{EX} the thermal conductivity can be calculated as

$$\kappa_l = \lambda \mathbf{b} \cdot \mathbf{f}^{EX} = \frac{-1}{N_{\mathbf{q}} \Omega_{cell} k_B T^2} \sum_{\mathbf{q}\mu} v_\mu(\mathbf{q}) \omega_\mu(\mathbf{q}) n_B(\omega_\mu(\mathbf{q})) [n_B(\omega_\mu(\mathbf{q})) + 1] f_{\mathbf{q}\mu}^{EX}, \quad (4.15)$$

where $\lambda = 1/(N_{\mathbf{q}} \Omega_{cell} k_B T)$.

The main problem for calculating the lattice thermal conductivity is that the \mathbf{A} matrix is, in general, a large non-diagonal matrix which must be computed, stored and inverted, which makes the problem unsolvable for realistic systems. The simplest approximation one can do to solve the problem is the so called single mode relaxation time approximation (SMA).

4.1 Single mode relaxation time approximation (SMA)

In the SMA the BTE is solved for $n_{\mathbf{q}\mu}$ by setting \mathbf{A}^{in} to zero, in this way the problem is solvable as the matrix to invert is diagonal. So, now, the solution of the problem is

$$\mathbf{f}^{SMA} = (\mathbf{A}^{out})^{-1} \mathbf{b}, \quad (4.16)$$

which means that we are neglecting the role of the repopulation of the phonon modes. Within this approximation the lattice thermal conductivity can be written

as

$$\kappa_l^{SMA} = \lambda \mathbf{b} \cdot \mathbf{f}^{SMA} = \frac{1}{N_{\mathbf{q}} \Omega_{cell} k_B T^2} \sum_{\mathbf{q}\mu} v_\mu(\mathbf{q})^2 \omega_\mu(\mathbf{q})^2 n_B(\omega_\mu(\mathbf{q})) [n_B(\omega_\mu(\mathbf{q})) + 1] \tau_\mu(\mathbf{q}). \quad (4.17)$$

As we can see, the lattice thermal conductivity can be calculated with the knowledge of the phonon spectrum and the line width of the phonons, which can be calculated within perturbation theory or the SSCHA as discussed in sections 3.6 and 3.7, respectively.

The SMA has a conceptual problem that arises from its definition and it is that both normal and umklapp scattering processes contribute to the thermal resistivity of the solid. This is not actually what happens in real solids because, as we have already mentioned, normal processes do not create thermal resistivity. In other words, the thermal conductivity within the SMA does not account for the thermal repopulation given by the normal scattering processes. Anyway, the SMA remains a very good approximation in materials where the umklapp scattering dominates the phonon-phonon interaction. The simplest approximation one can do to go beyond the SMA is the so called Callaway model[93], which was proposed by Callaway in 1959 and it is still applied nowadays. Some years ago a very elegant and exact way of calculating the lattice thermal conductivity was proposed[91] and implemented based on a variational principle.

4.2 Exact solution of the linearized BTE

An exact way of solving the linearized BTE can be found by using the properties of the matrix \mathbf{A} and the variational principle. The exact solution of the BTE is the vector \mathbf{f}^{EX} , which maximizes or minimizes the quadratic form[97]

$$\mathcal{P}(\mathbf{f}) = \frac{1}{2} \mathbf{f} \cdot \mathbf{A} \mathbf{f} - \mathbf{b} \cdot \mathbf{f}, \quad (4.18)$$

for a generic vector \mathbf{f} . Since \mathbf{A} is positive definite the stationary point is the global minimum of this functional. The variational conductivity functional can be defined as

$$\kappa_l^V(\mathbf{f}) = -2\lambda \mathcal{P}(\mathbf{f}), \quad (4.19)$$

which fulfills the property $\kappa_l^V(\mathbf{f}^{EX}) = \kappa_l$, while any other value of $\kappa_l^V(\mathbf{f})$ underestimates κ_l . Thus, minimizing the quadratic form is equivalent to maximizing the thermal conductivity functional. Eq. 4.10 can be solved on a grid[91] by using the conjugate gradient method to obtain the exact solution of the BTE.

This method has proven to be extremely accurate in predicting the thermal conductivity of materials where the normal scattering processes are as important or even more than the umklapp scattering processes[98, 99].

Part II

Thermoelectric monochalcogenides

Chapter 5

Bulk SnSe

5.1 Introduction

Thermoelectricity is a technologically interesting material property that allows to transform residual heat into useful electricity[100, 101]. The efficiency of this energy transformation is controlled by the dimensionless figure of merit defined in Eq. 1. The thermal conductivity $\kappa = \kappa_e + \kappa_l$ is the sum of electronic κ_e and lattice κ_l thermal conductivities. Therefore, a good thermoelectric performance requires a high power factor $P_F = S^2\sigma$ together with a low thermal conductivity.

Monochalcogenides have proven to be efficient thermoelectric materials[9, 27, 102, 103] mainly due to their strongly anharmonic lattice that implies a low lattice thermal conductivity[104, 105, 106, 107, 17]. PbTe is an appropriate example of potential technological relevance of thermoelectric monochalcogenides: it shows a high ZT in the 600 – 800 K temperature range[108], as high as 2.2 when nanostructured[12], and has been successfully applied in spacecrafts[109]. In the last years SnSe has attracted a great deal of attention since it was measured to be the most efficient intrinsic thermoelectric material[6]. Its figure of merit soars to 2.6 after a structural phase transition[6, 110, 111, 112, 113] at around 800 K from the low-symmetry *Pnma* phase to the high-symmetry *Cmcm*. See Fig. 5.1 for the crystal structure of the two phases. In the high-symmetry phase the band gap is reduced without affecting the ultralow thermal conductivity, providing the record ZT .

The phase transition takes the system from the orthorhombic *Pnma* phase to a more symmetric base-centered orthorhombic *Cmcm* structure. The order of the phase transition is not clear: some works[6, 110, 111, 113] claim it is a second-order phase transition and others[112] indicate it has a first-order character. A recent work[114] argues that the transition occurs in two steps, where increasing temperature induces first a change in the lattice parameters that later triggers a lattice instability. On the other hand, there is an inelastic scattering experiment for the high-temperature phase, showing a prominent phonon collapse at the transition temperature, which suggests that the transition is of the second-order type[113].

The most interesting thermoelectric properties appear in the high-temperature phase, where the reduction of the electronic band gap increases the number of carriers providing a higher P_F , while the thermal conductivity remains very low. The value of the intrinsic κ_l of SnSe remains controversial, as the extremely low isotropic 0.3 W/mK values at 800 K reported by Zhao et al.[6] could not be reproduced in other experiments, where a clear anisotropy is shown and the in-plane thermal conductivity is considerably larger[115, 116, 117]. The lattice thermal conductivity of the

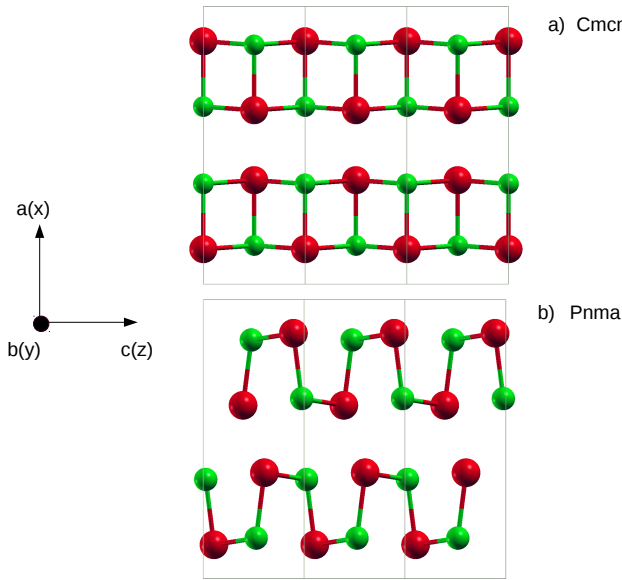


FIGURE 5.1: SnSe crystal structure in the (a) *Pnma* and (b) *Cmcm* phases.

Pnma phase has been calculated[118, 119] from first principles solving the BTE using harmonic phonons and 3BFC obtained perturbatively as derivatives of the BOES. The *Cmcm* phase has imaginary phonons in the harmonic approximation[114, 119, 120], as expected for the high-symmetry phase in a second-order phase transition, hindering the calculation of κ_l .

In this chapter we study the vibrational and thermal properties of *Cmcm* SnSe by including anharmonicity at a nonperturbative level by using the SSCHA. We show that the phonon mode that drives the instability collapses at the transition temperature T_c demonstrating that the transition is second-order. Anharmonic effects are so large that the spectral function for some in-plane modes deviates from the Lorentzian-like shape and show broad peaks, shoulders and satellite peaks, as in other monochalcogenides[17, 105]. We calculate the lattice thermal conductivity of *Cmcm* SnSe by combining the anharmonic phonon spectra with perturbative and nonperturbative 3BFC. We show that nonperturbative anharmonic effects are not only crucial in the phonon spectra, but also in high-order force-constants, which have a huge impact on the calculated thermal conductivity. κ_l agrees with experiments[115] only with nonperturbative 3BFC.

5.2 Structure and high symmetry points

The *Cmcm* and *Pnma* phases are orthorhombic and their structure is shown in Fig. 5.1. The *Cmcm* phase has a centering in the XZ plane of the rectangular conventional cell and contains 4 atoms in the primitive cell. The primitive cell of the *Pnma* phase contains 8 atoms. The primitive lattice vectors of the *Cmcm* structure are: $\mathbf{a}_1 = (a/2, 0, c/2)$, $\mathbf{a}_2 = (-a/2, 0, c/2)$ and $\mathbf{a}_3 = (0, b, 0)$, where a (long axis), b and c are the lattice constants of the conventional cell.

Symmetry point	Reduced \mathbf{q} vector
Z	0.0, 0.0, 0.5
R	0.5, 0.0, 0.5
S	0.5, 0.0, 0.0
Γ	0.0, 0.0, 0.0
Y	0.5, -0.5, 0.0
T	0.5, -0.5, 0.5

TABLE 5.1: Reduced \mathbf{q} vectors of the high symmetry points in the Brillouin zone of the $Cmcm$ phase. The coordinates are given with respect to the reciprocal lattice vectors of the primitive cell.

The reciprocal lattice of the $Cmcm$ phase is shown in Fig. 5.2. The reciprocal lat-

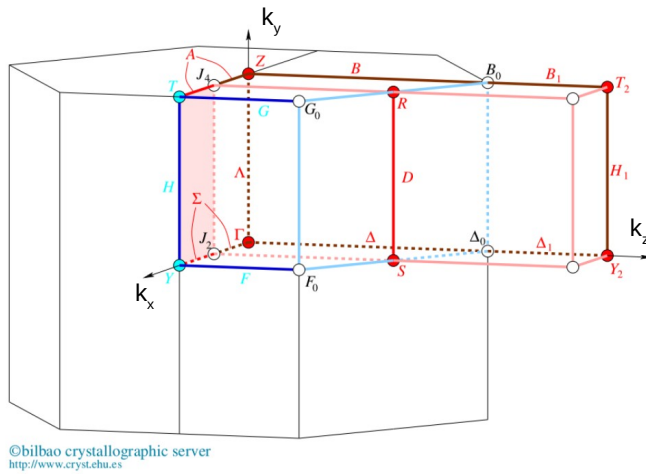


FIGURE 5.2: 1BZ of $Cmcm$ SnSe. The figure is taken from the Bilbao crystallographic server.

tice vectors of the $Cmcm$ primitive 1BZ are $\mathbf{b}_1 = 2\pi(1/a, 0, 1/c)$, $\mathbf{b}_2 = 2\pi(-1/a, 0, 1/c)$ and $\mathbf{b}_3 = 2\pi(0, 1/b, 0)$. The high symmetry points and their coordinates used in phonon dispersion figures are listed in table 5.1.

In both phases, $Cmcm$ and $Pnma$, the Sn and Se atoms are located in the 4c Wyckoff positions. In the $Cmcm$ phase this Wyckoff position has only one free parameter and it is of the form $(x, 1/4, 0)$. In the $Pnma$ phase there are two free parameters $(x, 1/4, z)$. When the system transforms from the $Pnma$ to the $Cmcm$ phase, the free z parameter of the 4c Wyckoff position is forced to be in the high symmetry position. As the $Cmcm$ phase has a centering, this high symmetry position can be 0 or 0.5.

5.3 Calculation details

Our calculations are based on DFT using the QUANTUM-ESPRESSO[16] software package. Harmonic phonons were calculated within DFPT and perturbative 3BFC

were calculated within DFPT or finite differences[83]. Anharmonic phonons and nonperturbative 3BFC were calculated using the SSCHA. For the exchange-correlation interaction we use the Perdew-Burke-Ernzerhof (PBE) generalized gradient approximation and the local density approximation (LDA) with ultrasoft (US) and Projector Augmented Wave (PAW) pseudopotentials, respectively. Due to limitations in the implementation of perturbative 3BFC within DFPT we use norm-conserving (NC) pseudopotentials only for the perturbative 3BFC calculation. We use a cutoff energy of 70 Ry and a grid of $16 \times 16 \times 16$ k points to sample the first Brillouin zone. For the harmonic phonon calculations we use a $6 \times 6 \times 6$ supercell and a $2 \times 2 \times 2$ one for the 3BFC. We impose the acoustic sum rule to the third-order force-constants with an iterative method prior to their Fourier interpolation[18, 89]. For the SSCHA calculation we use a $2 \times 2 \times 2$ supercell. Then, for the anharmonic phonon dispersion, we interpolate the difference between the harmonic and anharmonic force-constants in the $2 \times 2 \times 2$ supercell to the $6 \times 6 \times 6$ and we add it to the $6 \times 6 \times 6$ harmonic force-constants (see appendix B for more details). For the linewidth calculations we use a $20 \times 20 \times 20$ q points grid obtained by Fourier interpolation with a smearing of 1 cm^{-1} . For the thermal conductivity calculation we use a $10 \times 10 \times 10$ grid of q points to sample the first Brillouin zone. We have done calculations in denser grids to test these parameters. We have done SSCHA calculations using different lattice volumes. When we talk about the "theory" (theoretical) lattice we are referring to the relaxed lattice at DFT level. When we talk about the "exp" (experimental) lattice we refer to the experimental lattice parameters at the transition temperature between *Cmcm* and *Pnma* phases. The "stretched" lattice refers to a stretched lattice with respect to the "theory" in the PBE case. The lattice parameters and the experimental references are listed in table 5.2. We have only included the effective charges in the calculation of the harmonic phonons in Figs. 5.7 and 5.6. We have seen that the effect of the effective charges is negligible in the thermal conductivity. In order to account for the effective charges within the SSCHA, we include the effective charges in the dynamical matrices after the SSCHA minimization.

5.4 Phase transition

The group/subgroup index of the *Cmcm*/*Pnma* transition is 2, making a displacive second-order transition possible[121]. In this scenario, the transition temperature T_c is defined as the temperature at which the second derivative of the free energy F with respect to the order parameter Q that transforms the structure continuously from the *Cmcm* phase ($Q = 0$) into the *Pnma* ($Q \neq 0$) vanishes. As it was already pointed out[111], symmetry[122, 123] dictates that the amplitude of the transition is dominated by the distortion pattern associated to a non-degenerate mode (Y_1) at the zone border Y point with irreducible representation Y_2^+ (see Fig. 5.3 for the distortion pattern). This means that $\partial^2 F / \partial Q^2$ is proportional to the eigenvalue of the free energy Hessian matrix associated to this irreducible representation: $\Omega_{Y_1}^{(F)2}$. This frequency can be calculated within the SSCHA using Eq. 3.76.

The calculated temperature dependence of $\Omega_{Y_1}^{(F)2}$ is shown in Fig. 5.4 for LDA and PBE for two different lattice volumes in each case. In all cases $\Omega_{Y_1}^{(F)2}$ is positive at high temperatures, but it rapidly decreases with lowering the temperature, vanishing at T_c . This phonon collapse is consistent with a second-order phase transition between the *Pnma* and *Cmcm*. We check that a SSCHA calculation at $T > T_c$ ($T = 800$ K) starting from the relaxed low-symmetry *Pnma* phase (relaxed at DFT

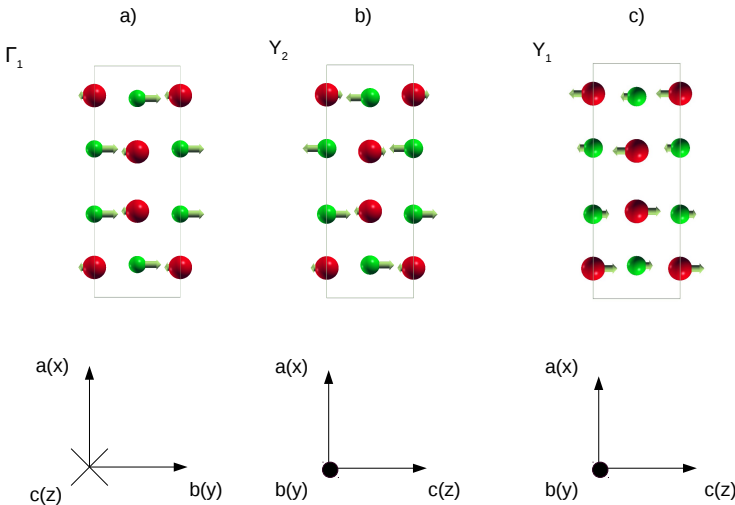


FIGURE 5.3: (a) Atomic displacements of mode Γ_1 . (b) Atomic displacements of mode Y_2 . (c) Atomic displacements of mode Y_1 .

static level) yields the high-symmetry $Cmcm$ atomic positions for the \mathcal{R} centroids. The SSCHA relaxation is shown in Fig. 5.5. As we can see, the z free Wyckoff parameters of the 4c Wyckoff positions of the $Pnma$ phase relax to the high symmetry positions 0 (atoms 5, 6, 7, and 8) and 0.5 (atoms 1, 2, 3, and 4). The new Wyckoff position is the 4c wyckoff position of the $Cmcm$ phase. The error in this relaxation is smaller than $0.04 a_0$. Thus, the $Pnma$ is not a local minimum of the free energy above T_c , ruling out the first-order transition.

Our result disagrees with the conclusions drawn in Ref. [114]. First, because at the T_c calculated in the reference above, which is estimated by comparing the free energies of the two structures, the Y_1 mode of the $Cmcm$ phase is stable, which implies

	a	b	c	P_{xx}	P_{yy}	P_{zz}
LDA theory	21.58	7.90	7.90	0.4	0.6	0.7
LDA Exp.	22.13	8.13	8.13	-1.1	-2.0	-2.2
PBE theory	22.77	8.13	8.13	0.5	1.1	1.0
PBE Exp.	22.13	8.13	8.13	1.8	1.3	1.2
PBE Stretched	23.48	8.27	8.27	-0.3	-0.7	-0.7

TABLE 5.2: Experimental[6] and theoretical (DFT at static level) LDA and PBE lattice parameters used in this work. The stretched cell used in some calculations is also given. a , b , and c lattice parameters are given in Bohr unit length (a_0) and the three components of the stress tensor in GPa units. The pressure is calculated including vibrational terms at an anharmonic level at the following temperatures for each case: 200 K (LDA theory), 600 K (LDA Exp.), 400 K (PBE Exp.), 400 K (PBE theory), and 400 K (PBE stretched).

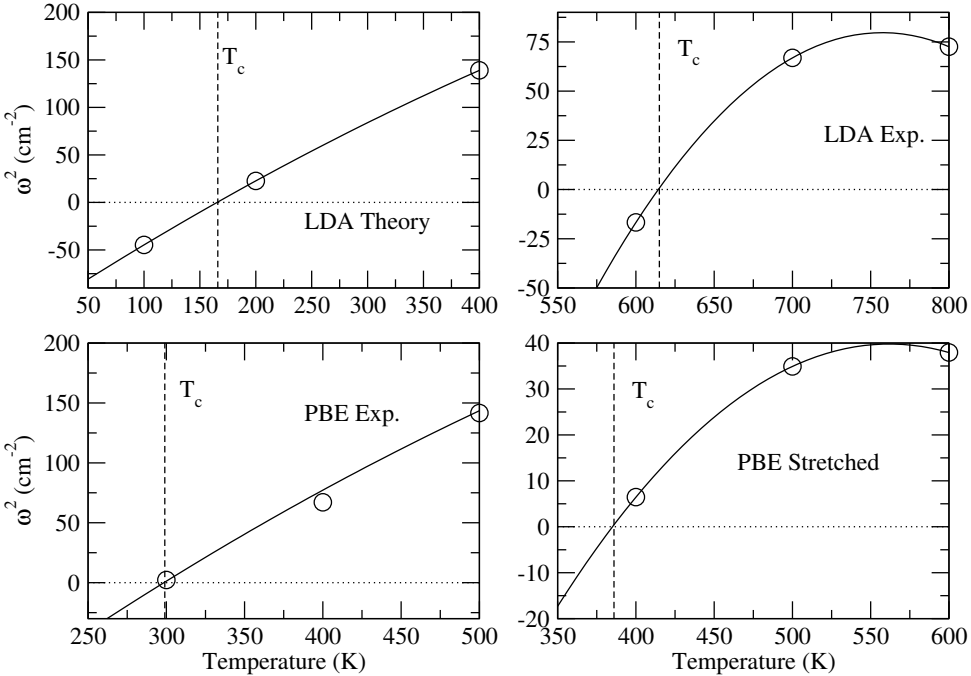


FIGURE 5.4: $\Omega_{Y_1}^{(F)2}$ as a function of temperature within LDA and PBE approximations for different lattice volumes (circles). In the LDA we compare the results obtained with the theoretical and experimental[6] lattice parameters. In the PBE calculation we present the results for the experimental lattice parameters and a stretched unit cell (see Table 5.2 for the lattice parameters). The solid lines correspond to a polynomial fit.

this phase is a local minimum at T_c , and, thus, the transition is of first-order type. And second, because it is argued that the instability at Y is produced by a slight change in the in-plane lattice parameters induced by temperature (from $c/b > 1$ to $c/b < 1$), which makes the transition a two-step process. We do not see this sudden appearance of the instability. In order to compare with the calculations in Ref. [114] and see whether the change from $c/b > 1$ to $c/b < 1$ is responsible for creating the instability at the point Y , we have done the phonon calculation using the lattice parameters of Ref. [114]. The result is shown in Fig. 5.6. It is clear that the change in the lattice parameters does not alter the instability, as expected for such a small change.

The obtained transition temperature strongly depends on the exchange-correlation functional and volume, as it occurs in similar monochalcogenides[17]. This volume dependence can be also appreciated in the harmonic phonons. In Fig. 5.7 we can see the LDA and PBE harmonic phonon spectra in the theoretical and experimental structures. As we can see, within LDA, the difference between phonons in the theoretical and experimental structures is clearly visible. Due to the bigger volume in the experimental cell, there is a red shift of almost all the vibrational modes and, furthermore, more imaginary frequencies arise at the Γ and Y points. Within PBE, the phonon spectra in the theoretical and experimental structures are much more similar, because the lattice parameters in these structures are very similar as well. We conclude that the harmonic phonons of SnSe are very sensitive to the volume of

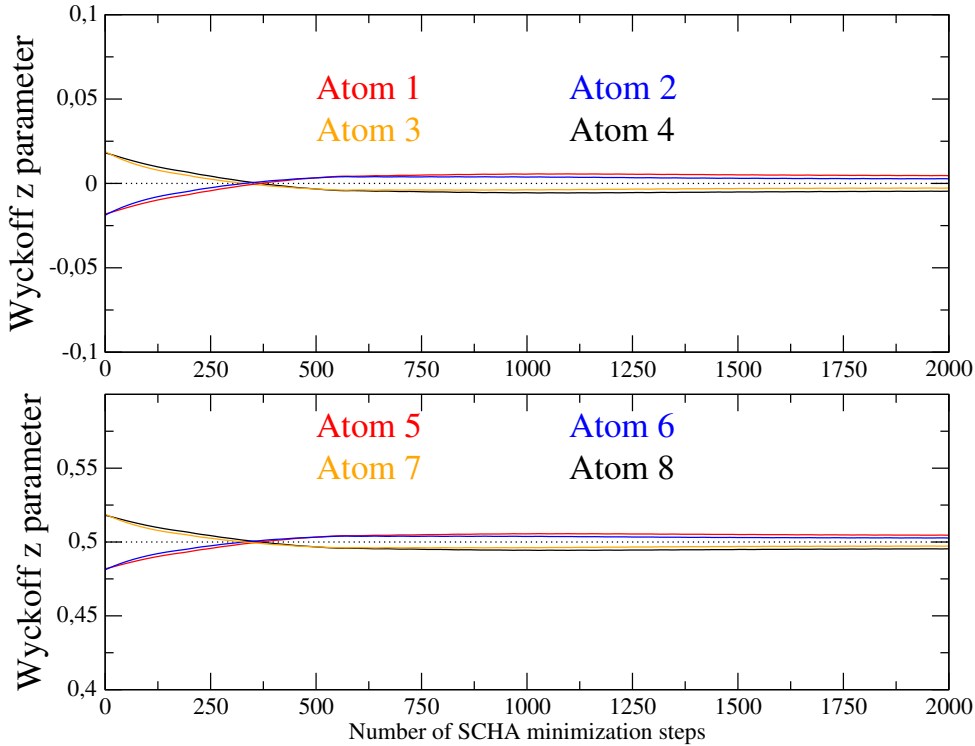


FIGURE 5.5: Wyckoff z parameter of the 4c Wyckoff position in the $Pnma$ phase as a function of the SSCHA minimization step. Each color corresponds to a different atom in a given high symmetry position in the $Cncm$ phase.

the unit cell. The volume dependence of the harmonic phonons also arises in the transition temperature. Within LDA T_c ranges between 168 K with theoretical lattice parameters and 616 K with experimental lattice parameters. Within PBE T_c barely changes between the experimental and theoretical lattice parameters. We attribute this result to the fact that the in-plane lattice parameters b and c are in good agreement with the experimental results within PBE, while LDA clearly underestimates them.

The theoretical lattice parameters are estimated neglecting vibrational contributions to the free energy. In order to estimate the role of the thermal expansion, we calculate the stress tensor including vibrational contributions at the anharmonic level as explained in section 3.7.1. The in-plane contribution of the stress tensor calculated at the temperature closest to T_c , P_{zz} , shows that both theoretical LDA and PBE lattices should be stretched. Within LDA it is clear that stretching the lattice increases T_c . Within PBE, when we take a stretched lattice to reduce P_{zz} , T_c increases from 299 K to 387 K. In all cases the other in-plane component of the stress tensor, P_{yy} , is very similar to P_{zz} . The LDA transition temperature with the experimental lattice parameters yields the transition temperature in closest agreement with experiments ($T_c \simeq 800$ K). The underestimation of the transition temperature may be due to the approximated exchange-correlation or the finite $2 \times 2 \times 2$ supercell size taken for the SSCHA.

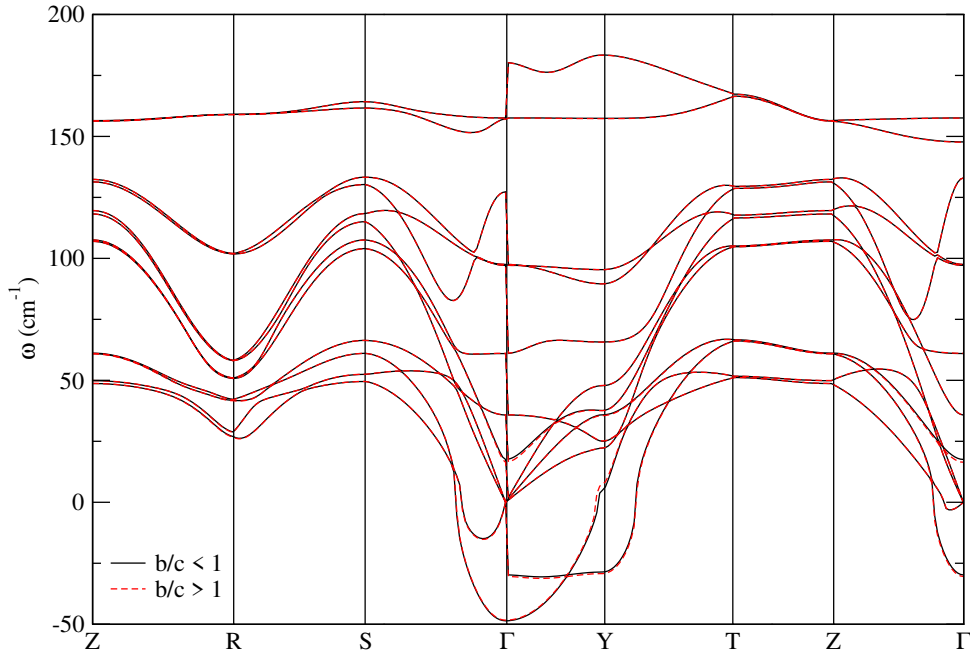


FIGURE 5.6: PBE harmonic phonon spectra with the following lattice parameters: $a = 22.492$, $b = 8.094$ and $c = 8.090$ (in Bohr units) (red) in one case and exchanging b and c (black) in the other. We have done the calculation in a $2 \times 2 \times 2$ supercell and Fourier interpolated to plot the spectrum. The effective charges are included in the calculations.

5.5 Phonons in $Cmcm$ SnSe

The predicted phonon collapse should be measurable by inelastic neutron scattering experiments (INS). INS experiments[124] show a softening of a zone-center optical mode of the $Pnma$ phase upon heating, which is consistent with the condensation of the Y_1 mode after the transition. The condensation of the Y_1 mode was experimentally measured in another work[113].

First of all, in Fig. 5.8, we compare the harmonic phonon spectrum with the anharmonic one in the Lorentzian (see Eqs. 3.53 and 3.54) approximation obtained at 800 K within LDA in the experimental lattice (the results below are also obtained within LDA in the experimental lattice). The anharmonic line shift is large for most of the modes across the 1BZ. Within the harmonic approximation there are five unstable modes: two (Γ_1, Γ_2) at Γ , two (Y_1, Y_3) at Y and one (R_1) at R . These instabilities appear when we do the harmonic calculation in the experimental cell, in the theoretically relaxed cell only appear instabilities Γ_1 and Y_1 . The instabilities at Γ would cause ferroelectric transitions[119, 125], but they suffer an anharmonic renormalization that prevents it. Y_3 and R_1 are also stabilized by anharmonic effects. The Y_1 mode however remains unstable at 600 K and it is stabilized after the transition (see Fig. 5.10).

In Fig. 5.9 we compare our harmonic and anharmonic phonons with available INS experimental results[113] at 853 K. As we can see, we get a good agreement with the experimental points. If we have a look to the lowest energy acoustic branch, we can see that the anharmonic phonons agree very well with the experimental values.

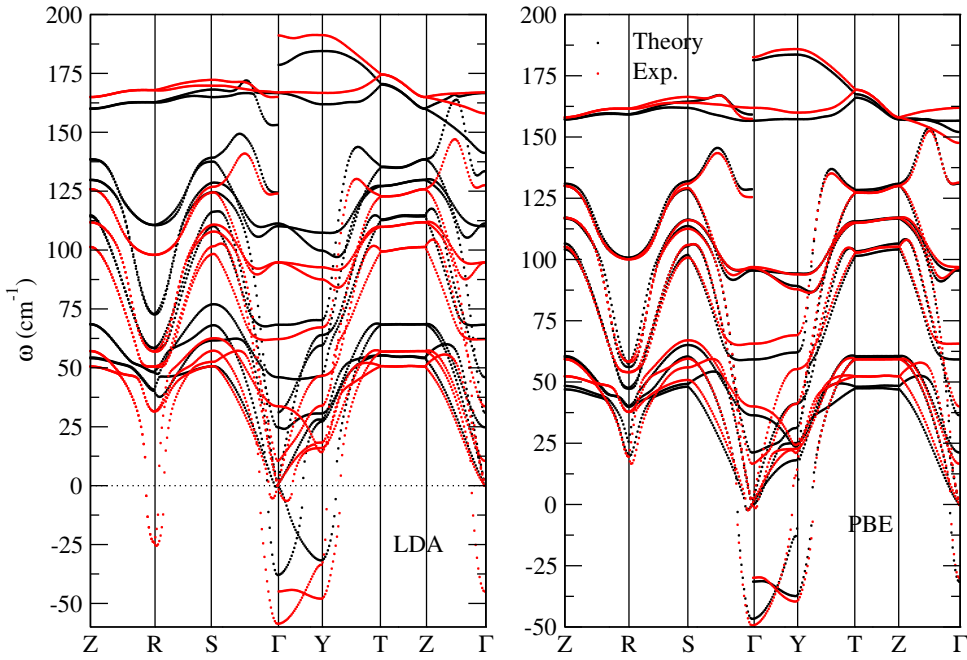


FIGURE 5.7: (a) LDA harmonic phonon spectra in the theoretical and experimental structures. (b) The same as (a) within PBE. The effective charges are included in the calculations.

In this case the harmonic result completely fails as it is imaginary at the Y point. We also get a fairly good agreement in the $25 - 100 \text{ cm}^{-1}$ energy range. The worst agreement appears in the highest energy optical modes, where we underestimate the values.

In highly anharmonic materials[17, 105, 126, 104, 86], the spectral functions show broad peaks, shoulders and satellite peaks, strongly deviating from the Lorentzian picture. In Fig. 5.10 we show the spectral function keeping the full frequency dependence (see Eq. 3.51) on the self-energy, without assuming the Lorentzian lineshape. The spectral function clearly reproduces the collapse of the Y_1 mode at the transition temperature. The calculated spectral functions show that the strong anharmonicity present on the phonon frequency renormalization is also reflected on the spectral function. The anharmonic features specially affect the in-plane modes in the $25 - 75 \text{ cm}^{-1}$ energy range. For instance, at the Γ point the Γ_1 mode, who describes a vibration along the in-plane y axis in opposite direction for the Sn and Se atoms (see Fig. 5.3) and is stabilized by anharmonicity, shows a double peak structure and a broad shoulder (see Fig. 5.10). The mode that describes the same vibration (Γ_2) but in the other in-plane z direction also shows a complex non-Lorentzian shape. The overall $\tilde{\sigma}(q = \Gamma, \omega)$ consequently has a broad shoulder at $\simeq 25 \text{ cm}^{-1}$ as marked in Fig. 5.10 (c), which is less acute as temperature increases. At the Y point there are also two modes, Y_2 , whose eigenvector is plotted in Fig. 5.3, and Y_3 , which describes the same displacement but in the other y in-plane direction, that show a strongly anharmonic non-Lorentzian shape. The modes with complex lineshapes are those that show the largest linewidth in the Lorentzian limit (see Fig. 5.8). These modes have strongly anomalous spectral functions and large linewidths because they can easily scatter with an optical mode close in energy and an acoustic mode close to Γ . We identify this by directly analyzing which phonon triplets contribute more to the

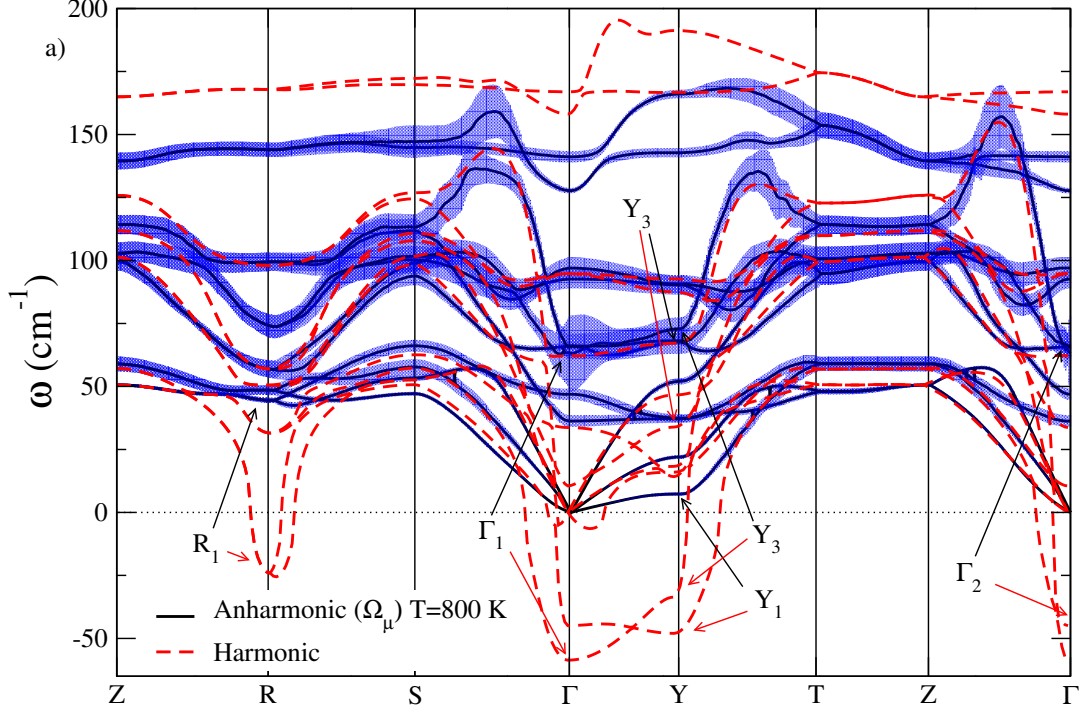


FIGURE 5.8: Harmonic and anharmonic phonons in the Lorentzian approximation ($\Omega_\mu(\mathbf{q})$). The length of the bars corresponds to the linewidth (full length of the line is the full width at half maximum divided by a factor of 1.5). The calculations are done within LDA in the experimental structure using SSCHA 3BFC at 800 K and $\Omega_\mu^{(S)}(\mathbf{q})$ at 800 K.

linewidth. It is interesting to remark that if the phonon self-energy is calculated by substituting Φ by ϕ , changing the nonperturbative 3BFC by the perturbative ones, the anomalies of these modes become weaker. We show the spectral function at the points Γ and Y calculated with the perturbative and nonperturbative 3BFC in Fig. 5.11. This underlines that in the *Cmcm* phase the third-order derivative of the BOES are not sufficient to calculate the phonon linewidths and that higher order terms are important, which are effectively captured by Φ .

5.6 Lattice thermal conductivity of *Cmcm* SnSe

In Fig. 5.12 we present the lattice thermal conductivity calculated with the SSCHA frequencies ($\Omega_\mu^{(S)}(\mathbf{q})$) and nonperturbative 3BFC (Φ). For comparison we also calculate κ_l substituting Φ by ϕ . The calculation is performed solving the BTE assuming the single-mode relaxation times approximation (SMA) (see chapter 4). The thermal conductivity of SnSe is very low, mainly because the contribution of optical modes is strongly suppressed by the large anharmonicity and the contribution of acoustic modes is also reduced due to the large scattering among themselves and with the Γ_1 mode. In Fig. 5.13 we plot the group velocity, linewidth, cumulative lattice thermal conductivity ($\kappa_l^c(\omega) = \int_0^\omega \kappa(\omega) d\omega$) and the phonon density of states (PDOS).

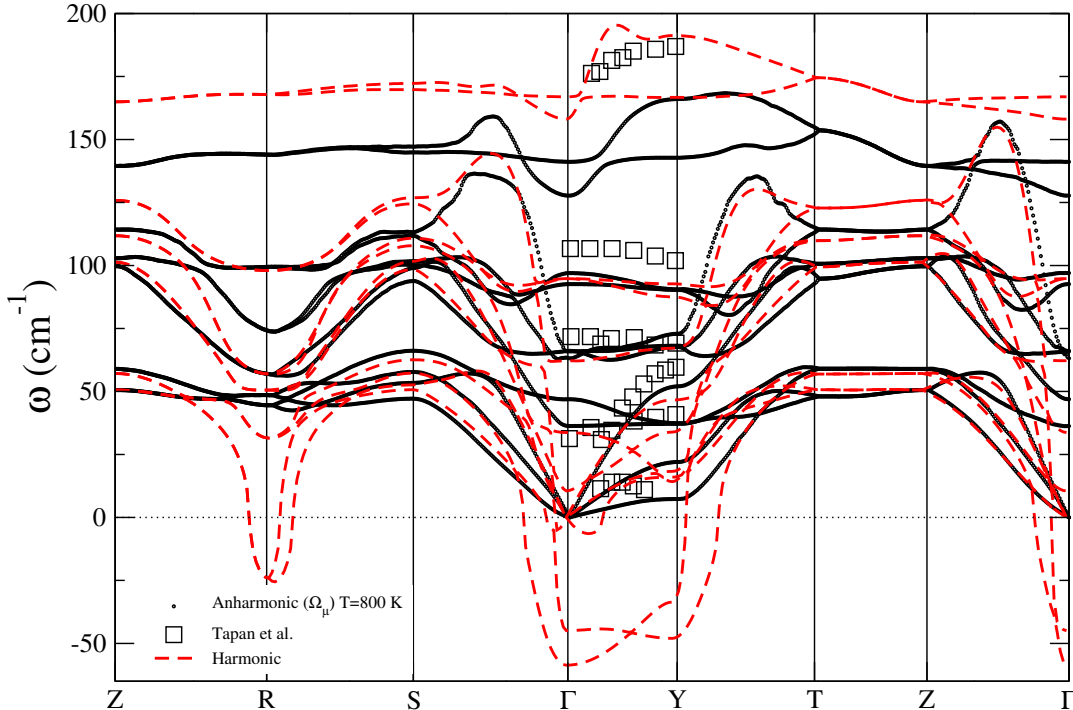


FIGURE 5.9: Harmonic and anharmonic phonons in the Lorentzian approximation ($\Omega_\mu(\mathbf{q})$). We include experimental points[113] at 853 K.

As we see in Fig. 5.13 (a), due to the layered structure of the system, the group velocity is much lower in the out-of-plane direction x , leading to a reduced thermal conductivity. The two in-plane directions show very similar group velocities, as we would expect in this high symmetry phase. Interestingly, we can see in Fig. 5.13 (b) that the nonperturbative linewidth has a similar dispersion to the perturbative one, however, it is homogeneously higher in the whole frequency range. In agreement with the spectral function, this makes clear the need for a nonperturbative treatment of SnSe and yields a much lower thermal conductivity as we can see in Fig. 5.13 (c). From Fig. 5.13 (c) we can also extract that almost the entire contribution to the thermal conductivity is coming from vibrational modes with frequency smaller than 100 cm^{-1} . Furthermore, more than 50% of the thermal conductivity is coming from the acoustic modes ($\omega < 75 \text{ cm}^{-1}$) which, looking at the phonon density of states in Fig. 5.13 (d), is mainly coming from the vibrations of Sn atoms. The rest of the in-plane thermal conductivity is coming from the Sn and Se vibrations at around 90 cm^{-1} . The situation is different for the out-of-plane component due to its very low group velocity in the $50 - 150 \text{ cm}^{-1}$ frequency range. The rest of its contribution is coming from high energy modes where group velocities are higher. The contribution of the optical modes is strongly suppressed by the large phonon linewidths, which are a consequence of the strong anharmonicity of this compound. The contribution of the acoustic modes is particularly low, which ensures a low κ_l , specially because they can strongly scatter among themselves and with the Γ_1 mode. Therefore, the strongly anharmonic modes (Γ_1, Γ_2) provide an important scattering channel for lowering the thermal conductivity and making SnSe a very good thermoelectric material.

We compare our results with the values obtained by Zhao et al.[6] above the transition at 800 K. We also include in the figure the results obtained by Ibrahim et

al.[115] above 600 K (only the in-plane κ_l is reported at these temperatures) in the *Pnma* phase. Even if the results belong to different phases, comparing our calculations for the *Cmcm* phase with those obtained in the latter work is insightful because the thermal conductivity of these two phases is very similar close to the transition, as expected in a second-order phase transition. We include the measurement by Wei et al.[127] as well. They show measurements for both phases. We do not distinguish between the two in-plane measurements of Wei et al. as the difference is difficult to extract from their data. They measure the phase transition at around 800 K in agreement with Zhao et al.[6].

Though direct comparison should be taken carefully where compared with the results by Ibrahim et al.[115], the lattice thermal conductivity is in better agreement with the experimental results using $\Phi^{(3)}$ instead of $\phi^{(3)}$, which overestimates the lattice thermal conductivity along in-plane directions. This is consistent with the larger phonon linewidths obtained with the nonperturbative 3BFCs. The agreement for the in-plane $\kappa_{yy} \sim \kappa_{zz}$ with the measurements by Ibrahim et al.[115] and Wei et al.[127] is good in the nonperturbative limit, contrary to previous calculations that underestimate it[119]. The calculated out-of-plane κ_{xx} is also in good agreement with the results by Zhao et al.[6], but we find that their ultralow results for the in-plane κ_l , in contradiction with the values in Refs. [115, 127], are underestimated. These results suggest that the thermal conductivity measured by Zhao et al. may have non-intrinsic effects as it has already been pointed out[128]. In the work by Wei et al. they measure the maximum *ZT* of fully dense *Cmcm* SnSe and it is shown to be around 1, much lower than the 2.6 value measured by Zhao et al.[6]. This fact also suggests the non-intrinsic effects in the results by Zhao et al.[6].

5.7 Conclusions

In conclusion, we show that the vibrational properties of SnSe in the *Cmcm* phase are dominated by huge nonperturbative anharmonic effects. We show how the collapse of the Y_1 mode is responsible for the second-order phase transition. We verify that the transition is actually second-order by making a SSCHA atomic relaxation starting from the low symmetry phase and verifying that the system goes to the high symmetry phase, clarifying that the low symmetry phase is not a local minimum in the free energy. The calculated transition temperature is volume and functional dependent. We get the best agreement with experiments by using the experimental lattice parameters within LDA. The spectral functions of in-plane modes are characterized by anomalous features deviating from the Lorentzian-like shape. These results will be crucial to interpret future INS experiments for the high-temperature phase. The calculated in-plane thermal conductivity is in good agreement with the experiments by Ibrahim et al.[115] and Wei et al.[127], but not with those by Zhao et al.[6], which show low anisotropy. These results suggest that the isotropic ultralow values by Zhao et al. could be the observation of a non-intrinsic property. Our results show for the first time that the inclusion of nonperturbative effects is crucial for obtaining third-order force-constants that yield a lattice thermal conductivity in agreement with experiments.

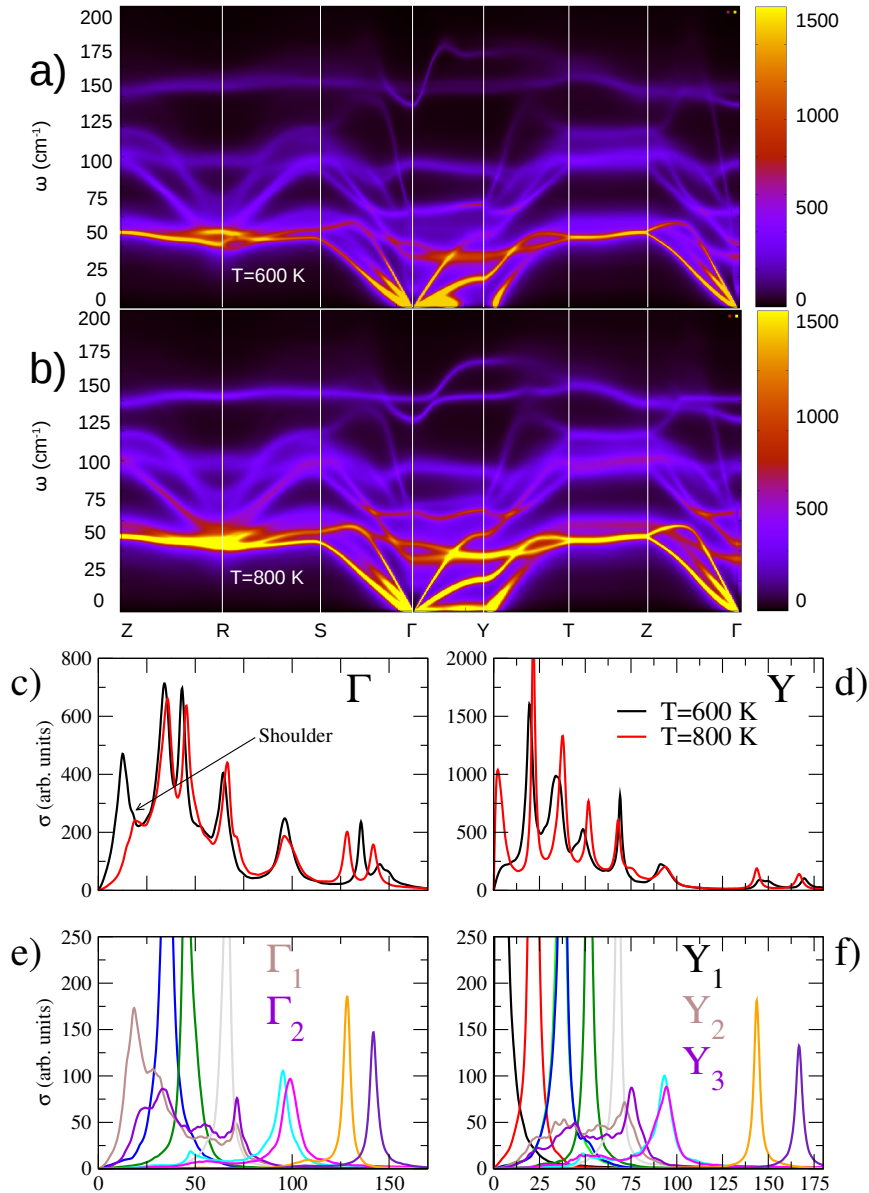


FIGURE 5.10: Spectral function of SnSe in the $Cmcm$ phase calculated at (a) 600 K and (b) 800 K using the SSCHA 3BFC at the corresponding temperature. The spectral function at the (c) Γ and (d) Y points at 600 and 800 K. The contribution of each mode to the spectral function is also shown at the Γ point (e) and the Y point (f) at 800 K. Different colors correspond to different modes. All the calculations are performed within LDA in the experimental structure. In each case we use $\Omega_{\mu}^{(S)}(\mathbf{q})$ calculated at the same temperature as the SSCHA 3BFC.

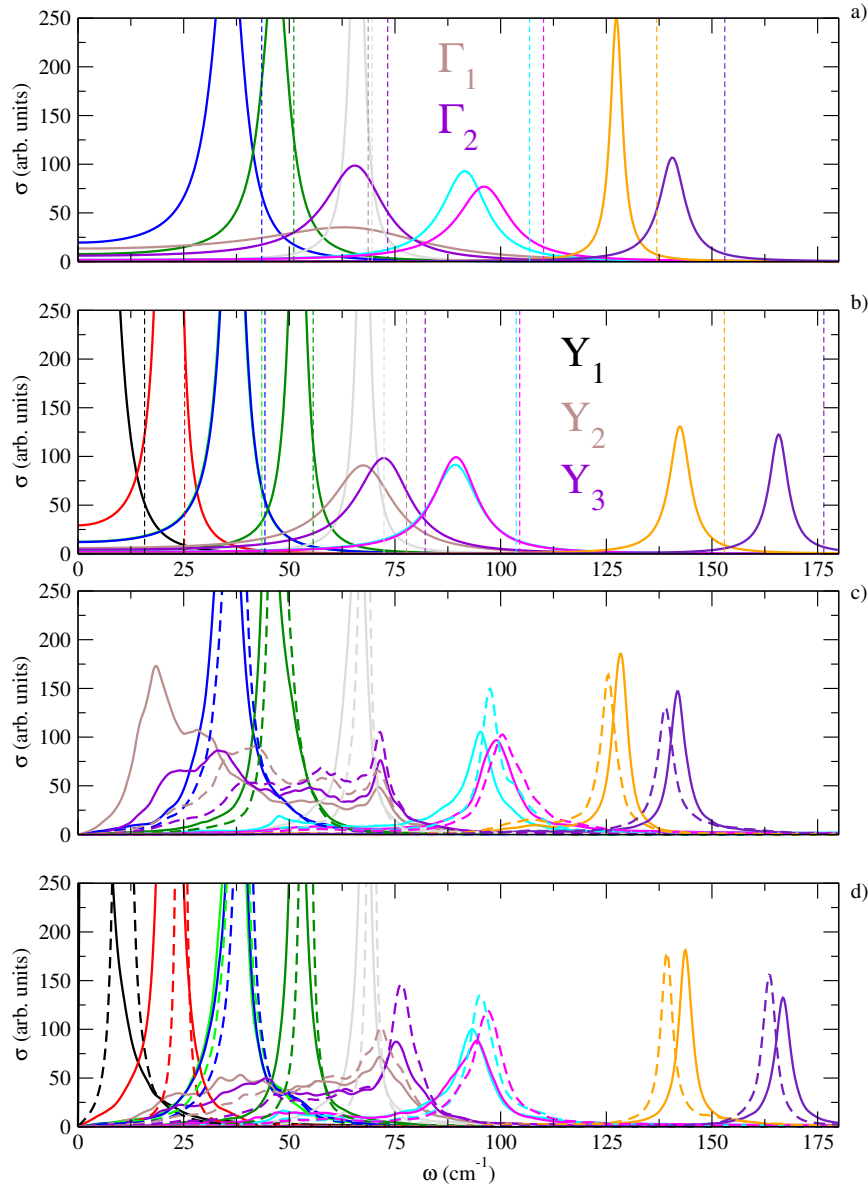


FIGURE 5.11: (a) Nonperturbative spectral functions calculated in the Lorentzian approximation at the Γ point. (b) The same as (a) at the point Y . Dashed vertical lines correspond to $\Omega_\mu^{(S)}$ frequencies. (c) Nonperturbative (solid lines) and perturbative (dashed lines) spectral functions calculated at the Γ point. (d) The same as (c) at the point Y . The calculations are done using $\Omega_\mu^{(S)}$ SSCHA frequencies at 800 K within LDA in the experimental structure. Nonperturbative calculations are done with 3BFC at 800 K.

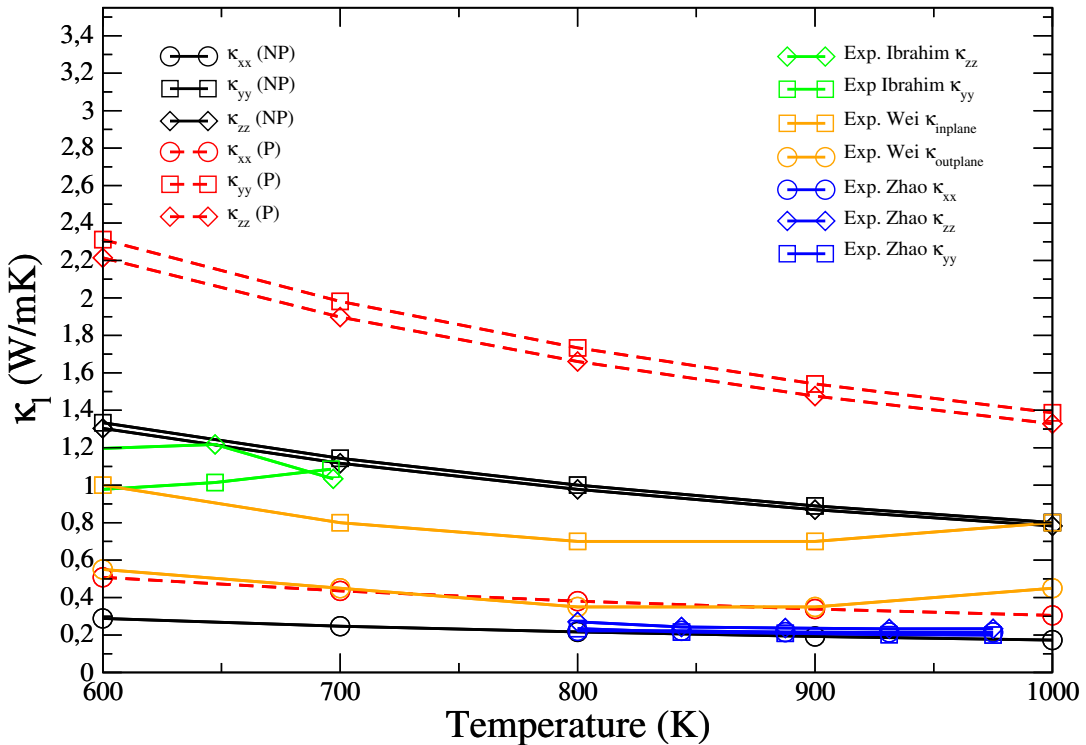


FIGURE 5.12: Lattice thermal conductivity of SnSe calculated with perturbative (P) and nonperturbative (NP) at 800 K compared to the experiments by Ibrahim et al.[115], Zhao et al.[6], and Wei et al.[127]. We use the $\Omega_\mu^{(S)}(\mathbf{q})$ phonon frequencies calculated at 800 K at all temperatures. Calculations are performed within LDA using the experimental structure.

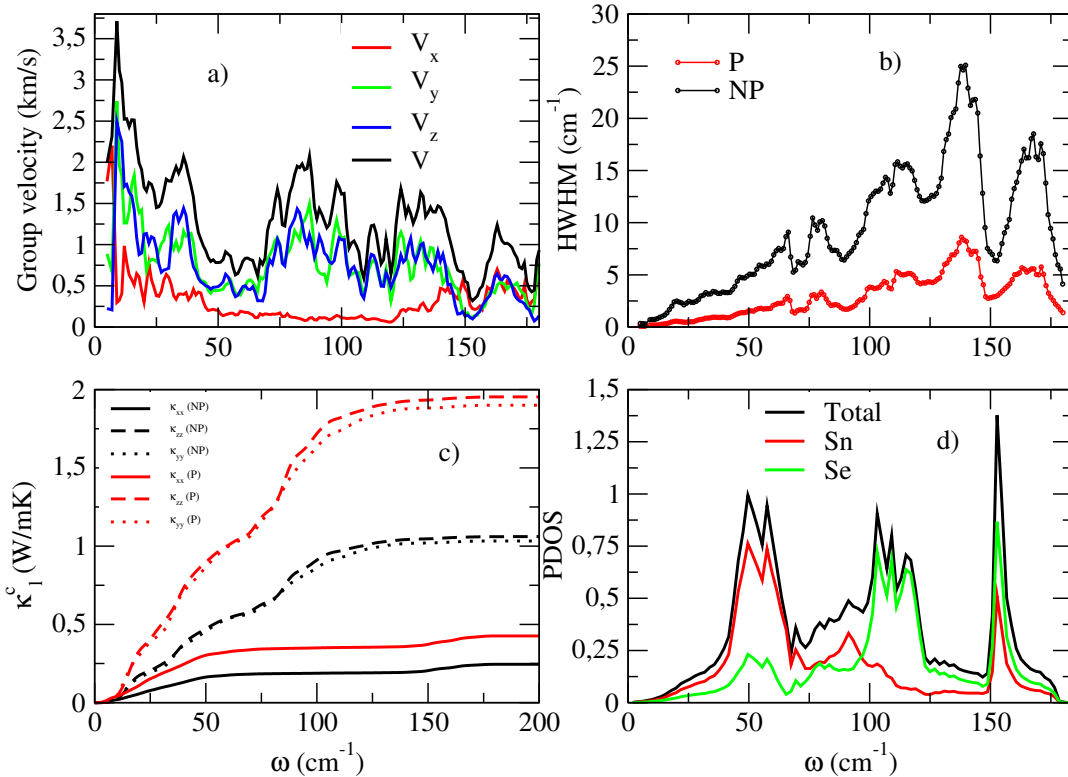


FIGURE 5.13: (a) Absolute value of the phonon group velocity and absolute values of the group velocity Cartesian components. (b) Average linewidth as a function of frequency for perturbative (P) (red) and nonperturbative (NP) (black) approaches. (c) Diagonal components of the cumulative thermal conductivity as a function of frequency at 800 K for perturbative (P) (red) and nonperturbative (NP) (black) approaches. (d) Phonon density of states and the projections in Sn and Se atoms. The calculations are done within LDA in the experimental structure using $\Omega_\mu^{(S)}$ frequencies and nonperturbative 3BFC at 800 K.

Chapter 6

Bulk SnS

6.1 Introduction

SnS is isoelectronic to SnSe and shows very similar electronic and vibrational properties[129] at low temperatures. Experimentally it also shows a phase transition[111, 112] from the *Pnma* to the *Cmcm* structure and a very low thermal conductivity in the former[14, 130] phase. Therefore, it is expected to be a very efficient thermoelectric material in the high temperature phase, which together with the fact that S is much more abundant in the earth than Se, makes it a very interesting candidate for technological applications. Actually, in Refs. [14, 130] it is shown how the *ZT* of undoped SnS increases very fast before the phase transition, as in the case of SnSe. However, as far as we know, there are no experimental transport measurements for the high temperature phase of SnS. First-principles calculations of the thermoelectric properties are also absent in the literature, hindered by the unstable modes obtained within the harmonic approximation, as in the case of SnSe[119, 114].

In this chapter, we propose that *Cmcm* SnS is expected to be a very efficient intrinsic thermoelectric material, as good as SnSe in this phase. We show that the P_F of SnSe and SnS are expected to be very similar in this phase, as long as the electronic relaxation time is similar in both materials. By including anharmonicity in the phonon calculation at a nonperturbative level within the SSCHA we show that the phonon spectrum of SnS suffers a strong anharmonic renormalization. The phase transition is driven by the collapse of a zone-border phonon. Anharmonicity is so large that the spectral function of some vibrational modes deviates from the Lorentzian-like shape as it happens in other monochalcogenides[17, 105]. Finally, we calculate the lattice thermal conductivity of *Cmcm* SnS obtaining very low values below $\simeq 1.0$ W/mK. Nonperturbative anharmonic corrections to the 3BFC are important in this calculation as it happens in SnSe. There is a clear anisotropy between in-plane and out-of-plane thermal conductivities. The similarity of the power factors and the lattice thermal conductivities of SnSe and SnS suggest that the latter may be an earth abundant efficient thermoelectric material and motivates more experimental effort to measure its *ZT* in the high temperature phase.

6.2 Calculation details

We calculate the electronic bands using *ab initio* DFT calculations within the local density approximation (LDA)[45] and the generalized gradient approximation in the Perdew Burke Ernzerhof (PBE) parametrization[46] as implemented in the QUANTUM ESPRESSO[16] software package. Harmonic phonons and perturbative 3BFC

⁽³⁾ ϕ are calculated using Density Functional Perturbation Theory[59, 18]. We use projector augmented wave[52] (PAW) pseudopotentials that include $5s^2$ $5p^2$ $4d^{10}$ electrons in the case of Sn and $3s^2$ $3p^4$ in the case of S. For the perturbative 3BFC we use norm-conserving pseudopotentials which were shown[89] to provide very similar third-order force-constants compared to the PAW result. A $16 \times 16 \times 16$ sampling of the first Brillouin zone of the primitive cell and an energy cutoff of 70 Ry are employed for the DFT self-consistent calculation. For the electronic transport calculations we use the Boltztrap software package[131]. For the self-consistent DFT calculation we use a $30 \times 30 \times 30$ sampling of the first Brillouin zone. We use experimental lattice parameters at the transition temperature as we got better agreement with experiments for SnSe in the previous chapter. The experimental lattice parameters taken from Refs.[110, 111] are $a = 21.69$ a₀, $b = 7.84$ a₀, $c = 7.84$ a₀ (a₀ is the Bohr length). The structures of the high temperature *Cmcm* and low temperature *Pnma* phases are shown in Fig. 5.1. Anharmonic phonons and nonperturbative third-order force-constants are calculated within the SSCHA using a $2 \times 2 \times 2$ supercell. For the SSCHA calculation we use forces calculated within DFT. Once we get the anharmonic force-constants, we subtract the harmonic ones and interpolate the difference to a $6 \times 6 \times 6$ grid. Then, we add this interpolated difference to the harmonic dynamical matrices in a $6 \times 6 \times 6$ grid, which yields anharmonic force-constants in a fine grid (see appendix B for more details). By Fourier interpolating the latter we can calculate phonon frequencies at any point in the Brillouin zone. We impose the acoustic sum rule to the third-order force-constants with an iterative method prior to their Fourier interpolation[18, 89]. The lattice thermal conductivity is calculated in a $10 \times 10 \times 10$ grid. For the calculation of the phonon linewidths we use a $20 \times 20 \times 20$ mesh with a Gaussian smearing of 1 cm^{-1} for the Dirac deltas.

6.3 Electronic transport

Within the semiclassical Boltzmann transport theory[132] the electrical conductivity and the Seebeck coefficient can be calculated respectively as

$$\sigma(T, \mu) = \int_{-\infty}^{\infty} d\epsilon \left[-\frac{\partial f(T, \mu, \epsilon)}{\partial \epsilon} \right] \Sigma(\epsilon) \quad (6.1)$$

$$S(T, \mu) = \frac{1}{T\sigma(T, \mu)} \int_{-\infty}^{\infty} d\epsilon \left[-\frac{\partial f(T, \mu, \epsilon)}{\partial \epsilon} \right] \Sigma(\epsilon)(\epsilon - \mu), \quad (6.2)$$

where μ the chemical potential, $f(T, \mu, \epsilon)$ the Fermi-Dirac distribution function, and $\Sigma(\epsilon)$ the transport distribution function. The latter is defined as

$$\Sigma(\epsilon) = \frac{1}{\Omega_{cell} N_{\mathbf{k}}} \sum_{n\mathbf{k}} \tau_{n\mathbf{k}}^e |\mathbf{v}_{n\mathbf{k}}|^2 \delta(\epsilon - \epsilon_{n\mathbf{k}}), \quad (6.3)$$

where Ω_{cell} is the unit cell volume, $N_{\mathbf{k}}$ the number of \mathbf{k} points in the sum, and $\epsilon_{n\mathbf{k}}$, $\mathbf{v}_{n\mathbf{k}}$ and $\tau_{n\mathbf{k}}^e$ are, respectively, the energy, Fermi velocity and relaxation time of the electronic state with band index n and crystal momentum \mathbf{k} . Our goal here is to compare the power factors $P_F(T, \mu) = \sigma(T, \mu)S^2(T, \mu)$ of SnSe and SnS coming from their different band structure without explicitly calculating the electronic relaxation times. We thus assume that $\tau_{n\mathbf{k}}^e = \tau^e$ is just the same constant for both compounds.

Under these conditions it is easy to see from Eqs. (6.1)-(6.3) that the power factor is proportional to τ^e . In the following we will limit ourselves to the analysis of $P_F(T, \mu)/\tau^e$, which only depends on the band structure of the compounds.

Fig. 6.1 (a) shows the electronic band structures of SnS and SnSe in the high symmetry phase. It shows that the electronic properties of these materials are very

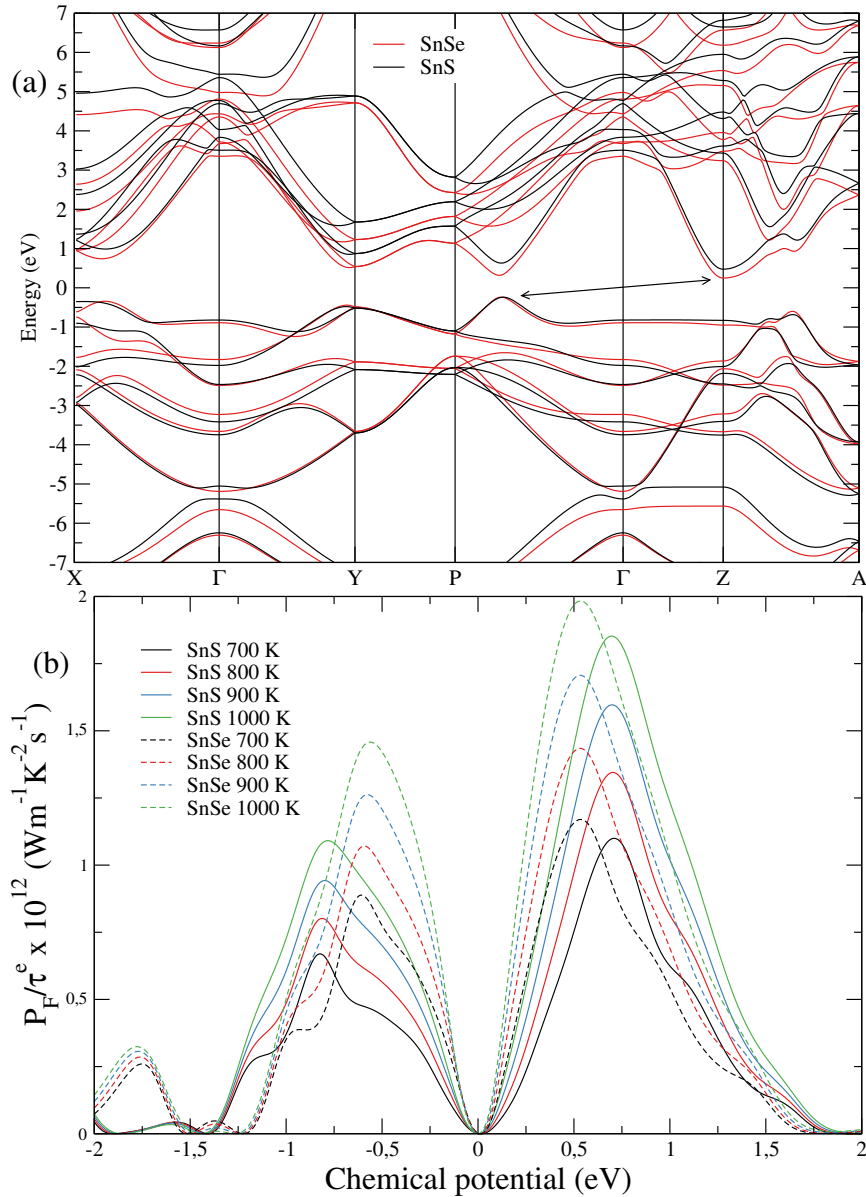


FIGURE 6.1: (a) Electronic band structure of *Cmcm* SnS and SnSe using experimental lattice parameters. (b) P_F/τ^e of *Cmcm* SnS and SnSe for different temperatures as a function of the chemical potential. The 0 value corresponds to the middle of the gap in both figures.

similar because their electronic band structures are basically the same as expected for isoelectronic compounds with the same atomic structure. The major difference is that the indirect (the conduction and valence bands that constitute the gap are denoted with an arrow in Fig. 6.1 (a)) energy gap (0.45 eV for SnSe and 0.7 eV for SnS) is

higher in the case of SnS, in agreement with experiments[133, 6] and previous calculations[129]. As expected, the calculated electronic gaps within LDA underestimate the experimental values (0.86 – 0.948 eV for SnSe[6] and 0.9 – 1.142 eV for SnS[133]).

Using these band structures we have calculated the Seebeck coefficient, which within the approximation of a constant electronic relaxation time it is independent of it, and the electric conductivity over the electronic relaxation time σ/τ^e . The Seebeck coefficient is very similar for both materials, but σ/τ^e is slightly larger in the case of SnSe due to the smaller electronic gap. Using these two quantities we have calculated P_F/τ^e , shown in Fig. 6.1 (b). As we can see, P_F/τ^e is very similar for both materials, but slightly higher in the case of SnSe. This is in qualitative agreement with the calculations in the low temperature phases of SnS and SnSe[129], where the electrical conductivities and Seebeck coefficients of both materials are similar in the low temperature phase. This justifies, in qualitative terms, the same constant relaxation time for both materials in the high temperature phase. As we can see, P_F/τ^e increases with temperature and the difference between the maxima of SnSe and SnS is less than 5% at 1000 K. The application of a scissor operator to match the band gaps with the experimental ones just slightly changes the doping level needed to reach the maximum power factor.

These results make clear that regarding the electronic transport properties these two materials are very similar in the high temperature phase provided that the relaxation time for the electrons is similar for both materials, which is expected for isoelectronic and isostructural compounds.

6.4 Phase transition

As it was already pointed out in the previous chapter, symmetry[122, 123] dictates that it is possible to have a second-order phase transition between the *Cmcm* and *Pnma* phases. The transition is dominated by the distortion pattern associated to a non-degenerate mode (Y_1) at the zone border Y point. The transition temperature is calculated as in chapter 5.

Fig. 6.2 shows $\Omega_{Y_1}^{(F)2}(T)$ within the LDA and PBE approximations. As in the case of SnSe in chapter 5, the second derivative of the free energy is positive at high temperatures and decreases lowering the temperature. For both approximations, it becomes negative at the critical temperature T_c , which means that the *Cmcm* phase is not any longer a minimum of the free energy and the structure distorts adopting the *Pnma* phase. T_c strongly depends on the approximation of the exchange-correlation functional: it is 600 K for LDA and 465 K for PBE. Our LDA calculation gets closer to the experimental value, around 900 K[111]. We associate the discrepancy between LDA and PBE to the different pressures obtained in the transition direction, P_{zz} . In fact, as shown in the case of SnSe in chapter 5, T_c depends strongly on the pressure in this z direction. The pressure in Fig. 3.7 includes anharmonic vibrational effects on the energy following the procedure outlined in section 3.7.1. For the same lattice parameter LDA displays a much smaller pressure, as generally LDA predicts smaller lattice volumes than PBE. The underestimation with respect to experiments may be attributed to the small supercell size used for the SSCHA calculations ($2 \times 2 \times 2$). Even if experimentally T_c is around 100 K higher in SnS than in SnSe, our LDA calculations give basically the same transition temperature for both materials, as

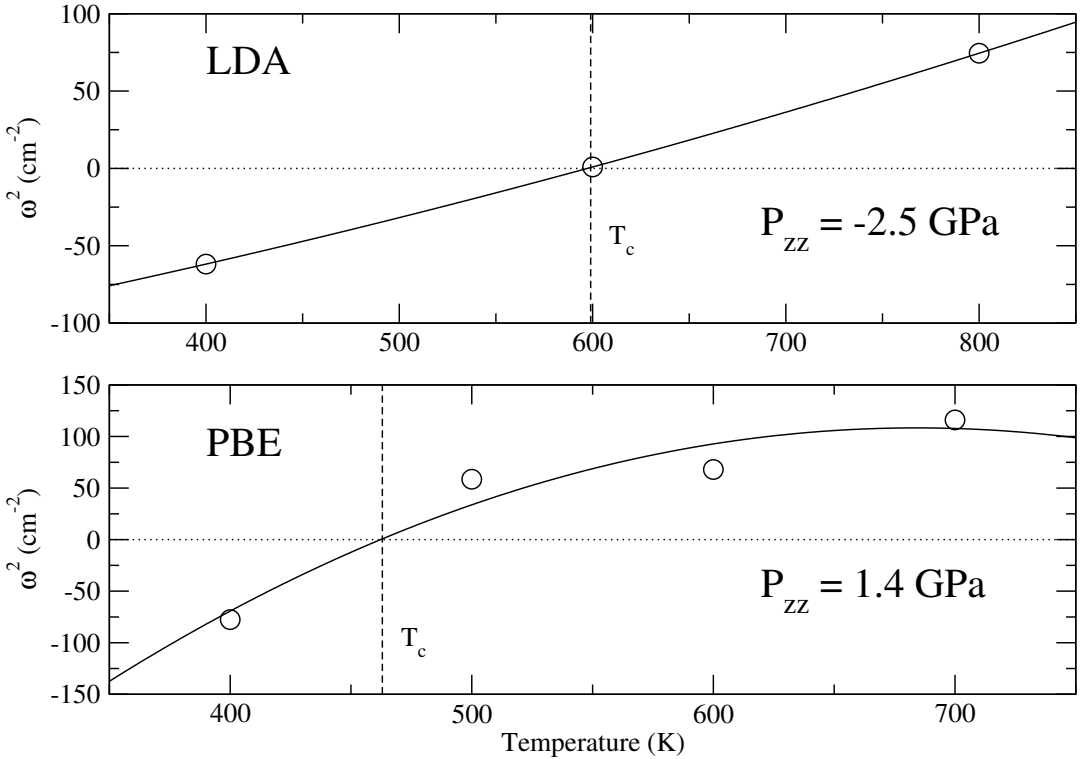


FIGURE 6.2: $\Omega_{Y_1}^{(F)2}$ as a function of temperature within LDA and PBE approximations using the experimental lattice parameters (circles). The solid lines correspond to a polynomial fit. We include the pressure component P_{zz} , which is the pressure in the direction where the atoms move in the transition. This pressure is calculated including the anharmonic vibrational energy within the SSCHA.

$T_c = 616$ K in SnSe in the previous chapter. However, within PBE SnSe does show a lower transition temperature ($T_c = 299$ K).

6.5 Phonons in *Cmcm* SnS

Fig. 6.3 (a) compares the harmonic phonon spectrum with the anharmonic one calculated within the Lorentzian approximation at 800 K within the LDA. In the displayed anharmonic spectrum the phonon energies correspond to the $\Omega_\mu(\mathbf{q})$ values of Eq. 3.53. The linewidth (Eq. 3.54) obtained in the Lorentzian approximation is also shown. The phonon spectrum suffers from a huge anharmonic renormalization. The harmonic spectrum shows broad instabilities, which are stabilized by anharmonicity. The volume increase in the experimental cell is responsible for the appearance of additional instabilities that are stabilized by anharmonic effects. The Y_1 mode is unstable below the transition temperature, but it is stabilized after the transition. By having a look at the phonon linewidths, we can see that two modes at the Γ point (Γ_1 and Γ_2) not only suffer a strong anharmonic renormalization, but they also have a large linewidth compared to the rest of the modes in the first Brillouin zone. These modes describe optical in-plane atomic displacements (see Fig. 5.3, Γ_2 has the same atomic displacements as Γ_1 but in the other in-plane direction), which are the same atomic displacements of Y_2 and Y_3 at the point Y with a different periodicity due to the different momentum. The Y_2 and Y_3 in-plane modes also show a very large

linewidth. On the contrary, the linewidth of mode Y_1 is not so large even if it is responsible for the phase transition (see Fig. 5.3).

In Figs. 6.3 (b) and (c) we show the spectral function keeping the full frequency dependence on the self-energy. The calculation is done for the Γ and Y points. The great majority of the modes describe a Lorentzian shape. However, the modes with a large linewidth within the Lorentzian approximation (see Fig. 6.3 (a)) are those that clearly deviate from the Lorentzian profile ($\Gamma_1, \Gamma_2, Y_2, Y_3$). This non-Lorentzian shape makes clear that these modes are strongly anharmonic and the frequency dependence of the self-energy is crucial to account for their spectral function. In this case, as we can see in Figs. 6.3 (b) and (c), the non-Lorentzian shapes of the strongly anharmonic modes do not create appreciable shoulders or satellite peaks in the total spectral function, however, their contribution is far from trivial.

6.6 Lattice thermal conductivity of $Cmcm$ SnS

In Fig. 6.4 (a) we show the lattice thermal conductivity of $Cmcm$ SnS as a function of temperature calculated using $\overset{(3)}{\Phi}$ and $\overset{(3)}{\phi}$ for solving the BTE within the SMA (see chapter 4). In Fig. 6.4 (b) we show the lattice thermal conductivities of $Cmcm$ SnS and SnSe using $\overset{(3)}{\Phi}$. We can see that the nonperturbative calculation using $\overset{(3)}{\Phi}$ is lower than the perturbative one using $\overset{(3)}{\phi}$ for the three Cartesian directions. This result makes clear that the nonperturbative anharmonicity is very important to calculate the thermal conductivity in this kind of thermoelectric materials. By looking at the values of the lattice thermal conductivity we can see that both materials show very similar ultralow values, below $\approx 1.0 \text{ W m}^{-1} \text{ K}^{-1}$. In-plane results are slightly higher for SnSe and out-of-plane calculations higher for SnS. In-plane results are against physical intuition as materials with heavier elements are supposed to have lower thermal conductivity. However, the same counterintuitive effect has been calculated for the low-temperature $Pnma$ phase as well [134, 129]. Experimentally the situation for the $Pnma$ phase is not so clear. Recent experiments do not agree in the value of the thermal conductivity[14, 130], even if there is a work[135] where it is shown that the thermal conductivity of SnSe is higher than the one of SnS. In our calculations both materials show a clear anisotropy between in-plane and out-of-plane calculations in agreement with experimental results[115] for the low-temperature phase close to the phase transition. Our calculations show that SnS and SnSe have very similar thermal conductivities in the three Cartesian directions

6.7 Conclusions

In conclusion, we have calculated the electronic and vibrational transport properties of $Cmcm$ SnS using first-principles calculations. We have seen that the electronic transport properties of SnS and SnSe are comparable and that a similar power factor is expected for these isoelectronic and isostructural compounds. As in the case of SnSe, SnS suffers a second-order phase transition from the $Cmcm$ to the $Pnma$ phase driven by the collapse of a zone border phonon. We have also seen that SnS shows a strongly anharmonic phonon spectrum. Many phonon modes have a very large linewidth and show non-Lorentzian profiles in the spectral function. Finally, we have calculated the lattice thermal conductivity of $Cmcm$ SnS and we have

seen that nonperturbative anharmonicity substantially corrects the third order force-constants. The thermal conductivity of both materials is very similar and ultralow. Therefore, by comparing the electronic and vibrational transport properties of SnS and SnSe in the *Cmcm* high-temperature phase, we conclude both should be good thermoelectrics. Thus, we suggest that SnS may be an earth-abundant very efficient high-temperature thermoelectric material. As shown in the last section of chapter 5, the maximum *ZT* of *Cmcm* SnSe is around 1. Actually, this *ZT* is very similar to the *ZT* measured for SnS by Wenke et al[14] for the low temperature *Pnma* phase. These results reinforce our conclusions, as they show that SnSe and SnS show very similar thermoelectric properties, given by very similar electronic, vibrational, and thermal properties.

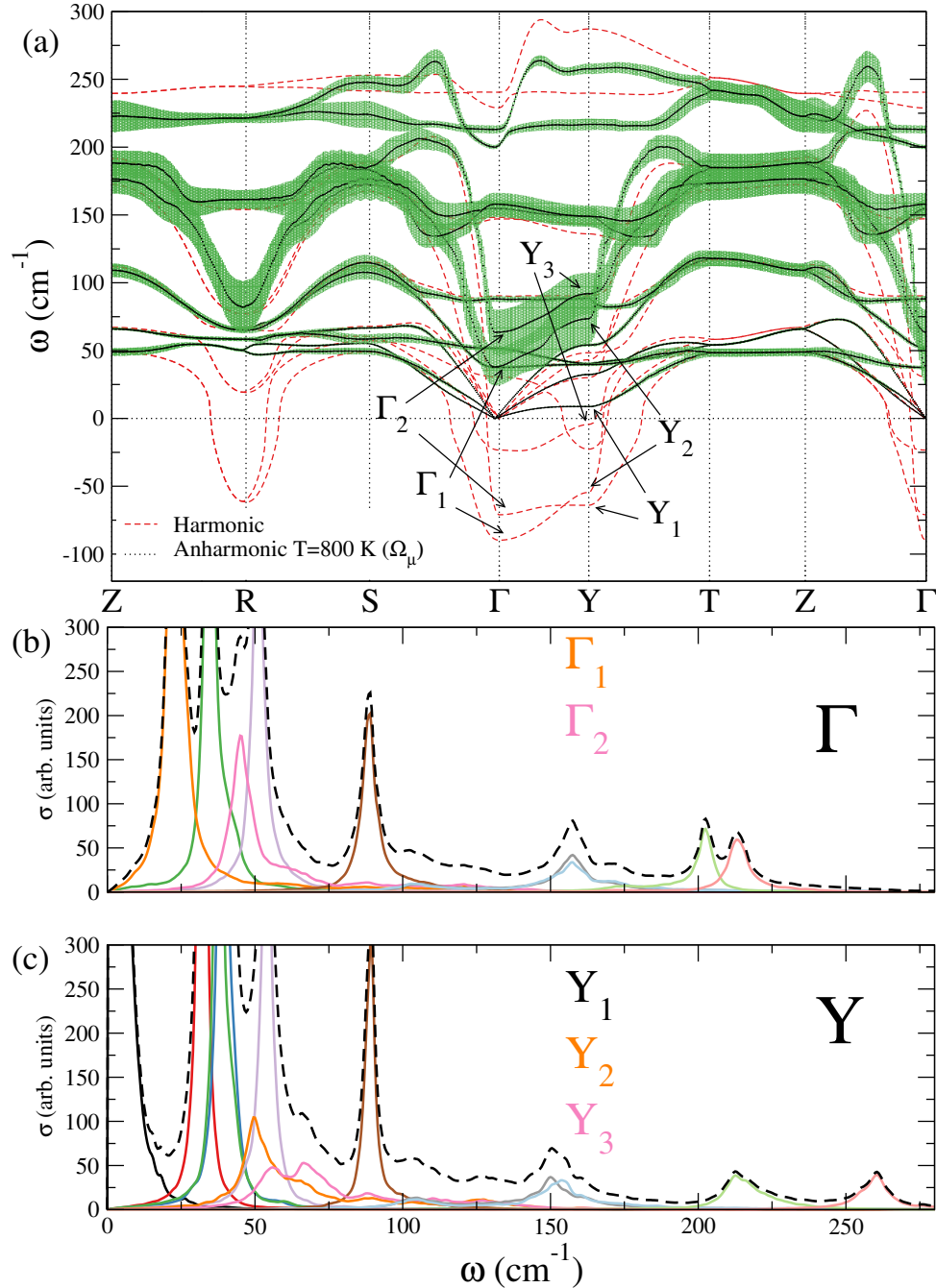


FIGURE 6.3: (a) Harmonic and anharmonic [$\Omega_\mu(\mathbf{q})$] phonon spectra within the Lorentzian approximation. The length of the bars corresponds to the linewidth (full length of the line is the half width at half maximum). The calculations are done within the LDA using SSCHA 3BFCs at 800 K and $\Omega_\mu^{(S)}(\mathbf{q})$ at 800 K. (b) and (c) $\tilde{\sigma}(\omega)$ spectral functions at the points Γ and Y , respectively. Solid lines correspond to individual modes and dashed lines are the total spectral functions.

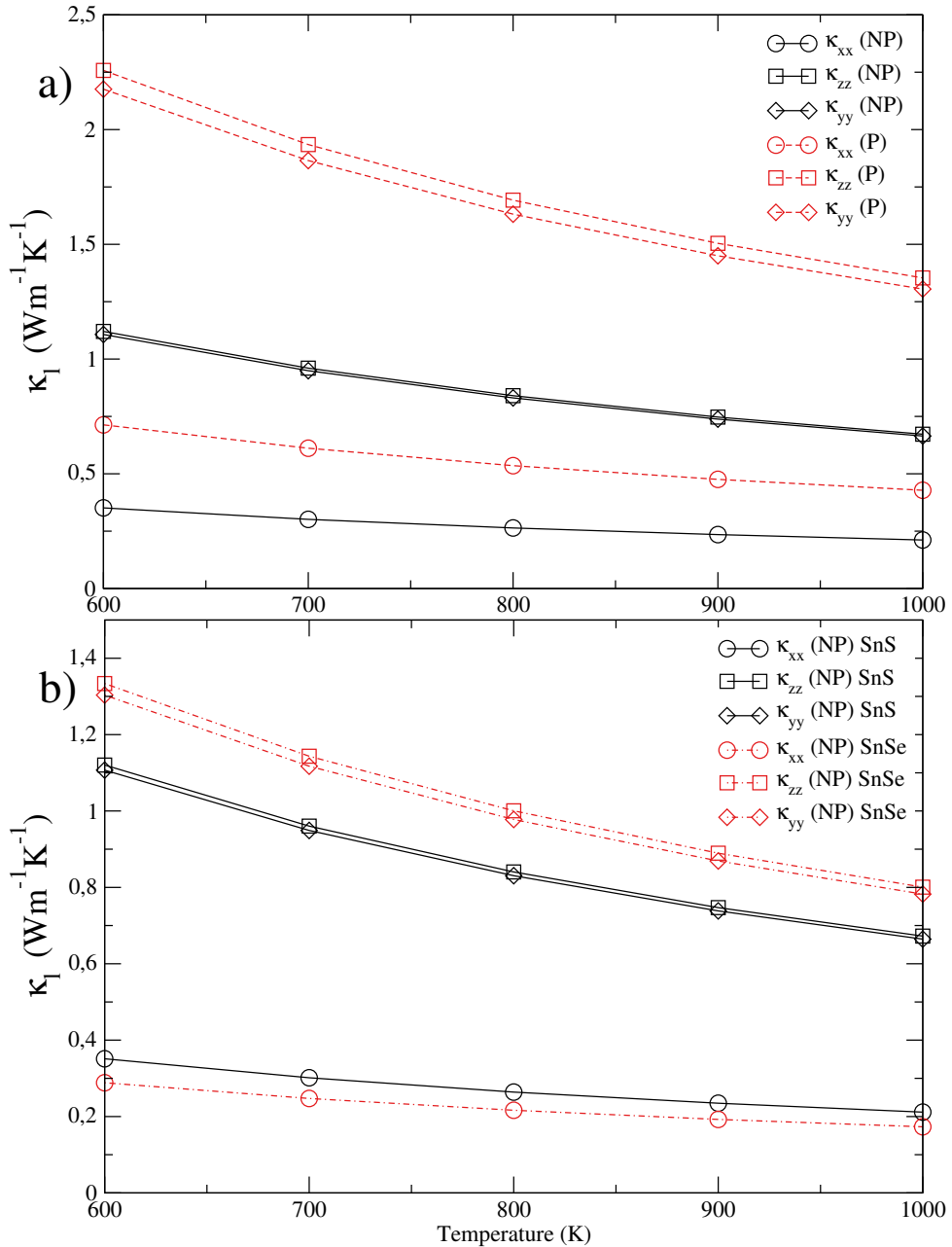


FIGURE 6.4: (a) Lattice thermal conductivity of *Cmcm* SnS calculated within nonperturbative (NP) and perturbative (P) approaches. We have used $\Omega_\mu^{(S)}(\mathbf{q})$ at 800 K for both and SSCHA 3BFCs at 800 K for the calculation in both cases. Calculations are within the LDA. (b) Lattice thermal conductivity of *Cmcm* SnS and SnSe calculated within the nonperturbative (NP) approach.

Chapter 7

Monolayer SnSe

7.1 Introduction

Thin film ferroelectrics are key for modern device applications[28]. However, it is known that there is a critical thickness for thin ferroelectrics, below which the depolarization field destroys the ferroelectric state[29, 30, 31]. This effect decreases the transition temperature to the ferroelectric state as a function of the sample thickness[32, 33] and sets a fundamental limit for technological applications.

Layered Van der Waals materials have been proposed to be good candidates to overcome this limitation[136, 137]. Bulk monochalcogenides studied in chapters 5 and 6 are inside the family of Van der Waals materials, which in principle, could be exfoliated to get monolayer materials. Actually, it has been experimentally shown that it is possible to synthesize monolayer SnSe[138, 139]. On top of this, it has been shown in monolayer SnTe, another monochalcogenide material, that monolayer materials can show a robust ferroelectric state with a higher transition temperature than its bulk counterpart[26]. These properties make very interesting the theoretical study of the ferroelectric transition in SnSe. Actually, in a very recent experimental work[34], they show how the polarization of monolayer SnSe can be switched at room temperature.

Thermoelectric properties of bulk SnSe have been explained in chapter 5. As can be seen in Fig. 7.1, monolayer SnSe has the same structure of the bulk, but the unit cell only contains one bilayer with four atoms (the bulk has two bilayers with 8 atoms, see Fig. 5.1). The electronic band gap is bigger in the monolayer[140, 141], due to quantum confinement effects. According to several theoretical studies[140, 141] in the monolayer low symmetry phase, the lattice thermal conductivity is of the same order of magnitude compared to the bulk counterpart. These theoretical works show that, monolayer SnSe in the *Pnm2₁* (low symmetry) structure could have a higher thermoelectric figure of merit[140, 141] than bulk *Pnma* (low symmetry). This makes very interesting the study of thermoelectric properties of monolayer SnSe in the *Pnmm* (high symmetry) structure as in the bulk the high symmetry *Cmcm* phase is a better thermoelectric material at high temperatures than the *Pnma*.

Experimentally, there are no measurements for the ferroelectric phase transition temperature of monolayer SnSe. However, it seems to crystallize in the *Pnm2₁* structure at room temperature[138, 34], therefore, the ferroelectric transition temperature must be higher. According to theoretical studies applying molecular dynamics simulations[142, 143] the transition temperature is around 200 K. Another work applying DFT and an effective Hamiltonian claims[137] that the transition occurs at around 320 K. Regarding the thermoelectric properties in monolayer SnSe in the

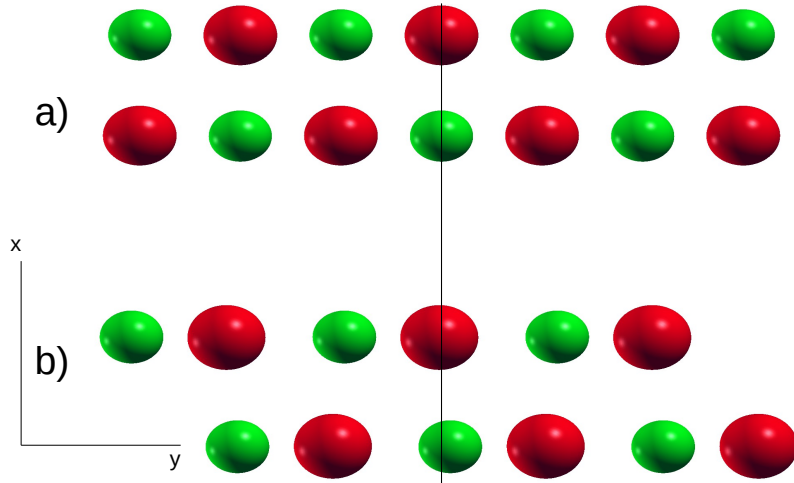


FIGURE 7.1: Monolayer SnSe crystal structure in the (a) $Pnmm$ (high symmetry) and (b) $Pnm2_1$ (low symmetry) phases.

$Pnmm$ structure, there are no theoretical calculations of the lattice thermal conductivity, as it has an imaginary phonon frequency at the Γ point within the harmonic approximation (see Fig. 7.3), which hinders the calculation of κ_l .

In this chapter we study the vibrational properties of $Pnmm$ monolayer SnSe and the associated transition to the ferroelectric state. According to our calculations monolayer SnSe suffers a second-order phase transition to the ferroelectric $Pnm2_1$ phase at around 107 K. We also try to calculate the lattice thermal conductivity of $Pnm2_1$ monolayer SnSe in order to compare it with the bulk, however, we will see that it is not possible due to a problem generated by the two dimensional character of the system. This last result will be an extra motivation for the last chapter of this thesis.

7.2 Crystal structure and high symmetry points

The $Pnmm$ and $Pnm2_1$ phases are rectangular and their two dimensional structure is shown in Fig. 7.1. The primitive cell of both structures contains 4 atoms in the primitive cell. The primitive lattice vectors of both structures are: $\mathbf{a}_1 = (a, 0)$ and $\mathbf{a}_2 = (0, b)$, where a and b are the lattice constants.

The reciprocal lattice vectors of the $Cmcm$ primitive 1BZ are $\mathbf{b}_1 = 2\pi(1/a, 0)$ and $\mathbf{b}_2 = 2\pi(0, 1/b)$. The high symmetry points and their coordinates used in phonon dispersion figures are listed in table 7.1. The theoretical lattice parameters within LDA are $a = b = 7.94 a_0$ and within PBE $a = b = 8.17 a_0$.

7.3 Calculation details

Our calculations are based on DFT using the QUANTUM-ESPRESSO[16] software package. Harmonic phonons were calculated within DFPT. Anharmonic phonons were calculated within the SSCHA. For the exchange-correlation interaction we use the Perdew-Burke-Ernzerhof (PBE) generalized gradient approximation and the local density approximation (LDA) with ultrasoft (US) and Projector Augmented Wave

Symmetry point	Reduced \mathbf{q} vector
X	0.5, 0.0
Y	0.0, 0.5
R	0.5, 0.5
Γ	0.0, 0.0

TABLE 7.1: Reduced \mathbf{q} vectors of the high symmetry points in the Brillouin zone of the $Pnmm$ and $Pnm2_1$ phases.

method (PAW) pseudopotentials, respectively. We use a cutoff energy of 70 Ry and a grid of $16 \times 16 k$ points to sample the first Brillouin zone. For the harmonic phonon calculations we use a 6×6 supercell for both harmonic and SSCHA calculations.

7.4 Ferroelectric phase transition

As in the bulk structures described in chapters 5 and 6, symmetry[122, 123] dictates that it is possible to have a second-order phase transition between the $Pnmm$ and $Pnm2_1$ phases. In this case, The transition is dominated by the distortion pattern associated to a mode (Γ_1) at the zone center. The distortion of this mode is shown in Fig. 7.2 and it corresponds to the imaginary phonon in Fig. 7.3.

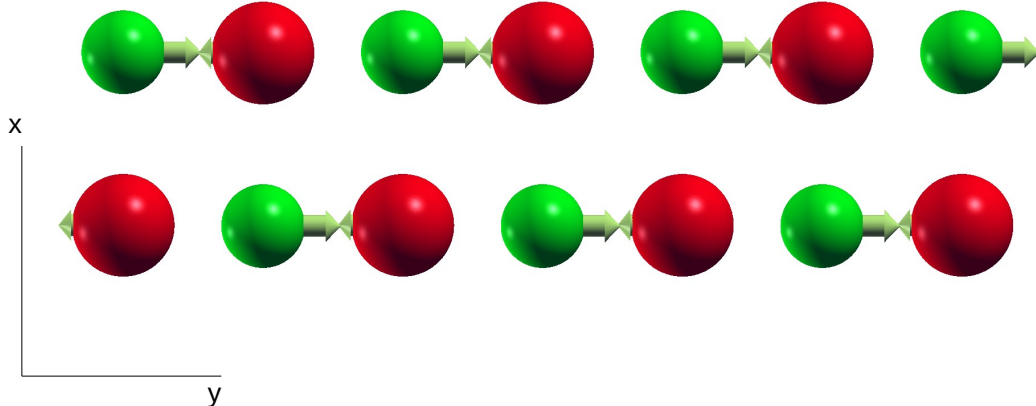


FIGURE 7.2: Distortion pattern associated to the Γ_1 mode.

The phonon mode that transforms bulk SnSe from the $Cmcm$ to $Pnma$ structure is different. The distortion is associated to a mode at the zone border. In the monolayer the second bilayer does not exist, that is why the mode is at the zone center. This fact makes that bulk $Pnma$ is centrosymmetric but not the monolayer $Pnm2_1$, which has no inversion symmetry and it is a ferroelectric phase.

In a second-order displacive phase transition scenario, the transition temperature T_c is defined as $\partial^2 F / \partial Q^2(T = T_c) = 0$ where Q is the order parameter that

transforms the system continuously from the $Pnm2_1$ ($Q \neq 0$, low symmetry) to the $Pnmm$ ($Q = 0$, high symmetry) phase. As the distortion is dominated by the Γ_1 phonon, $\partial^2 F / \partial Q^2(T)$ is proportional to $\Omega_{\Gamma_1}^{(F)2}(T)$, which can be calculated using Eq. 3.76.

In the bulk, in both LDA and PBE approximations the Γ_1 is unstable within the harmonic approximation, which is the typical scenario for a second-order phase transition. In Fig. 7.3 we show the harmonic phonon spectrum of monolayer SnSe in the $Pnmm$ structure within the LDA and PBE approximations. As we can see,

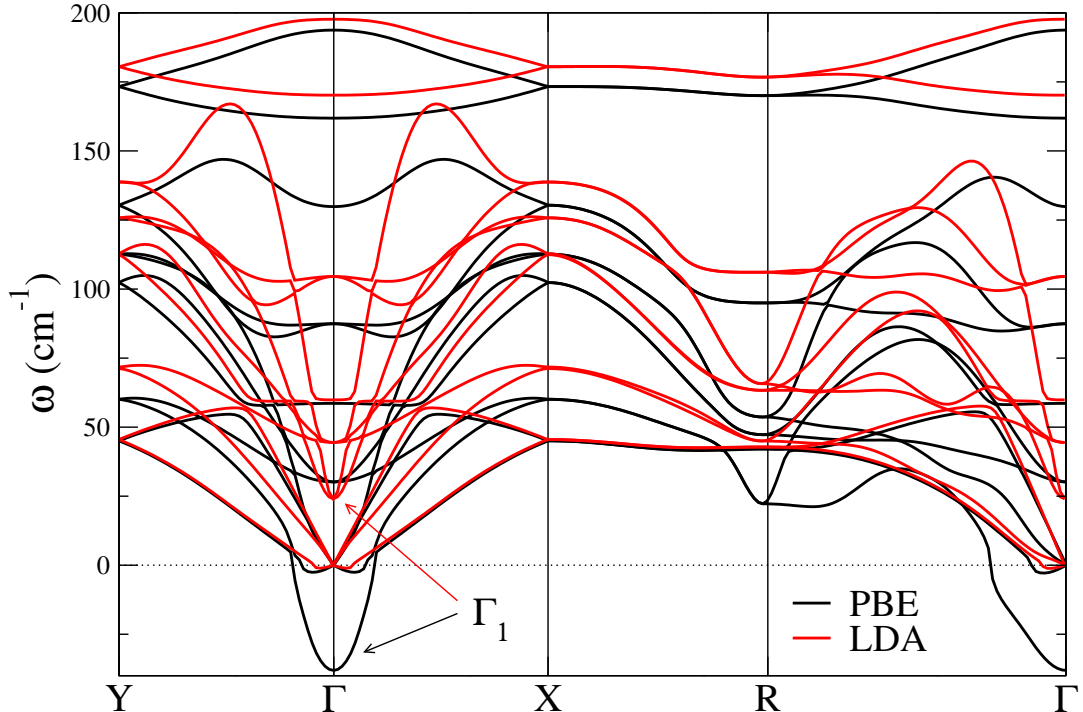


FIGURE 7.3: Harmonic phonons of monolayer SnSe in the $Pnmm$ phase within the LDA and PBE approximations in the theoretical structure.

the instability Γ_1 appears within PBE but not within LDA. This result again shows the huge volume dependence of the vibrational properties of SnSe, which was also discussed in chapter 5. According to this result, the second-order phase transition scenario only appears within the PBE in the case of the monolayer. From now on we will only show results within the PBE.

Fig. 7.4 shows $\Omega_{\Gamma_1}^{(F)2}(T)$ within the PBE approximation. As in the cases of bulk SnSe and SnS, the second derivative of the free energy is positive at high temperatures and decreases lowering the temperature. It becomes negative at the critical temperature $T_c = 107$ K in the 6×6 supercell, which means that the $Pnmm$ phase is not any longer a minimum of the free energy and the structure distorts adopting the $Pnm2_1$ phase. The transition temperature is around 50 K in the 4×4 supercell and the transition does not occur in the 2×2 supercell. This supercell dependence suggest that the calculation may not be fully converged. It could also explain why we do not get a better agreement for the transition temperature in the bulk case.

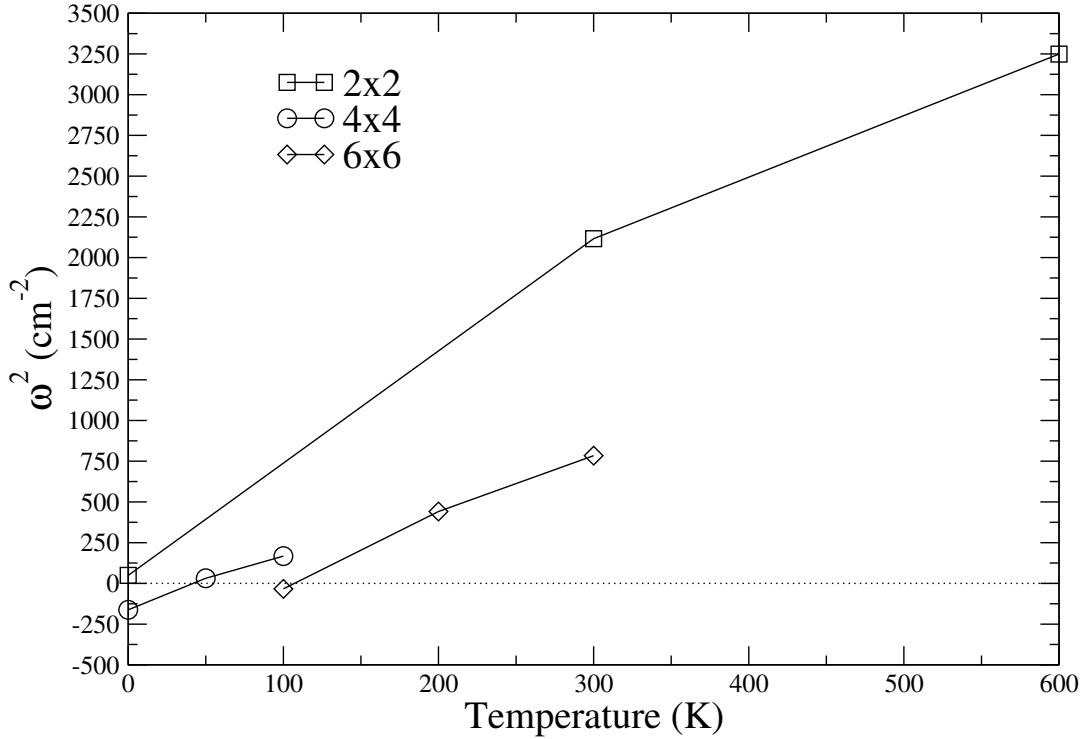


FIGURE 7.4: $\Omega_{\Gamma_1}^{(F)2}$ as a function of temperature within PBE using the theoretical lattice parameters. We show the calculation for the 2×2 , 4×4 , and 6×6 supercells.

Our results are consistent with other theoretical works[142, 143, 137], where the same ferroelectric transition is predicted. From a quantitative point of view, our transition temperature of 107 K is lower than the $\simeq 180 - 200$ K value obtained in molecular dynamics simulations[142, 143]. As already mentioned, the discrepancy probably arises due to the different exchange-correlation or the smaller supercell we have used to calculate the transition temperature.

7.5 Problem for calculating lattice thermal conductivity

As shown in chapters 3, 5, and 6, the SSCHA phonons ($\Omega_{\mu}^{(S)}$) are a properly defined basis for the three phonon scattering phase space and provide an accurate lattice thermal conductivity. In Fig. 7.5 we show the SSCHA phonons of monolayer SnSe in the *Pnmm* structure at 300 K, which is a temperature where the high symmetry phase is stable (see Fig. 7.4). As we can see, there is a small instability in the lowest energy acoustic branch very close to the point Γ . This small instability could be an artifact of the Fourier interpolation, which is needed to get information about the acoustic branches at very small momenta. It could also be that the lattice parameter is too small once the fluctuations of the ions are taken into account. In principle, if we would be able to do a calculation in an infinitely big supercell and relax the lattice parameters including the ionic fluctuations, the problem would disappear, but obviously, this is not possible. However, we could ask ourselves why this problem appears in the monolayer and not in the bulk. Actually, there is a very fundamental reason for this. As it is shown in appendix C, the lowest energy acoustic branch in monolayer materials has a quadratic dispersion as a function of momentum within

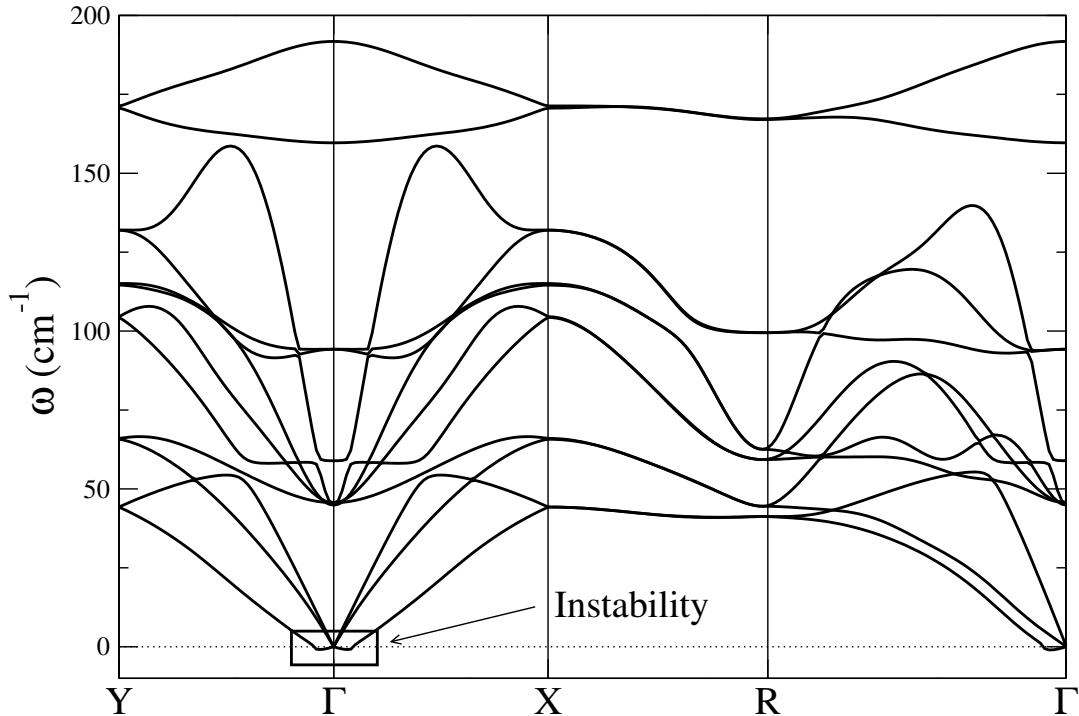


FIGURE 7.5: $\Omega_{\mu}^{(S)}(\mathbf{q})$ phonon spectrum at 300 K within PBE using the theoretical lattice parameters.

the harmonic approximation, which makes it to have very low frequencies compared to the other two linear acoustic branches. The linear dispersion is not kept in the SS-CHA phonon dispersion, however, still the frequency of the lowest energy acoustic mode is substantially lower. Because of this reason we are not able to calculate the lattice thermal conductivity of monolayer SnSe, as we need the phonon frequencies at small momenta in order to calculate the phonon linewidths. In chapter 8 we include a deep analysis about the anharmonic effects on the lowest energy acoustic branch of monolayer materials.

7.6 Conclusions

In conclusion, we have shown that a ferroelectric transition is possible from the high symmetry (centrosymmetric) $Pnmm$ phase to the low symmetry (no centrosymmetric) $Pnm2_1$ phase. We have seen that this phase transition is different to the one that appears in the bulk, in which the two phases are centrosymmetric. We have seen that this phase transition actually happens at around 107 K, which is in qualitative agreement with previous theoretical calculations. Quantitative disagreement may be due to exchange correlation or supercell effects, which are very big in this kind of materials. Finally, we have tried to calculate the lattice thermal conductivity of $Pnmm$ monolayer SnSe but we have found problems related to the 2D character of the material, which makes the lowest energy acoustic branch very soft. We will see in the next chapter what is the effect of anharmonic effects in this mode and its role on the mechanical stability of 2D materials.

Part III

Phonons in 2D materials

Chapter 8

2D materials: Graphene

8.1 Introduction

The discovery of graphene[144, 145, 146, 147] proved the existence of 2D materials and launched their science and technology. Graphene is already a reality in different industrial products[148] that benefit from its fantastic properties. In particular, its mechanical and thermal properties are crucial for many of its current and future applications. For instance, uneven strength, stiffness, and lightness[149] of graphene have been used to make stronger but lighter macroscopic objects, such as tennis rackets, shoes, and so on. Graphene, due to its very high thermal conductivity[150], has been already incorporated into electronic devices like mobile phones for efficient heat dissipation.

The understanding of the mechanical and thermal properties of graphene, and in general of any 2D material, is, however, far from trivial. Even the possibility of having crystalline order in 2D has been long questioned[36, 37]. Indeed, the root mean square displacement calculated within the harmonic approximation diverges in the long wave-length limit, which means that the larger the sample of a 2D material the bigger the atomic displacements, preventing any crystalline order[36]. In Fig. 8.1 we show the atomic displacements of carbon atoms in graphene as a function of the sample size, or the supercell used for the calculation. As the figure clearly shows, the root mean square atomic displacements diverge at finite temperatures as a function of the sample size. Mermin's theorem[37] proves that, even without assuming the harmonic approximation, long-range crystalline order is not possible in a two-dimensional crystal described by a pair potential. Experimentally, however, crystalline order has been observed in suspended graphene[151], although it shows ripples that seem to be intrinsic[152].

Most of the problems related to the mechanical stability of graphene are caused by the quadratic dispersion of the acoustic out-of-plane (ZA) mode that is obtained in the harmonic approximation. The harmonic phonon spectrum of graphene is shown in Fig. 8.2. The calculation is done following the finite displacement procedure explained in chapter 3 and using a 6×6 supercell. We can see that the LA and TA modes have a linear dispersion close to the point Γ as it happens in 3D crystals. However, the ZA mode, with atomic displacements along the out-of-plane direction, has a quadratic dispersion. This is very clear in the logarithmic scale plot, where we have included a quadratic line for reference. The quadratic dispersion is given by the rotational symmetry, together with the fact that in a strictly two-dimensional system force constants involving an in-plane and an out-of-plane displacement vanish[38]. The mathematical proof of the quadratic dispersion is given in appendix C.

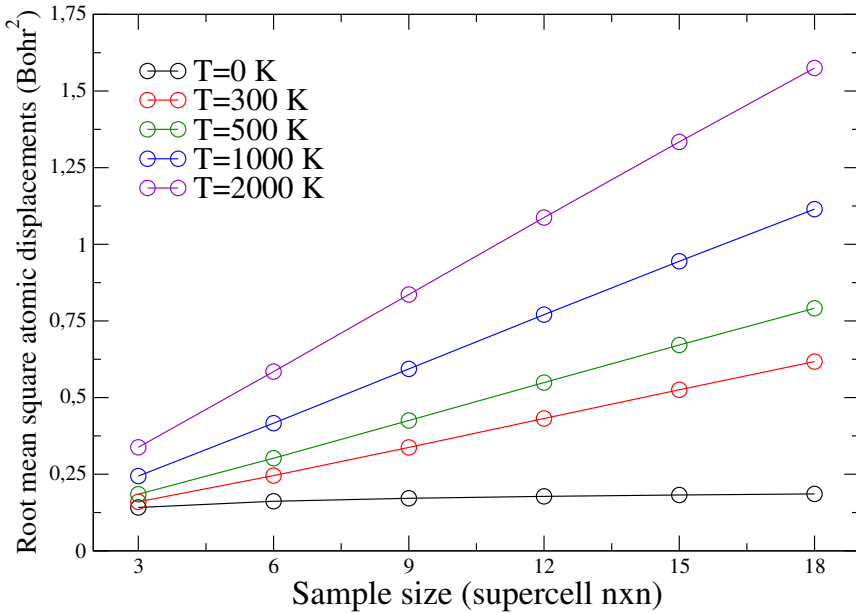


FIGURE 8.1: Root mean square atomic displacements of carbon atoms in graphene calculated using the harmonic dispersion as a function of the supercell size for different temperatures. The calculation is done by using the harmonic formula for $\langle u^2 \rangle$ [40].

The quadratic dispersion also creates spurious divergences in physical properties calculated perturbatively on top of the harmonic result. The phonon linewidths of the in-plane acoustic longitudinal (LA) and transverse (TA) phonons calculated perturbatively do not vanish as the momentum decreases[18], precisely, because of the $\sim q^2$ dispersion of the ZA modes[153]. The linewidths of the LA and TA modes are shown in Fig. 8.3 (a). The calculation is done applying the perturbative procedure explained in chapter 3 in the potential in Eq. 8.1. The figure clearly shows how the linewidths do not vanish at small momenta. This yields to the conclusion that for small enough momentum phonons do not live long enough for vibrating one period and the quasiparticle picture is lost. Consequently, the thermal conductivity calculated with the perturbative phonon lifetimes[91, 98] does not converge with the sample size[153]. In Fig. 8.3 (b) we can see the FWHM divided by the phonon frequency. When this number is around 1 the phonon picture is lost because the phonons do not live long enough for vibrating one period. Therefore, the longitudinal and transversal acoustic phonons with a frequency smaller than $\simeq 1 \text{ cm}^{-1}$ do not propagate in graphene. The mentioned region is shadowed in the figure. This means that sound does not propagate in graphene because the highest frequency that the human ear can hear is around 10^{-4} cm^{-1} . The application of strain linearizes the dispersion of the ZA phonons and makes the linewidth of the LA and TA phonon modes vanish together with their frequency at small momenta, keeping the phonon picture[153].

It has been argued[154, 155, 38, 156, 157, 158, 159] that the anharmonic coupling between in-plane and out-of-plane phonon modes renormalizes the dispersion of the ZA phonon modes, providing it with a linear term at small momenta that somewhat cures the pathologies. This conclusion has been drawn by Monte Carlo simulations with empirical potentials[154, 155, 38, 156] and by using a membrane continuum Hamiltonian that mimics the interaction among acoustic modes[157, 158],

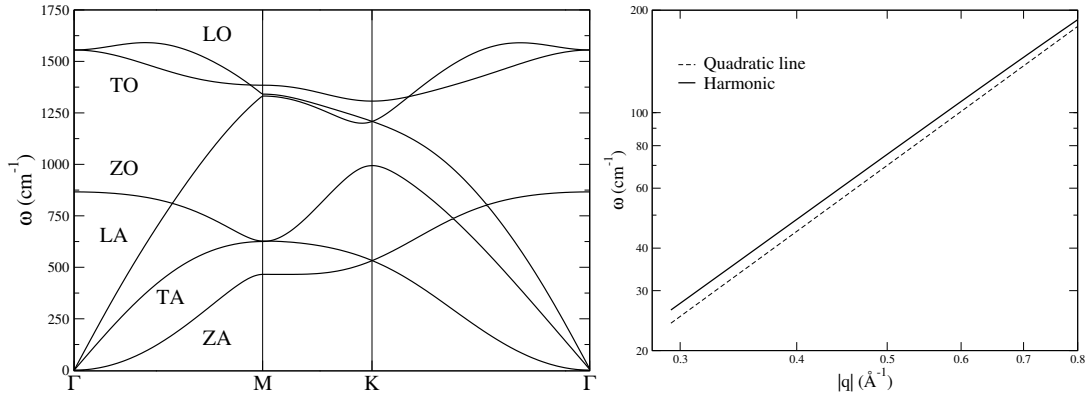


FIGURE 8.2: Left: Harmonic phonon spectrum of graphene. Right: Harmonic ZA phonon dispersion of graphene in logarithmic scale. We include a quadratic line for reference.

[159]. Anharmonic phonons expected experimentally should be calculated from the phonon spectral function. For low energy modes, as it happens for the ZA mode, the phonon peaks of the spectral function coincide with the phonons defined from the free energy Hessian, i.e., diagonalizing the $[\frac{\partial F}{\partial \mathcal{R}_a \partial \mathcal{R}_b}]_0 / \sqrt{m_a m_b}$ matrix, where F is the free energy calculated including anharmonic effects and \mathcal{R} the centroid positions that determine the most probable ionic positions[24]. As shown in section 3.7.3, the phonons given by the free energy Hessian are equivalent to the phonons calculated from the spectral function in the static limit. We will name the phonons defined from the phonon spectral function $\Omega_\mu(q)$ "Physical" phonons and the phonons defined from the free energy Hessian "Physical static" phonons. If phonons are calculated from the free energy Hessian, as F obeys the same symmetry properties as U , a similar $\sim q^2$ dispersion would be expected for the ZA mode even if anharmonic effects are included in the calculation of F . Actually, measurements done with helium diffraction show a ZA mode with a quadratic dispersion[160, 161, 162], though the linearization regime may not be seen and substrate effects may be important. The remaining question is thus, whether the ZA modes really have a quadratic dispersion, and, if it is so, how the mechanical stability, thermal properties, and sound propagation in graphene can be explained.

In this chapter we show that a quadratic dispersion of the ZA mode is actually expected for graphene provided that it is calculated from the phonon spectral function, and that it is compatible with sound propagation. We estimate F within the self-consistent harmonic approximation (SCHA). We apply the SCHA in its stochastic implementation (SSCHA) making use of a machine learning atomistic potential trained with density functional theory[163]. We also solve the SCHA equations in a membrane continuum Hamiltonian which provides results at smaller momenta.

8.2 Crystal structure

The direct lattice of graphene has a hexagonal structure with two atoms per unit cell. The two vectors of the direct lattice in Cartesian coordinates are the following:

- $\mathbf{a}_1 = a(1, 0)$,
- $\mathbf{a}_2 = a\left(-\frac{1}{2}, \frac{\sqrt{3}}{2}\right)$,

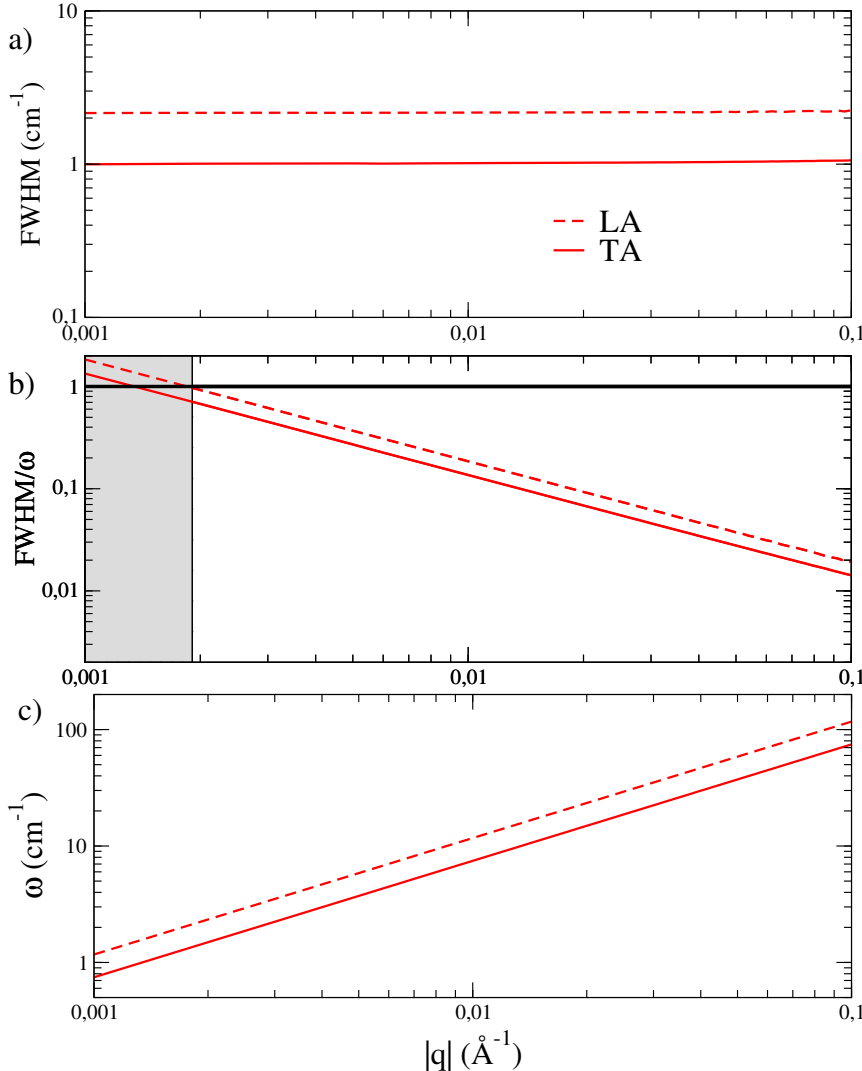


FIGURE 8.3: (a) Linewidths (full width at half maximum, FWHM) of the LA and TA modes calculated using perturbation theory at 300 K. (b) FWHM divided by the phonon frequency. We shadow the region where $FWHM/\omega > 1$. All the calculations are done in the membrane model in Eq. 8.1. (c) LA and TA harmonic frequencies within the membrane model.

where one atom is at the origin and the other in $a(0, 1/\sqrt{3})$. Then, the reciprocal lattice is:

- $\mathbf{b}_1 = \frac{2\pi}{a} \left(1, \frac{1}{\sqrt{3}}\right)$,

- $\mathbf{b}_2 = \frac{2\pi}{a} \left(0, \frac{2}{\sqrt{3}}\right)$.

The reciprocal lattice of graphene is equivalent to the direct one but rotated by 60 degrees. The high symmetry points in the first Brillouin zone of graphene are $K = \frac{2\pi}{a} \left(\frac{1}{3}, \frac{1}{\sqrt{3}}\right)$ and $M = \frac{2\pi}{a} \left(0, \frac{1}{\sqrt{3}}\right)$.

8.3 Empirical potential benchmark and calculation parameters

For calculating the forces needed in the SSCHA minimization[23] we have used an empirical potential trained with machine learning and density functional theory (DFT) forces. The details about the machine learning training are explained in Ref. [163]. Here we have benchmarked the ability of the potential to account for the anharmonic effects. For that purpose we have applied the SSCHA method by using DFT and empirical forces in a 2×2 supercell and we have checked the anharmonic lineshifts in the optical modes at the Γ point. The machine learning potential is trained with the exchange-correlation in Ref. [164], which accounts for Van der Waals corrections. For the DFT calculations we have applied a PBE[46] ultrasoft pseudopotential[51] with Van der Walls corrections[165] within the semiempirical Grimme's method. The results are shown in Figs. 8.4 and 8.5. As we can see in Fig.

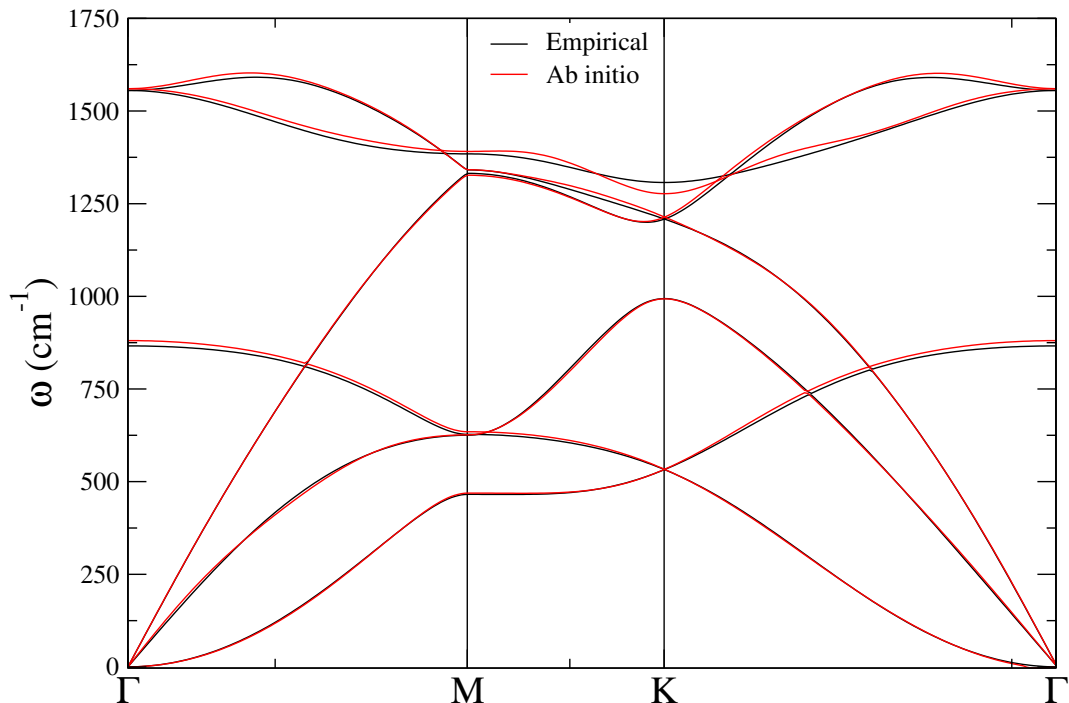


FIGURE 8.4: Harmonic phonon spectrum of graphene calculated with the empirical potential and *ab initio*. The calculations are done in a 6×6 supercell.

8.4, the two potentials provide very similar harmonic phonons, or what is the same, very similar forces. Due to the different exchange correlation functional, there is a slight offset in Fig. 8.5, however, the anharmonic lineshifts in both $D^{(S)}$ and $D^{(F)}$ are very well captured within the empirical potential.

For the self-consistent DFT calculations we have used a plane wave cutoff of 70 Ry and a 700 Ry cutoff for the density. For the Brillouin zone integration we have used a Monkhorst pack grid[48] of 32×32 points with a Gaussian smearing of 0.02 Ry. For the linewidth calculations we have used a 400×400 grid with a Gaussian smearing of 1 cm^{-1} . The interpolation is done from a 10×10 supercell for the 2BFC and from a 3×3 supercell for the 3BFC. For the stress calculation in order to account for the thermal expansion we have used a 10×10 supercell. We have used the same

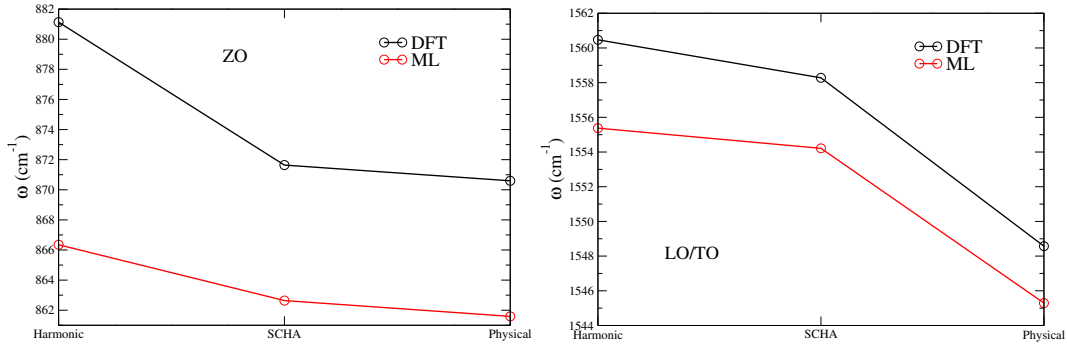


FIGURE 8.5: Harmonic, SSCHA and physical static frequencies using the DFT and machine learning (ML) forces. The left panel shows the in-plane optical frequency at the Γ point and the right panel the out-of-plane one.

supercell for the harmonic, SSCHA and physical frequency calculations. We have tested all the calculations with denser grids and bigger supercells.

8.4 Graphene without stress

In order to calculate phonon spectra in unstrained graphene at any temperature, we calculate the SSCHA stress tensor following the procedure in section 3.7.1 and pick the lattice parameter that sets it to zero at each temperature. For that purpose, we calculate the stress in ranges of 0.0005 \AA and then we interpolate the result, which is fitted very accurately with a linear function. The results are shown in Fig. 8.6. The

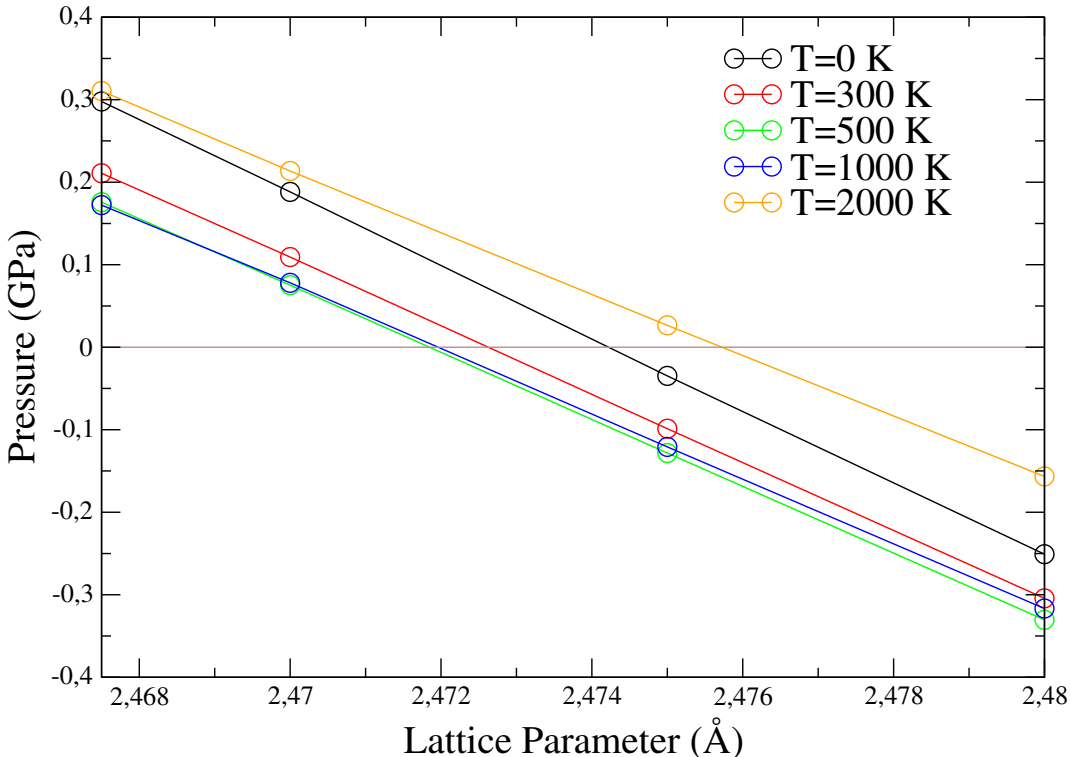


FIGURE 8.6: Pressure as a function of the lattice parameter calculated with the atomistic potential for different temperatures.

lattice parameter calculated in this way includes anharmonic effects as well as the effect of quantum and thermal fluctuations. In order to properly account for thermal expansion, all the phonon spectra shown in this work that are obtained with the atomistic potential are calculated with the lattice parameter that gives a null SSCHA stress at each temperature. The harmonic spectra on the contrary is always calculated at the lattice parameter that minimizes U .

The temperature dependence of the lattice parameter and the thermal expansion coefficient are shown in Fig. 8.7. We include the results of Rowe et al.[163],

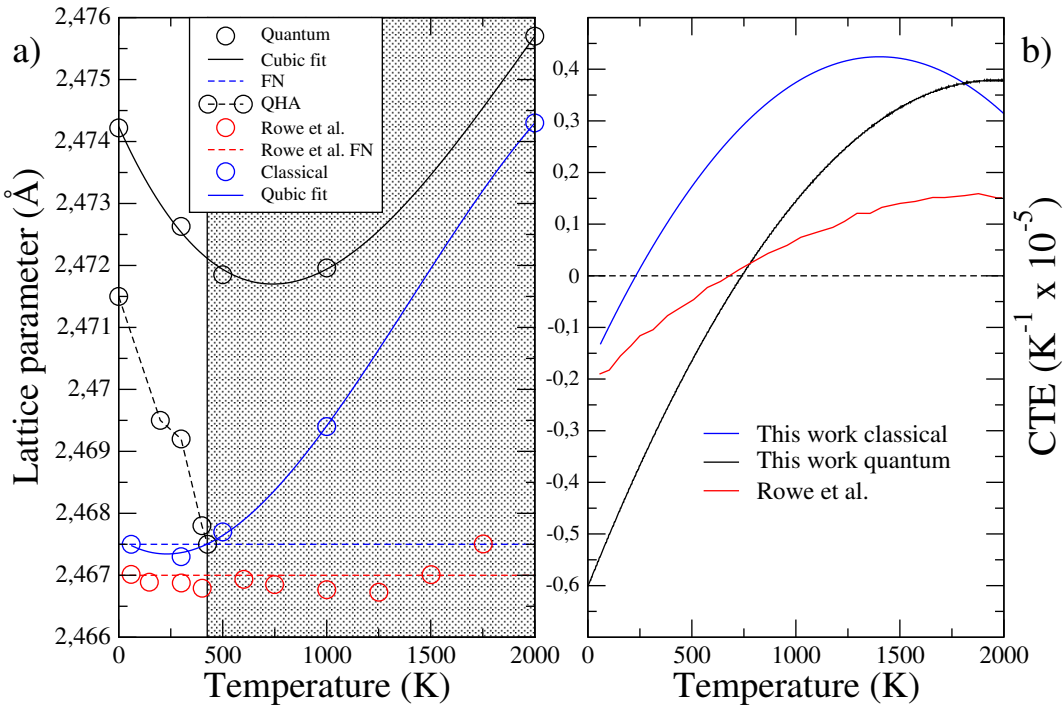


FIGURE 8.7: (a) Lattice parameter of graphene as a function of temperature obtained with the SSCHA using a machine learning atomistic potential. Both quantum (black) and classical (blue) calculations are included. The classical result is calculated setting $\hbar = 0$ in the SSCHA free energy. The temperature-independent frozen nuclei (FN) result corresponds to the lattice parameter that minimizes the Born Oppenheimer potential U . Results obtained by Rowe et al.[163] are also included for comparison. Solid black and blue lines correspond to cubic fits. The black dashed line corresponds to the quasiharmonic result (QHA). (b) Thermal expansion coefficient (CTE) calculated as $\text{CTE} = \frac{1}{A} \frac{\partial A}{\partial T}$, A being the area of the membrane. Red line is directly taken from [163]. Black and blue lines are calculated using the cubic fits in (a).

which do not account for quantum effects as they are done with molecular dynamics (MD). They use the same potential as we do. For comparison we also include SSCHA calculations in the classical limit and within the quasiharmonic approximation[82] (QHA). The classical calculations are done by increasing the mass of the carbon atom by a factor of 10000. This is equivalent to setting $\hbar = 0$. Our quantum calculations correctly capture the negative thermal expansion of graphene up to ~ 750 K that has been estimated in previous theoretical works[163, 156]. Our quantum calculations show a larger lattice parameter and a more pronounced thermal

expansion (in absolute value) at low temperatures. This is not surprising as classical calculations neglect quantum fluctuations and, consequently, underestimate the fluctuations associated to the high-energy optical modes (the highest energy phonon modes require temperatures of around 2000 K to be thermally populated). Actually, the classical result approaches the quantum one at high temperatures. This remarks the importance of considering quantum effects in the evaluation of thermodynamic properties of graphene. Our classical results and the MD calculations of Rowe et al.[163] are in agreement (within their error of 0.0005 Å) at low temperatures. A source of discrepancy could be the inherent noise of the atomistic potential, which is shown in Fig. 8.8. The minimum of this potential provides the classical value at 0

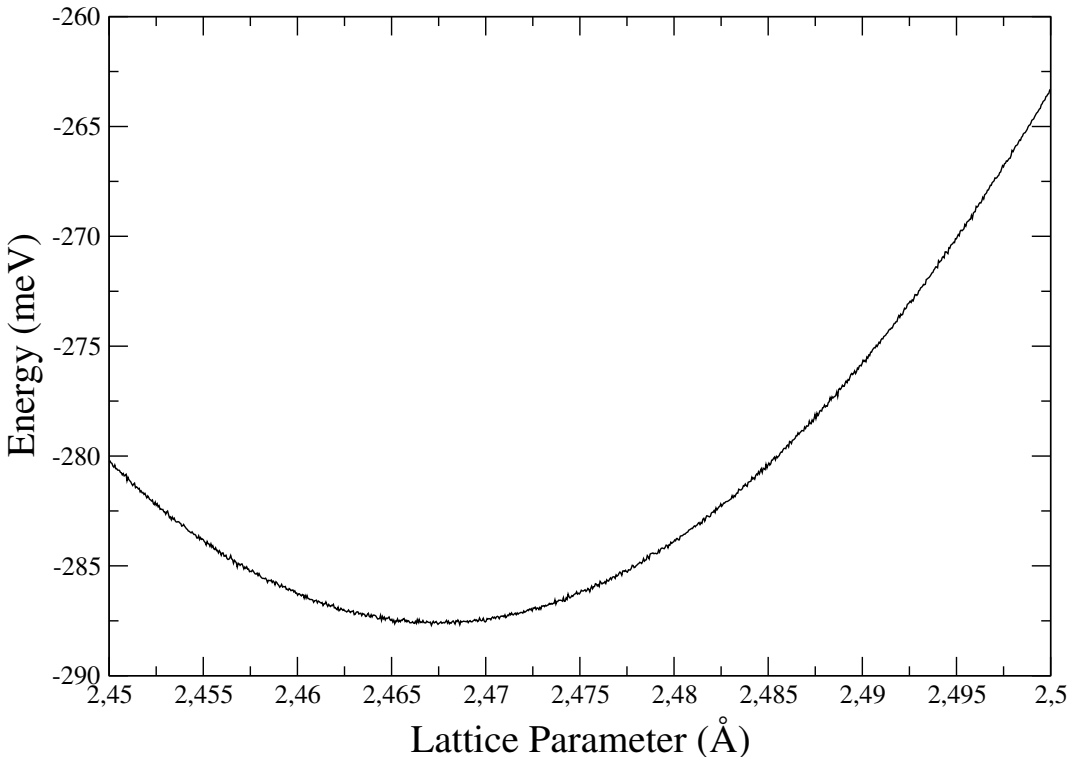


FIGURE 8.8: Graphene total energy U as a function of the lattice parameter.

K. At high temperature, our classical results and the ones of Rowe et al.[163] deviate.

It has been shown that at high temperature graphene may be in a corrugated state[166, 155]. The fact of being corrugated means that the averages of all the carbon atomic positions are not in the plane. It can be measured by calculating out-of-plane position correlation functions. The corrugation is not captured in our formalism as the centroids are forced to stay in the plane of the membrane. In order to clarify this disagreement we have performed MD calculation with the same potential at 2000 K. We have performed MD calculation in the microcanonical ensemble at fixed lattice parameters 2.465 Å, 2.47 Å, and 2.48 Å. The result with $a = 2.48$ Å is shown in Fig. 8.9. We start the MD simulation from a SSCHA configuration at 4000 K. Due to the equipartition theorem, the system reaches a temperature of 2000 K and stays stable. We can see in the figure that the temperature and pressure are stable. By taking averages, we can calculate the pressure for different lattice parameters and see at what lattice parameter the pressure is 0. We show the results in Fig. 8.10. As we can see, our MD results agree with the result of Rowe et al. This suggests that graphene is in

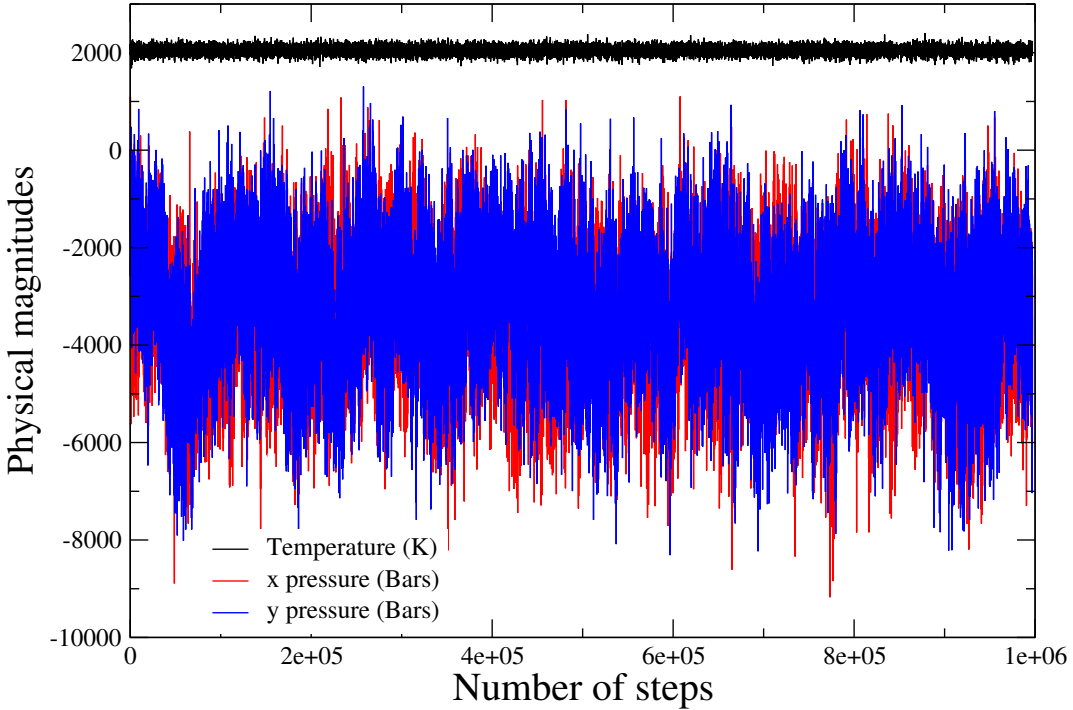


FIGURE 8.9: Temperature and in-plane pressure Cartesian components as a function of the step number. Each steps corresponds to 0.001 ps. The Temperatures is in K and the pressure in Bars. The lattice parameter is fixed to 2.48 Å. The simulation is done in the microcanonical ensemble.

a corrugated state at high temperatures and the corrugation is not captured within our framework.

In Fig. 8.7 we have also included the quasiharmonic (QHA) result. The lattice parameter within the QHA is obtained by calculating the harmonic free energy for different temperatures and lattice parameters. The lattice parameter dependence comes from the different harmonic phonons at different lattice parameters. Then, we take the lattice parameter that minimizes the harmonic free energy at each temperature. In Fig. 8.11 we show the quasiharmonic free energy of graphene at 0 K. The noise is inherent of the machine learning atomistic potential. The lattice parameter is obtained from the minimum of that function. It is worth noting that this approximation is not valid to calculate the thermal expansion of graphene due to the imaginary phonon frequencies that appear close to Γ for the ZA mode already at 500 K. In the shadowed region in Fig. 8.7 the QHA is not valid. These features question the validity of the results obtained with this approach that yield a negative thermal expansion at all temperatures[167].

8.5 Graphene phonons

In Fig. 8.12 we compare the ZA harmonic phonon spectra with the one obtained from the SSCHA dynamical matrix $D^{(S)}$ as well as the spectra obtained from the SSCHA spectral function $\Omega_\mu(q)$. The main conclusion is that while the dispersion of the ZA modes obtained from $D^{(S)}$ is linearized, the physical phonons become close to a quadratic dispersion and approach the harmonic dispersion, as expected

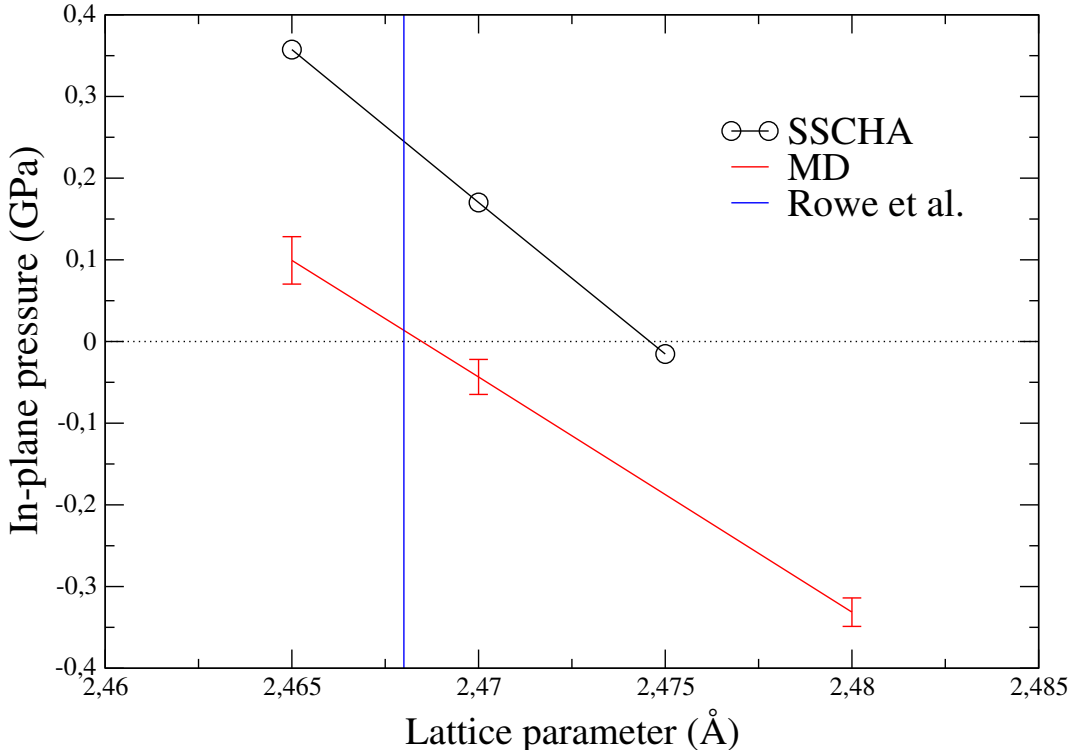


FIGURE 8.10: SSCHA and MD in-plane pressure as a function of the lattice parameter at 2000 K. The results of Rowe et al. is included as a vertical line.

by symmetry. The SSCHA ZA frequencies suffer a blue-shift with respect to the harmonic ones, but are red-shifted once the spectral function is calculated. Both shifts are bigger when the temperature is increased, but the quadratic behavior of the ZA modes is always recovered regardless of the temperature. The quadratic dispersion is clear from panels (d), (e), and (f), where the frequency is divided by the squared momentum, therefore, the lines with a quadratic dispersion become flat. We show in Fig. 8.13 that the static phonons ($\Omega_{\mu}^{(F)}(q)$) agree with those derived from the dynamical (see section 3.7.4) theory ($\Omega_{\mu}(q)$) and are thus good representatives of the physical phonons expected experimentally. The calculation at 2000 K deviates a little bit, which we believe it is a numerical issue. Static phonons are calculated from the free energy Hessian, which is rotationally invariant. Therefore, physical phonons are quadratic because of symmetry.

In Fig. 8.14 we make a similar study for the highest energy optical E_{2g} mode at the Γ point. This mode is interesting because the theoretical results can be compared to Raman experiments[168]. By looking at Fig. 8.14 (a), we observe that both SCHA and physical frequencies red-shift with increasing temperature in agreement with experiments and theory[171, 82]. Actually, for this mode the difference between the SCHA and physical frequencies is not so crucial. By looking at Fig. 8.14 (b) we can see how big are the dynamical effects and the effect of the thermal expansion. For this high energy mode it is crucial to include the dynamical effects, otherwise the shift is overestimated. The static calculation is done by setting $z = 0$ in Eqs. 3.86 and 3.78. This means that, for these high energy modes, setting $z = 0$ in the denominator of Eq. 3.78 is not a good approximation. The thermal expansion provides a positive shift at low temperatures.

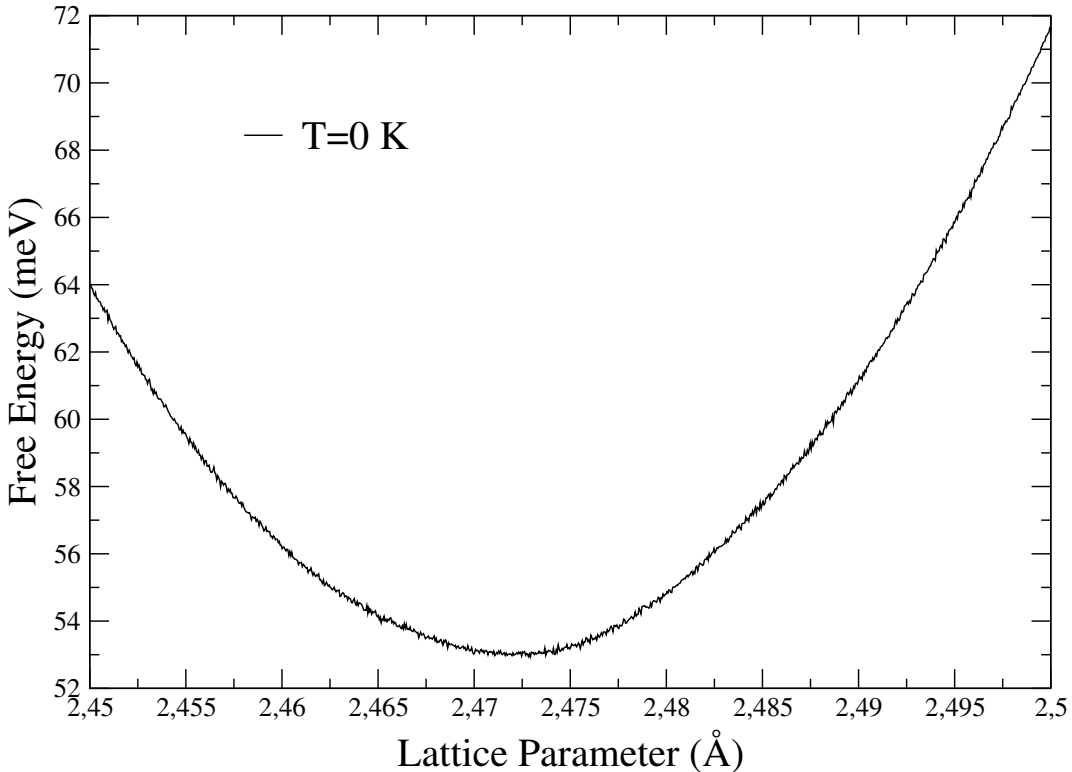


FIGURE 8.11: Quasiharmonic free energy of graphene at 0 K.

8.6 Root mean square displacements and linewidths

Even if the anharmonic correction to the phonon spectra may look small in Fig. 8.12, it has a huge impact on the mechanical and thermal properties of graphene. As shown in Fig. 8.15 (a), when calculating the root mean square atomic displacement with the SSCHA density matrix as $\sqrt{\langle \mathbf{u}^2 \rangle_{\rho_H}}$, the dramatic divergences with the sample size obtained in the harmonic case are partially suppressed, clearly showing the contribution of anharmonicity to the crystalline order of graphene. The divergences are reduced precisely because the SSCHA phonon frequencies obtained from $\mathbf{D}^{(S)}$ that build ρ_H are linear at small momenta (see Fig. 8.12). Thus, even if the phonons obtained from the SSCHA free energy Hessian $\mathbf{D}^{(F)}$ are quadratic, the fact that the density matrix used to compute thermodynamic properties is built with linearized phonons is responsible for reducing the divergences.

The SSCHA phonon frequencies obtained from $\mathbf{D}^{(S)}$ also provide an appropriate basis to calculate phonon linewidths[24, 89]. The results presented in Fig. 8.15 (b) clearly show that the linearization of the SSCHA frequencies dramatically changes the linewidth of the LA and TA modes at small momenta by making them smaller as momentum decreases. This result recovers the quasiparticle picture for these modes. Similar results are obtained in Ref. [153]. However, in this chapter linewidths of LA and TA modes at small momenta only vanish when strain is applied. Somewhat strain has an analogous effect to anharmonicity by linearizing the ZA dispersion. The problem is that strain linearizes physical phonons. We show here that there is no need of strain to have physically well-defined phonon linewidths. Anharmonicity is responsible for it.

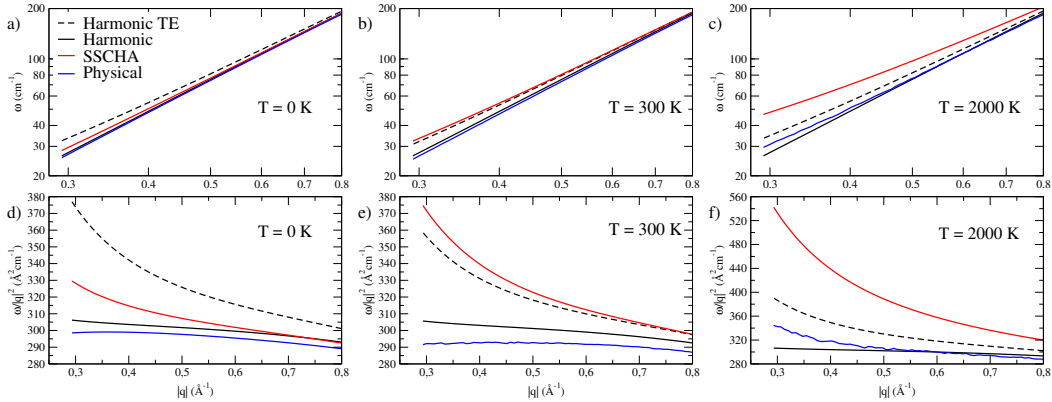


FIGURE 8.12: Harmonic ZA phonon spectra in logarithmic scale together with the SSCHA phonons, $D^{(S)}$, (labeled as “SSCHA”) and those obtained from the phonon spectral function, $\Omega_\mu(q)$, (labeled as “Physical”). Results at 0 K (a), 300 K (b), and 2000 K (c) are shown. (d), (e) and (f) show the frequency divided by the squared momentum. The dispersion corresponds to the GM direction. For reference, the M point is at 1.4662^{-1} at 0 K, at 1.4671^{-1} at 300 K, and at 1.4652^{-1} at 2000 K. The harmonic result (solid black) is computed at the lattice parameter that minimizes U , while the other results include thermal expansion (see Fig. 8.7). The dashed black lines correspond to harmonic calculations including thermal expansion (TE). All these calculations are performed with the machine learning atomistic potential.

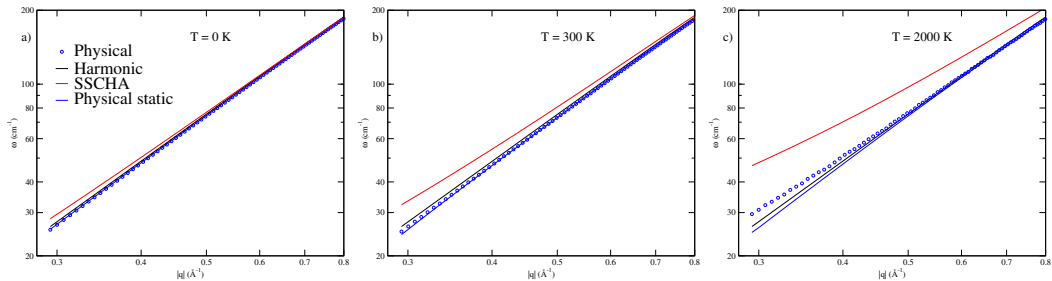


FIGURE 8.13: Harmonic, SSCHA, and physical phonons (static and dynamic) calculated at 0 K (a), 300 K (b), and 2000 K (c).

8.7 SCHA applied to a continuum membrane Hamiltonian

In order to obtain results at very small momenta and reinforce the conclusions drawn with the atomistic calculations with the machine learning potential, we also solve the SCHA equations in a continuum membrane Hamiltonian. This model has been widely used in the literature to describe graphene as an elastic membrane as well as to account for the coupling between in-plane and out-of plane acoustic modes[157, 158, 159]. The most general rotationally invariant continuum model potential for phonons in free-standing 2D membranes up to the fourth-order with respect to the

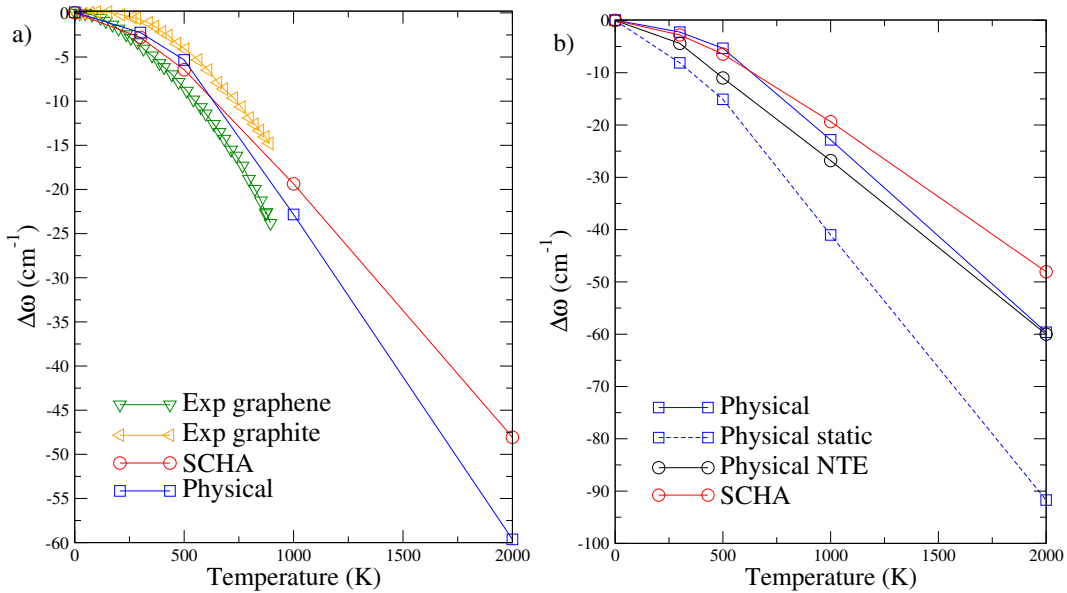


FIGURE 8.14: (a) SCHA and physical E_{2g} phonon frequency shift as a function of temperature. We include experimental results in graphene[168] and graphite[169, 170]. (b) The same as (a) without experiments and including the physical phonons without thermal expansion (Physical NTE) and the physical static phonons.

phonon fields has the following form:

$$\begin{aligned} U = \frac{1}{2} \int_{\Omega} d^2x [\kappa(\partial^2 h)^2 + C^{ijkl} \partial_i u_j \partial_k u_l + C^{ijkl} \partial_i u_j \partial_k h \partial_l h + \\ + \frac{C^{ijkl}}{4} \partial_i h \partial_j h \partial_k h \partial_l h + \frac{C^{ijkl}}{2} \partial_i \mathbf{u} \cdot \partial_j \mathbf{u} \partial_k h \partial_l h + \\ + C^{ijkl} \partial_i u_j \partial_k \mathbf{u} \cdot \partial_l \mathbf{u} + \frac{C^{ijkl}}{4} \partial_i \mathbf{u} \cdot \partial_j \mathbf{u} \partial_k \mathbf{u} \cdot \partial_l \mathbf{u}]. \quad (8.1) \end{aligned}$$

$\mathbf{u}(x)$ and $h(x)$ are the in-plane and out-of-plane displacement fields, respectively, and x is the 2D position vector in the membrane. κ is the bending rigidity of the membrane and the tensor $C^{ijkl} = \lambda\delta^{ij}\delta^{kl} + \mu(\delta^{ik}\delta^{jl} + \delta^{il}\delta^{jk})$ contains Lame's coefficients, λ and μ , and Kronecker deltas. As it is a continuum model it only accounts for acoustic modes and the second-order terms in the potential are the harmonic terms. The harmonic frequencies in normal coordinates space are $\omega_{ZA}(\mathbf{q}) = \sqrt{\phi_{ZA}(\mathbf{q})/\rho}$, $\omega_{LA}(\mathbf{q}) = \sqrt{(\phi_{LA}(\mathbf{q})/\rho)}$, and $\omega_{TA}(\mathbf{q}) = \sqrt{\phi_{TA}(\mathbf{q})/\rho}$, where ρ is the mass density of the membrane and $\phi_{ZA}(\mathbf{q}) = \kappa|\mathbf{q}|^4$, $\phi_{LA}(\mathbf{q}) = (\lambda + \mu)|\mathbf{q}|^2$, and $\phi_{TA}(\mathbf{q}) = \mu|\mathbf{q}|^2$ are the harmonic 2BFC. LA and TA correspond to the in-plane longitudinal and transversal phonons and ZA corresponds to the out-of-plane phonons. The higher-order terms account for the phonon-phonon anharmonic interactions. The thermal expansion is included in this formalism by changing the in-plane derivatives $\partial_i u_j \rightarrow \partial_i u_j + \delta^{ij}\delta a$, with $\delta a = (a - a_0)a_0$, a_0 being the lattice parameter that minimizes U .

It is not possible to apply the SCHA analytically in Eq. 8.1. As far as we know, the simplest approximation that allows applying the SCHA analytically is to neglect fourth-order terms including in-plane phonon fields. In that case, the potential can

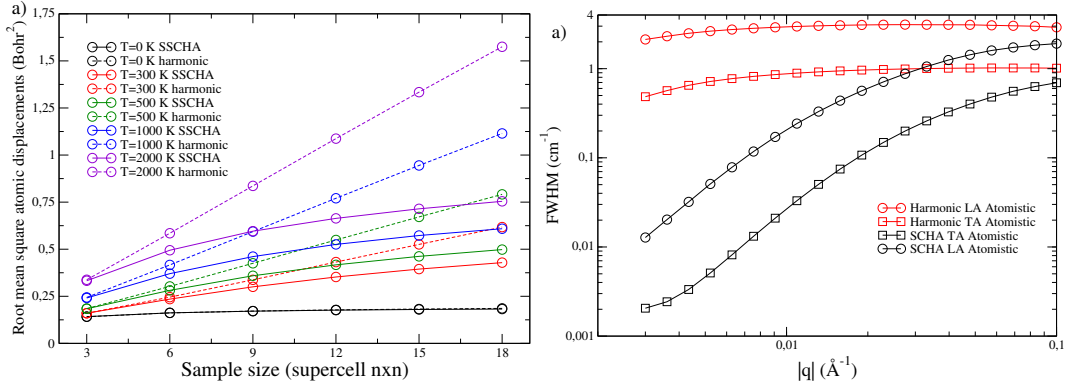


FIGURE 8.15: (a) Root mean square atomic displacement of carbon atoms in graphene calculated using the harmonic and the SSCHA density matrices. The harmonic result is always computed at the lattice parameter that minimizes U , while the SSCHA results include thermal expansion (see Fig. 8.7). (b) Linewidths (full width at half maximum) of LA and TA phonon modes at 300 K calculated within perturbation theory and the SSCHA. Results in both figures are obtained with the machine learning atomistic potential.

be written as

$$U = \frac{1}{2} \int_{\Omega} d^2x [C^{ijkl} \partial_i u_j \partial_k u_l + \kappa (\partial^2 h)^2 + C^{ijkl} \partial_i u_j \partial_k h \partial_l h + \frac{C^{ijkl}}{4} \partial_i h \partial_j h \partial_k h \partial_l h] + 2\Omega(\lambda + \mu)(\delta a)^2 + \delta a(\lambda + \mu) \int_{\Omega} d^2x \partial_k h \partial_k h. \quad (8.2)$$

By Fourier transforming this potential in \mathbf{q} space and applying Eq. 3.59, we arrive to the SCHA equations (see appendix A for further derivations)

$$\frac{\partial \mathcal{F}}{\partial \delta a} = 0 \rightarrow \delta a = -\frac{1}{4\Omega} \sum_{\mathbf{q}} |\mathbf{q}|^2 g[\Omega_{ZA}^{(S)}(\mathbf{q})], \quad (8.3)$$

$$\frac{\partial \mathcal{F}}{\partial \Phi_{ZA}(\mathbf{q})} = 0 \rightarrow \Phi_{ZA}(\mathbf{q}) = \kappa |\mathbf{q}|^4 + 2\delta a(\lambda + \mu) |\mathbf{q}|^2 + \frac{\lambda + 2\mu}{2\Omega} \sum_{\mathbf{k}} g[\Omega_{ZA}^{(S)}(\mathbf{k})] [|\mathbf{q}|^2 |\mathbf{k}|^2 + 2(\mathbf{q} \cdot \mathbf{k})^2]. \quad (8.4)$$

$\Phi_{ZA}(\mathbf{q})$ are the SCHA 2BFC that correspond to the out-of-plane modes and the frequencies are $\Omega_{ZA}^{(S)}(\mathbf{q}) = \sqrt{\Phi_{ZA}(\mathbf{q})/\rho}$. The function g is defined as $g(x) = \coth(x/2T)/2\rho x$, T being the temperature. Already from Eq. 8.4 it can be seen that the non-zero δa provides the SCHA frequency with a linear term. By inserting Eq. 8.3 in Eq. 8.4 the SCHA 2BFC can be written as $\Phi_{ZA}(\mathbf{q}) = \kappa |\mathbf{q}|^4 + \gamma |\mathbf{q}|^2$. The expression for γ is given in appendix A. Therefore, we have shown that the SCHA flexural acoustic (ZA) modes have a linear dispersion close to the point Γ .

For calculating the physical static phonons, given by the second derivative of the free energy, an analogous formula to Eq. 3.76 can be found within the membrane formalism (see appendix A). By applying this formula we arrive to the following expression for the physical 2BFC at $T = 0$

$$\Phi_{ZA}^{(F)}(\mathbf{q}) = \kappa |\mathbf{q}|^2 + (\gamma - \sigma) |\mathbf{q}|^2 + O(|\mathbf{q}|^4), \quad (8.5)$$

where

$$\sigma = \frac{\rho\sqrt{\gamma}}{8\pi\kappa^{3/2}} \sum_{\alpha=LA,TA} v_\alpha f(\Lambda\sqrt{\kappa/\gamma}, v_\alpha\sqrt{\rho/\gamma}), \quad (8.6)$$

with

$$f(x, y) = \int_0^x ds \frac{s^2}{\sqrt{1+s^2}[\sqrt{1+s^2}+y]}. \quad (8.7)$$

The positive number σ makes the linear term in the physical phonon frequencies 40% smaller than in the SCHA case, however, it does not remove it. Actually, it can be argued that this non-zero linear term in the physical static frequencies arises because the potential in Eq. 8.2 is not rotationally invariant. In order to clarify these results we have applied the SCHA numerically in the full potential.

By taking the full potential in Eq. 8.1, Fourier transforming it and applying Eq. 3.59 we arrive to the SCHA equations for the rotationally invariant membrane

$$\begin{aligned} \frac{\partial \mathcal{F}(\mathcal{V})}{\partial \delta a} = 0 = & 2\Omega(2\delta a + 3\delta a^2 + \delta a^3)(\lambda + \mu) + \frac{1}{2} \sum_{\mathbf{q}} g[\Omega_{ZA}^{(S)}(\mathbf{q})] 2(1 + \delta a)(\lambda + \mu)|\mathbf{q}|^2 \\ & + \frac{1}{2} \sum_{\mathbf{q}} g[\Omega_{LA}^{(S)}(\mathbf{q})] [2(1 + \delta a)(\lambda + 2\mu)|\mathbf{q}|^2 + 2(1 + \delta a)(\lambda + \mu)|\mathbf{q}|^2] + \\ & \frac{1}{2} \sum_{\mathbf{q}} g[\Omega_{TA}^{(S)}(\mathbf{q})] [2(1 + \delta a)\mu|\mathbf{q}|^2 + 2(1 + \delta a/2)(\lambda + \mu)|\mathbf{q}|^2], \end{aligned} \quad (8.8)$$

$$\begin{aligned} \Phi_{ZA}(\mathbf{q}) = & \kappa|\mathbf{q}|^4 + 2(1 + \delta a/2)\delta a(\lambda + \mu)|\mathbf{q}|^2 + \frac{\lambda + 2\mu}{2\Omega} \sum_{\mathbf{k}} g[\Omega_{ZA}^{(S)}(\mathbf{k})] [|\mathbf{q}|^2|\mathbf{k}|^2 + 2(\mathbf{q} \cdot \mathbf{k})^2] + \\ & \frac{1}{2\Omega} \sum_{\mathbf{k}} \{g[\Omega_{LA}^{(S)}(\mathbf{k})] + g[\Omega_{TA}^{(S)}(\mathbf{k})]\} [\lambda|\mathbf{q}|^2|\mathbf{k}|^2 + 2\mu(\mathbf{q} \cdot \mathbf{k})^2], \end{aligned} \quad (8.9)$$

$$\begin{aligned} \Phi_{LA}(\mathbf{q}) = & (\lambda + 2\mu)|\mathbf{q}|^2 + 2(1 + \delta a/2)\delta a(\lambda + 2\mu)|\mathbf{q}|^2 + 2(1 + \delta a/2)\delta a(\lambda + \mu)|\mathbf{q}|^2 \\ & + \frac{1}{2\Omega} \sum_{\mathbf{k}} g[\Omega_{ZA}^{(S)}(\mathbf{k})] [\lambda|\mathbf{q}|^2|\mathbf{k}|^2 + 2\mu(\mathbf{q} \cdot \mathbf{k})^2] + \\ & \frac{1}{4\Omega} \sum_{\mathbf{k}} \{4g[\Omega_{TA}^{(S)}(\mathbf{k})] [\lambda(\mathbf{q} \cdot \mathbf{k})^2 + \mu|\mathbf{q}|^2|\mathbf{k}|^2 + \mu(\mathbf{q} \cdot \mathbf{k})^2] (\hat{\mathbf{q}}_\perp \cdot \hat{\mathbf{k}}) + \\ & 2g[\Omega_{TA}^{(S)}(\mathbf{k})] [\lambda|\mathbf{q}|^2|\mathbf{k}|^2 + 2\mu(\mathbf{q} \cdot \mathbf{k})^2] + \\ & 2g[\Omega_{LA}^{(S)}(\mathbf{k})] [\lambda|\mathbf{q}|^2|\mathbf{k}|^2 + 2\mu(\mathbf{q} \cdot \mathbf{k})^2] + \\ & 4g[\Omega_{LA}^{(S)}(\mathbf{k})] [\lambda(\mathbf{q} \cdot \mathbf{k})^2 + \mu|\mathbf{q}|^2|\mathbf{k}|^2 + \mu(\mathbf{q} \cdot \mathbf{k})^2] (\hat{\mathbf{q}} \cdot \hat{\mathbf{k}})\} \end{aligned} \quad (8.10)$$

and,

$$\begin{aligned} \Phi_{TA}(\mathbf{q}) = & \mu|\mathbf{q}|^2 + 2(1 + \delta a/2)\delta a\mu|\mathbf{q}|^2 + 2(1 + \delta a/2)\delta a(\lambda + \mu)|\mathbf{q}|^2 \\ & + \frac{1}{2\Omega} \sum_k g[\Omega_{ZA}^{(S)}(\mathbf{k})][\lambda|\mathbf{q}|^2|\mathbf{k}|^2 + 2\mu(\mathbf{q} \cdot \mathbf{k})^2] + \\ & \frac{1}{4\Omega} \sum_k \{4g[\Omega_{TA}^{(S)}(\mathbf{k})][\lambda(\mathbf{q} \cdot \mathbf{k})^2 + \mu|\mathbf{q}|^2|\mathbf{k}|^2 + \mu(\mathbf{q} \cdot \mathbf{k})^2](\hat{\mathbf{q}}_\perp \cdot \hat{\mathbf{k}}_\perp)] + \\ & 4g[\Omega_{LA}^{(S)}(\mathbf{k})][\lambda(\mathbf{q} \cdot \mathbf{k})^2 + \mu|\mathbf{q}|^2|\mathbf{k}|^2 + \mu(\mathbf{q} \cdot \mathbf{k})^2](\hat{\mathbf{q}}_\perp \cdot \hat{\mathbf{k}}) + \\ & 2g[\Omega_{TA}^{(S)}(\mathbf{k})][\lambda|\mathbf{q}|^2|\mathbf{k}|^2 + 2\mu(\mathbf{q} \cdot \mathbf{k})^2]\}. \quad (8.11) \end{aligned}$$

We have solved these equations by using the Newton-Raphson method[172] in a circular discretized grid of 60×60 \mathbf{q} points. The results are shown in Fig. 8.16. All con-

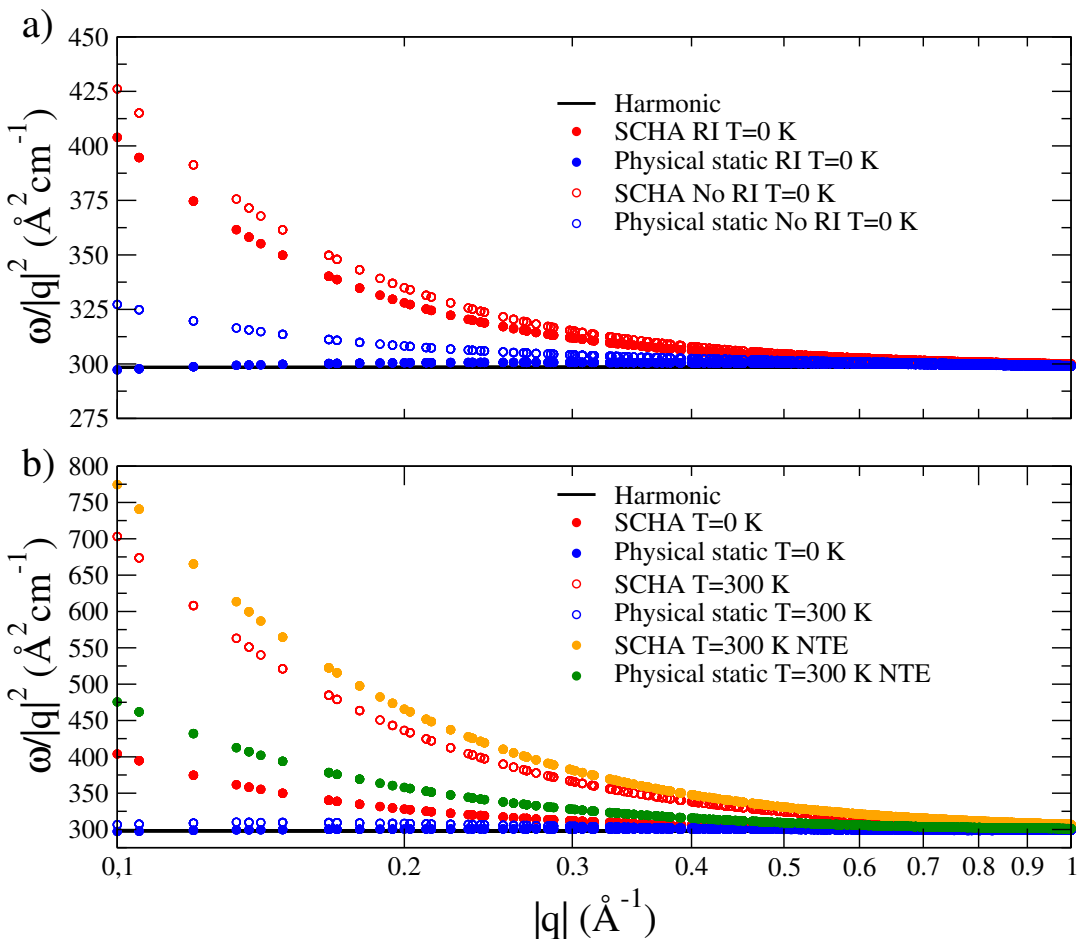


FIGURE 8.16: (a) Frequency of the ZA mode divided by the squared momentum in the harmonic approximation, within the SCHA and obtained from the Hessian of the SCHA (labeled as “Physical static”) at 0 K in the membrane model. We name rotationally invariant (RI) the results considering the full potential in Eq. 8.1. We name no rotationally invariant (No RI) the results neglecting the last three terms in Eq. 8.1. (b) Frequency of the ZA mode in the harmonic approximation, within the SCHA and obtained from the Hessian of the SCHA at 0 K and 300 K in the membrane model. We also include the SCHA and physical phonons at 300 K without considering thermal expansion (NTE).

clusions drawn with the atomistic model are confirmed and put in solid grounds. Again the ZA phonons obtained from the SCHA force constants get linearized at small momenta and the linearization is bigger for higher temperatures. These results are consistent with the anharmonic linearization obtained for this mode in previous calculations[157, 158, 159]. However, when the phonons are calculated from the free energy Hessian, the ZA phonon frequencies get basically on top of the harmonic values recovering a quadratic dispersion. This means that the physical phonons have a quadratic dispersion for small momenta in an unstrained membrane, as it is expected by symmetry. We also show that accounting correctly for the thermal expansion is crucial to recover the $\sim q^2$ behavior as shown in Fig. 8.16 (b). The membrane potential is able to capture the negative thermal expansion at small temperatures, as it is shown in Fig. 8.17. Finally, it is important to remark that a fully rotationally

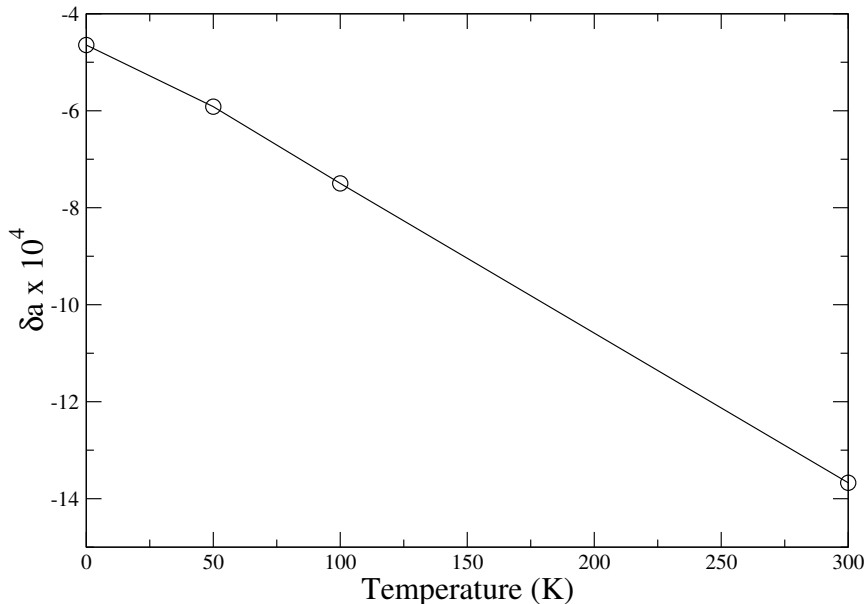


FIGURE 8.17: δa as a function of temperature in the membrane model.

invariant potential is needed to recover the quadratic dispersion (see Fig. 8.16 (b)). If the last three terms in Eq. 8.1 are neglected, which breaks the rotational symmetry of the potential, the quadratic dispersion is not recovered. This means that it is very important to keep these terms in the potential to correctly estimate the mechanical properties of membranes even if they are usually neglected[157, 158, 159].

In Fig. 8.18 we show the linewidths of the LA and TA modes calculated within the membrane model. We also include the atomistic results for comparison. The results clearly show that the linearization of the SCHA frequencies dramatically changes the linewidth of the LA and TA modes at small momenta by making them smaller as momentum decreases. This result is equivalent in the atomistic case. When the ratio between the FWHM and the frequency of the mode is 1 or bigger, the quasiparticle picture is lost. According to our calculations in Fig. 8.18 (b) this value is reached in the $0.001\text{-}0.002 \text{ \AA}^{-1}$ momentum range when the linewidth is calculated on top of the harmonic dispersion within perturbation theory. We shadow the region where the membrane LA mode is not well defined. However, when the linewidth is calculated within the SCHA, the ratio never gets bigger than 0.05. These results recover the quasiparticle picture for these modes and are in agreement with experiments[173], where they clearly see that in this momentum range ($0.001\text{-}0.002 \text{ \AA}^{-1}$) the

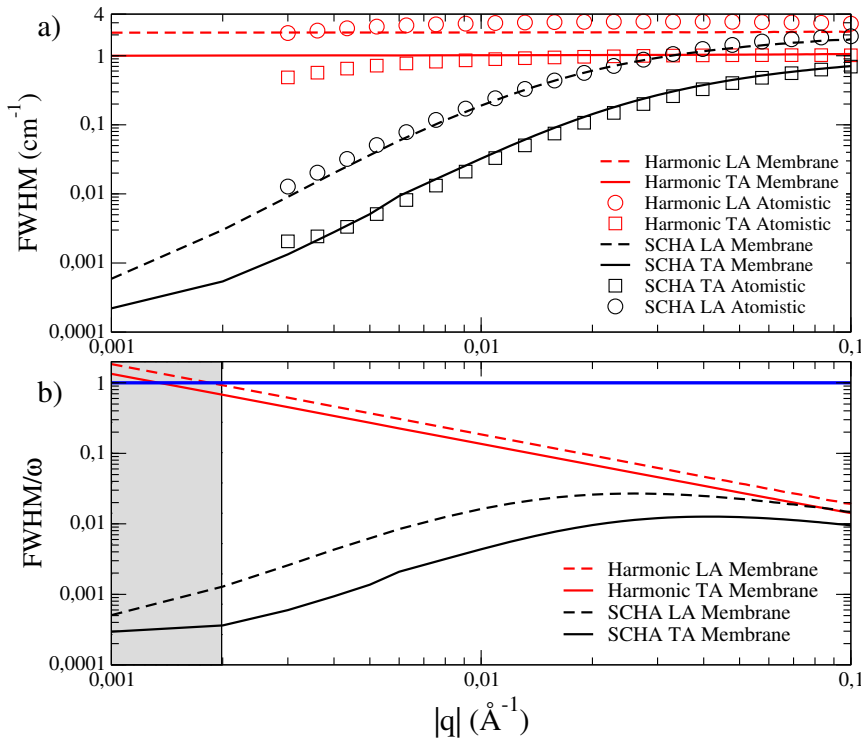


FIGURE 8.18: (a) Atomistic and membrane linewidths calculated within the SSCHA and within perturbation theory at 300 K. (b) Membrane linewidths at 300 K divided by the phonon frequency calculated within the SCHA and perturbation theory.

quasiparticle picture is hold. It also means that sound can propagate in graphene, which does not happen within perturbation theory.

In the last part of this section we will prove that neglecting the fourth-order tensor in the SSCHA self-energy and assuming the Lorentzian approximation are good approximations. For studying the effect of the fourth-order tensor in the SSCHA self-energy we Taylor expand Eq. 3.86

$$\begin{aligned} \Pi(z) = & \mathbf{M}^{-\frac{1}{2}} \overset{(3)}{\Phi} \Lambda(z) [\mathbf{1} - \overset{(4)}{\Phi} \Lambda(z)]^{-1} \overset{(3)}{\Phi} \mathbf{M}^{-\frac{1}{2}} \simeq \\ & \mathbf{M}^{-\frac{1}{2}} \overset{(3)}{\Phi} \Lambda(z) \overset{(3)}{\Phi} \mathbf{M}^{-\frac{1}{2}} + \mathbf{M}^{-\frac{1}{2}} \overset{(3)}{\Phi} \Lambda(z) \overset{(4)}{\Phi} \Lambda(z) \overset{(3)}{\Phi} \mathbf{M}^{-\frac{1}{2}} + \dots, \quad (8.12) \end{aligned}$$

and we calculate the contribution of the term containing the fourth-order tensor to the linewidth. We also calculate the spectral function with and without including the frequency dependence of the self energy. We show the results in Fig. 8.19. The figure clearly shows that the contribution of the fourth-order tensor is at least one order of magnitude smaller than the main term and, what is more important, it also decays as momentum decreases. The figure also shows that the Lorentzian approximation is justified for the acoustic modes in graphene.

8.8 Conclusions

In conclusion, we show that anharmonic effects are crucial to mechanically stabilize graphene and to guarantee its phonon modes make physical sense and propagate

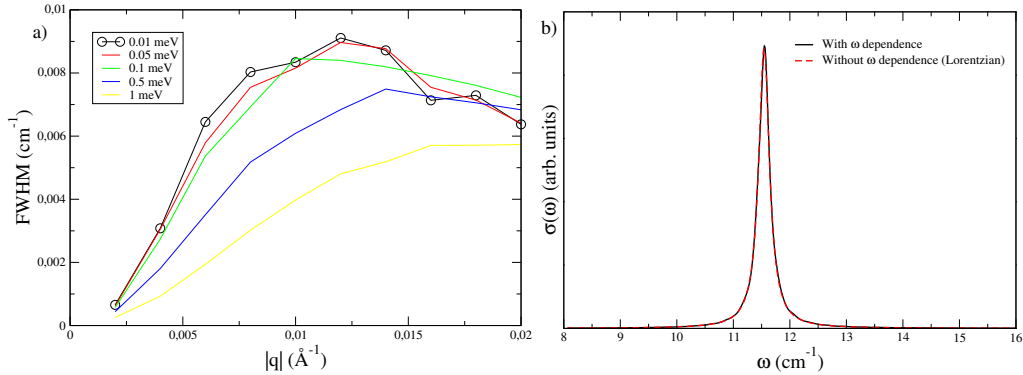


FIGURE 8.19: (a) Linewidth (full width at half maximum, FWHM) contribution of the term containing the fourth-order tensor of the LA mode calculated in the membrane model at 100 K using the harmonic and SCHA phonons. The value of the smearing is in the legend. (b) Spectral function of the LA mode with momentum 0.01 \AA^{-1} at 100 K with and without considering the frequency dependence of the self energy.

sound at small momenta. Moreover, we determine that, despite the relevance of anharmonic effects, the out-of-plane acoustic modes should show a quadratic dispersion experimentally. We estimate anharmonic effects within the self-consistent harmonic approximation both with an atomistic machine learning potential and with a membrane model, obtaining consistent results in both cases. Our results show how all the divergences in the atomic displacements reduce and sound can propagate in graphene. These conclusions can be extrapolated to any strictly 2D material and will have a large impact on the understanding of their mechanical and thermal properties.

Conclusions

The main goal of this thesis was to understand and predict the phase transitions that occur in high efficiency thermoelectric materials SnSe and SnS. Another purpose was to calculate the lattice thermal conductivity in these materials to understand the experimental results and find the origin of such a low thermal conductivity.

We have seen that both SnSe and SnS suffer second-order phase transitions from the low symmetry low temperature *Pnma* phase to the high symmetry high temperature *Cmcm* phase. This means that they suffer continuous displacive phase transitions. As it is expected in a second-order phase transition, the thermal conductivity is very similar for both phases close to the transition temperature. This together with the fact that the *Cmcm* phase has a higher *PF* due to a smaller band gap, makes these materials to have the maximum *ZT* just after the phase transition. Therefore, the role of the phase transition is key for having a high thermoelectric efficiency.

The thermal conductivity of both materials is ultralow, around 0.3-1.0 W/mK at around 800 K. We have seen that the main contribution to the lattice thermal conductivity comes from the acoustic modes. Their values are low due to the high anharmonicity of the material and low group velocities. Perturbation theory breaks down in the calculation of second-order and high-order force-constants and the inclusion of anharmonicity at a nonperturbative level is crucial for a proper description of the lattice thermal conductivity. We have seen that we only get results in agreement with experiments when we include anharmonic effects at a nonperturbative level.

From a qualitative point of view our transition temperature T_c calculations are in agreement with experiments. We have seen that an accurate quantitative agreement in T_c is out of the scope of this thesis. This happens because the vibrational properties are very sensitive to the volume of the unit cell. Regarding the lattice thermal conductivity we get a very good agreement with experimental results and this has helped clarifying many experimental uncertainties. In the work by Zhao et al.[6] they showed ultralow and isotropic values of the lattice thermal conductivity, lower than our calculations for the in-plane results. These results led to $ZT_{max} = 2.6$, the maximum *ZT* so far. Later experiments[115, 127] have shown that the in-plane thermal conductivity is higher and are in good agreement with our results. It seems that the origin of the low in-plane lattice thermal conductivity of Zhao et al. is due to Sn vacancies. The later experimental works have shown that, due to the higher in-plane lattice thermal conductivity, the ZT_{max} of intrinsic SnSe is around 1. Our calculations suggest that SnSe and SnS have very similar thermoelectric properties and, therefore, SnS may be an efficient thermoelectric material in the high temperature phase. This is also partially supported by experiments as both systems seem to have very similar *ZTs* in the low temperature phase close to the phase transition. Of course, this is not true if we consider the results by Zhao et al.

Another important conclusion of this thesis is related to the experimental measurement of the phonon spectral function. We have seen that the Lorentzian approximation breaks down for some vibrational modes in SnSe and SnS. This is in principle not an unexpected results as we have shown that they are strongly anharmonic materials. The breakdown of the Lorentzian approximation given by the strong anharmonicity creates shoulders and double peaks in the phonon spectral function, which makes it more difficult to understand. These results are key for the understanding of future inelastic scattering experiments in this kind of materials.

Another purpose of this thesis was to study the ferroelectric phase transition and thermal conductivity in monolayer SnSe. We have seen that monolayer SnSe suffers a second-order phase transition from the low symmetry low temperature $Pnm2_1$ to the high symmetry high temperature $Pnmm$ phase. The low symmetry $Pnm2_1$ phase has no inversion symmetry and, therefore, it is a ferroelectric phase. As it happens in the bulk case, the agreement with experiments is not quantitatively good as experimentally it is measured to be in the $Pnm2_1$ phase at 300 K. According to our calculations the phase transition occurs at around 110 K. Regarding the calculation of the lattice thermal conductivity, we have found obstacles partially related to the two dimensional nature of the system. This has motivated the last chapter of this thesis.

The acoustic out-of-plane modes (ZA) of planar materials have a quadratic dispersion within the harmonic approximation. This dispersion is fixed by the two dimensional (2D) symmetry and creates problematic results, such as, diverging atomic displacements as a function of the sample size or finite line width of acoustic in-plane phonons (LA/TA) at vanishing momenta. Therefore, there seems to be a conflict between the symmetry forced quadratic dispersion, which is expected to be measured experimentally, and the magnitudes that can be calculated using it. We have shown that such a conflict does not exist, anharmonicity is the answer to the problem. We have applied the SSCHA to include anharmonic effects. In order to calculate physical properties, such as, atomic displacements or line widths, the SSCHA formalism uses the SSCHA auxiliary phonons frequencies. We have seen that the SSCHA ZA phonons have a linear dispersion, as a result, diverging atomic displacements reduce and finite line widths disappear. However, when the physical phonons are calculated within the SSCHA, the ones that are supposed to be measured experimentally, the quadratic dispersion is recovered as expected by symmetry.

To sum up, we have shown that nonperturbative anharmonicity is key for understanding all the physics that appear in the systems under study in this thesis. However, there are still open questions and work to do in this field. For example, the quantitative agreement of the transition temperature is one of them. As we have seem, the phonon frequencies are extremely sensitive to the volume of the unit cell in monochalcogenide materials. With the current exchange correlation functionals and the available computational resources for the supercell calculations, the T_c calculations are still a very challenging task. An interesting future research is the limitation of the Lorentzian approximation to calculate the lattice thermal conductivity in systems where the Lorentzian approximation fails to describe the phonons. This is actually the case in monochalcogenide materials. It would be interesting, from a fundamental point of view, to understand what is the effect of not assuming the Lorentzian approximation when calculating the lattice thermal conductivity in SnSe and SnS. Another interesting future research project is the calculation of the lattice

thermal conductivity in graphene. As we have seen, the inclusion of anharmonicity at a nonperturbative level, dramatically changes the line widths of acoustic modes. This will have a non-negligible effect in the lattice thermal conductivity of graphene and also in all the two dimensional materials.

Part IV

Appendices

Appendix A

Mathematical formulas and derivations for the membrane model

In this appendix we include all the mathematical derivations and calculation details of the membrane model.

The general rotationally invariant potential for a membrane can be written as follows

$$U = \frac{1}{2} \int_{\Omega} d^2x \left(\kappa (\partial^2 h)^2 + \sum_{n \geq 2} u_{i_1 j_1} \dots u_{i_n j_n} C_{i_1 j_1 \dots i_n j_n}^{(2n)} \right), \quad (\text{A.1})$$

where Ω is the area of the membrane in equilibrium, κ is the bending rigidity, h is the out-of-plane component of the displacement field and the rotationally invariant strain tensor u_{ij} is defined using the in-plane displacement field u_i

$$u_{ij} = \frac{1}{2} (\partial_i u_j + \partial_j u_i + \partial_i \mathbf{u} \cdot \partial_j \mathbf{u} + \partial_i h \partial_j h). \quad (\text{A.2})$$

$C_{i_1 j_1 \dots i_n j_n}^{(2n)}$ is the generic elastic tensor of rank $2n$. In the previous expression the subscripts label the 2d coordinates x, y and the sum over indices is assumed. The second-order expansion of Eq. A.1 with respect to the phonon fields is given by

$$U = \frac{1}{2} \int_{\Omega} d^2x \left(\kappa (\partial^2 h)^2 + C_{ijkl}^{(4)} u_{ij} u_{il} \right), \quad (\text{A.3})$$

with $C_{ijkl}^{(4)} = \lambda \delta_{ij} \delta_{kl} + \mu (\delta_{ik} \delta_{jl} + \delta_{il} \delta_{jk})$. By using equation A.2 and $C_{ijkl}^{(4)} = C^{ijkl}$, equation A.3 can be rewritten as

$$\begin{aligned} U = \frac{1}{2} \int_{\Omega} d^2x & [\kappa (\partial^2 h)^2 + C^{ijkl} \partial_i u_j \partial_k u_l + C^{ijkl} \partial_i u_j \partial_k h \partial_l h + \frac{C^{ijkl}}{4} \partial_i h \partial_j h \partial_k h \partial_l h + \\ & + \frac{C^{ijkl}}{2} \partial_i \mathbf{u} \cdot \partial_j \mathbf{u} \partial_k h \partial_l h + C^{ijkl} \partial_i u_j \partial_k \mathbf{u} \cdot \partial_l \mathbf{u} + \frac{C^{ijkl}}{4} \partial_i \mathbf{u} \cdot \partial_j \mathbf{u} \partial_k \mathbf{u} \cdot \partial_l \mathbf{u}]. \end{aligned} \quad (\text{A.4})$$

If we allow the lattice spacing a to be a variable, we can vary it by simply shifting the derivatives of the in-plane displacements according to $\partial_i u_j \rightarrow \partial_i u_j + \delta^{ij} \delta a$, where $\delta a = (a - a_0)/a_0$. Then, by taking into account periodic boundary conditions

$\int_{\Omega} d^2x \partial_i u_j = 0$ we can rewrite the potential

$$\begin{aligned} U \rightarrow U + 2\Omega(1 + \delta a)(\lambda + \mu)\delta a^2 + (1 + \frac{\delta a}{2})\delta a(\lambda + \mu) \int_{\Omega} d^2x \partial_k h \partial_k h + \frac{\delta a}{2} \int_{\Omega} d^2x C^{ijkl} \partial_i u_j \partial_k h \partial_l h + \\ (1 + \frac{\delta a}{2})\delta a \int_{\Omega} d^2x C^{ijkl} \partial_i u_j \partial_k u_l + (1 + \frac{\delta a}{2})\delta a(\lambda + \mu) \int_{\Omega} d^2x \partial_k \mathbf{u} \cdot \partial_k \mathbf{u} + \frac{\delta a^4 \Omega}{2}(\lambda + \mu) + \\ \frac{\delta a}{4} \int_{\Omega} d^2x C^{ijkl} [\partial_i \mathbf{u} \cdot \partial_j \mathbf{u} \partial_k u_l + \partial_i u_j \partial_k \mathbf{u} \cdot \partial_l \mathbf{u}]. \quad (\text{A.5}) \end{aligned}$$

If we Fourier transform the potential and we apply $\langle u_{\alpha}(\mathbf{q}) u_{\alpha}(-\mathbf{q}) \rangle_{\rho_H} = g[\Omega_{\alpha}^{(S)}(\mathbf{q})]$ ($\alpha = \text{LA,TA}$), $\langle h(\mathbf{q}) h(-\mathbf{q}) \rangle_{\rho_H} = g[\Omega_{ZA}^{(S)}(\mathbf{q})]$, the SCHA free energy can be written as (we use $\hbar = k_B = 1$)

$$\begin{aligned} \mathcal{F}(\mathcal{U}) = F_U + 2\Omega(1 + \delta a + \frac{\delta a^2}{4})(\lambda + \mu)\delta a^2 + \frac{1}{2} \sum_{\mathbf{q}} \{g[\Omega_{ZA}^{(S)}(\mathbf{q})] \kappa |\mathbf{q}|^4 + \\ \{(\lambda + 2\mu)g[\Omega_{LA}^{(S)}(\mathbf{q})] + \mu g[\Omega_{TA}^{(S)}(\mathbf{q})]\} |\mathbf{q}|^2 + \\ \frac{\lambda + 2\mu}{4\Omega} \sum_{\mathbf{k}} g[\Omega_{ZA}^{(S)}(\mathbf{q})] g[\Omega_{ZA}^{(S)}(\mathbf{k})] [|\mathbf{q}|^2 |\mathbf{k}|^2 + 2(\mathbf{q} \cdot \mathbf{k})^2] + \\ \frac{1}{2\Omega} \sum_{\mathbf{k}} g[\Omega_{ZA}^{(S)}(\mathbf{k})] \{g[\Omega_{LA}^{(S)}(\mathbf{q})] + g[\Omega_{TA}^{(S)}(\mathbf{q})]\} [\lambda |\mathbf{q}|^2 |\mathbf{k}|^2 + 2\mu(\mathbf{q} \cdot \mathbf{k})^2] + \\ + 2(1 + \frac{\delta a}{2})\delta a(\lambda + \mu)g[\Omega_{ZA}^{(S)}(\mathbf{q})] |\mathbf{q}|^2 + 2(1 + \frac{\delta a}{2})\delta a \{(\lambda + 2\mu)g[\Omega_{LA}^{(S)}(\mathbf{q})] + \mu g[\Omega_{TA}^{(S)}(\mathbf{q})]\} |\mathbf{q}|^2 + \\ 2(1 + \frac{\delta a}{2})\delta a(\lambda + \mu) \{g[\Omega_{LA}^{(S)}(\mathbf{q})] + g[\Omega_{TA}^{(S)}(\mathbf{q})]\} |\mathbf{q}|^2 - g[\Omega_{ZA}^{(S)}(\mathbf{q})] \Phi_{ZA}^{(S)}(\mathbf{q}) - \\ \sum_{\alpha} g[\Omega_{\alpha}^{(S)}(\mathbf{q})] \Phi_{\alpha}^{(S)}(\mathbf{q}) + \\ \frac{1}{4\Omega} \sum_{qk} [4g[\Omega_{LA}^{(S)}(\mathbf{q})] g[\Omega_{TA}^{(S)}(\mathbf{k})] [\lambda(\mathbf{q} \cdot \mathbf{k})^2 + \mu |\mathbf{q}|^2 |\mathbf{k}|^2 + \mu(\mathbf{q} \cdot \mathbf{k})^2] (\hat{\mathbf{q}}_{\perp} \cdot \hat{\mathbf{k}}) + \\ 2g[\Omega_{LA}^{(S)}(\mathbf{q})] g[\Omega_{TA}^{(S)}(\mathbf{k})] [\lambda |\mathbf{q}|^2 |\mathbf{k}|^2 + 2\mu(\mathbf{q} \cdot \mathbf{k})^2] + \\ (g[\Omega_{LA}^{(S)}(\mathbf{q})] g[\Omega_{LA}^{(S)}(\mathbf{k})] + g[\Omega_{TA}^{(S)}(\mathbf{q})] g[\Omega_{TA}^{(S)}(\mathbf{k})]) [\lambda |\mathbf{q}|^2 |\mathbf{k}|^2 + 2\mu(\mathbf{q} \cdot \mathbf{k})^2] + \\ 2(g[\Omega_{LA}^{(S)}(\mathbf{q})] g[\Omega_{LA}^{(S)}(\mathbf{k})]) [\lambda(\mathbf{q} \cdot \mathbf{k})^2 + \mu |\mathbf{q}|^2 |\mathbf{k}|^2 + \mu(\mathbf{q} \cdot \mathbf{k})^2] (\hat{\mathbf{q}} \cdot \hat{\mathbf{k}}) + \\ 2(g[\Omega_{TA}^{(S)}(\mathbf{q})] g[\Omega_{TA}^{(S)}(\mathbf{k})]) [\lambda(\mathbf{q} \cdot \mathbf{k})^2 + \mu |\mathbf{q}|^2 |\mathbf{k}|^2 + \mu(\mathbf{q} \cdot \mathbf{k})^2] (\hat{\mathbf{q}}_{\perp} \cdot \hat{\mathbf{k}}_{\perp})] \}, \quad (\text{A.6}) \end{aligned}$$

where $g(\omega) = \coth((\omega/2T))/(2\rho\omega)$ and $\Omega_{\alpha}^{(S)}(\mathbf{q}) = \sqrt{\Phi_{\alpha}(\mathbf{q})/\rho}$ ($\alpha = \text{ZA,LA and, TA}$) is the SCHA frequency. ρ is the mass density. In Eq. A.6 the in plane displacement vector $\mathbf{u}(\mathbf{q})$ is separated into longitudinal and transversal components $\mathbf{u}(\mathbf{q}) = u_{LA}(\mathbf{q})\hat{\mathbf{q}} + u_{TA}(\mathbf{q})\hat{\mathbf{q}}_{\perp}$, $\hat{\mathbf{q}}_{\perp}$ being the unitary vector perpendicular to $\hat{\mathbf{q}}$. F_U is the harmonic free energy of the harmonic trial potential \mathcal{U} . Now, by taking the derivative of the SCHA free energy with respect to the lattice constant and SCHA

2BFC, we arrive to the SCHA equations

$$\begin{aligned} \frac{\partial \mathcal{F}(\mathcal{U})}{\partial \delta a} = 0 &= 2\Omega(2\delta a + 3\delta a^2 + \delta a^3)(\lambda + \mu) + \frac{1}{2} \sum_{\mathbf{q}} g[\Omega_{ZA}^{(S)}(\mathbf{q})] 2(1 + \delta a)(\lambda + \mu)|\mathbf{q}|^2 \\ &+ \frac{1}{2} \sum_{\mathbf{q}} g[\Omega_{LA}^{(S)}(\mathbf{q})] [2(1 + \delta a)(\lambda + 2\mu)|\mathbf{q}|^2 + 2(1 + \delta a)(\lambda + \mu)|\mathbf{q}|^2] + \\ &\frac{1}{2} \sum_{\mathbf{k}} g[\Omega_{TA}^{(S)}(\mathbf{k})] [2(1 + \delta a)\mu|\mathbf{k}|^2 + 2(1 + \delta a/2)(\lambda + \mu)|\mathbf{k}|^2], \quad (\text{A.7}) \end{aligned}$$

$$\begin{aligned} \Phi_{ZA}(\mathbf{q}) &= \kappa|\mathbf{q}|^4 + 2(1 + \delta a/2)\delta a(\lambda + \mu)|\mathbf{q}|^2 + \frac{\lambda + 2\mu}{2\Omega} \sum_{\mathbf{k}} g[\Omega_{ZA}^{(S)}(\mathbf{k})] [|\mathbf{q}|^2|\mathbf{k}|^2 + 2(\mathbf{q} \cdot \mathbf{k})^2] + \\ &\frac{1}{2\Omega} \sum_{\mathbf{k}} \{g[\Omega_{LA}^{(S)}(\mathbf{k})] + g[\Omega_{TA}^{(S)}(\mathbf{k})]\} [\lambda|\mathbf{q}|^2|\mathbf{k}|^2 + 2\mu(\mathbf{q} \cdot \mathbf{k})^2], \quad (\text{A.8}) \end{aligned}$$

$$\begin{aligned} \Phi_{LA}(\mathbf{q}) &= (\lambda + 2\mu)|\mathbf{q}|^2 + 2(1 + \delta a/2)\delta a(\lambda + 2\mu)|\mathbf{q}|^2 + 2(1 + \delta a/2)\delta a(\lambda + \mu)|\mathbf{q}|^2 \\ &+ \frac{1}{2\Omega} \sum_{\mathbf{k}} g[\Omega_{ZA}^{(S)}(\mathbf{k})] [\lambda|\mathbf{q}|^2|\mathbf{k}|^2 + 2\mu(\mathbf{q} \cdot \mathbf{k})^2] + \frac{1}{4\Omega} \sum_{\mathbf{k}} \{4g[\Omega_{TA}^{(S)}(\mathbf{k})] [\lambda(\mathbf{q} \cdot \mathbf{k})^2 + \\ &\mu|\mathbf{q}|^2|\mathbf{k}|^2 + \mu(\mathbf{q} \cdot \mathbf{k})^2](\hat{\mathbf{q}}_{\perp} \cdot \hat{\mathbf{k}}) + \\ &2g[\Omega_{TA}^{(S)}(\mathbf{k})] [\lambda|\mathbf{q}|^2|\mathbf{k}|^2 + 2\mu(\mathbf{q} \cdot \mathbf{k})^2] + \\ &2g[\Omega_{LA}^{(S)}(\mathbf{k})] [\lambda|\mathbf{q}|^2|\mathbf{k}|^2 + 2\mu(\mathbf{q} \cdot \mathbf{k})^2] + \\ &4g[\Omega_{LA}^{(S)}(\mathbf{k})] [\lambda(\mathbf{q} \cdot \mathbf{k})^2 + \mu|\mathbf{q}|^2|\mathbf{k}|^2 + \mu(\mathbf{q} \cdot \mathbf{k})^2](\hat{\mathbf{q}} \cdot \hat{\mathbf{k}})\} \quad (\text{A.9}) \end{aligned}$$

and,

$$\begin{aligned} \Phi_{TA}(\mathbf{q}) &= \mu|\mathbf{q}|^2 + 2(1 + \delta a/2)\delta a\mu|\mathbf{q}|^2 + 2(1 + \delta a/2)\delta a(\lambda + \mu)|\mathbf{q}|^2 \\ &+ \frac{1}{2\Omega} \sum_{\mathbf{k}} g[\Omega_{ZA}^{(S)}(\mathbf{k})] [\lambda|\mathbf{q}|^2|\mathbf{k}|^2 + 2\mu(\mathbf{q} \cdot \mathbf{k})^2] + \frac{1}{4\Omega} \sum_{\mathbf{k}} \{4g[\Omega_{TA}^{(S)}(\mathbf{k})] [\lambda(\mathbf{q} \cdot \mathbf{k})^2 + \\ &\mu|\mathbf{q}|^2|\mathbf{k}|^2 + \mu(\mathbf{q} \cdot \mathbf{k})^2](\hat{\mathbf{q}}_{\perp} \cdot \hat{\mathbf{k}}_{\perp}) + \\ &4g[\Omega_{LA}^{(S)}(\mathbf{k})] [\lambda(\mathbf{q} \cdot \mathbf{k})^2 + \mu|\mathbf{q}|^2|\mathbf{k}|^2 + \mu(\mathbf{q} \cdot \mathbf{k})^2](\hat{\mathbf{q}}_{\perp} \cdot \hat{\mathbf{k}}) + \\ &2g[\Omega_{SCHA}^{(TA)}(\mathbf{k})] [\lambda|\mathbf{q}|^2|\mathbf{k}|^2 + 2\mu(\mathbf{q} \cdot \mathbf{k})^2]\}. \quad (\text{A.10}) \end{aligned}$$

We have solved this equations in a circular grid with 60×60 \mathbf{q} points with a radius of 1^{-1} by applying the Newton-Raphson method. We have checked the convergency of the results with denser grids. The parameters which have been calculated by using the atomistic empirical potential are the following: $\lambda = 4.32 \text{ eV}^{-2}$, $\mu = 9.32 \text{ eV}^{-2}$, $\kappa = 1.49 \text{ eV}$ and, $\rho/\hbar^2 = 1090.64 \text{ eV}^{-4}$.

Regarding the second derivative of the free energy, the physical phonons in the static approach, the most general formula for the correction to the SCHA phonon frequencies ($\mathbf{D}^{corr}(-\mathbf{q}, \mathbf{q}) = \mathbf{D}^{(F)}(-\mathbf{q}, \mathbf{q}) - \mathbf{D}^{(S)}(-\mathbf{q}, \mathbf{q})$) is

$$D_{\alpha\beta}^{corr}(-\mathbf{q}, \mathbf{q}) = \sum_{\gamma\delta\epsilon\zeta} \sum_{pk} {}^{(3)}D_{\alpha\gamma\delta}(-\mathbf{q}, \mathbf{p}, \mathbf{q} - \mathbf{p}) [1 - {}^{(4)}D_{\gamma\delta\epsilon\zeta}(-\mathbf{p}, \mathbf{p} - \mathbf{q}, \mathbf{k}, \mathbf{q} - \mathbf{k})]^{-1} {}^{(3)}D_{\epsilon\zeta\beta}(-\mathbf{k}, \mathbf{k} - \mathbf{q}, \mathbf{q}), \quad (\text{A.11})$$

where the subindexes run on the normal coordinates $\alpha, \beta, \gamma, \delta, \epsilon, \zeta = h, u_{LA}, u_{TA}$ and the dynamical matrices in normal coordinates are defined as

$${}^{(3)}D_{\alpha\beta\gamma}^{(S)}(\mathbf{q}, \mathbf{k}, \mathbf{p}) = \frac{1}{\rho^{3/2}} \left\langle \frac{\partial^3 V}{\partial \alpha(\mathbf{q}) \partial \beta(\mathbf{k}) \partial \gamma(\mathbf{p})} \right\rangle_{\rho_h} \sqrt{G_{\beta\gamma}(\mathbf{k}, \mathbf{p})}, \quad (\text{A.12})$$

$${}^{(4)}D_{\alpha\beta\gamma\epsilon}^{(S)}(\mathbf{q}, \mathbf{q}', \mathbf{k}, \mathbf{k}') = \frac{1}{\rho^2} \left\langle \frac{\partial^4 V}{\partial \alpha(\mathbf{q}) \partial \beta(\mathbf{q}') \partial \gamma(\mathbf{k}) \partial \epsilon(\mathbf{k}')} \right\rangle_{\rho_h} \sqrt{G_{\alpha\beta}(\mathbf{q}, \mathbf{k}) G_{\gamma\epsilon}(\mathbf{q}', \mathbf{k}')}. \quad (\text{A.13})$$

The matrix $G_{\alpha\beta}(\mathbf{q}, \mathbf{k})$ is defined as

$$G_{\alpha\beta}(\mathbf{q}, \mathbf{k}) = \frac{F(0, \Omega_{\alpha}^{(S)}(\mathbf{q}), \Omega_{\beta}^{(S)}(\mathbf{k}))}{\Omega_{\alpha}^{(S)}(\mathbf{q}) \Omega_{\beta}^{(S)}(\mathbf{k})}, \quad (\text{A.14})$$

$F(0, \Omega_{\alpha}^{(S)}(\mathbf{q}), \Omega_{\beta}^{(S)}(\mathbf{k}))$ being the function defined in Eq. 3.79. We are interested in the corrections to the out-of-plane modes, therefore, we are interested in the terms of the type

$$D_{hh}^{corr}(-\mathbf{q}, \mathbf{q}) = \sum_{\gamma\delta\epsilon\zeta} \sum_{pk} {}^{(3)}D_{h\gamma\delta}^{(S)}(-\mathbf{q}, \mathbf{p}, \mathbf{q} - \mathbf{p}) [1 - {}^{(4)}D_{\gamma\delta\epsilon\zeta}^{(S)}(-\mathbf{p}, \mathbf{p} - \mathbf{q}, \mathbf{k}, \mathbf{q} - \mathbf{k})]^{-1} {}^{(3)}D_{\epsilon\zeta h}^{(S)}(-\mathbf{k}, \mathbf{k} - \mathbf{q}, \mathbf{q}), \quad (\text{A.15})$$

By looking at Eq. A.5 we can see that only the terms of the type $\int_{\Omega} d^2x C^{ijkl} \partial_i u_j \partial_k h \partial_l h$ will contribute to the statistical average in Eq. A.12. Therefore, Eq. A.11 can be rewritten as

$$D_{hh}^{corr}(-\mathbf{q}, \mathbf{q}) = 4 \sum_{\alpha\beta} \sum_{pk} {}^{(3)}D_{hh\alpha}^{(S)}(-\mathbf{q}, \mathbf{p}, \mathbf{q} - \mathbf{p}) [1 - {}^{(4)}D_{h\alpha h\beta}^{(S)}(-\mathbf{p}, \mathbf{p} - \mathbf{q}, \mathbf{k}, \mathbf{q} - \mathbf{k})]^{-1} {}^{(3)}D_{hh\beta}^{(S)}(\mathbf{q}, -\mathbf{k}, \mathbf{k} - \mathbf{q}), \quad (\text{A.16})$$

where now the subindexes only run in $\alpha, \beta = u_{LA}, u_{TA}$. Now, we can calculate the statistical averages

$$\left\langle \frac{\partial^3 V}{\partial h(\mathbf{k}_1) \partial h(\mathbf{k}_2) \partial u_{LA}(\mathbf{k}_3)} \right\rangle_{\rho_h} = \frac{1 + \delta a}{\sqrt{\Omega}} \delta_{k_1+k_2+k_3,0} \left[\lambda |\mathbf{k}_3| \mathbf{k}_1 \cdot \mathbf{k}_2 + 2\mu \frac{(\mathbf{k}_3 \cdot \mathbf{k}_1)(\mathbf{k}_3 \cdot \mathbf{k}_2)}{|\mathbf{k}_3|} \right], \quad (\text{A.17})$$

$$\left\langle \frac{\partial^3 V}{\partial h(\mathbf{k}_1) \partial h(\mathbf{k}_2) \partial u_{TA}(\mathbf{k}_3)} \right\rangle_{\rho_h} = \frac{\mu(1 + \delta a)}{\sqrt{\Omega}} \delta_{k_1+k_2+k_3,0} \left[\frac{(\mathbf{k}_3 \cdot \mathbf{k}_1)(\mathbf{k}_{3\perp} \cdot \mathbf{k}_2) + (\mathbf{k}_3 \cdot \mathbf{k}_2)(\mathbf{k}_{3\perp} \cdot \mathbf{k}_1)}{|\mathbf{k}_3|} \right], \quad (\text{A.18})$$

$$\left\langle \frac{\partial^4 V}{\partial h(\mathbf{k}_1) \partial h(\mathbf{k}_2) \partial u_{LA}(\mathbf{k}_3) \partial u_{LA}(\mathbf{k}_4)} \right\rangle_{\rho_h} = \frac{1}{\Omega} \delta_{k_1+k_2+k_3+k_4,0} \frac{\mathbf{k}_3 \cdot \mathbf{k}_4}{|\mathbf{k}_3||\mathbf{k}_4|} [\lambda(\mathbf{k}_3 \cdot \mathbf{k}_4)(\mathbf{k}_1 \cdot \mathbf{k}_2) + \mu(\mathbf{k}_3 \cdot \mathbf{k}_1)(\mathbf{k}_4 \cdot \mathbf{k}_2) + \mu(\mathbf{k}_3 \cdot \mathbf{k}_2)(\mathbf{k}_4 \cdot \mathbf{k}_1)], \quad (\text{A.19})$$

$$\left\langle \frac{\partial^4 V}{\partial h(\mathbf{k}_1) \partial h(\mathbf{k}_2) \partial u_{TA}(\mathbf{k}_3) \partial u_{TA}(\mathbf{k}_4)} \right\rangle_{\rho_h} = \frac{1}{\Omega} \delta_{k_1+k_2+k_3+k_4,0} \frac{\mathbf{k}_{3\perp} \cdot \mathbf{k}_{4\perp}}{|\mathbf{k}_3||\mathbf{k}_4|} [\lambda(\mathbf{k}_3 \cdot \mathbf{k}_4)(\mathbf{k}_1 \cdot \mathbf{k}_2) + \mu(\mathbf{k}_3 \cdot \mathbf{k}_1)(\mathbf{k}_4 \cdot \mathbf{k}_2) + \mu(\mathbf{k}_3 \cdot \mathbf{k}_2)(\mathbf{k}_4 \cdot \mathbf{k}_1)], \quad (\text{A.20})$$

and

$$\left\langle \frac{\partial^4 V}{\partial h(\mathbf{k}_1) \partial h(\mathbf{k}_2) \partial u_{LA}(\mathbf{k}_3) \partial u_{TA}(\mathbf{k}_4)} \right\rangle_{\rho_h} = \frac{1}{\Omega} \delta_{k_1+k_2+k_3+k_4,0} \frac{\mathbf{k}_3 \cdot \mathbf{k}_{4\perp}}{|\mathbf{k}_3| |\mathbf{k}_4|} [\lambda(\mathbf{k}_3 \cdot \mathbf{k}_4)(\mathbf{k}_1 \cdot \mathbf{k}_2) + \mu(\mathbf{k}_3 \cdot \mathbf{k}_1)(\mathbf{k}_4 \cdot \mathbf{k}_2) + \mu(\mathbf{k}_3 \cdot \mathbf{k}_2)(\mathbf{k}_4 \cdot \mathbf{k}_1)]. \quad (\text{A.21})$$

The equations cannot be further simplified but we have all the ingredients to calculate them numerically. We have checked numerically that, as in the atomistic case, the contribution of $\overset{(4)}{D}$ is completely negligible.

By neglecting the fourth-order terms containing in-plane displacement fields in Eq. A.1, the SCHA can be applied analytically in this model. The SCHA equations simplify to

$$\delta a = -\frac{1}{4\Omega} \sum_{\mathbf{q}} |\mathbf{q}|^2 g[\Omega_{ZA}^{(S)}(\mathbf{q})], \quad (\text{A.22})$$

$$\Phi_{ZA}(\mathbf{q}) = \kappa |\mathbf{q}|^4 + 2\delta a(\lambda + \mu) |\mathbf{q}|^2 + \frac{\lambda + 2\mu}{2\Omega} \sum_{\mathbf{k}} g[\Omega_{ZA}^{(S)}(\mathbf{k})] [|\mathbf{q}|^2 |\mathbf{k}|^2 + 2(\mathbf{q} \cdot \mathbf{k})^2]. \quad (\text{A.23})$$

By inserting Eq. A.22 in Eq. A.23 and considering the infinite volume limit ($\Omega \rightarrow \infty$), we obtain

$$\Phi_{ZA}(\mathbf{q}) = \kappa |\mathbf{q}|^4 + \gamma |\mathbf{q}|^2, \quad (\text{A.24})$$

where γ is given by the solution of

$$\gamma = \gamma \frac{\lambda + 3\mu}{16\pi\kappa\sqrt{\rho\kappa}} \int_0^{\Lambda\sqrt{\kappa/\gamma}} ds \frac{s^2 \coth[\gamma s \sqrt{1+s^2}/(2T\sqrt{\rho\kappa})]}{\sqrt{1+s^2}}. \quad (\text{A.25})$$

Λ is an ultraviolet cutoff that avoids divergencies. Eqs. A.24 and A.25 show that the dispersion of the SCHA ZA modes is linear. By calculating the correction for getting the physical phonons in the static approach in Eq. A.16 (in this case the fourth-order tensor is 0) the result is

$$\Phi_{ZA}^{(F)}(\mathbf{q}) = \kappa |\mathbf{q}|^4 + (\gamma - \sigma) |\mathbf{q}|^2 + O(|\mathbf{q}|^4), \quad (\text{A.26})$$

where at $T = 0$ K

$$\sigma = \frac{\rho\sqrt{\gamma}}{8\pi\kappa^{3/2}} \sum_{\alpha=LA,TA} v_{\alpha} f(\Lambda\sqrt{\kappa/\gamma}, v_{\alpha}\sqrt{\rho/\gamma}), \quad (\text{A.27})$$

with

$$f(x, y) = \int_0^x ds \frac{s^2}{\sqrt{1+s^2} [\sqrt{1+s^2} + y]}. \quad (\text{A.28})$$

By setting the ultraviolet cutoff to the value of the Debye momentum, $\Lambda = \sqrt{\frac{8\pi}{3^{1/2}a_0}} = 1.55$, we obtain $1 - \sigma/\gamma = 20\%$. This means that the linear component of the Physical frequencies turns out to be a factor of 40% smaller than the one of the SCHA frequency. The non zero linear term in the physical frequencies appears because neglecting the fourth-order terms including in-plane displacements break the rotational invariance of the potential.

Appendix B

Interpolation of SSCHA dynamical matrices

In the SSCHA forces are calculated in supercells and, therefore, anharmonic dynamical matrices are obtained in a commensurate \mathbf{q} points grid. Computational costs increase enormously with the supercell size making dense sampling calculations extremely time-demanding. Therefore, whenever a fine sampling of the 1BZ is required, we have used the following interpolation scheme.

Let us call the anharmonic dynamical matrices obtained in the output of the SSCHA calculation in a coarse \mathbf{q} point grid (small supercell) $D_{coarse}^S(\mathbf{q})$. We will name the harmonic dynamical matrices obtained in the same grid as $D_{coarse}(\mathbf{q})$. Our goal is to obtain anharmonic dynamical matrices in a finer grid, written as $D_{fine}^{(S)}(\mathbf{q})$, by taking advantage of having the fine grid harmonic dynamical matrices $D_{fine}(\mathbf{q})$ already computed (which are faster to obtain than the anharmonic ones). Assuming that

$$\tilde{D}_{coarse}(\mathbf{q}) \equiv D_{coarse}^{(S)}(\mathbf{q}) - D_{coarse}(\mathbf{q}) \quad (\text{B.1})$$

is slowly varying in the reciprocal space (*i.e.* the differences between the SSCHA and the harmonic force constant matrices are more localized in real space than the harmonic force constant matrices) we can interpolate $\tilde{D}_{coarse}(\mathbf{q})$ using Fourier interpolation to the fine grid of our choice to obtain $\tilde{D}_{fine}(\mathbf{q})$. Now, it is straightforward to obtain

$$D_{fine}^{(S)}(\mathbf{q}) = D_{fine}(\mathbf{q}) + \tilde{D}_{fine}(\mathbf{q}). \quad (\text{B.2})$$

Appendix C

Mathematical proof of quadratic harmonic ZA dispersion

In this section we prove that the dispersion of the ZA phonon modes close to the point Γ is quadratic in the harmonic approximation.

For that purpose, by using the inversion symmetry and the ASR in Eq. 3.4 we will rewrite Eq. 3.8 in section 3.1 as

$$\begin{aligned}\phi_{s_1 s_2}^{\alpha_1 \alpha_2}(\mathbf{q}) &= \sum_{\mathbf{T}} \phi_{s_1 s_2}^{\alpha_1 \alpha_2}(\mathbf{T}, 0) e^{-i \mathbf{q} \cdot \mathbf{T}} = \\ \frac{1}{2} \sum_{\mathbf{T}} \phi_{s_1 s_2}^{\alpha_1 \alpha_2}(\mathbf{T}, 0) (e^{-i \mathbf{q} \cdot \mathbf{T}} + e^{i \mathbf{q} \cdot \mathbf{T}} - 2) &= -2 \sum_{\mathbf{T}} \phi_{s_1 s_2}^{\alpha_1 \alpha_2}(\mathbf{T}, 0) \sin^2(\mathbf{q} \cdot \mathbf{T}/2).\end{aligned}\quad (\text{C.1})$$

And by Taylor expanding this equation close to the point Γ we get

$$\phi_{s_1 s_2}^{\alpha_1 \alpha_2}(\mathbf{q}) \simeq -\frac{1}{2} \sum_{\alpha \beta} q_\alpha q_\beta \sum_{\mathbf{T}} \phi_{s_1 s_2}^{\alpha_1 \alpha_2}(\mathbf{T}) T_\alpha T_\beta + O(q^4), \quad (\text{C.2})$$

α, β being x, y , and z Cartesian components.

The fact that a material is bidimensional and the equilibrium atomic positions are contained in the $z = 0$ plane, makes that all the 2BFC of the type $\phi_{s_1 s_2}^{xz}(\mathbf{T}), \phi_{s_1 s_2}^{yz}(\mathbf{T})$ are zero. This is translated into the fact that the out-of-plane z direction is an eigendirection of the system and the harmonic frequency of the ZA mode is given by

$$\omega_{ZA}^2(\mathbf{q}) = \sum_{s_2} D_{1s_2}^{zz}(\mathbf{q}). \quad (\text{C.3})$$

Therefore, by looking at Eq. C.2 we can see that for proving that the dispersion of the ZA modes is quadratic we need to prove that $\sum_{\mathbf{T}} \phi_{s_1 s_2}^{zz}(\mathbf{T}) T_\alpha T_\beta = 0$. Actually, this equality is enforced by the rotational invariance of the system.

In conclusion, the 2D character of the 2BFC and the rotational invariance of the system make the harmonic dispersion of the ZA modes close to the point Γ to be quadratic.

Part V

Bibliography

Bibliography

- [1] Qiang Li, Zhiwei Lin, and Juan Zhou. "Thermoelectric materials with potential high power factors for electricity generation". In: *Journal of electronic materials* 38.7 (2009), pp. 1268–1272.
- [2] Jihui Yang and Thierry Caillat. "Thermoelectric materials for space and automotive power generation". In: *MRS bulletin* 31.3 (2006), pp. 224–229.
- [3] Francis J DiSalvo. "Thermoelectric cooling and power generation". In: *Science* 285.5428 (1999), pp. 703–706.
- [4] Dongliang Zhao and Gang Tan. "A review of thermoelectric cooling: materials, modeling and applications". In: *Applied Thermal Engineering* 66.1-2 (2014), pp. 15–24.
- [5] Xiao Zhang and Li-Dong Zhao. "Thermoelectric materials: Energy conversion between heat and electricity". In: *Journal of Materomics* 1.2 (2015), pp. 92–105.
- [6] Li-Dong Zhao et al. "Ultralow thermal conductivity and high thermoelectric figure of merit in SnSe crystals". In: *Nature* 508.7496 (2014), p. 373.
- [7] Gun-Ho Kim et al. "Engineered doping of organic semiconductors for enhanced thermoelectric efficiency". In: *Nature materials* 12.8 (2013), pp. 719–723.
- [8] Yanzhong Pei et al. "Stabilizing the optimal carrier concentration for high thermoelectric efficiency". In: *Advanced materials* 23.47 (2011), pp. 5674–5678.
- [9] Joseph P Heremans et al. "Enhancement of thermoelectric efficiency in PbTe by distortion of the electronic density of states". In: *Science* 321.5888 (2008), pp. 554–557.
- [10] Christopher J Vineis et al. "Nanostructured thermoelectrics: big efficiency gains from small features". In: *Advanced Materials* 22.36 (2010), pp. 3970–3980.
- [11] AJL Minnich et al. "Bulk nanostructured thermoelectric materials: current research and future prospects". In: *Energy & Environmental Science* 2.5 (2009), pp. 466–479.
- [12] Kuei Fang Hsu et al. "Cubic AgPbmSbTe_{2+m}: bulk thermoelectric materials with high figure of merit". In: *Science* 303.5659 (2004), pp. 818–821.
- [13] Huili Liu et al. "Ultrahigh thermoelectric performance by electron and phonon critical scattering in Cu₂Se_{1-x}I_x". In: *Advanced Materials* 25.45 (2013), pp. 6607–6612.
- [14] Wenke He et al. "Remarkable electron and phonon band structures lead to a high thermoelectric performance ZT> 1 in earth-abundant and eco-friendly SnS crystals". In: *Journal of Materials Chemistry A* 6.21 (2018), pp. 10048–10056.
- [15] David A Broido et al. "Intrinsic lattice thermal conductivity of semiconductors from first principles". In: *Applied Physics Letters* 91.23 (2007), p. 231922.

- [16] Paolo Giannozzi et al. "QUANTUM ESPRESSO: a modular and open-source software project for quantum simulations of materials". In: *Journal of physics: Condensed matter* 21.39 (2009), p. 395502.
- [17] Guilherme AS Ribeiro et al. "Strong anharmonicity in the phonon spectra of PbTe and SnTe from first principles". In: *Physical Review B* 97.1 (2018), p. 014306.
- [18] Lorenzo Paulatto, Francesco Mauri, and Michele Lazzeri. "Anharmonic properties from a generalized third-order ab initio approach: Theory and applications to graphite and graphene". In: *Physical Review B* 87.21 (2013), p. 214303.
- [19] Olle Hellman et al. "Temperature dependent effective potential method for accurate free energy calculations of solids". In: *Physical Review B* 87.10 (2013), p. 104111.
- [20] Mathias P Ljungberg and Jorge Íñiguez. "Temperature-Dependent Classical Phonons from Efficient Nondynamical Simulations". In: *Physical review letters* 110.10 (2013), p. 105503.
- [21] Ioan B Magdău and Graeme J Ackland. "Identification of high-pressure phases III and IV in hydrogen: Simulating Raman spectra using molecular dynamics". In: *Physical Review B* 87.17 (2013).
- [22] Ion Errea, Matteo Calandra, and Francesco Mauri. "First-principles theory of anharmonicity and the inverse isotope effect in superconducting palladium-hydride compounds". In: *Physical review letters* 111.17 (2013), p. 177002.
- [23] Ion Errea, Matteo Calandra, and Francesco Mauri. "Anharmonic free energies and phonon dispersions from the stochastic self-consistent harmonic approximation: Application to platinum and palladium hydrides". In: *Physical Review B* 89.6 (2014), p. 064302.
- [24] Raffaello Bianco et al. "Second-order structural phase transitions, free energy curvature, and temperature-dependent anharmonic phonons in the self-consistent harmonic approximation: Theory and stochastic implementation". In: *Physical Review B* 96.1 (2017), p. 014111.
- [25] Lorenzo Monacelli et al. "Pressure and stress tensor of complex anharmonic crystals within the stochastic self-consistent harmonic approximation". In: *Physical Review B* 98.2 (2018), p. 024106.
- [26] Kai Chang et al. "Discovery of robust in-plane ferroelectricity in atomic-thick SnTe". In: *Science* 353.6296 (2016), pp. 274–278.
- [27] Qian Zhang et al. "High thermoelectric performance by resonant dopant indium in nanostructured SnTe". In: *Proceedings of the National Academy of Sciences* 110.33 (2013), pp. 13261–13266.
- [28] Mickaël Lallart. *Ferroelectrics: Applications*. BoD–Books on Demand, 2011.
- [29] IP Batra, P Wurfel, and BD Silverman. "New type of first-order phase transition in ferroelectric thin films". In: *Physical Review Letters* 30.9 (1973), p. 384.
- [30] W Zhong, RD King-Smith, and David Vanderbilt. "Giant LO-TO splittings in perovskite ferroelectrics". In: *Physical review letters* 72.22 (1994), p. 3618.
- [31] Matthew Dawber, KM Rabe, and JF Scott. "Physics of thin-film ferroelectric oxides". In: *Reviews of modern physics* 77.4 (2005), p. 1083.
- [32] Dillon D Fong et al. "Ferroelectricity in ultrathin perovskite films". In: *Science* 304.5677 (2004), pp. 1650–1653.

- [33] DD Fong et al. "Stabilization of monodomain polarization in ultrathin PbTiO₃ films". In: *Physical review letters* 96.12 (2006), p. 127601.
- [34] Kai Chang et al. "Controlled switching of ferroelectric SnSe monolayers at room temperature". In: *arXiv preprint arXiv:2004.03884* (2020).
- [35] L Lindsay, DA Broido, and Natalio Mingo. "Flexural phonons and thermal transport in graphene". In: *Physical Review B* 82.11 (2010), p. 115427.
- [36] L. D. Landau and E. M. Lifshitz. *Statistical Physics*. Pergamon, 1980.
- [37] N David Mermin. "Crystalline order in two dimensions". In: *Physical Review* 176.1 (1968), p. 250.
- [38] Mikhail I Katsnelson and Annalisa Fasolino. "Graphene as a prototype crystalline membrane". In: *Accounts of chemical research* 46.1 (2013), pp. 97–105.
- [39] Richard M Martin and Richard Milton Martin. *Electronic structure: basic theory and practical methods*. Cambridge university press, 2004.
- [40] Neil W Ashcroft and N David Mermin. "Solid State Physics. Thomson Learning". In: *Inc., Florence* (1976).
- [41] John C Slater. "Note on Hartree's method". In: *Physical Review* 35.2 (1930), p. 210.
- [42] Pierre Hohenberg and Walter Kohn. "Inhomogeneous electron gas". In: *Physical review* 136.3B (1964), B864.
- [43] Walter Kohn and Lu Jieu Sham. "Self-consistent equations including exchange and correlation effects". In: *Physical review* 140.4A (1965), A1133.
- [44] David M Ceperley and BJ Alder. "Ground state of the electron gas by a stochastic method". In: *Physical Review Letters* 45.7 (1980), p. 566.
- [45] John P Perdew and Alex Zunger. "Self-interaction correction to density-functional approximations for many-electron systems". In: *Physical Review B* 23.10 (1981), p. 5048.
- [46] John P Perdew, Kieron Burke, and Matthias Ernzerhof. "Generalized gradient approximation made simple". In: *Physical review letters* 77.18 (1996), p. 3865.
- [47] MC Pyne et al. "Iterative minimization techniques for ab initio total-energy calculations: molecular dynamics and conjugate gradients". In: *Rev. Mod. Phys* 64.4 (1992), p. 1045.
- [48] Hendrik J Monkhorst and James D Pack. "Special points for Brillouin-zone integrations". In: *Physical review B* 13.12 (1976), p. 5188.
- [49] DR Hamann, M Schlüter, and C Chiang. "Norm-conserving pseudopotentials". In: *Physical Review Letters* 43.20 (1979), p. 1494.
- [50] Norman Troullier and José Luís Martins. "Efficient pseudopotentials for plane-wave calculations". In: *Physical review B* 43.3 (1991), p. 1993.
- [51] David Vanderbilt. "Soft self-consistent pseudopotentials in a generalized eigenvalue formalism". In: *Physical review B* 41.11 (1990), p. 7892.
- [52] Peter E Blöchl. "Projector augmented-wave method". In: *Physical review B* 50.24 (1994), p. 17953.
- [53] Gerald D Mahan. *Many-particle physics*. Springer Science & Business Media, 2013.

- [54] Max Born and Kun Huang. *Dynamical theory of crystal lattices*. Clarendon press, 1954.
- [55] HGA Hellmann. *Forces in molecules*. 1937.
- [56] Richard Phillips Feynman. "Forces in molecules". In: *Physical Review* 56.4 (1939), p. 340.
- [57] Stefano Baroni, Paolo Giannozzi, and Andrea Testa. "Green's-function approach to linear response in solids". In: *Physical Review Letters* 58.18 (1987), p. 1861.
- [58] Xavier Gonze. "Adiabatic density-functional perturbation theory". In: *Physical Review A* 52.2 (1995), p. 1096.
- [59] Stefano Baroni et al. "Phonons and related crystal properties from density-functional perturbation theory". In: *Reviews of Modern Physics* 73.2 (2001), p. 515.
- [60] RM Sternheimer. "Electronic polarizabilities of ions from the Hartree-Fock wave functions". In: *Physical Review* 96.4 (1954), p. 951.
- [61] Xavier Gonze and Changyol Lee. "Dynamical matrices, Born effective charges, dielectric permittivity tensors, and interatomic force constants from density-functional perturbation theory". In: *Physical Review B* 55.16 (1997), p. 10355.
- [62] Miguel Borinaga et al. "Anharmonicity and the isotope effect in superconducting lithium at high pressures: A first-principles approach". In: *Physical Review B* 96.18 (2017), p. 184505.
- [63] Yi Zhang et al. "Anomalous lattice dynamics near the ferroelectric instability in PbTe". In: *Physical review letters* 107.17 (2011), p. 175503.
- [64] TE Kidd et al. "Electron-hole coupling and the charge density wave transition in TiSe₂". In: *Physical review letters* 88.22 (2002), p. 226402.
- [65] Maxime Leroux et al. "Strong anharmonicity induces quantum melting of charge density wave in H-NbSe₂ under pressure". In: *Physical Review B* 92.14 (2015), p. 140303.
- [66] Olle Hellman and Igor A Abrikosov. "Temperature-dependent effective third-order interatomic force constants from first principles". In: *Physical Review B* 88.14 (2013), p. 144301.
- [67] Olle Hellman, IA Abrikosov, and SI Simak. "Lattice dynamics of anharmonic solids from first principles". In: *Physical Review B* 84.18 (2011), p. 180301.
- [68] CZ Wang, CT Chan, and KM Ho. "Tight-binding molecular-dynamics study of phonon anharmonic effects in silicon and diamond". In: *Physical Review B* 42.17 (1990), p. 11276.
- [69] Dong-Bo Zhang, Tao Sun, and Renata M Wentzcovitch. "Phonon quasiparticles and anharmonic free energy in complex systems". In: *Physical review letters* 112.5 (2014), p. 058501.
- [70] Nico de Koker. "Thermal conductivity of MgO periclase from equilibrium first principles molecular dynamics". In: *Physical review letters* 103.12 (2009), p. 125902.
- [71] David M Ceperley. "Path integrals in the theory of condensed helium". In: *Reviews of Modern Physics* 67.2 (1995), p. 279.

- [72] Ion Errea, Bruno Rousseau, and Aitor Bergara. "Anharmonic stabilization of the high-pressure simple cubic phase of calcium". In: *Physical review letters* 106.16 (2011), p. 165501.
- [73] Bartomeu Monserrat, ND Drummond, and RJ Needs. "Anharmonic vibrational properties in periodic systems: energy, electron-phonon coupling, and stress". In: *Physical Review B* 87.14 (2013), p. 144302.
- [74] Terumasa Tadano and Shinji Tsuneyuki. "Self-consistent phonon calculations of lattice dynamical properties in cubic SrTiO₃ with first-principles anharmonic force constants". In: *Physical Review B* 92.5 (2015), p. 054301.
- [75] Ionuț Georgescu and Vladimir A Mandelshtam. "Self-consistent phonons revisited. I. The role of thermal versus quantum fluctuations on structural transitions in large Lennard-Jones clusters". In: *The Journal of chemical physics* 137.14 (2012), p. 144106.
- [76] Sandra E Brown, Ionuț Georgescu, and Vladimir A Mandelshtam. "Self-consistent phonons revisited. II. A general and efficient method for computing free energies and vibrational spectra of molecules and clusters". In: *The Journal of chemical physics* 138.4 (2013), p. 044317.
- [77] Christopher E Patrick, Karsten W Jacobsen, and Kristian S Thygesen. "Anharmonic stabilization and band gap renormalization in the perovskite CsSnI₃". In: *Physical Review B* 92.20 (2015), p. 201205.
- [78] DJ Hooton. "LI. A new treatment of anharmonicity in lattice thermodynamics: I". In: *The London, Edinburgh, and Dublin Philosophical Magazine and Journal of Science* 46.375 (1955), pp. 422–432.
- [79] AA Maradudin and AE Fein. "Scattering of neutrons by an anharmonic crystal". In: *Physical Review* 128.6 (1962), p. 2589.
- [80] Matteo Calandra, Michele Lazzeri, and Francesco Mauri. "Anharmonic and non-adiabatic effects in MgB₂: Implications for the isotope effect and interpretation of Raman spectra". In: *Physica C: Superconductivity* 456.1-2 (2007), pp. 38–44.
- [81] Mois I Aroyo et al. "Crystallography online: Bilbao crystallographic server". In: *Bulg. Chem. Commun* 43.2 (2011), pp. 183–197.
- [82] Nicola Bonini et al. "Phonon anharmonicities in graphite and graphene". In: *Physical review letters* 99.17 (2007), p. 176802.
- [83] Wu Li et al. "ShengBTE: A solver of the Boltzmann transport equation for phonons". In: *Computer Physics Communications* 185.6 (2014), pp. 1747–1758.
- [84] Xavier Gonze and J-P Vigneron. "Density-functional approach to nonlinear-response coefficients of solids". In: *Physical Review B* 39.18 (1989), p. 13120.
- [85] Evgeny Mikhailovich Lifshitz, LP Pitaevskii, and VB Berestetskii. "Landau and Lifshitz Course of Theoretical Physics". In: *Statistical physics* 5 (1980).
- [86] Lorenzo Paulatto et al. "First-principles calculations of phonon frequencies, lifetimes, and spectral functions from weak to strong anharmonicity: The example of palladium hydrides". In: *Physical Review B* 91.5 (2015), p. 054304.
- [87] Ion Errea et al. "Quantum hydrogen-bond symmetrization in the superconducting hydrogen sulfide system". In: *Nature* 532.7597 (2016), p. 81.
- [88] Raffaello Bianco et al. "Quantum Enhancement of Charge Density Wave in NbS₂ in the Two-Dimensional Limit". In: *Nano letters* 19.5 (2019), pp. 3098–3103.

- [89] Unai Aseginolaza et al. "Phonon collapse and second-order phase transition in thermoelectric SnSe". In: *Physical review letters* 122.7 (2019), p. 075901.
- [90] Terry M Tritt. *Thermal conductivity: theory, properties, and applications*. Springer Science & Business Media, 2005.
- [91] Giorgia Fugallo et al. "Ab initio variational approach for evaluating lattice thermal conductivity". In: *Physical Review B* 88.4 (2013), p. 045430.
- [92] Rudolf Peierls. "Zur kinetischen theorie der wärmeleitung in kristallen". In: *Annalen der Physik* 395.8 (1929), pp. 1055–1101.
- [93] Joseph Callaway. "Model for lattice thermal conductivity at low temperatures". In: *Physical Review* 113.4 (1959), p. 1046.
- [94] J Yang et al. "Influence of electron-phonon interaction on the lattice thermal conductivity of Co 1- x Ni x Sb 3". In: *Physical Review B* 65.9 (2002), p. 094115.
- [95] John M Ziman. *Electrons and phonons: the theory of transport phenomena in solids*. Oxford university press, 2001.
- [96] A Sparavigna. "Lattice thermal conductivity in cubic silicon carbide". In: *Physical Review B* 66.17 (2002), p. 174301.
- [97] PG Klemens. "Thermal conductivity and lattice vibrational modes". In: *Solid state physics*. Vol. 7. Elsevier, 1958, pp. 1–98.
- [98] Giorgia Fugallo et al. "Thermal conductivity of graphene and graphite: collective excitations and mean free paths". In: *Nano letters* 14.11 (2014), pp. 6109–6114.
- [99] Andrea Cepellotti et al. "Phonon hydrodynamics in two-dimensional materials". In: *Nature communications* 6 (2015), p. 6400.
- [100] H Julian Goldsmid. *Introduction to thermoelectricity*. Vol. 121. Springer, 2010.
- [101] Kamran Behnia. *Fundamentals of thermoelectricity*. OUP Oxford, 2015.
- [102] S He Yang et al. "Nanostructures in high-performance (GeTe) x (AgSbTe2) 100- x thermoelectric materials". In: *Nanotechnology* 19.24 (2008), p. 245707.
- [103] JY Cho et al. "Thermoelectric properties and investigations of low thermal conductivity in Ga-doped Cu 2 GeSe 3". In: *Physical Review B* 84.8 (2011), p. 085207.
- [104] Olivier Delaire et al. "Giant anharmonic phonon scattering in PbTe". In: *Nature materials* 10.8 (2011), p. 614.
- [105] CW Li et al. "Phonon self-energy and origin of anomalous neutron scattering spectra in SnTe and PbTe thermoelectrics". In: *Physical review letters* 112.17 (2014), p. 175501.
- [106] Masashi Iizumi et al. "Phase transition in SnTe with low carrier concentration". In: *Journal of the Physical Society of Japan* 38.2 (1975), pp. 443–449.
- [107] Christopher D O'Neill et al. "Inelastic x-ray investigation of the ferroelectric transition in SnTe". In: *Physical Review B* 95.14 (2017), p. 144101.
- [108] IUrii Isaakovich Ravich. *Semiconducting lead chalcogenides*. Vol. 5. Springer Science & Business Media, 2013.
- [109] David Michael Rowe. *Thermoelectrics handbook: macro to nano*. CRC press, 2018.
- [110] K Adouby. "Structure and temperature transformation of SnSe. Stabilization of phase Sn4Bi2Se7". In: *Z. Kristallogr* 213 (1998), pp. 343–349.

- [111] T Chatopadhyay, J Pannetier, and HG Von Schnering. "Neutron diffraction study of the structural phase transition in SnS and SnSe". In: *Journal of Physics and Chemistry of Solids* 47.9 (1986), pp. 879–885.
- [112] Hans Georg Von Schnering and Heribert Wiedemeier. "The high temperature structure of β -SnS and β -SnSe and the B16-to-B33 type λ -transition path". In: *Zeitschrift für Kristallographie-Crystalline Materials* 156.1-4 (1981), pp. 143–150.
- [113] Tapan Chatterji et al. "Soft-phonon dynamics of the thermoelectric β -SnSe at high temperatures". In: *Physics Letters A* 382.29 (2018), pp. 1937–1941.
- [114] Antoine Dewandre et al. "Two-step phase transition in SnSe and the origins of its high power factor from first principles". In: *Physical review letters* 117.27 (2016), p. 276601.
- [115] D Ibrahim et al. "Reinvestigation of the thermal properties of single-crystalline SnSe". In: *Applied Physics Letters* 110.3 (2017), p. 032103.
- [116] S Sassi et al. "Assessment of the thermoelectric performance of polycrystalline p-type SnSe". In: *Applied Physics Letters* 104.21 (2014), p. 212105.
- [117] Cheng-Lung Chen et al. "Thermoelectric properties of p-type polycrystalline SnSe doped with Ag". In: *Journal of Materials Chemistry A* 2.29 (2014), pp. 11171–11176.
- [118] Jesús Carrete, Natalio Mingo, and Stefano Curtarolo. "Low thermal conductivity and triaxial phononic anisotropy of SnSe". In: *Applied Physics Letters* 105.10 (2014), p. 101907.
- [119] Jonathan M Skelton et al. "Anharmonicity in the High-Temperature Cmcm Phase of SnSe: Soft Modes and Three-Phonon Interactions". In: *Physical review letters* 117.7 (2016), p. 075502.
- [120] Hulei Yu, Shuai Dai, and Yue Chen. "Enhanced power factor via the control of structural phase transition in SnSe". In: *Scientific reports* 6 (2016), p. 26193.
- [121] Jean-Claude Toledano and Pierre Toledano. *The Landau theory of phase transitions: application to structural, incommensurate, magnetic and liquid crystal systems*. Vol. 3. World Scientific Publishing Company, 1987.
- [122] Danel Orobengoa et al. "AMPLIMODES: symmetry-mode analysis on the Bilbao Crystallographic Server". In: *Journal of Applied Crystallography* 42.5 (2009), pp. 820–833.
- [123] JM Perez-Mato, D Orobengoa, and MI Aroyo. "Mode crystallography of distorted structures". In: *Acta Crystallographica Section A: Foundations of Crystallography* 66.5 (2010), pp. 558–590.
- [124] Chen W Li et al. "Orbitally driven giant phonon anharmonicity in SnSe". In: *Nature Physics* 11.12 (2015), p. 1063.
- [125] Jiawang Hong and Olivier Delaire. "Electronic instability and anharmonicity in SnSe". In: *arXiv preprint arXiv:1604.07077* (2016).
- [126] Raffaello Bianco et al. "High-pressure phase diagram of hydrogen and deuterium sulfides from first principles: Structural and vibrational properties including quantum and anharmonic effects". In: *Physical Review B* 97.21 (2018), p. 214101.
- [127] Pai-Chun Wei et al. "Thermoelectric Figure-of-Merit of Fully Dense Single-Crystalline SnSe". In: *ACS omega* 4.3 (2019), pp. 5442–5450.

- [128] Pai-Chun Wei et al. "The intrinsic thermal conductivity of SnSe". In: *Nature* 539.7627 (2016), E1.
- [129] Ruiqiang Guo et al. "First-principles study of anisotropic thermoelectric transport properties of IV-VI semiconductor compounds SnSe and SnS". In: *Physical Review B* 92.11 (2015), p. 115202.
- [130] Qing Tan et al. "Thermoelectrics with earth abundant elements: low thermal conductivity and high thermopower in doped SnS". In: *Journal of Materials Chemistry A* 2.41 (2014), pp. 17302–17306.
- [131] Georg KH Madsen and David J Singh. "BoltzTraP. A code for calculating band-structure dependent quantities". In: *Computer Physics Communications* 175.1 (2006), pp. 67–71.
- [132] TJ Scheidemantel et al. "Transport coefficients from first-principles calculations". In: *Physical Review B* 68.12 (2003), p. 125210.
- [133] Julien Vidal et al. "Band-structure, optical properties, and defect physics of the photovoltaic semiconductor SnS". In: *Applied Physics Letters* 100.3 (2012), p. 032104.
- [134] Jonathan M Skelton et al. "Lattice dynamics of the tin sulphides SnS 2, SnS and Sn 2 S 3: Vibrational spectra and thermal transport". In: *Physical Chemistry Chemical Physics* 19.19 (2017), pp. 12452–12465.
- [135] JD Wasscher, W Albers, and C Haas. "Simple evaluation of the maximum thermoelectric figure of merit, with application to mixed crystals SnS_{1-x}Sex". In: *Solid-State Electronics* 6.3 (1963), pp. 261–264.
- [136] Sharmila N Shirodkar and Umesh V Waghmare. "Emergence of ferroelectricity at a metal-semiconductor transition in a 1 T monolayer of MoS 2". In: *Physical review letters* 112.15 (2014), p. 157601.
- [137] Ruixiang Fei, Wei Kang, and Li Yang. "Ferroelectricity and phase transitions in monolayer group-IV monochalcogenides". In: *Physical review letters* 117.9 (2016), p. 097601.
- [138] Lun Li et al. "Single-layer single-crystalline SnSe nanosheets". In: *Journal of the American Chemical Society* 135.4 (2013), pp. 1213–1216.
- [139] Shuli Zhao et al. "Controlled synthesis of single-crystal SnSe nanoplates". In: *Nano research* 8.1 (2015), pp. 288–295.
- [140] Fancy Qian Wang et al. "Thermoelectric properties of single-layered SnSe sheet". In: *Nanoscale* 7.38 (2015), pp. 15962–15970.
- [141] Zi-Yu Hu et al. "High thermoelectric performances of monolayer SnSe allotropes". In: *Nanoscale* 9.41 (2017), pp. 16093–16100.
- [142] Mehrshad Mehboudi et al. "Structural phase transition and material properties of few-layer monochalcogenides". In: *Physical review letters* 117.24 (2016), p. 246802.
- [143] Salvador Barraza-Lopez et al. "Tuning the ferroelectric-to-paraelectric transition temperature and dipole orientation of group-IV monochalcogenide monolayers". In: *Physical Review B* 97.2 (2018), p. 024110.
- [144] Kostya S Novoselov et al. "Electric field effect in atomically thin carbon films". In: *science* 306.5696 (2004), pp. 666–669.
- [145] Kostya S Novoselov et al. "Two-dimensional gas of massless Dirac fermions in graphene". In: *nature* 438.7065 (2005), pp. 197–200.

- [146] Kostya S Novoselov et al. "Two-dimensional atomic crystals". In: *Proceedings of the National Academy of Sciences* 102.30 (2005), pp. 10451–10453.
- [147] Yuanbo Zhang et al. "Experimental observation of the quantum Hall effect and Berry's phase in graphene". In: *nature* 438.7065 (2005), pp. 201–204.
- [148] Wei Kong et al. "Path towards graphene commercialization from lab to market". In: *Nature nanotechnology* 14.10 (2019), pp. 927–938.
- [149] Changgu Lee et al. "Measurement of the elastic properties and intrinsic strength of monolayer graphene". In: *science* 321.5887 (2008), pp. 385–388.
- [150] dS Ghosh et al. "Extremely high thermal conductivity of graphene: Prospects for thermal management applications in nanoelectronic circuits". In: *Applied Physics Letters* 92.15 (2008), p. 151911.
- [151] Jannik C Meyer et al. "The structure of suspended graphene sheets". In: *Nature* 446.7131 (2007), pp. 60–63.
- [152] Annalisa Fasolino, JH Los, and Mikhail I Katsnelson. "Intrinsic ripples in graphene". In: *Nature materials* 6.11 (2007), pp. 858–861.
- [153] Nicola Bonini, Jivtesh Garg, and Nicola Marzari. "Acoustic phonon lifetimes and thermal transport in free-standing and strained graphene". In: *Nano letters* 12.6 (2012), pp. 2673–2678.
- [154] Hengjia Wang and Murray S Daw. "Anharmonic renormalization of the dispersion of flexural modes in graphene using atomistic calculations". In: *Physical Review B* 94.15 (2016), p. 155434.
- [155] JH Los et al. "Scaling properties of flexible membranes from atomistic simulations: application to graphene". In: *Physical Review B* 80.12 (2009), p. 121405.
- [156] KV Zakharchenko, MI Katsnelson, and Annalisa Fasolino. "Finite temperature lattice properties of graphene beyond the quasiharmonic approximation". In: *Physical review letters* 102.4 (2009), p. 046808.
- [157] Eros Mariani and Felix Von Oppen. "Flexural phonons in free-standing graphene". In: *Physical review letters* 100.7 (2008), p. 076801.
- [158] Bruno Amorim et al. "Thermodynamics of quantum crystalline membranes". In: *Physical Review B* 89.22 (2014), p. 224307.
- [159] PL De Andres, F Guinea, and MI Katsnelson. "Bending modes, anharmonic effects, and thermal expansion coefficient in single-layer and multilayer graphene". In: *Physical Review B* 86.14 (2012), p. 144103.
- [160] Amjad Al Taleb et al. "Acoustic surface phonons of graphene on Ni (111)". In: *Carbon* 99 (2016), pp. 416–422.
- [161] Amjad Al Taleb et al. "Helium diffraction and acoustic phonons of graphene grown on copper foil". In: *Carbon* 95 (2015), pp. 731–737.
- [162] Amjad Al Taleb et al. "Resolving localized phonon modes on graphene/Ir (111) by inelastic atom scattering". In: *Carbon* 133 (2018), pp. 31–38.
- [163] Patrick Rowe et al. "Development of a machine learning potential for graphene". In: *Physical Review B* 97.5 (2018), p. 054303.
- [164] Max Dion et al. "Van der Waals density functional for general geometries". In: *Physical review letters* 92.24 (2004), p. 246401.
- [165] Vincenzo Barone et al. "Role and effective treatment of dispersive forces in materials: Polyethylene and graphite crystals as test cases". In: *Journal of computational chemistry* 30.6 (2009), pp. 934–939.

- [166] Monica Pozzo et al. "Thermal expansion of supported and freestanding graphene: lattice constant versus interatomic distance". In: *Physical review letters* 106.13 (2011), p. 135501.
- [167] Nicolas Mounet and Nicola Marzari. "First-principles determination of the structural, vibrational and thermodynamic properties of diamond, graphite, and derivatives". In: *Physical Review B* 71.20 (2005), p. 205214.
- [168] S Linas et al. "Interplay between Raman shift and thermal expansion in graphene: Temperature-dependent measurements and analysis of substrate corrections". In: *Physical Review B* 91.7 (2015), p. 075426.
- [169] Hiroyuki Kagi et al. "Proper understanding of down-shifted Raman spectra of natural graphite: Direct estimation of laser-induced rise in sample temperature". In: *Geochimica et Cosmochimica Acta* 58.16 (1994), pp. 3527–3530.
- [170] PingHeng Tan et al. "The intrinsic temperature effect of the Raman spectra of graphite". In: *Applied physics letters* 74.13 (1999), pp. 1818–1820.
- [171] I Calizo et al. "Temperature dependence of the Raman spectra of graphene and graphene multilayers". In: *Nano letters* 7.9 (2007), pp. 2645–2649.
- [172] Tjalling J Ypma. "Historical development of the Newton–Raphson method". In: *SIAM review* 37.4 (1995), pp. 531–551.
- [173] ZK Wang et al. "Brillouin scattering study of low-frequency bulk acoustic phonons in multilayer graphene". In: *Carbon* 46.15 (2008), pp. 2133–2136.